

Spring 2008

Micro, meso and macro materials processing using high-speed liquid projectiles

Veljko Samardzic

New Jersey Institute of Technology

Follow this and additional works at: <https://digitalcommons.njit.edu/dissertations>



Part of the [Mechanical Engineering Commons](#)

Recommended Citation

Samardzic, Veljko, "Micro, meso and macro materials processing using high-speed liquid projectiles" (2008). *Dissertations*. 867.
<https://digitalcommons.njit.edu/dissertations/867>

This Dissertation is brought to you for free and open access by the Theses and Dissertations at Digital Commons @ NJIT. It has been accepted for inclusion in Dissertations by an authorized administrator of Digital Commons @ NJIT. For more information, please contact digitalcommons@njit.edu.

Copyright Warning & Restrictions

The copyright law of the United States (Title 17, United States Code) governs the making of photocopies or other reproductions of copyrighted material.

Under certain conditions specified in the law, libraries and archives are authorized to furnish a photocopy or other reproduction. One of these specified conditions is that the photocopy or reproduction is not to be “used for any purpose other than private study, scholarship, or research.” If a user makes a request for, or later uses, a photocopy or reproduction for purposes in excess of “fair use” that user may be liable for copyright infringement,

This institution reserves the right to refuse to accept a copying order if, in its judgment, fulfillment of the order would involve violation of copyright law.

Please Note: The author retains the copyright while the New Jersey Institute of Technology reserves the right to distribute this thesis or dissertation

Printing note: If you do not wish to print this page, then select “Pages from: first page # to: last page #” on the print dialog screen



The Van Houten library has removed some of the personal information and all signatures from the approval page and biographical sketches of theses and dissertations in order to protect the identity of NJIT graduates and faculty.

ABSTRACT

MICRO, MESO AND MACRO MATERIAL PROCESSING USING HIGH-SPEED LIQUID PROJECTILES

by

Veljko Samardzic

The objective of this research is development of a knowledge base of materials processing by the impact of high-speed liquid projectiles. The work involved experimental study of generation and applications of high-speed liquid projectiles. The projectiles were generated by the launchers, which used gunpowder as an energy source. The experiments were carried out at the low (0.35g of the powder), middle (1.2g) and high (10g to 70g) levels of energy consumptions and at several different launchers modification.

Experimental investigation of effect of gun powder mass on energy of projectile was conducted for ductile and brittle targets. An array of experimental techniques for projectile's external ballistics investigation was developed. Laser Particle Velocimeter (PIV) and high speed filming were used for velocity measurements and visualization of images of water projectiles high speed filming revealed pulsing nature of projectile. A piezoelectric sensor and a pendulum were used to monitor the impact force and the projectile momentum.

Range of materials was investigated in this study. Namely, investigation of deformation, forming, micro-forming, and welding of ductile materials was carried out. Demolition and boring of brittle materials was performed. Modes and mechanisms of deformation of ductile and brittle materials were studied and explained. High plasticity, high rate of deformation, temperature at the impact zone, hardness and micro-hardness distribution and degree of deformation work for ductile materials were determined and

materials behavior knowledge base needed for materials processing was acquired. Modes and mechanisms of failure of ductile, brittle and composite materials were studied. Fractography study revealed three mechanisms: ductile overload fracture, brittle fracture and combination of the two. Six failure modes: brittle fracture, radial fracture, ductile hole growth, plugging, fragmentation and petaling were identified.

An array of material processing operations using high speed projectiles impact was investigated. Full scale experimental investigation of terminal ballistics of high speed water projectiles was performed. Material processing operations included: piercing of metals, piercing of composite targets, explosive set ups neutralization, demolition of brittle materials, boring of granite and marble, punching of steel plates, complex shape punching in steel, forging of metals on macro and meso scale. Mechanisms of punching and forming of metals were identified and proposed. Welding of similar and dissimilar metals was conducted and high potential for novel stitch and spot welding formations was confirmed. Micro scale materials processing investigation involved range of studies. Submillimeter geometry scale forming of metals, fine stamping, micron scale forming and micron scale extrusion investigation were conducted and validation of novel technologies was achieved. Full scale topography and surface characterization of generated geometries was conducted and obtained quality proved to be at a competitive level with existing technologies. State of the art methods were used for investigation of generated samples. Scanning electron microscopy, infinite focus microscopy, 3 D digital microscopy, optical microscopy, 3-D digital profiler, Knoop and Vickers micro hardness testers, nano hardness indenter were used for characterization of generated samples. Full scale characterization on all levels of conducted materials processing was conducted and effect

of high speed water projectile impact on mechanical properties of impacted materials was quantified and presented. Investigation of peculiarities of impact based micro-forming was conducted. The info acquired as result of investigation of geometry and topography of micro-forming processing. Accuracy of micro scale deformation was estimated, particularly it was shown that deviation of actual part from the die was at the acceptable level. Also was shown that size of generated parts was rather stable and roughness and waviness of the generated surfaces was in the acceptable range.

The foundation of knowledge base for liquid based forming, welding and demolition processes was developed and the process technology will be developed on the base of the acquired knowledge. Theory of impact based high rate material deformation was enhanced. The emerging industrial scale demolition, forming and welding technologies will utilize the acquired knowledge.

**MICRO, MESO AND MACRO MATERIALS PROCESSING USING
HIGH-SPEED LIQUID PROJECTILES**

**by
Veljko Samardzic**

**A Dissertation
Submitted to the Faculty of
New Jersey Institute of Technology
in Partial Fulfillment of the Requirements for the Degree of
Doctor of Philosophy in Mechanical Engineering**

Department of Mechanical Engineering

May 2008

Copyright © 2008 by Veljko Samardzic

ALL RIGHTS RESERVED

APPROVAL PAGE

**MICRO, MESO AND MACRO MATERIALS PROCESSING USING
HIGH-SPEED LIQUID PROJECTILES**

Veljko Samardzic

Dr. Ernest S. Geskin, Dissertation Advisor
Professor of Mechanical Engineering, NJIT
Date 12/17/07

Dr. Bernard Koplik, Committee Member
Professor of Mechanical Engineering, NJIT
Date 12/17/07

Dr. Rajpal Sodhi, Committee Member
Professor of Mechanical Engineering, NJIT
Date 12/17/07

Dr. Avraham Harnoy, Committee Member
Professor of Mechanical Engineering, NJIT
Date Dec. 17, 07

Dr. Nuggehalli Ravindra, Committee Member
Professor of Physics, NJIT
Date Dec. 17, '07

BIOGRAPHICAL SKETCH

Author: Veljko Samardzic
Degree: Doctor of Philosophy
Date: May 2008

Date of Birth:

Place of Birth:

Undergraduate and Graduate Education:

- Doctor of Philosophy in Mechanical Engineering, New Jersey Institute of Technology, Newark, NJ, 2007
- Bachelor of Science in Mechanical Engineering, New Jersey Institute of Technology, Newark, NJ, 2001
- Bachelor of Science in Aeronautical Engineering, Belgrade University, Belgrade, Yugoslavia, 1991

Major: Mechanical Engineering

Presentations and Publications:

Samardzic, V., Geskin, E. S., Atanov, G. A., Semko, A. N., G., Atanov, G. A., Semko, A. N., Kovaliov, A. V. (2007). Liquid Based Material Micro-Forming Technology. *ASM International Journal of Materials Engineering and Performance*, 16(3) p.p. 375-389.

Samardzic, V., Geskin, E. S., Atanov, G. A., Semko, A. N., G., Atanov, G. A., Semko, A. N., Kovaliov, A. V. (2007). Investigation of Material Welding Using the High Speed Liquid Impact. *ASM International Journal of Materials Engineering and Performance*, Accepted for publication.

Samardzic, V., Geskin, E. S., Atanov, G. A., Semko, A. N., G., Atanov, G. A., Semko, A. N., Kovaliov, A. V. (2007). Investigation of Liquid Impact Based Macro, Meso and Micro-Forming processes. *ASM International Journal of Materials Engineering and Performance*, Accepted for publication.

- Samardzic, V., Geskin, E. S., Atanov, G. A., Semko, A. N., Kovaliov, A. V. (Aug. 2007). Investigation of the Metal Processing Using a High Speed Liquid Impact. (Aug.2007). *Proceedings of the 2007 Waterjet Technology Conference*. Houston, TX.
- Samardzic, V., K.Kluz, Petrenko,O.P,Geskin, E. S., Mazurkievitz, M., Berger,A., (Aug. 2007). Investigation of Granite Boring Using a High-Speed Liquid Impact. (Aug.2007). *Proceedings of the 2007 Waterjet Technology Conference*. Houston, TX.
- Samardzic, V., Geskin, E. S., Atanov, G. A., Semko, A. N., Kovaliov, A. V. (Aug. 2007). Investigation of the Micro-Forming of Metal in the Course of High speed Liquid Impact. (Aug.2007). *Proceedings of the 2007 Waterjet Technology Conference*. Houston, TX.
- Geskin, E. S, Samardzic, V., Petrenko O. P., Bitadse, T. G., Atanov, G. A., Semko, A. N., Kovaliov, A. V, Rusanova, O. A. (2005). Feasibility Study of the Solid Freeform Fabrication of Heterogeneous Parts Using the Liquid Impact // *Proceedings of 2005 NSF DMII Grantees Conference*. Scottsdale, Arizona.
- Samardzic, V., Petrenko,O.P., Geskin, E. S., Petrova, R. S.,(2005). Investigation of Residual Metal Deformation in the Course of ballistic Testing. *Material Science&Technology* 2005, Pittsburgh, PA.
- Samardzic, V., Geskin, E. S., (Nov. 2005). Feasibility study of High Rate Room Temperature Material Processing Using Liquid Impact. *Sigma Xi Annual Meeting and Student Research Conference 2005*, Seattle,WA.
- Samardzic, V., Petrenko, O. Geskin, E. S., Atanov, G. A., Semko, A. N., Kovaliov, A. V, (2005). Inovative Jet-based Material Processing Technology (Aug. 2005). *Proceedings of the 2005 Waterjet Technology Conference*. Houston, TX.
- Samardzic, V., Petrenko, O. Geskin, E. S., Atanov, G. A., Semko, A. N., Kovaliov, A. V, (2005). Examination of Metal Transformation in the Course of High Speed Liquid Impact. *Annual SJU Sigma Xi Student Research Symposium 2005*, Philadelphia, PA.
- Samardzic, V., Petrenko, O. Geskin, E. S., (2005). Investigation of Material Processing by high Speed Liquid Projectiles *Procedings of Einstein in the City Student Research Conference, 2005*, The City College of New York, NY, April 2005.
- Samardzic, V., Petrenko, O. Geskin, E. S., (2005). Investigation of Material Processing by high Speed Liquid Projectiles, *Poster presentation a Einstein in the City Student Research Conference, 2005*, The City College of New York, NY, April 2005.
- Samardzic, V., Geskin, E. S., (Feb. 2005). Solid Free Form fabrication Using A Liquid Impact . *TMS Annual Meeting 2005*, San Francisco, CA.

- Atanov, G. A., Semko, A. N., Geskin, E. S., Samardzic, V., Kovaliov, A. V, Petrenko, O., (2004). Investigation of Material Piercing by Liquid Impact, *Kiev Journal of Hydrodynamics*, Aug. 2004, Kiev, Ukraine.
- Kluz, K., Geskin, E. S., Samardzic, V., Shishkin, D.V., Goldenberg, B., (2003), Investigation of Heat Transfer and Thermodynamics in the Course of Ice Powder Formation. *Proceedings of IMECE'03: 2003 ASME International Mechanical Engineering Congress & Exposition*. Washington, D.C. November 16-21, 2003.
- Petrenko, O. P., Samardzic, V., Geskin, E. S., Atanov, G. A., Semko, A. N., Goldenberg, B. (Aug. 2003). Investigation of High-Speed Water Slugs. *Proceedings of the 2003 Waterjet Technology Conference*. Houston, TX.
- Atanov, G. A., Semko, A. N., Petrenko, O. P., Geskin, E. S., Samardzic, V. Goldenberg, B. (Nov. 16-21, 2003). Peculiarities of the Powder Hydrocannon Operation. *Proceedings of IMECE'03: 2003 ASME International Mechanical Engineering Congress & Exposition*. Washington, D.C.
- Petrenko, O. P., Geskin E. S., Samardzic, V., Golodenberg, B., Atanov, G. A., Semko, A. N., Kovalev, A. V. (2003). Numerical and Experimental Investigation of Formation and Application of High Speed Slugs. Presentation at *NSF Grantees conference*. Birmingham, AL.
- Petrenko, O. P., Samardzic, V., Geskin, E. S., Goldenberg, B., Atanov, G. A., Semko, A. N., (Nov. 2003). Application of High-Speed Water Slug Technology in Security Tasks. Presentation at *Symposium on homeland security*. New Brunswick, NJ.
- Geskin, E. S., Goldenberg, B., Petrenko, O. P., V. Samardzic, Atanov, G. A., Semko, A. N. (Jan. 2002). Investigation of Material Fracturing by High-Speed Water Slugs. Presentation at *Annual Meeting of National Science Foundation Division of Design Manufacturing and Innovating Engineering*. San Juan, Puerto Rico.
- Geskin, E. S., Goldenberg, B., Petrenko, O. P., V. Samardzic, Atanov, G. A., Semko, A. N., (Jan 2003). Investigation of Material Fracturing by High-Speed Water Slugs. Presentation at *Annual Meeting of National Science Foundation Division of Design Manufacturing and Innovating Engineering*. Birmingham, AL.
- Geskin, E. S., Goldenberg, B., Petrenko, O. P., Samardzic, V, Atanov, G. A., Semko, A. N. (Jan 2004). Investigation of Material Fracturing by High-Speed Water Slugs. Presentation at *Annual Meeting of National Science Foundation Division of Design Manufacturing and Innovating Engineering*, Dallas, TX.

To my late father, Radoje, my lovely mother, Ljeposava,
My sister, Zorka and her family,
My brothers, Zoran and Strahinja and their families.

ACKNOWLEDGEMENT

I would like to express my sincere gratitude to my research advisor, Professor Ernest Geskin, for his remarkable guidance, friendship and moral support throughout this research. His gentle guidance made a difference during difficult and pleasant times.

I express special thanks to Professors Bernard Koplik, Rajpal Sodhi, Avraham Harnoy and Nuggehalli Ravindra for the help and suggestions, for their warm and humble guidance, and for serving as members of the committee. I

As a recipient of two Civilian Research Development Foundation Junior Scientist Travel Fellowships, I would like to express warm thanks to the Civilian Research Development Foundation project directors William Freeman and Adam Easter whose true support and readiness to help in every way made a difference during my two trips to Ukraine. These trips resulted in fruitful corroboration. I would like to express thanks to the collaborating team from Dontetsk National University: Dr. Gennadiy Atanov, Mr. Anatoliy Kovalov and Dr. Aleksandr Semko.

I would like to express appreciation to all the helpful colleagues in the Department of Mechanical Engineering, Oleg Petrenko, Boris Goldenberg, and K. Kluz. I appreciate the help of the Graduate Studies office staff especially Dr. Ronald Kane and Mrs. Clarisa Gonzalez-Lenahan.

Finally, I would like to thank everybody who was supportive and helpful during these years, first of all my family for the exceptional support and encouragement.

TABLE OF CONTENTS

Chapter	Page
1 INTRODUCTION	1
1.1 Background Information.....	1
1.2 Survey of Literature.....	2
1.2.1 Compressed-Water Cannons for Civil Engineering [32]	2
1.2.2 High Speed Impact of Liquid Jets on Solids [33].....	4
1.2.3 The Impulsive Water Jet Device: A New Machine for Breaking Rocks [34]	6
1.2.4 Impulsive Hydrodynamic Method of Breaking Rocks and Concrete [35]	8
1.2.5 Water Jet Driven Shock Waves in Gases [36].....	10
1.2.6 Cavitation and Erosion in Submerged Water Jet [37].....	10
1.2.7 Flow Characteristics and Impact Phenomena of Pulsed Water Jets [38]	10
2 EXTERNAL BALLISTICS OF HIGH SPEED WATER PROJECTILES.....	12
2.1 Objectives and Introduction.....	12
2.2 Particle Image Velocimetry	13
2.3 Projectile Reaction Force Measurements	17
2.4 High Speed Filming for Velocity Measurements and Imaging of Ultra High Speed Water Projectiles	18
2.5 Pulsing Nature of Ultra High Speed Water Projectiles	34
2.6 Laser Beam Projectile Interception Velocity Measurement.....	38
2.6.1 Velocity Measurement.....	38

TABLE OF CONTENTS
(Continued)

Chapter	Page
2.6.2 Velocity and Momentum Measurement	41
2.7 Conclusion	44
3 INVESTIGATION OF PROJECTILE ENERGY	45
3.1 Introduction	45
3.2 Experimental Technique	45
3.3 Experimental Investigation of Effect of Water-Projectile Mass on Energy of Projectile	46
3.4 Experimental Investigation of Effect of Gun Powder Mass on Energy of Projectile	48
3.5 Analytical Investigation of Effect of Water-Projectile Mass on Energy of Projectile	49
3.6 Analytical Investigation of Effect of Gun Powder Mass on Energy of Projectile	52
3.7 Conclusion	55
4 INVESTIGATION OF RESIDUAL DEFORMATION OF METALS IN THE COURSE OF LIQUID IMPACT	56
4.1 Introduction	56
4.2 Experimental Procedure	57
4.3 Piercing of Metal Plates	58
4.4 Characterization of Deformation of Pierced Plates	60
4.5 Mechanism of Piercing of Metals	69
4.6 Conclusion	70
5 INVESTIGATION OF FAILURE OF MATERIALS UNDER HIGH SPEED LIQUID IMPACT	71

TABLE OF CONTENTS
(Continued)

Chapter	Page
5.1 Introduction	71
5.2 Failure of Metals Under High Speed Liquid Impact	71
5.3 Modes of Failure of Materials Under High Speed Liquid Impact.....	79
5.4 Discussion of Results and Conclusions	83
6 FORMING OF METALS USING HIGH SPEED WATER PROJECTILES.....	84
6.1 Introduction	84
6.2 Experimental Procedure	84
6.3 Experimental Investigation of Punching of Steel Plates	85
6.3.1 Punching of Circular Openings	85
6.3.2 Experimental Study of Complex Shape Openings in Steel	93
6.3.3 Mechanism of Punching of Steel Plates	95
6.4 Experimental Study of Forging by High Speed Water Projectiles.....	100
6.5 Mechanism of Forging of Steel Plates.....	106
6.6 Discussion of Results.....	107
6.7 Conclusions	108
7 LIQUID IMPACT BASED MICRO AND MESO FORMING TECHNOLOGY... 109	
7.1 Introduction	109
7.2 Existing Micro-Forming Technologies	111
7.3 Experimental Technique.....	112
7.4 Details of an Experimental Procedure and Results	114
7.4.1 Formation of Sub Millimeter Scale Grooves.....	114

TABLE OF CONTENTS
(Continued)

Chapter	Page
7.4.2 Fine Stamping.....	121
7.4.3 Microns Scale Forming	124
7.4.4 Micron Scale Extrusion	133
7.5 Discussion of Results.....	139
7.6 Conclusions	141
8 INVESTIGATION OF GEOMETRY OF GENERATED MICROPARTS	142
8.1 Introduction	142
8.2 Measurement of Generated Surface Areas	142
8.3 Measurement of Extruded Volume.....	143
8.4 Investigation of Geometry Complacence between Die and Product	147
8.5 Discussion of Results and Conclusions	151
9 MECHANICAL PROPERTIES OF FORMED METAL SURFACE	152
9.1 Introduction	152
9.2 Experimental Procedure and Results.....	152
9.3 Discussion and Conclusions	157
10 WELDING OF SIMILAR AND DISSIMILAR METALS USING IMPACT OF HIGH SPEED WATER PROJECTILES	158
10.1 Introduction	158
10.2 Experimental Procedure	158
10.3 Experimental Results.....	160
10.4 Nondestructive Testing.....	165

TABLE OF CONTENTS
(Continued)

Chapter	Page
10.5 Discussion of Results.....	175
10.6 Conclusions	178
11 INVESTIGATION OF GRANITE BORING USING HIGH SPEED LIQUID PROJECTILES	179
11.1 Introduction	179
11.2 Experimental Procedure	181
11.3 Experimental Results.....	184
11.3.1 Investigation of the Effect of the Standoff Distance on the Granite Excavation (Figs 11.4-11.6)	184
11.3.2 Investigation of the Water Load on the Material Removal	185
11.3.3 Investigation of the Granite Boring Same Site Impact (Figs. 11.9, 11.11).....	185
11.3.4 Investigation of the Granite Boring (Figs. 11.12, 11.13)	185
11.3.5 Investigation of the Granite Boring Using Distributed Impacts (Figs. 11.14-11.17)	186
11.3.6 Investigation of the Stress Induced on a Granite Target (Fig. 11.18) ...	187
11.3.7 Investigation of the Granite Removal Using Low power Projectile	187
11.3.8 Investigation of Marble Removal by a Water Projectile (Fig. 11.19) ...	187
11.3.9 Investigation of Size Distribution of the Granite Particles Generated in the Course of a Single Shot	188
11.3.10 High Speed Filming of the Projectile Motion (Fig. 11.20)	188
11.4 Evaluation of the Feasibility of the Use of a Launcher as a Boring Tool	188
11.5 Conclusions	190

TABLE OF CONTENTS
(Continued)

Chapter	Page
11.6 Nomenclature.....	191
12 CONCLUSIONS	202
REFERENCES	204

LIST OF TABLES

Table	Page
2.1 Projectile's Forefront Velocity Statistics.....	31
2.2 Summarized Data of Observed Pulsing Projectiles.....	36
2.3 Experimental Results of Standoff Distance Investigation.....	40
2.4 Experimental Results of Velocity Measurements	43
3.1 Results of Punching of 4mm Steel Plates.....	48
3.2 Results of Computations of Parameters of Water Projectile for Various Water Loads Masses	50
3.3 Results of Computations of Parameters of Water Projectile for Various Gun Powder Masses	53
6.1 Punching of Steel Experimental Results (Figures 6.5, 6.6, 6.7, 6.8, 6.9, and 6.10).....	88
6.2 Forming of Steel Experimental Results.....	105
7.1 Designed Parameters of the Grooves to be Generated on the Die Surface. Notice Difference in Groove Geometry at Different Sections	116
8.1 Examples of Measurements of Increase in Formed Surface Area.....	144
8.2 Examples of Measurements of Extruded Volume	146
9.1 Results from Nano-Indentation Testing of Brass Sample, Showing Increased Hardness Inside Track When Compared to the Top Surface of Sample.....	154
9.2 Results from Nano-Indentation Testing of Steel Sample, Showing Increased Hardness Inside Track When Compared to the Top Surface of Sample.....	155
9.3 Results from Nano-Indentation Testing of Steel Sample, Showing Increased Hardness Inside Track When Compared to the Top Surface of Sample	156
10.1 Experimental Results of Welding by Water Projectile Impact.....	164

LIST OF FIGURES

Figure	Page
2.1 Experimental set up for measurements of high speed water slug.....	14
2.2 Conceptual schematic of PIV operation (LaVision).....	15
2.3 Images of sequential projectile development in the air obtained by 2-D PIV: a) jet exiting the nozzle; b) SOD=21.5mm, average velocity=128.3m/s;c) and d) SOD=36mm, average velocity =200m/s; e) SOD=84mm, average velocity=500m/s.	16
2.4 Stand of distance vs. projectile forefront velocity for extruder testing.	17
2.5 Schematic of set up for projectile reaction force measurement.....	18
2.6 Schematic of set up for high speed filming for velocity measurements.....	19
2.7 Development of water projectile between nozzle exit and slug-target interface for stand of distance 20 cm.....	20
2.8 Velocity vs. distance dependence for SOD=20cm.	21
2.9 Distance vs. time dependence for SOD=20cm.....	22
2.10 Bell curve distribution of projectile's forefront velocity for SOD= 20cm.....	22
2.11 Development of water projectile between nozzle exit and slug-target interface for stand of distance of 60cm.	23
2.12 Velocity (m/s) vs. distance (mm) dependence for SOD=60cm.....	24
2.13 Distance (mm) vs. time (μ s) chart for SOD=60cm.	24
2.14 Bell curve distribution of projectile's forefront velocity for SOD=60cm.....	25
2.15 Development of water projectile between nozzle exit and slug-target interface for stand of distance of 40cm.	26
2.16 Velocity (m/s) vs. distance (mm) chart for SOD=40cm.....	27
2.17 Distance (mm) vs. time (μ s) chart for SOD=40cm.	27
2.18 Bell curve distribution of projectile's forefront velocity for SOD=40cm.....	28
2.19 Development of water projectile between nozzle exit and slug-target interface for stand of distance of 16cm.	29

LIST OF FIGURES

Figure	Page
2.20 Velocity (m/s) vs. distance (mm) chart for SOD=16cm.....	30
2.21 Distance (mm) vs. time (μ s) chart for SOD=16cm.	30
2.22 Bell curve distribution of projectile's forefront velocity for SOD=16cm.....	31
2.23 Development of water projectile generated by medium launcher nozzle.	32
2.24 Development of water projectile generated by medium launcher nozzle for stand of distance of 26.6cm.	33
2.25 Development of water projectile generated by water extruder for stand off distance of 32cm.....	34
2.26 Schematic interpretation of pulsing development of water projectile.....	35
2.27 Pulsing flow left cavity indicating two pulses.....	37
2.28 Pulsing flow left cavity indicating one pulse.	38
2.29 Schematic of experimental set up: 1 - HC, 2-jet, 3- laser beam sources, 4- velocity measuring system, 5- laser beams, intercepting the projectile, 6- target.	39
2.30 Water jet, 2 – laser beams, 3 – speedometer, 4- pendulum, 5 – water cannon....	41
2.31 Schematic of experimental set up: 1 –water cannon, 2 – first laser beam, 3 – second laser beam, 4 –ballistic pendulum, 5-water projectile.....	42
3.1 Schematic of the experimental setup. Notice that mounting of the target on a ballistic pendulum allows measuring the impact momentum.....	45
3.2 Working sample-1, clamping plate-2, die holder-3, die-4, high speed liquid projectile-5.....	47
3.3 Dependence of maximal outflow velocity and maximal pressure in the nozzle on the water projectile mass (40g to 250g).....	51
3.4 Dependence of projectile impulse on water projectile mass.	51
3.5 Dependence of pendulum displacement angle on water projectile mass.	52
3.6 Dependence of maximal outflow velocity and maximal pressure in the nozzle on the gun powder mass (10g to 72g).....	54

LIST OF FIGURES

Figure	Page
3.7 Dependence of projectile impulse on gun powder mass.	54
3.8 Dependence of pendulum displacement angle on water projectile mass.	55
4.1 Metal plates piercing experimental set up schematic..	57
4.2 Side view of three 4.8 mm steel plates simultaneously pierced by 230g water-slug with 64.69g of riffle powder charge; b) Top view of back plate.	60
4.3 a) Two 9.9 mm thick Aluminum plates pierced by 230g water- with 57g of powder; b) Captured fragments; c) Top view of front plated) Top view of back plate.	62
4.4 Metal plates piercing experimental set up schematic..	64
4.5 A 3-D reproduction of upper surface of deformed plate	64
4.6 Percent elongation in longitudinal (X-axes, above) and transversal direction (Y-axes, below).	66
4.7 Node displacements in impact direction (Z –axes).	67
4.8 Microstructure from non-deformed and fracture zones in transversal direction.	68
4.9 Schematic of phases of piercing: 1- initial state, 2-beginning of plastic deformation, 3-plastic dome forming, and 3-final shape forming.....	69
5.1 General view of 4.8mm thick steel plate pierced by 230g water projectile.	72
5.2 Fractograph (X1000) generated from fractured surface of steel plate shown on Fig. 5.1. Ductile overload is the failure mode corresponding to the shown field of view.	73
5.3 SEM micrograph (X1100) of solidified egg like droplet formed in the final stage of steel failure.....	74
5.4 SEM micrograph (X950) of solidified spill like droplet formed in the final stage of steel failure.....	74
5.5 SEM micrograph (X750) of solidified combination of egg like droplet and pipe like formed in the final stage of steel failure.	76

LIST OF FIGURES

Figure	Page
5.6 SEM micrograph (X950) of solidified spill like droplet formed in the final stage of steel failure.....	77
5.7 SEM micrograph (X950) of solidified spill like droplet formed in the final stage of steel failure.....	77
5.8 SEM micrograph (X950) of solidified spill like droplet formed in the final stage of steel failure.....	78
5.9 3-D image of portion fractured surface of aluminum plate. The appearance is typical for brittle fracture.....	79
5.10 Graphic representation of ductile hole growth mode of failure (see Fig 3.27) ...	80
5.11 Graphic representation of radial fracture mode of failure (see Fig. 5.4d).....	80
5.12 Graphic representation of plugging mode of failure (see Figs 6.7 and 6.18).....	81
5.13 Graphic representation of fragmentation mode of failure (see Fig 4.4 c).	81
5.14 Graphic representation of petaling mode of failure (see Figs. 4.3 and 5.1).	82
5.15 Example of brittle fracture mode of failure (concrete demolition).	82
6.1 Sample-1, clamping plate-2, die holder-3, die-4, high speed liquid projectile-5.	85
6.2 Piercing of 4mm steel plates. Notice feasibility of generating different openings using the same jet.	86
6.3 Dies for punching of metals, diameters 25, 16.5 and 12mm.....	87
6.4 Impact side views of punched openings in plates 4, 8 and 10mm thick. Punching was done against die opening 25mm in diameter.....	89
6.5 Punched opening of 10mm thick steel plate against 25mm diameter opening of die. Exit (25mm) and impact side (22.5mm) views.	90
6.6 A 10 mm thick plate with 25mm punched opening with punched part.....	91
6.7 Impact side views of punched openings in plates 8, 6 and 4mm thick. Punching was performed against die opening of 16.5mm in diameter.	91
6.8 Projectile exit-side view of punched openings in plates 8, 6 and 4mm thick. Punching was done against die opening 16.5mm in diameter.....	91

LIST OF FIGURES

Figure	Page
6.9 Example of punching of 4 mm thick steel plate against die of 45mm diameter. Punched piece was barely holding on the plate.....	92
6.10 Piercing of spring steel. Notice feasibility of precision deformation of a difficult-to-shape material. $h=3.175\text{mm}$, $D=10\text{mm}$..	93
6.11 Formation of shaped openings using a round jet. Notice that the workpiece thickness does not affect the accuracy of the piercing..	93
6.12 Formation of triangular openings using a round jet. Notice that the workpiece thickness does not affect the accuracy of the piercing.	94
6.13 Formation of the multiple openings by a single impact of a round jet. Steel sheet thickness is 2.5mm and the opening diameter is 4mm. Notice that the liquid penetration into the workpiece can be controlled by the impact condition.....	94
6.14 Failed punching of 10mm thick steel plate against 16.5mm die diameter. Impacted and die side views.....	95
6.15 Schematic presentation of characteristics of punched hole.....	96
6.16 Schematic presentation of characteristics of punched hole and the blank.	97
6.17 Cross-section of uncompleted punching of two 4mm diameter holes (see Fig.6.14).	99
6.18 Adiabatic shear bands in intermediate phase of blanking of steel.....	99
6.19 Dies for forming.	100
6.20 Concentric grooves (1mm deep, with 2mm pitch and 90 degrees inclination) on a 2.5mm thick steel plate formed by the impact of 200g of water against the die. Notice the compliance of the die and the part geometry.	101
6.21 . Results of forming of 2.5mm thick, ductile steel sample against shallow die M1. Die side (left), die (middle) and impact side (right) views.....	102
6.22 Results of forming of 2.5mm thick, ductile steel sample against medium die M2.Die side (left), and impact side (right), views.....	102
6.23 Results of forming of 2.5mm thick, ductile steel sample against deep die M3. Notice the compliance of geometries of the die and the generated part.....	102

LIST OF FIGURES

Figure	Page
6.24 Results of forging against deep die M3. High ductility 2.5mm thick sample (left), and 6mm thick carbon steel 1020 sample (right).	104
6.25 Hemispherical dome is being formed during intermediate phase of forming process.	106
6.26 Schematic presentation of characteristics of punched hole and the blank.	107
7.1 Schematic of Water Cannon. 1-powder charge, 2-water load (projectile), 3-barrel, 4-nozzle, 5-cylindrical attachment (collimator), 6-partitions, 7-primer.	109
7.2 General view of the die used for fine forging of samples. Notice complexity of die geometry. Numbers 1-5 correspond to sections on the die surface. The ridges geometry of different section (Table 7.1) is different.....	114
7.3 Desired geometry of the ridges.....	115
7.4 Segment of concentric grooves and ridges formed on brass. Notice that ridges and grooves of the work piece surface have the forms of a trapezium which is similar to a corresponding segment of the die.....	118
7.5 General view of concentric grooves and ridges formed on the surface of brass sample. Notice precise geometry of the generated grooves.	118
7.6 The profile of concentric grooves and ridges formed on a brass sample.	119
7.7a Surface waviness of grooves formed on a brass sample.	119
7.7b Surface roughness of grooves formed on a brass sample.....	119
7.8 General view of concentric grooves and ridges formed on the surface of a copper sample.....	120
7.9 Segment of concentric grooves and ridges formed on a copper sample.	120
7.10 Surface waviness of grooves formed on a copper sample.....	121
7.11 Surface roughness of a groove formed on a copper sample.	121
7.12 General view of a coin stamped on aluminum and copper samples. Notice reproduction of fine details of the coin on the sample surface.....	122
7.13 Image of coin stamped on steel created using 3-D profile analyzer.....	123

LIST OF FIGURES

Figure	Page
7.14 Example of profile of a coin stamped on a steel sample.	123
7.15 Roughness of the surface of steel sample stamped by a coin.	123
7.16 Intersection of two micro channels formed on the brass surface by 7 μ diameter tungsten wire.	125
7.17 . A view of the 7 μ tungsten wire embedded into brass surface generated by SEM.	125
7.18 Intersection of two micro channels formed on a brass sample by 40 μ diameter tungsten wires.	126
7.19 A 3D image of a section of the micro channel formed on a brass surface by 40 μ diameter tungsten wire; the image is generated by the 3-D digital microscope.	128
7.20 A 3D image of an intersection of the micro channels formed on a brass surface by 40 μ diameter tungsten wire; the image is generated by the 3-D digital microscope.	129
7.21 A profile of the channel formed on a brass sample by the 40 μ wire. Notice that the depth and width of the channel are approximately equal to the wire diameter.	129
7.22 Profile of the channel formed by a 7 μ diameter wire. Notice the compliance between profile of the channel and the die.	130
7.23 Profile of the channel formed by 7 μ diameter wire. Notice the compliance between profile of the channel and the die and almost identity of profiles Figs.7.22&7.23.	130
7.24 Profiles of two adjacent channels 40 μ and 7 μ wide.	131
7.25 Surface roughness of a channel formed by the 40 μ wide wire.	131
7.26 A channel network on the surface of the brass sample, a) 2-D image, b) 3-D image, 20x.	132
7.27 Zoomed in view of the portion of channel network shown on Fig. 27, a) 2-D image, b) 3-D image,20x. Notice rectangular shape of the channel.	132

LIST OF FIGURES

Figure	Page
7.28 Average roughness of selected segments of channels. a) average roughness of 1.2mm long segment of 40mm wide channel was $16\ \mu$; b) average roughness of $530\ \mu$ long segment of $6\ \mu$ wide channel was 2.53.	133
7.29 .A die for ring formation: a) disassembled, b) assembled.	135
7.30 Extruded circular brass rings.	135
7.31 3-D image of a section of the extruded brass ring, the section is $1500\ \mu$ high, $150\ \mu$ thick.	136
7.32 Profile of a section of the extruded brass ring, the section is $1500\ \mu$ high, $150\ \mu$ thick.	136
7.33 Surface waviness of brass wall section.	136
7.34 Roughness of a section of the extruded brass ring.	137
7.35 A 3-D image of a section of the extruded copper ring. The section is $250\ \mu$ high, and $50\ \mu$ thick.	137
7.36 A profile of a section of the extruded copper ring. The section is $250\ \mu$ high, and $50\ \mu$ thick.	137
7.37 A 3-D image of a section of the extruded steel ring. The section is $400\ \mu$ high, $150\ \mu$ thick.	138
7.38 Profile of a section of the extruded steel ring. The section is $400\ \mu$ high, and $90\ \mu$ thick.	138
7.39 Extruded plain foils of nickel based alloy.	138
8.1 Example of measurement of generated area by extrusion of foil from copper sample.	143
8.2 Example of measurement of generated volume of extruded copper foil.	145
8.3 a) Example of measurement of generated volume of extruded brass foil; b) 2-D view of extruded foil; inscribed polygon indicates projected area of measurement.	145

LIST OF FIGURES

Figure	Page
8.4 a) Example of measurement of generated volume of extruded steel foil; b) 2-D view of extruded foil; inscribed polygon indicates projected area of measurement.....	146
8.5 3-A D image of die segment showing the gap.	148
8.6 3-D image of a section of the extruded copper foil. The section is 450 μ high, and 200 μ thick	148
8.7 Profile of a section of the extruded copper foil. Measurement of steepness of foil sides showed 19 degrees for left inclination angle and 10 degrees for right inclination angle.	149
8.8 General view of a coin used as a die for stamping on steel and 3-D reproduction of formed image.	150
8.9 SEM image of letter O from the die (coin).....	150
8.10 SEM image of letter O forged on steel.....	151
9.1 Cartoon image of areas where testing occurred on samples.....	153
9.2 Set of load-unload curves for steel sample testing.	154
9.3 Optical microscope images of areas tested on brass sample. a) inside track, b) next to track, c)control.....	155
9.4 SPM images after testing on brass showing residual indent impressions left on sample surface. a) inside track, b) next to track, c) control.....	155
9.5 Optical microscope images of areas tested on steel sample. a) inside track, b) next to track, c)control.....	156
9.6 SPM images after testing on steel showing residual indent impressions left on sample surface. a) inside track, b) next to track, c) control (taken before test)...	156
9.7 Optical microscope images of areas tested on copper sample. a) inside track, b) next to track, c)control.....	157
9.8 SPM images after testing on copper showing residual indent impressions left on sample surface. a) inside track, b) next to track, c) control.....	157

LIST OF FIGURES

Figure	Page
10.1 Schematic of impact zone for nested experimental set up: 1 –water projectile, 2 –nested metal samples to be welded, 3 – fasteners, 4 –back support.	159
10.2 Front view of nested experimental set up prior to assembly for welding. 1 – back support, 2 –rear copper plate to be welded, 3 –middle layer to be welded(nickel alloy coin), 4 –separation ring, 5 –fastener, 6 – impact side copper plate to be welded.....	160
10.3 Copper and nickel-alloy plates welded by the water projectile impact at the water velocity 1500 m/sec. Micrograph of wavy interface of joined copper-nickel plates.....	161
10.4 Copper plates welded by the water-projectile impact at the water velocity 1500m/sec and h=3mm. b) Zoomed-in section of micrograph of wavy interface of joined copper plates.....	162
10.5 Two copper plates welded by the water-projectile impact at the water velocity 1500m/sec and h=3mm. Notice uniformity of wavy seam along entire bond length(x100).	162
10.6 Copper –nickel alloy-copper plates welded by the water projectile impact at the water velocity 1500m/sec, and ultrasonic scan of welded plates.	165
10.7 General view of copper-nickel-alloy coin-copper plates welded by the water projectile impact in Exp. #12 at the water velocity 750m/sec.....	166
10.8 Ultrasonic verification of integrity of formed structure and metallurgical bonding of plates welded in experiment 12.....	167
10.9 General view of brass-nickel-alloy coin-brass plates welded by the water projectile impact in Exp. #13 at the water velocity 750m/sec.....	167
10.10 Ultrasonic scan of welded structure obtained in experiment 13. Brass-coin-brass combination.....	168
10.11 General view of copper and brass plates, welded by the water projectile impact at the water velocity 750 m/sec (Exp. 44, Table 10.1).	169
10.12 Ultrasonic verification of integrity of formed structure and metallurgical bonding of plates (Exp. 44, Table 10.1).	169

LIST OF FIGURES

Figure	Page
10.13 a) general view of impact side of two brass plates welded by the water projectile impact at the water velocity 750m/sec; b) back side view of same structure (Exp. 41, Table 10.1).....	170
10.14 Ultrasonic verification of integrity of formed structure and metallurgical bonding of two brass plates (Exp. 41, Table 10.1).....	171
10.15 General view of copper and steel plates welded by the water projectile impact at the water velocity 750m/sec (Exp. 43, Table 10.1).....	171
10.16 Ultrasonic verification of integrity of formed structure and metallurgical bonding of copper and steel plates (Exp. 43, Table 10.1).....	172
10.17 General view of two steel plates welded by the water projectile impact at the water velocity 750m/sec (Exp. 42, Table 10.1).....	172
10.18 Ultrasonic verification of integrity of formed structure and metallurgical bonding of two steel plates (Exp. 42, Table 10.1).....	173
10.19 General view of brass and steel plates welded by the water projectile impact at the water velocity 750m/sec (Exp. 45, Table 10.1).....	173
10.20 Ultrasonic verification of integrity of formed structure and metallurgical bonding of two brass and steel plates (Exp. 45, Table 10.1).....	174
10.21 General view of two cooper plates welded by the water projectile impact at the water velocity 750m/sec (Exp.28, Table 10.1).....	174
10.22 General view of nickel alloy coin and steel plate welded by the water projectile impact at velocity 750m/sec (Exp.14, Table 10.1).....	175
11.1 Launcher of high-speed water projectile.....	181
11.2 Modified Remington Power Tool.....	182
11.3 Experimental setup for investigation of high-speed liquid projectiles.....	183
11.4 Effect of the standoff distance on the granite removal.....	192
11.5 Effect of the standoff distance on the granite removal (High removal rate).....	192
11.6 Effect of the standoff distance on the weak granite removal (Low removal rate).....	193

LIST OF FIGURES

Figure	Page
11.7 Effect of the water load on the depth of penetration.	193
11.8 Effect of the water load on the granite removal.	194
11.9 Effect of cumulative (total) powder consumption on the depth of penetration...	194
11.10 Effect of total (cumulative) powder consumption on the granite removal. Here Vc-total removal, Vd-granite removal per a shot.	195
11.11 Boring of a granite plate by sequential impacts of projectiles at the same site.	195
11.12 Boring of granite by 52 sequential impacts. Notice dimensions of the generated cavity.	196
11.13 Boring of granite by 52 sequential impacts.	196
11.14 Two impacts with the distance of $\frac{3}{4}$ " between axes of the impact zone. Notice absence of interference.	197
11.15 Three impacts at the distance of $\frac{3}{4}$ " between axes of impact zones. Notice minimal interference.	197
11.16 Three impacts at the distance of $\frac{1}{2}$ " between axes of impact zones. Notice significant interference between two shots.	198
11.17 Boring of a granite plate by sequential impact with a cross-like pattern of impact distribution.	198
11.18 Setup for granite boring at induced compressive stresses.	199
11.19 Granite removal by impact of a projectile generated by low-power launcher .	199
11.20 Development of a water projectile in air. The distance above is the distance from the exit of the nozzle.	200
11.21 Numerical modeling of the variation of the water velocity at the launcher exit, Notice that the speed of the water at the head of the projectile was as high as 5,500m/s.	201
11.22 Impact of a granite plate at SOD=80mm. Notice intensive granite removal in the course of this impact.	201

NOMENCLATURE

a	number of pixels between first distinctive frame and a frame at particular time instance
$\%AR$	percent area reduction, %
b	number of pixels between first distinctive and last distinctive frames
b	depth (Table 7.1), mm
e	engineering strain
$\Delta E/E_0$	relative energy loss
$\%EL$	percent elongation, %
h	step (Table 7.1), mm
H	standoff distance, mm
I	analytical water projectile impulse, N·s, kg·m/s
L	original length, mm
L_f	final length, mm
L_i	initial length, mm
ΔL	elongation, mm
m	mass of the water, g
m_w	water mass, g
m_p	powder mass, g
M	mass of the powder, g
M_0	projectile momentum, kg·m/s
N	number of grooves
p_{\max}	maximal pressure in the nozzle, MPa
t	depth, mm

NOMENCLATURE

Δt	time difference, μs
T_1-T_4	time intervals between projectile pulses, μs
T	original length, mm
T_f	final thickness, mm
T_i	initial thickness, mm
$\%TR$	percent thickness reduction, %
v	removed volume, cm^3
v_{max}	maximal outflow velocity, m/sec
v_{in}	initial water velocity at the entrance of the nozzle, m/sec
w	mass of a boring media (water), g
α	ballistic pendulum displacement, $^\circ$
β	attenuation coefficient, s^{-1}
δ	maximaum relative elongation, %
λ	logarithmic decrement of attenuation
σ_c	breaking strength, MPa
σ_σ	ultimate strength, MPa
σ_T	elasticity limit, MPa

CHAPTER 1

INTRODUCTION

1.1 Background Information

The objective of this study is to demonstrate industrial applications of the impulsive water jets for various. The demand for new raw materials in industry is growing rapidly; therefore it is necessary to mine mineral bearing ores which quite often occur in hard and very hard rock formations. Traditional mining (rock fracturing) techniques such as drilling and blasting are quite often inefficient and uneconomical technologies which carry potential dangers for workers' health and safety especially in underground mining settlements. Mechanical mining does not seem to be a solution since it is slow and therefore costly. Pneumatic or hydraulic breakers are not an answer either since the tools on these machines get exposed to shock loading and therefore they are subjected to excessive wears. New tools such as laser, ultrasonic or water jets can considerably enhance productivity and safety of the mining operations. This study is focused on survey of the impulsive water jet systems.

Continuous high-pressure jetting systems that operate within a range of 200 to 400MPa have found wide spread acceptance for cutting and cleaning applications. These systems face limitations due to limited hydraulic power available, which therefore results in limited diameter and range of generated continuous jets. An impulsive jet provides much higher power, dynamic pressure and a size of the impact zone than a comparable continuous jet. The power of the impulsive jets can be in order of hundreds of megawatt and the jet's speed could be few kilometers per second. The impulsive fluid jets are

suitable for fragmenting hard materials such as concrete or rock which are not efficiently fragmented by the continuous water jets.. Another possible use of the impulsive jets is the explosion free explosive neutralization.

Entirely new jet application of the impulsive jets has been pioneered by the NJIT's Waterjet Laboratory. The intensive experimental study performed by the laboratory during last 10 years showed the feasibility of the use of the high speed liquid projectiles as an effective tool suitable for a wide range manufacturing, construction and mining operations. [1-31], therefore, the use of impulsive liquid jets is becoming a new qualitative step of hydro-mechanization.

1.2 Survey of Literature

1.2.1 Compressed-Water Cannons for Civil Engineering [32]

The author describes in this paper principles and applications of compressed water cannons. Design of these devices is based on fact that energy can be stored inside of them by compressing water to ultra-high pressure (ranging between 200 and 400MPa). By opening of a large valve discharge of the compressed water occurs which results in a high-power impulse of energy that is comparable to an impact breaker or pile driver hammer. This high-power water jet impulse generated by ultra-high pressure (UHP) water cannon can be used for various civil engineering applications such as: non explosive excavation of hard rock; heavy concrete demolition, foundation soil improvement and soil perforation for environmental remediation.

Device called compressed water cannon uses the energy stored by the potential energy of compression of the water. This energy can be used in the form of free jet or it can be released into a blind borehole for non-explosive excavation of hard brittle materials such as rock or concrete. The low compressibility of water means that little heat is generated so the compression/discharge cycle is nearly adiabatic and efficiency is almost 100%.

Impulsive energies of up to 250kJ have been generated by the water cannon systems discussed in this study. Consistent repeated pulses could be generated at the cycle rate of 1Hz with conventional ultra high-pressure power. The system may also be charged using a low cost air driven pump if rapid cycle time is not required. The advantage of a discharge valve on the water cannon is because it has only a single moving part and systems have been operated over 40,000 cycles without significant wear. From stagnation-profile analysis for free jet and blind hole applications stagnation-pressure reaches maximum value in the time frame between 2 and 4 milliseconds, which is the time frame for maximum energy extraction from a single cycle.

In pulsed-water soil penetration applications free jet pulse produced by a water cannon will penetrate most soil types including stiff clay, sand and crushed rock. In experiments supporting this study the penetration diameter of created holes varies from about 11mm at the entrance to a maximum of 50mm at the end, which is for a nozzle diameter of 11mm. The maximum pulsed jet penetration depth achieved is 6.7m and the depths of over 20m are feasible. Since the water cannon cycle time can be less than 1 second, which can be used, advantageously for rapid creation of large number of holes in process of soil remediation project or to improve the geo-technical properties of

foundation soils. Mathematical model for hydrodynamic penetration of soil with impulsive jets was developed as well.

1.2.2 High Speed Impact of Liquid Jets on Solids [33]

In this paper a method of producing of high velocity liquid jets is described and factors determining the form and shape of jet are analyzed. Analysis of some work on production and impact of small liquid jets with velocities up to about 1,500m/s was performed. This is done in order to investigate the mechanism of liquid impact damage with particular stress to the erosion of soils by liquid drop impingement and by cavitation. Three topics are considered in detail: (1) the production and behavior of high velocity jets, (2) the pressure and flow in the jet during impact, (3) the flow and fracture of solids under jet impact.

The set up for production of high velocity jets is consisted of fluid, which was contained in a cylindrical chamber with a small parallel-sided orifice at the end; the other end was sealed with neoprene disc. As per author for most liquids surface tension was sufficient to prevent leakage through open orifice. In order to create the jet liquid was forced through orifice by an impact of a small lead slug fired from a gas-powered gun. Neoprene disc would expand on an impact contact and therefore prevent slip of the liquid to the back of the chamber. Water slugs of about 20mm³ were used in this set up. The highest jet velocities of 1,800m/s were achieved. Clean and coherent jets were produced by optimal design of the nozzle, which eliminated radial flow and turbulence at the mouth of the orifice. To minimize turbulence the interior of the chamber was polished off. The entrance angle to the orifice is 60⁰; and the length of this section is a quarter of

chamber length. The head of the jet produced in this set up has a mushroom shape. Jets produced by conical and square sectioned chambers produced broken jets.

For jets with flat heads the maximum pressure generated during the normal impact of a steady, inviscid, incompressible two or three-dimensional jet against a rigid surface. Impact velocity of 100m/s, an impact pressure of 5MPa was generated. On the impact interface the radial flow of fluid takes place and it was found that radial flow velocity was up to twice the impact velocity.

Since the head of the jet has often curved configuration (mushroom shape) the early stages of jet impact should be simplified to the impact of a spherical drop on a solid surface. When a drop strikes a surface the flow does not occur immediately. Since compression of lower part of the drop takes place the flow begins when pressure waves generated in the impact overtake the edge of the drop as it expands outward across the surface of the solid. It is shown that this takes place when it is predicted that maximum pressures get generated at the edges and minimum pressures at the center of impact.

On an impact when the flow begins the liquid moves through an acute angle along the surface of the solid. For higher velocities (1,000m/s or higher), the stagnation pressure of the steady flow of the jet reaches values which are comparable to the range of failure stresses of structural materials. As a result damage and penetration of the jet takes place during of the impingement. Maximum tensile stresses produced during the loading determine the failure of the materials.

The failure of brittle materials is governed by the maximum tensile stresses generated during the loading. During the intercourse of high-speed impact of a liquid jet against a plane surface the max tensile stresses act in radial direction across the

circumference of the compressed (impacted) central region. In order to estimate the magnitude and distribution of these stresses we would need to know exact form of load distribution under the impact of the jet. Due to complexity of this interaction there is no simple way of measuring or calculating this distribution in sufficient detail to allow a determination of the stresses in a solid. In conclusion in brittle solids damage produced by reflection and subsequent interference of the original pulse is greater than the total damage in the impact area. Maximum damage in the contact area is produced by oblique impacts. Damage is significantly reduced by the presence of a thin liquid layer on the surface of the solid. In hypervelocity impacts against ductile solids most of the energy is used to widen the crater, rather than to deepen it.

1.2.3 The Impulsive Water Jet Device: A New Machine for Breaking Rocks [34]

In this paper technical advantages of the impulsive hydrodynamic method, including high-speed water jets, for breaking rocks are discussed. Comparison of this technology to the traditional rock breaking methods is presented as well. Continuous water jets had been used for mining applications but have limits since they can only break soft rocks, therefore impulsive liquid jets are advantageous for mining of hard and very hard sediments. It is so because impulsive liquid jets produce very high velocity liquid pulses (up to several km/s) and therefore they generate very high powers, which go up to the order of 100MW. Most likely that most of hard materials occurring in nature will not be able to withstand the impact from impulsive liquid jet of power of this level.

There are different ways of producing of impulsive water jets some of them are: cumulative method, the inertial principle and the electro-hydrodynamic technique. Impulsive water jet device (IWD) generates a pulse of high-speed water jet by extruding water through an opening. After pressurizing the gas chamber the piston accelerates and strikes the water slug located inside the barrel. The piston delivers kinetic energy to the water, which is driven through the nozzle in form of high velocity jet. This produces slug of water that lasts for a few milliseconds. By consecutive repeating the whole process we can achieve multiple pulses.

Analysis of hydrodynamic characteristics of IWD can be separated in three groups: problems of inertial ballistics, problems of external ballistics and the problem of the interaction of the jet with the target material. Processes occurring inside the chamber and the barrel last very short in comparison with the length of the entire pulse, therefore the physics of processes of internal ballistics can be described quasi-statistically. This simplification gives us opportunity to create a mathematical model for analysis of the pulse formulation, and the model reduces to a system of ordinary differential equations, which enables us to predict profile of pressure in the barrel as function of time. Magnitudes of attainable pressures go up to several hundreds of MPa and practically upper limit of the pressure is limited by the strength of the device. Experimental results come to a good agreement with theoretical predictions. Interaction of the jet with the target is understood too much lesser extend and there is no model explaining mechanism of collapsing of the rocks under the impact of the water slug.

1.2.4 Impulsive Hydrodynamic Method of Breaking Rocks and Concrete [35]

In this paper author discusses the impulsive hydrodynamic method of breaking rocks. Various ways for production of the impulsive liquid jets are presented and mechanisms of action of impulsive jets on rocks are described. The most complete investigation of internal ballistics is presented by Atanov (1982). He has a thorough investigation of internal ballistics, external ballistics and investigation of interaction of the jet with the target materials as well (1987). During investigations a whole variety of rocks such as: monolithic rocks, lumps, rock- and concrete blocks of wide range of properties have been broken.

There are various ways of producing impulsive water jets. Some of them are: the cumulative method, electro-hydraulic technique, extruding method, inertial principle, From several types of devices which had been designed the most investigated are: Impulsive Water Jet device (IJD) and the hydro cannon and electro impulsive water jet device in which due to a high-voltage discharge in water a result of stream-gas cavity originates which acts as piston and pushes the water toward tapered nozzle.

The dynamic pressure for IJD does not exceed the value of fluid pressure in the barrel, and maximal values are reached when the process becomes almost quasi-steady. As a result jets generated in IJD can not exceed velocities of range 1300-1400m/s. In order to reach those velocities a barrel pressure of 1.2GPa would be needed.

In case of hydro-cannons the dynamic pressure of the jet can reach values which are several times higher than the maximum pressure inside the barrel. This enables to

achieve jet speeds of several kilometers per second for the same pressure, as in Impulsive Jet Device.

When impulsive jet strikes the target a complex combination of processes take place in a target material. Each of these, if reaches required magnitude can cause a destruction of the target, this causes rise of shock waves which cause volatile rise of pressure. If magnitude of this pressure exceeds required limit for decomposition of the target material destruction takes place. For example if the target material is rock the shock wave propagates along the rock, but same wave can get reflected from interfaces inside the rock, this causes initiation of rarefaction wave which causes tensile stresses which can tear the rock from face.

Another way of interaction of impulsive water jet is when a jet is long enough and its dynamic pressure increases the rock liquid limit than the jet would penetrate the rock and make a hollow in it. Consequently a high pressure would arise inside and eventually would blow the rock apart. Also if the rock has cracks, under the action of hydraulic wedge the water would penetrate those cracks and cause their propagation, which would lead to the failure of the rock. As a conclusion after thorough analysis of these proceedings we realize that an impact of an impulsive liquid jet is more destructive than an impact of a solid body of the same impact speed.

Since most of destruction takes place at initial stage of interaction with the rock, for this short period of the pulse the impact of impulsive jet can be treated as an impact of the drop.

1.2.5 Water Jet Driven Shock Waves in Gases [36]

A method for producing moderately strong shock waves in gases at high-pressure levels employing a well-defined, stable interface between the driver and the driven gases is described. The method is based on unsteady acceleration of a liquid in a converging nozzle terminated in a shock tube. The high-speed water acts as a driver for the shock wave. The density ratio across the interface is such as to avoid Taylor instabilities. Furthermore, mixing is unlikely to take place at the interface as long as the driver is in liquid phase. Shock velocities of several km/s can be achieved.

1.2.6 Cavitation and Erosion in Submerged Water Jet [37]

An impulse force gauge measures impulse force generated by cavitation bubbles in the jet. The accumulated count of impulse force per unit time is shown against the impulse force and the standoff distance from the nozzle exit. It is found that there are maxima in impulse force at two different standoff distances of 30mm and 80mm, which are the values normalized by the nozzle diam. ($=1.5\text{mm}$), and that the impulse force mainly appears in frequencies of a few Hz. Laser-microscopic observations show that erosion patterns on aluminum surfaces are classified into two types depending on area and depth of pits.

1.2.7 Flow Characteristics and Impact Phenomena of Pulsed Water Jets [38]

The flow characteristics and jet-material impact phenomena of pulsed water jets are examined by numerical analysis and experiments. Pulsed water jets are produced by

piston impact using straight nozzles. The flow in nozzles is assumed to be compressible, non-viscous and axisymmetric, and is analyzed using 2 step Lax-Wendroff method. In the experiments, high-speed photographs of jet impact pressure are measured. And pure aluminum specimens are impacted by the jets to study its capability of material destruction. High pressure generated by piston impact extrudes water through a nozzle of outlet diameter 10 of 5mm at the velocities of 300m/s to 500m/s. The increase of nozzle outlet velocity causes the radial expansion of the jets in air, and the leading edge velocities also increase. After this short transition the flow in nozzles arrives at a quasi-steady state. When the jets impact the specimens, water-hammer pressure is produced and craters like deformations of the diameter 5mm to 15mm are formed. In these experiments, diameter of the jets proves to be important to the material destruction, because relatively low speed jets from the nozzle of large outlet diameter, form large and deep craters.

CHAPTER 2

EXPERIMENTAL INVESTIGATION OF EXTERNAL BALLISTICS OF ULTRA HIGH SPEED WATER PROJECTILES

2.1 Objectives and Introduction

Objective of this work was an experimental study of the external ballistics of ultra high speed water projectiles generated by family of water launchers. Essentially, despite sufficient understanding of water projectile formation and development inside a launcher the external behavior of projectiles is not adequately explored. The enormous energetic potential of water projectiles was recognized but not understood. Previous works [Atanov] [34, 35] contain limited information about separate stages of the projectile motion. To the best of our knowledge there were no attempts to construct a comprehensive description of the projectile's dynamics. The most complete investigation of the external ballistics was performed by Atanov et al [34, 35] that used a two wires anemometer for velocity measurements. This yielded error margin of about 25%, and provided the velocity magnitude order only. Motivation of this work was determined by a need for profound understanding of formation, development and behavior of liquid projectiles. In this study three kinds of water launchers were tested:

-laboratory scale launcher which has 10mm barrel diameter and 2mm nozzle exit diameter, it will be referred to as an extruder in this text;

-industrial scale launcher which has 30mm barrel diameter and 15mm nozzle exit diameter, it will be referred to as water cannon in this text;

-medium size water launcher which has 6mm barrel diameter and 2mm nozzle exit diameter, it will be referred to as medium launcher in this text.

An investigation of external ballistics of all three launchers was performed with the objectives to: monitor projectile development in the air between the nozzle and a target; to measure the axial and radial velocities of the projectiles at different stand off distances, to measure the reaction force exerted on a target material and to measure the impact momentum. As a result profound characterization of ultra high speed water projectiles was conducted and documented. Besides of characterization of the initially recognized parameters novel characteristics of projectile behavior were observed, characterized and investigated. Detailed description of the procedures and obtained results are presented in the sections pertinent to each part of investigation.

2.2 Particle Image Velocimetry

Experimental set up for the measurements of the water projectile reaction force and velocity is shown on Fig. 2.1. This set up was created for testing of laboratory scale water launchers such as water extruder and medium water launcher. For force measurements a Kistler Quartz 3-D Component Dynamometer type 9257B was used. For instantaneous 2-D velocity field measurements the set up (Fig. 2.1) consisted of the Flowmaster system (double-pulsed laser generating the background light, high-speed camera and the data processing system) [La Vision, MI], water extruder, extruder mounting and synchronization device. This 2-D Particle Image Velocimeter utilizes correlation between two consecutive high speed camera snap shots which are generated against a laser sheet background. Correlation between positions of particular particles on two snap shots gives

an opportunity to determine the velocity since time differential between the snapshots is controlled (Fig. 2.2). External triggering device was designed and manufactured in our laboratory in order to synchronize timing of the first camera shot with the PIV system. Stand of distance varied between 21.5mm and 84mm.

The extruder constituted a modified power tool where the powder charge accelerated a metal piston which expelled water load via a converging nozzle. A convergent nozzle, facilitated at the exit of the barrel, has an angle of 118 degrees, length of 1.95mm, and exiting diameter of 2mm while the barrel diameter is 10mm. In the performed experiments 4.2grams of water (water loads) were used for generation of projectiles. The piston was driven by a commercial nail gun charged by 0.3g of black gun powder which was designated as a charge number 6. At a stand off distance of 21.5mm we found that an average water projectile forefront velocity was 128.3m/s. At a stand off distance of 36 mm the average velocity was 200m/s, while at a stand of distance of 84

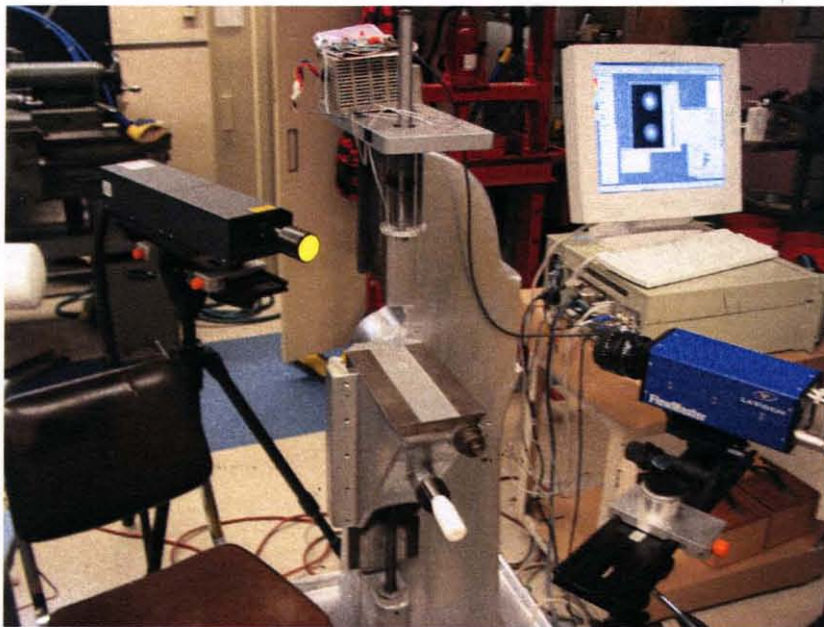


Figure 2.1 Experimental set up for measurements of high speed water slug.

mm an average velocity was 500m/s. The maximum radial velocity of the jet observed in these experiments was 175m/s. Figure 2.3 shows images generated at each reported stand off distance. At each experiment the images of the projectile's forefront were obtained. They all resemble a shape of a mushroom. It was found that a projectile was pulsing and generated transient spherical shapes (Fig. 2.3.c). This phenomenon is a consequence of the flow instabilities and constitutes an evidence of the velocity fluctuation within a projectile. Images, Fig. 2.3 include a captured projectile forefront which was developed during the travel from the nozzle exit to the maximal stand off distance of 84 mm. Dependence of the projectile-forefront velocity on a stand of distance is shown on Fig. 2.4.

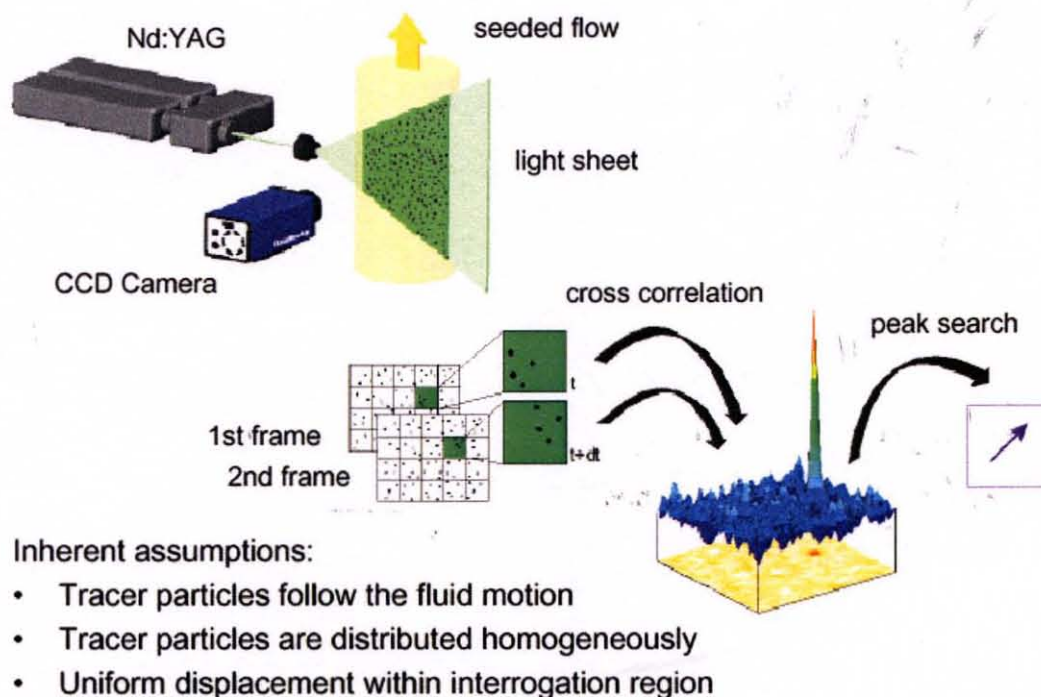


Figure 2.2 Conceptual schematic of PIV operation (LaVision).

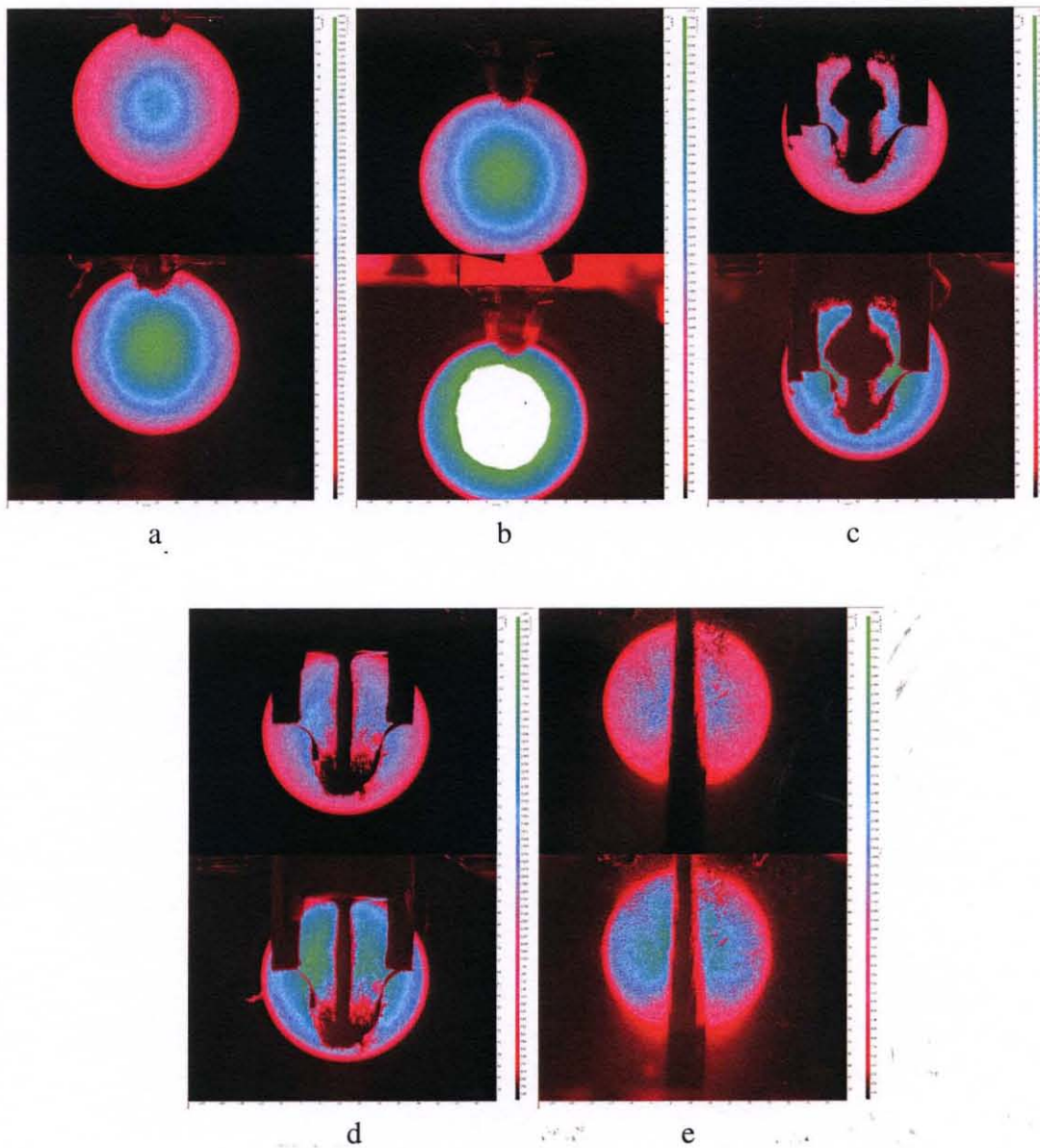


Figure 2.3 Images of sequential projectile development in the air obtained by 2-D PIV: a) jet exiting the nozzle; b) SOD=21.5mm, average velocity=128.3m/s;c) and d) SOD=36mm, average velocity =200m/s; e) SOD=84mm, average velocity=500m/s.

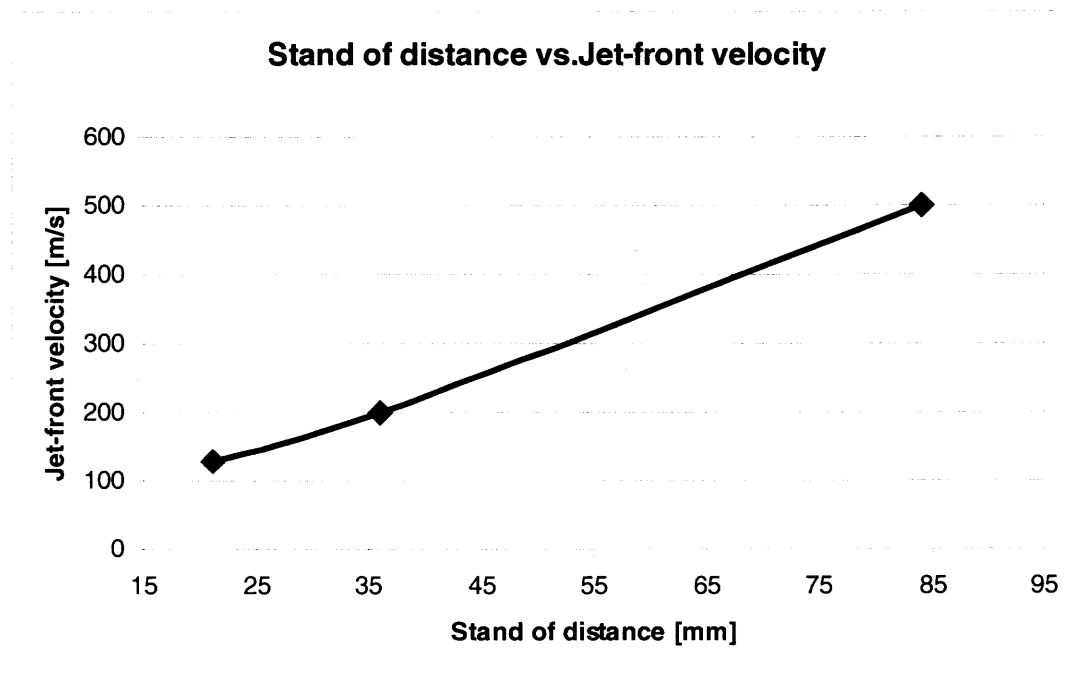


Figure 2.4 Stand of distance vs. projectile forefront velocity for extruder testing.

These 2-D velocity measurements yielded a novel knowledge about the external ballistics of ultra high speed water projectiles. The axial and radial velocities of the projectile's forefront were measured at a high accuracy since the images has been taken with the time difference resolution of $2\mu\text{s}$. The change of the projectile's forefront velocity along the stand off distance was monitored. Monitoring of ultra high speed water projectiles has been accomplished.

2.3 Projectile Reaction Force Measurement

Projectile reaction force was measured using a piezoelectric sensor which was coupled with charge amplifier and oscilloscope as shown on Fig. 2.5. Maximum measured force exerted by impact of 4.2g water projectile to the substrate in these experiments was 742N.

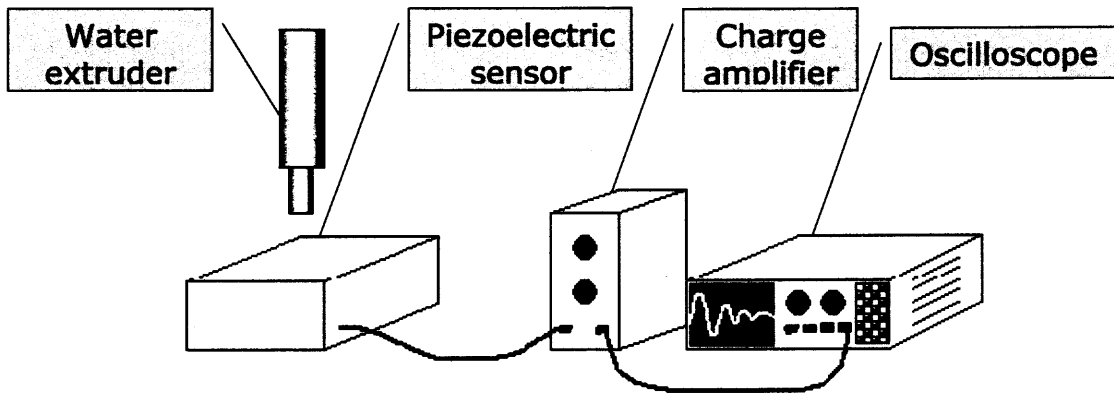


Figure 2.5 Schematic of set up for projectile reaction force measurement.

2.4 High Speed Filming for Velocity Measurements and Imaging of Ultra High Speed Water Projectiles

High speed filming was used for an investigation of external ballistics of all three launchers. Filming was performed with following objectives:

- to document a process of the emergence of a water projectile from a nozzle;
- to capture development of a projectile over a distance between the nozzle and a target;
- to obtain a high accuracy 2-D real time measurements of water projectile axial velocity at different instances of the flight,
- to monitor and characterize the radial spreading of a projectile during the flight, and
- to monitor interaction of the projectile with a target.

Schematic of an experimental setup is shown on Fig. 2.6. Phantom-V7.0 high-speed camera was used [Vision Research-Inc]. A high recording speed (up to 160,000pps), a high resolution (1,600x1,200 pixels) and a range of short shutting times (1 to 10 μ s) were key features of this camera which enabled velocity measurements and capturing imaging of ultra high speed water projectiles. Fine adjustability within the ranges of

features of the camera enabled us to tune the setup towards specific needs of the investigation.

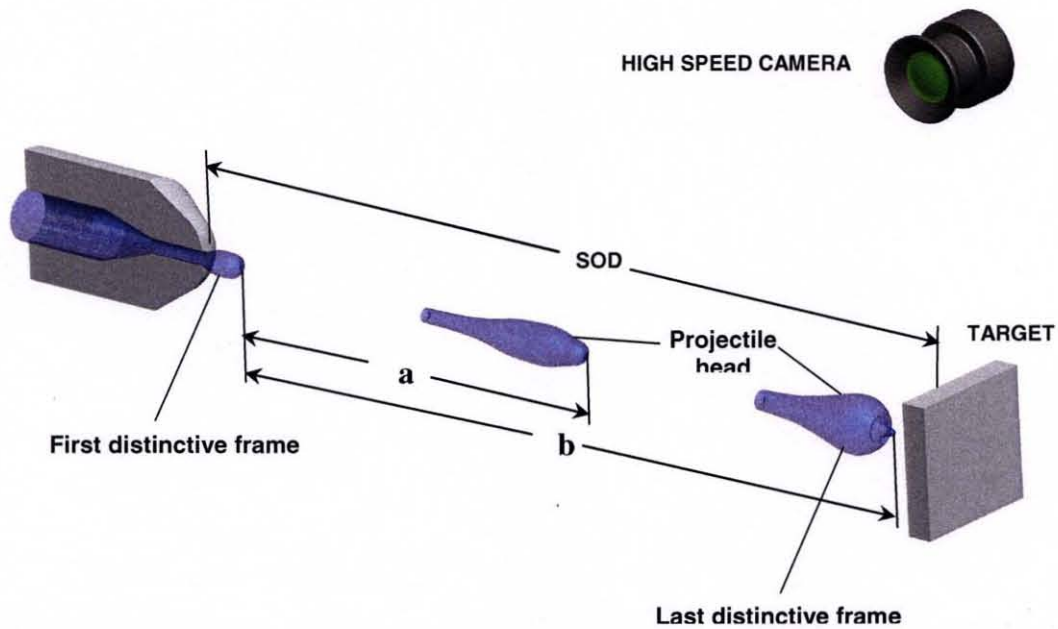


Figure 2.6 Schematic of set up for high speed filming for velocity measurements.

For each experiment the resolution was set depending on a standoff distance. Calculations of the velocity were performed correlating the pixel resolution of a field of view for each experiment with the real time monitoring of the projectile transformation in the air. Axial velocity of the projectile head and the radial velocity of spreading of the projectile were calculated using the formula:

$$V = \frac{a}{b} (SOD) \frac{1}{\Delta t} = \frac{21}{150} (0.2)m \left(\frac{10^6}{20} \right) \frac{\mu\text{sec}}{\text{sec } \mu\text{sec}} = 1400\text{m/sec} \quad (3.1)$$

where: V -stand for projectile velocity,

-SOD-stands for distance b between the nozzle and the target,

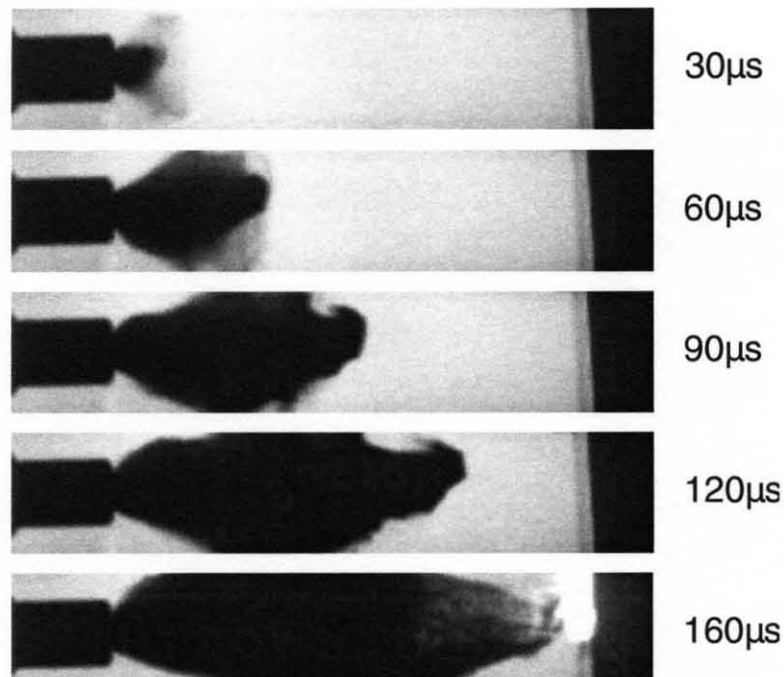


Figure 2.7 Development of water projectile between nozzle exit and slug-target interface for stand of distance 20 cm.

- a -stands for number of pixels between first distinctive frame and a frame at particular time instance,

- b -stands for number of pixels between first distinctive and last distinctive frames, and

- Δt -stands for elapsed time between two considered frames.

For the shown sample the calculation was performed at the SOD=20cm, $a=21$ pixels, $b=150$ pixels and $\Delta t = 20\mu\text{sec}$.

Testing of an industrial scale water launcher was performed at stand-off distances of 16, 20, 40 and 60cm. In each filming the field of view included the nozzle, end of the launcher, full view of the stand of distance and the side view of target plates. Sequential development of water projectile for the experiment at 20cm stand off distance is shown on Fig.2.7. The filming speed was 100,000 frames per second and the shutter time used in this experiment was $1\mu\text{s}$. Velocity measured in this experiment ranged between

1333.33m/s and 1600m/s. Radial spreading of projectile's forefront was monitored and characterized by measuring projectile's spreading angle in reference to the nozzle center. The spreading angle of the projectile measured in this experiment was 51 degrees. Velocity vs. distance dependence is shown on Fig. 2.8 which shows fluctuations of forefront velocity. The distance vs. time chart is shown on Fig. 2.9. Bell curve distribution of projectile's forefront velocity for SOD=20cm is shown on Fig. 2.10.

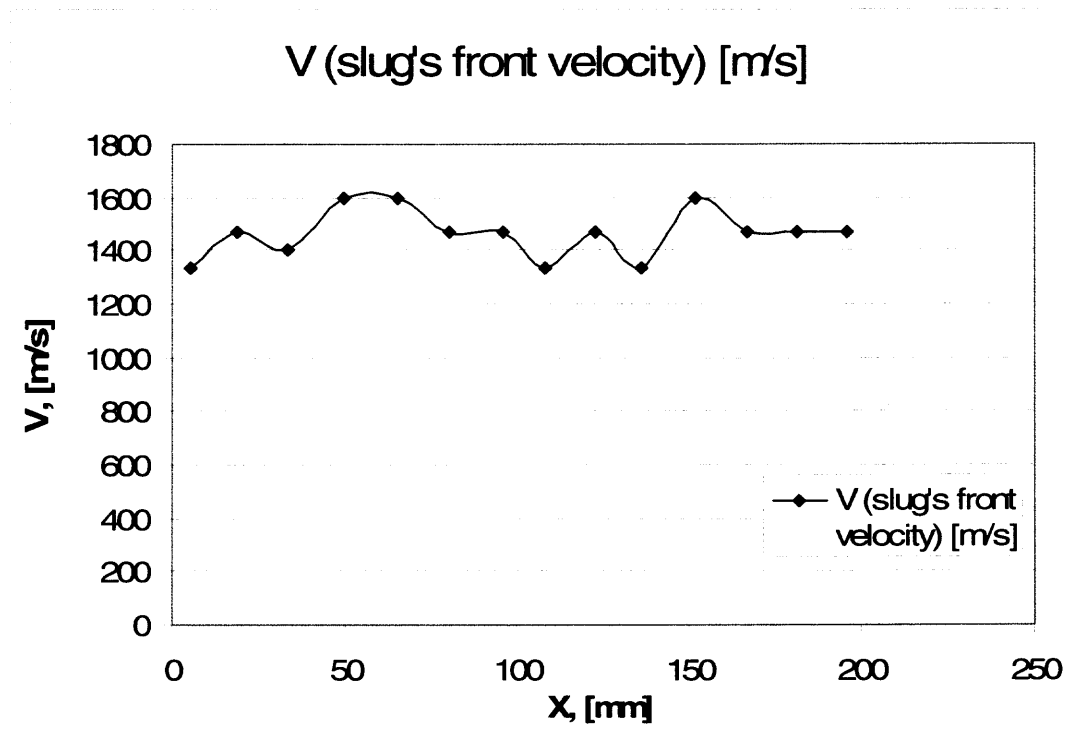


Figure 2.8 Velocity vs. distance dependence for SOD=20 cm.

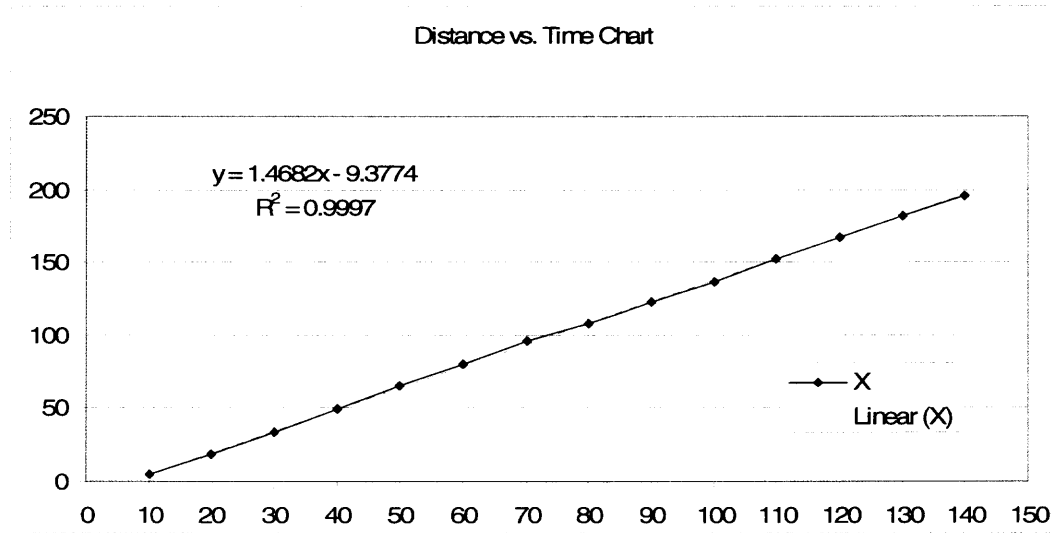


Figure 2.9 Distance vs. time dependence for SOD=20 cm.

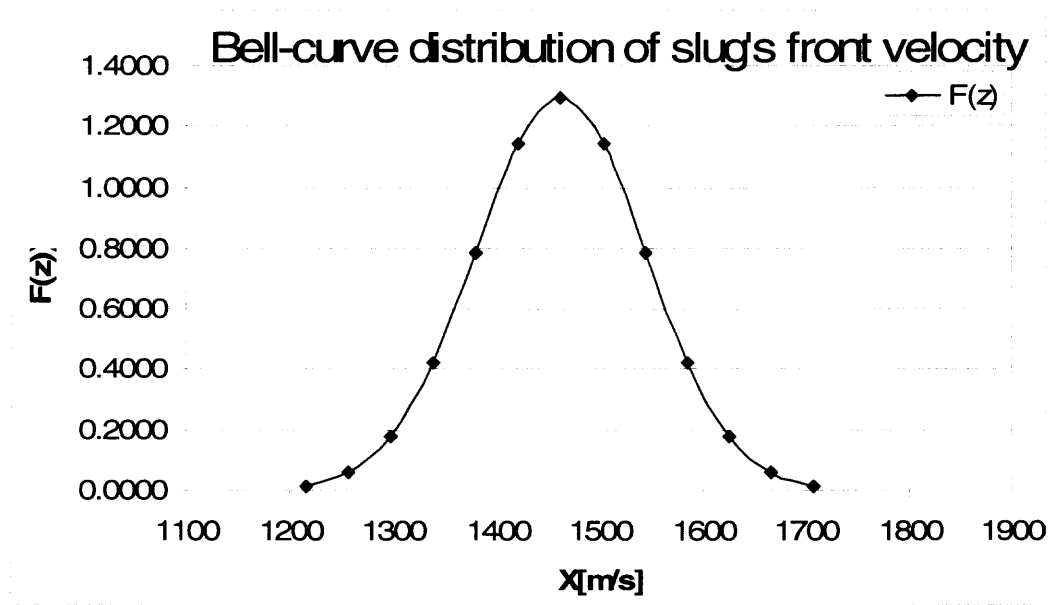


Figure 2.10 Bell curve distribution of projectile's forefront velocity for SOD=20cm.

Figure 2.11 shows development of water slug in the experiment on 60cm stand of distance. The filming speed was 50,000 frames per minute and the shutter time was $2\mu\text{s}$

and frame delay was $1\mu\text{s}$. Velocity measured in this experiment ranged between 1149.43m/s and 1379.31m/s . Maximal measured spreading angle of the projectile was 77 degrees at the $160\mu\text{s}$ frame (Fig. 2.11), 40 degrees at the $320\mu\text{s}$ frame, and 27 degrees at the $500\mu\text{s}$ frame. Velocity vs. distance dependence is shown on the Fig. 2.12 which also shows fluctuations of forefront velocity. Distance vs. time chart is shown on Fig.2.13. Bell curve distribution of projectile's forefront velocity for $\text{SOD}= 60\text{cm}$ is shown on Fig.2.14.

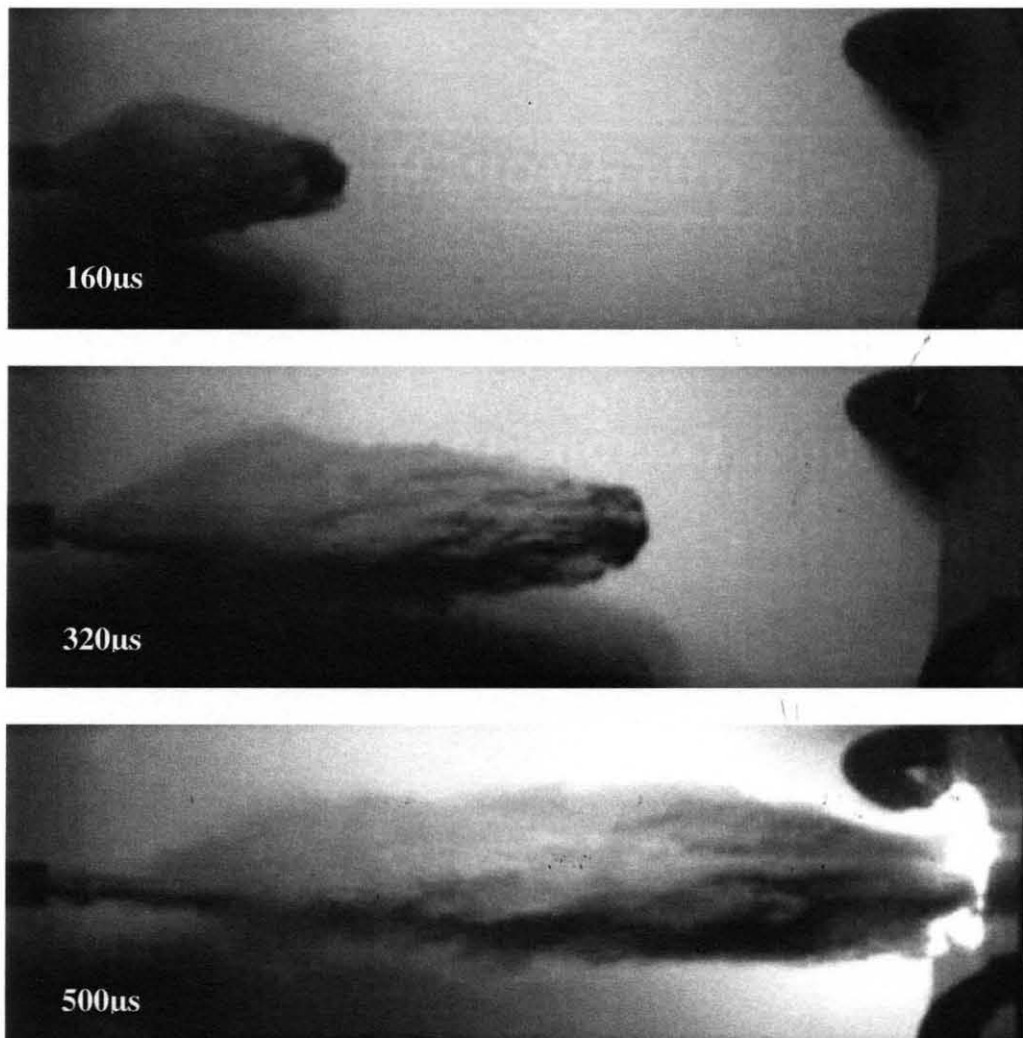


Figure 2.11 Development of water projectile between nozzle exit and slug-target interface for stand of distance of 60cm.

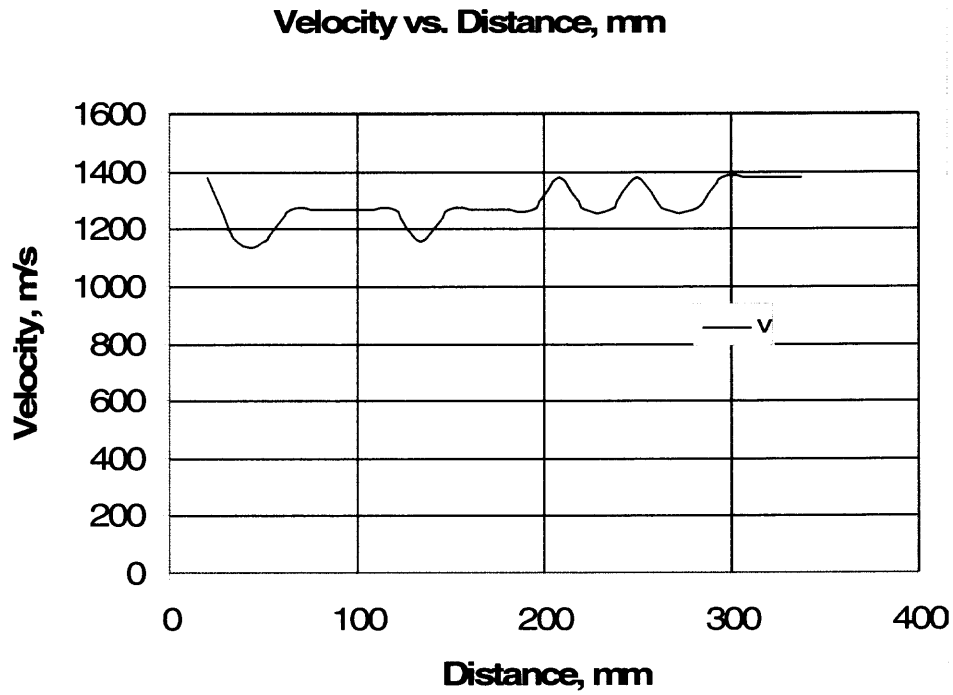


Figure 2.12 Velocity (m/s) vs. distance (mm) chart for SOD=60cm.

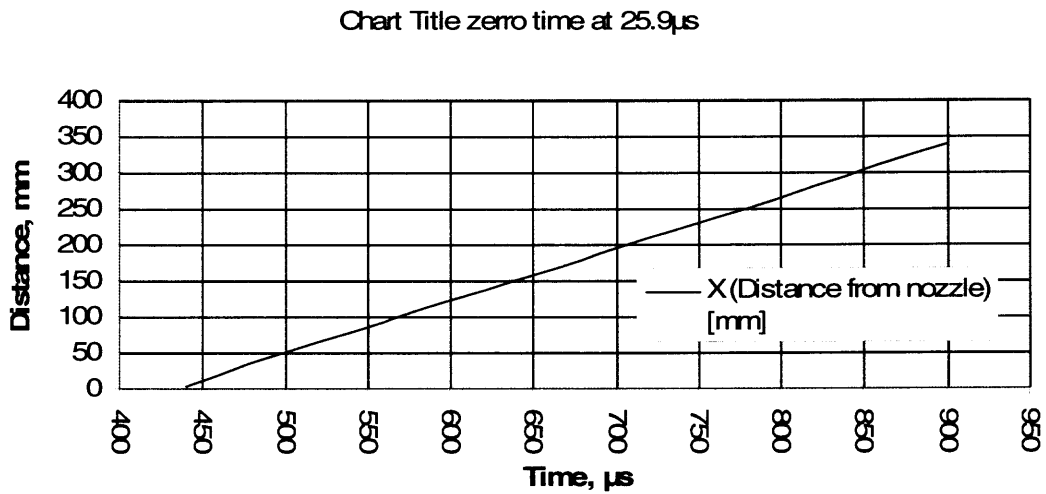


Figure 2.13 Distance (mm) vs. time (μ s) chart for SOD=60cm.

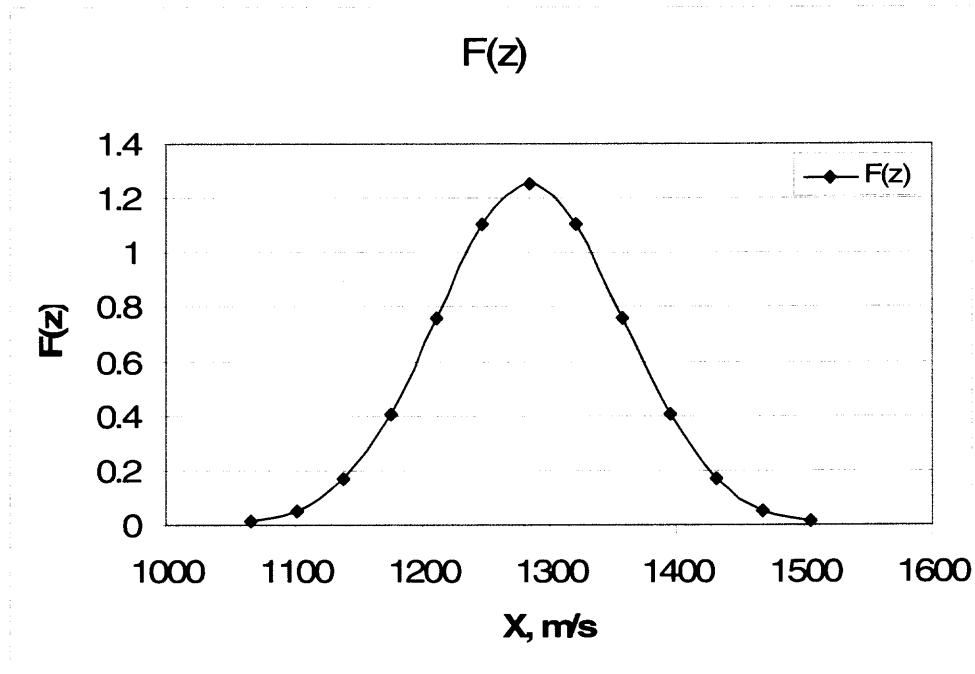


Figure 2.14 Bell curve distribution of projectile's forefront velocity for SOD=60cm.

Sequential development of water projectile for the experiment on 40cm stand of distance is shown on Fig.2.15. The filming speed was 100,000 frames per second and the shutter time used in this experiment was $1\mu\text{s}$ and image interval of $10\mu\text{s}$ and frame delay $1\mu\text{s}$. Velocity measured in this experiment ranged between 1408m/s and 1690m/s. Summary of statistical data is shown in Table1. Measured spreading angle of the projectile was 61 degrees at the $120\mu\text{s}$ frame (Fig. 2.15), 54 degrees at the $200\mu\text{s}$ frame, and 43 degrees at the $320\mu\text{s}$ frame. Velocity vs. distance dependence is shown on the Fig. 2.16 which shows fluctuations of forefront velocity. Distance vs. time chart is shown on Fig. 2.17. Bell curve distribution of projectile's forefront velocity for SOD= 40cm is shown on Fig.2.18.

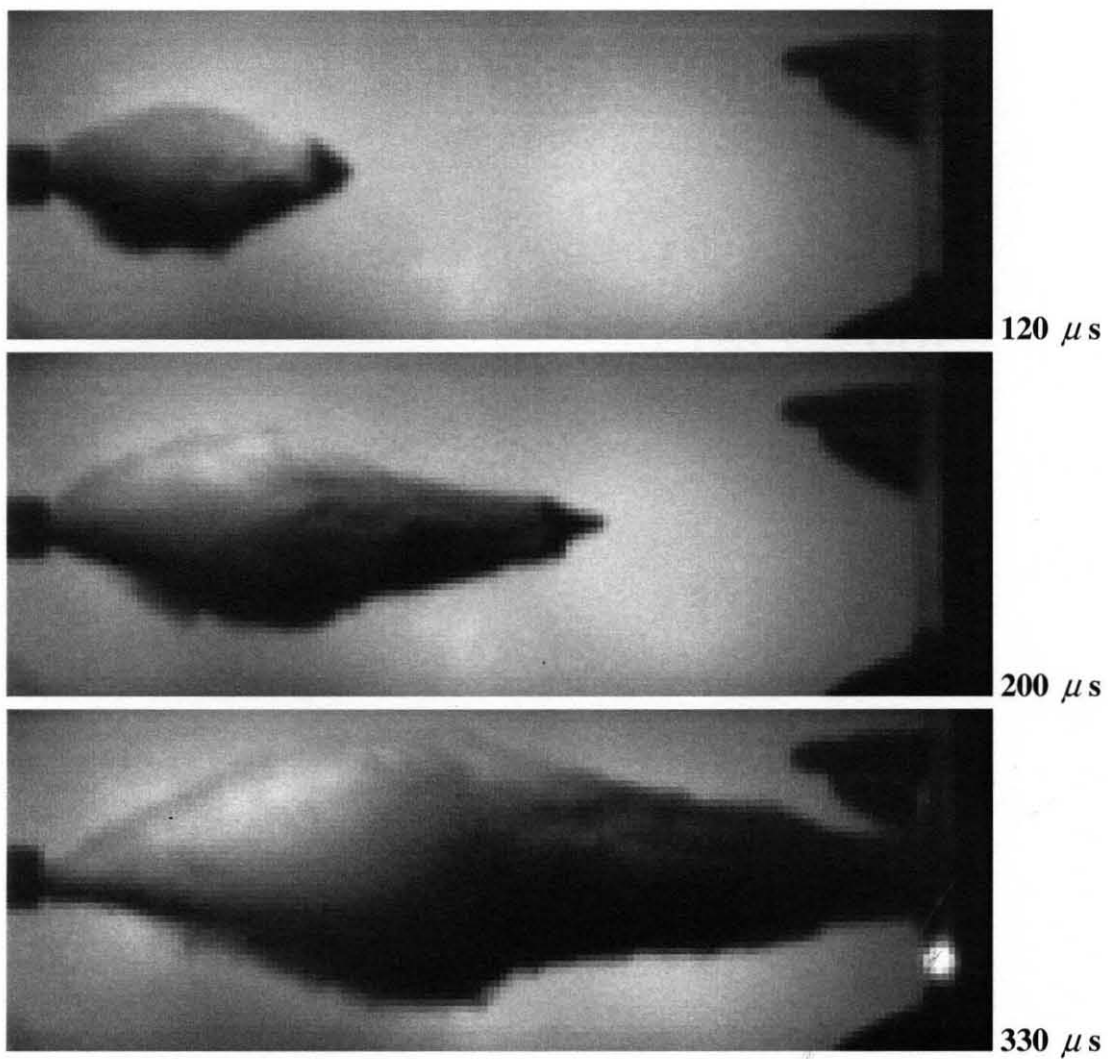


Figure 2.15 Development of water projectile between nozzle exit and slug-target interface for stand of distance of 40cm.

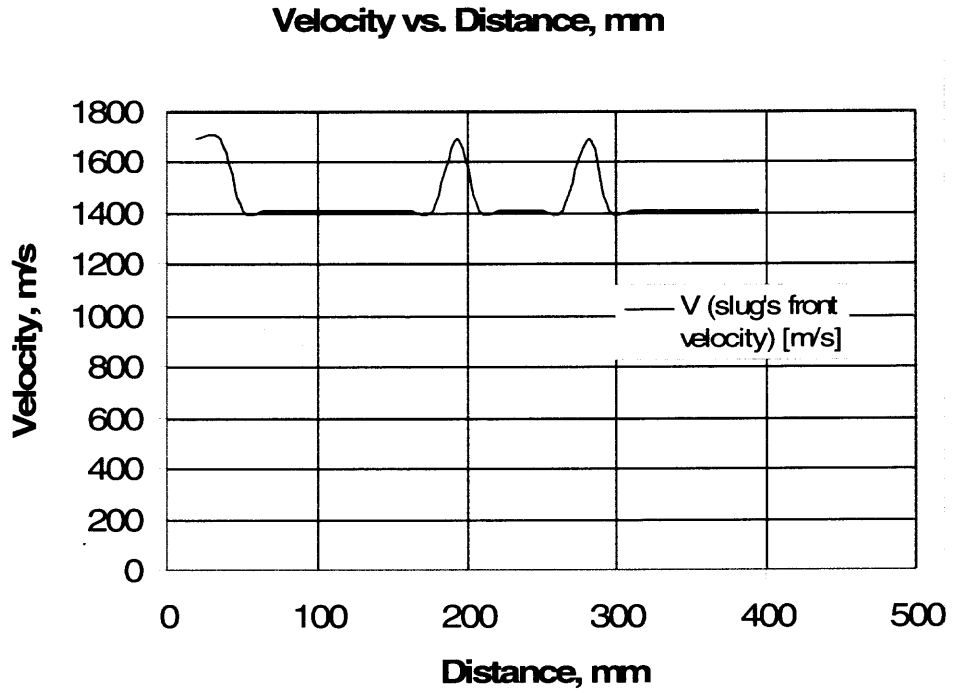


Figure 2.16 Velocity (m/s) vs. distance (mm) chart for SOD=40cm.

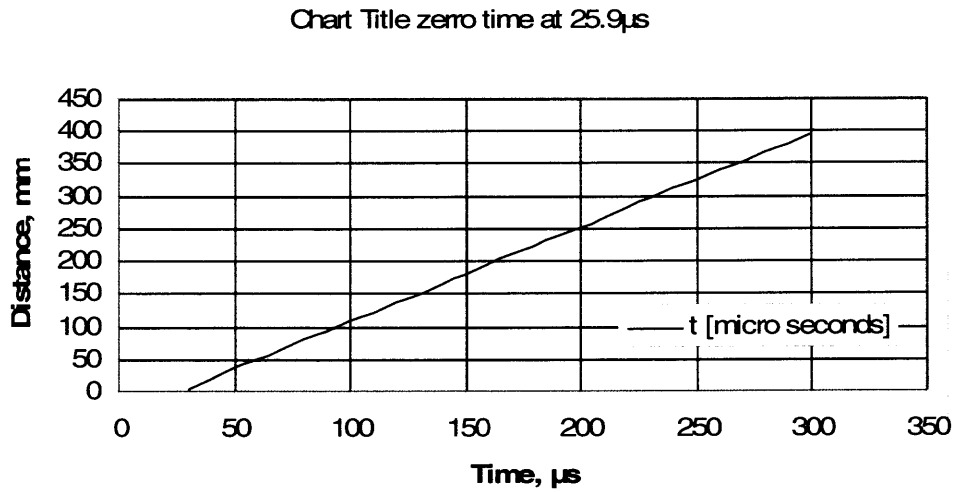


Figure 2.17 Distance (mm) vs. time (μ s) chart for SOD=40cm.

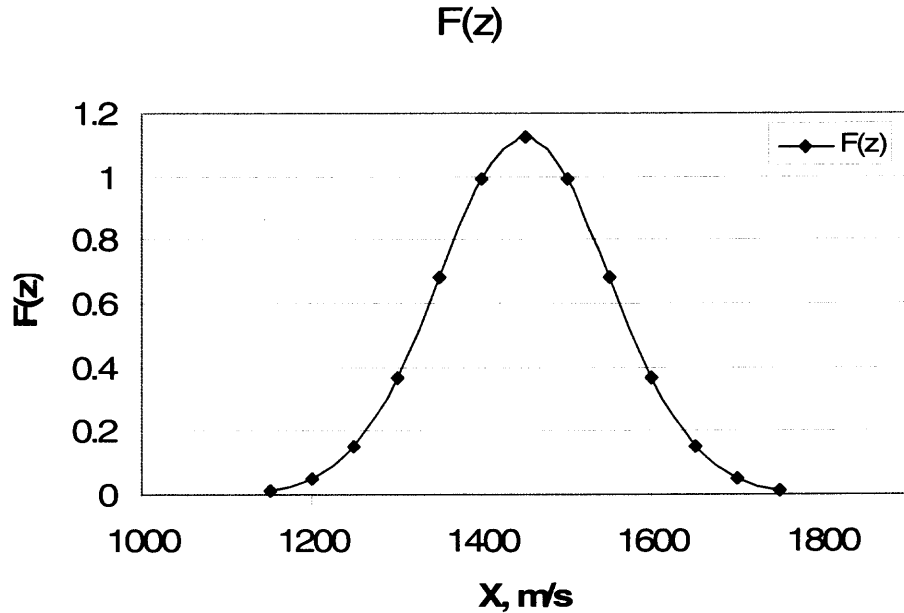


Figure 2.18 Bell curve distribution of projectile's forefront velocity for SOD= 40cm

Sequential development of water projectile for the experiment on 16 cm stand of distance is shown on Fig. 2.19. The filming speed was 100,000 frames per second and the shutter time used in this experiment was $3\mu\text{s}$ and image interval of $10\mu\text{s}$. Velocity measured in this experiment ranged between 1143m/s and 1714m/s. In this case short stand off distance prevented the projectile to fully develop. Approximate spreading angle of 68 degrees was measured at the $140\mu\text{s}$ frame. Velocity vs. distance dependence is shown on the Fig. 2.20, which confirms unstable nature of projectiles motion. Distance vs. time chart is shown on Fig.2.21. Bell curve distribution of projectile's forefront velocity for SOD=16cm is shown on Fig.2.22.

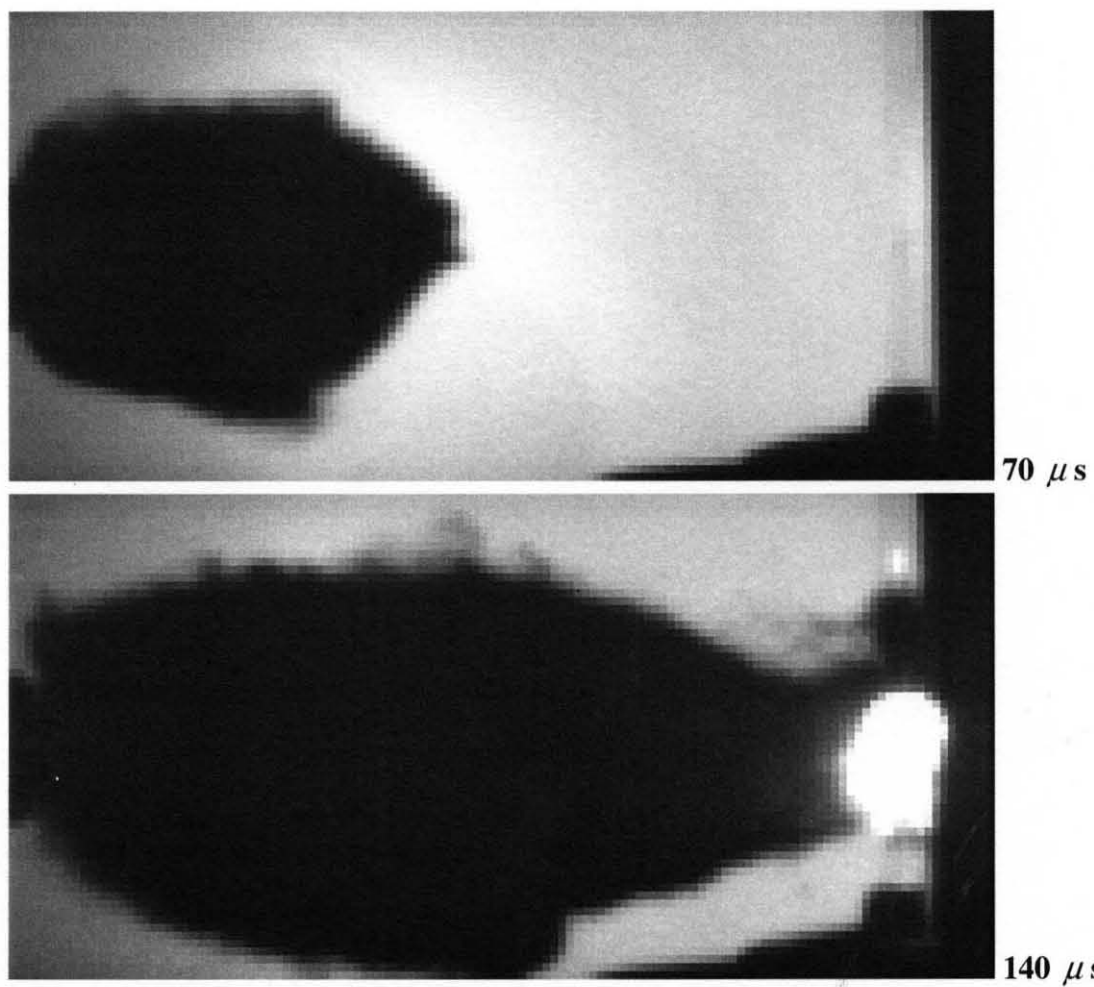


Figure 2.19 Development of water projectile between nozzle exit and slug-target interface for stand of distance of 16cm.

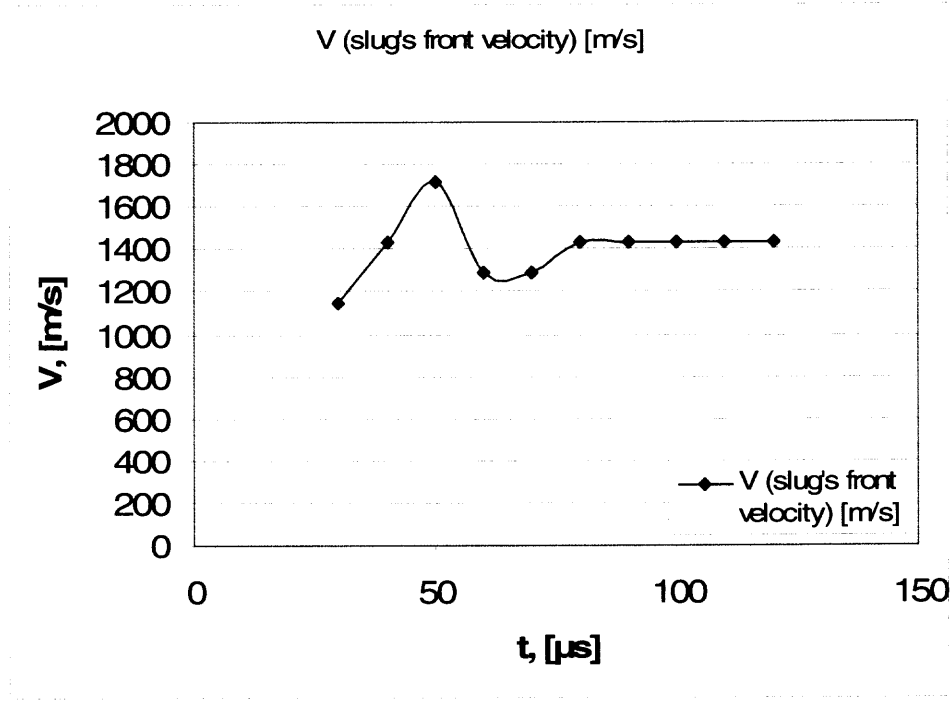


Figure 2.20 Velocity (m/s) vs. distance (mm) chart for SOD=16cm.

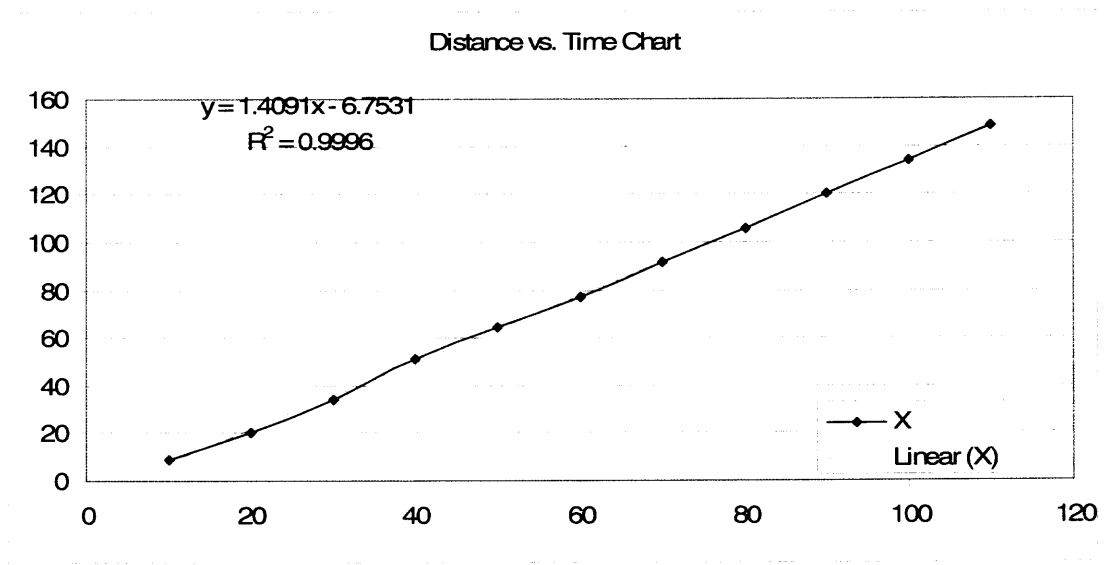


Figure 2.21 Distance (mm) vs. time (μs) chart for SOD=16cm.

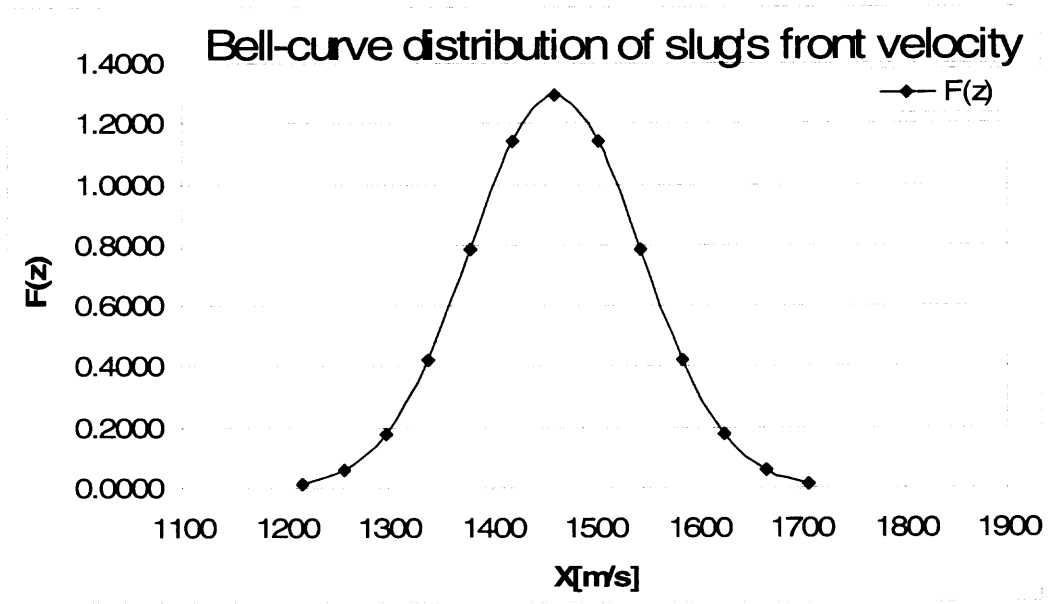


Figure 2.22 Bell curve distribution of projectile’s forefront velocity for SOD=16cm

Summarized statistics for all four experiments with water cannon are presented in Table

3.1.

Table 2.1 Projectile’s Forefront Velocity Statistics

Projectile’s Axial Velocity Statistics				
SOD [cm]	16	20	40	60
Vmax [m/s]	1714.286	1600	1690.1	1379.31
Vmin[m/s]	1142.857	1333.33	1408.5	1149.43
Range [m/s]	571.429	266.67	281.69	229.885
Mean [m/s]	1400	1461.90	1450.2	1284.36
St. Deviation [m/s]	139.97	82.0553	100.07	73.107
Intervals	4	5	6	6
Interval range	142.86	53.334	46.948	38.314
Mode	1428.571	1466.77	1408.5	1264.37

It is observed that projectiles adopt a missile like shape as a result of aerodynamic transformation during the flight. In all experiments it was observed that projectiles consist of two lobes, front (convergent-hemispherical) and rear (divergent-conical). This is a result of unique dynamics of water projectile's formation and development. As a result comet like water projectiles are produced. In all experiments it is observed that projectile flows in sequential pulsing mode. This issue will be presented at next section.

High speed filming of projectiles generated by a medium water launcher was performed at the stand off distance of 26.6cm. Five experiments were conducted with 8g of water and 1.2g of powder charge. The filming speed was ranged between 30,000 50,000 frames per second and the shutter time used in this experiment was ranged between $1\mu\text{s}$ and $3\mu\text{s}$. Pulsing fluctuation of projectile's forefront velocity was observed in all five experiments. This velocity ranged between 407m/s and 820m/s at the nozzle exit and 762m/s and 1054m/s prior to the impact. Sequential developments of water projectile for first two tests are shown on Figs. 2.23 and 2.24.

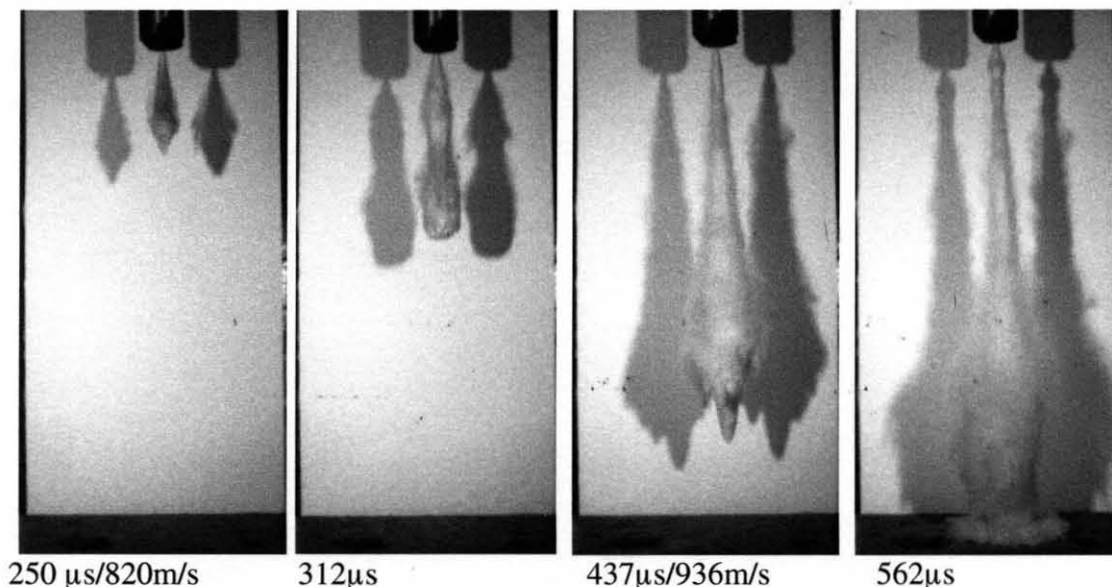


Figure 2.23 Development of water projectile generated by medium launcher nozzle.

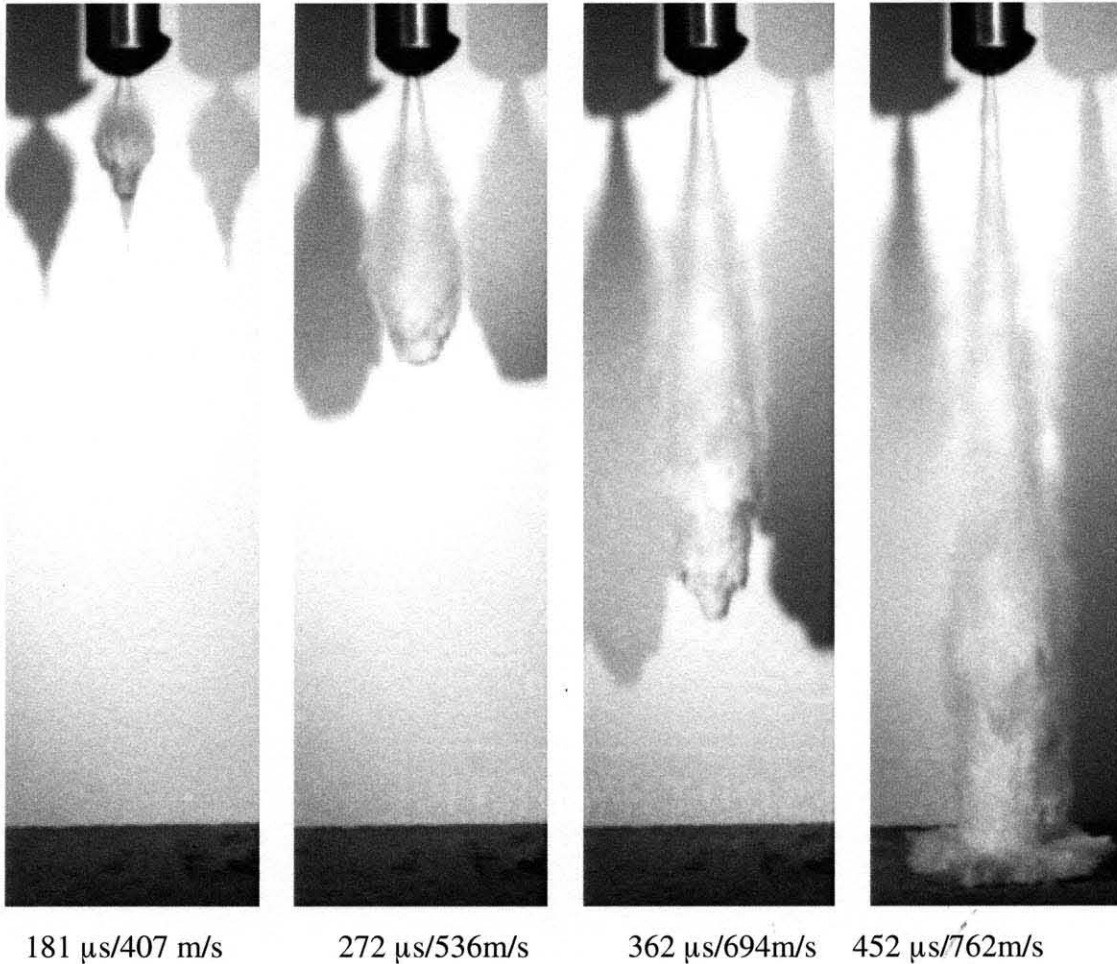


Figure 2.24 Development of water projectile generated by medium launcher nozzle for stand of distance of 26.6cm.

Testing of water extruder was performed at the stand off distance of 32cm. Experiment was conducted with 4.2g of water and 0.3g of powder charge. The filming speed was 50,000 frames per second and the shutter time used in this experiment was 1μ s. Pulsing fluctuation of projectile's forefront velocity was observed in this experiment as well. The forefront velocity ranged between 660m/s at the nozzle exit and 1062m/s prior to the impact. Sequential development of water projectile is shown on Fig. 2.25

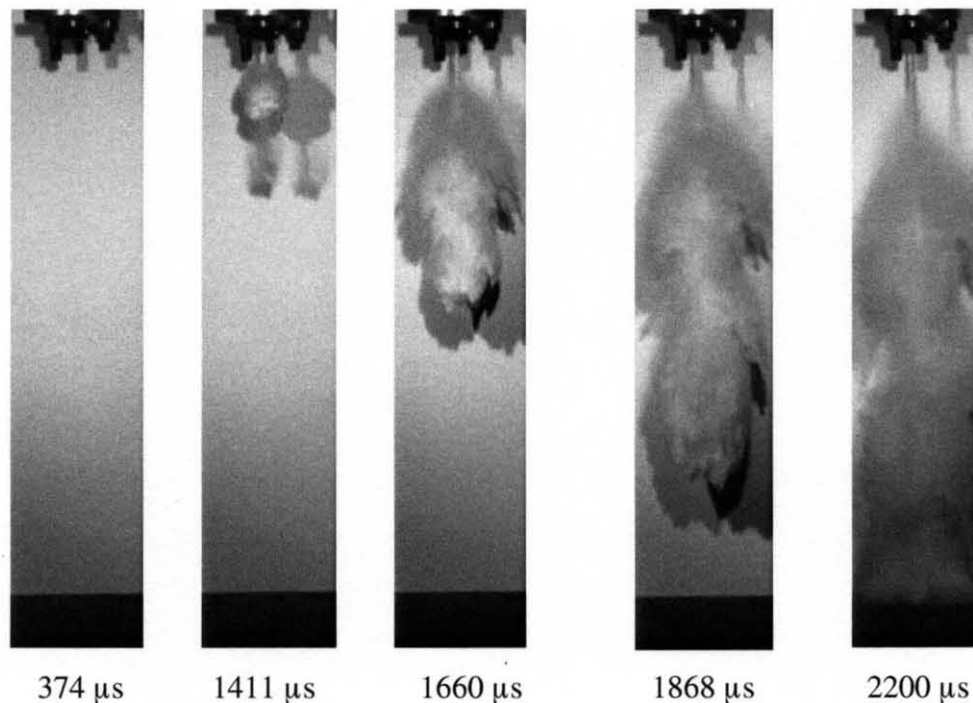


Figure 2.25 Development of water projectile generated by water extruder for stand off distance of 32cm.

2.5 Pulsing Nature of Ultra High Speed Water Projectiles

Investigation of filmed projectiles revealed pulsed nature of outflow of projectile mass. It is observed that water mass flows out in pulses of different masses and velocities. It is observed that first pulse carries the highest portion of the mass and it moves at highest velocity and following pulses carry lesser mass and move at decayed velocities from first to last. Artistic interpretation of actual pulses is shown on Fig. 2.26 where SOD stands for standoff distance and T_1 and T_2 stand for first and second observable pulse periods. Number of observed pulses varied between 2 and 5. Projectiles generated by water cannon had mass of 240g which flew out in 3-5 observed pulses. Projectiles generated by medium launcher had mass of 8g which flew out in 2-3 observed pulses. Projectiles

generated by water extruder had mass of 4.2g which flew out in 3 observed pulses. Table 1 summarizes data pertinent to observed pulses in all filmed projectiles.

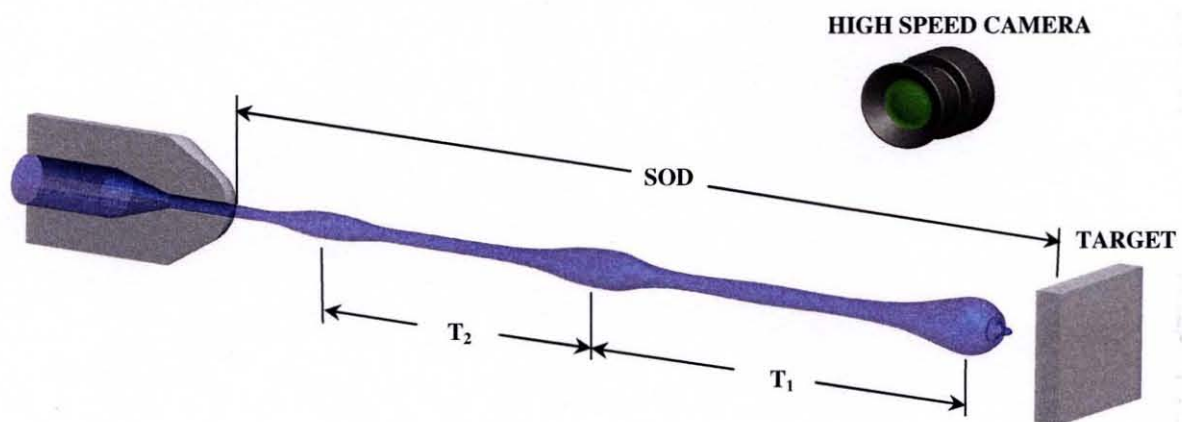


Figure 2.26 Schematic interpretation of pulsing development of water projectile.

Table 2.2 Summarized Data of Observed Pulsing Projectiles

	Cannon 1, SOD=20 cm	Cannon 2, SOD=40 cm	Cannon 3, SOD=60 cm	Cannon 4, SOD=16 cm	M- Launcher 1, SOD=27.6 cm	M- Launcher 2, SOD=27.6 cm	M- Launcher 3, SOD=27.6 cm	M- Launcher 4, SOD=27.6 cm	M- Launcher 5, SOD=27.6 cm	Extruder SOD=45 cm
Pulse 1	30 μ s	40 μ s	460 μ s	30 μ s	136 μ s	187 μ s	438 μ s	146 μ s	86 μ s	872 μ s
Pulse 2	470 μ s	480 μ s	920 μ s	480 μ s	498 μ s	562 μ s	813 μ s	497 μ s	430 μ s	1328 μ s
Pulse 3	710 μ s	710 μ s	1100 μ s	710 μ s			3938 μ s			2615 μ s
Pulse 4		1300 μ s	1680 μ s	1300 μ s						
Pulse 5		1630 μ s								
Interval 1- T_1	440 μ s	440 μ s	460 μ s	450 μ s	362 μ s	375 μ s	375 μ s	351 μ s	344 μ s	456 μ s
Interval 2- T_2	240 μ s	230 μ s 590 μ s	180 μ s	230 μ s			3125 μ s			1287 μ s
Interval 3- T_3			580 μ s	590 μ s						
Interval 4- T_4		330 μ s								

It is observed that for same conditions (launcher, water mass, powder mass) pulses emerge in steady intervals with interval time decay from first to last. Pulsing nature of water projectiles was documented in another experiment while impacting composite targets of aluminum pots filled with wax. Two experiments were conducted and in both cases cavities created in wax reveal pulsing flow. In first experiment (Fig.2.27), there is a trace of projectile's path through the wax content of the pot which indicates two pulses of the slug during piercing of the pot. They appear to be of compatible intensity and duration. The trace of the first pulse spreads between the entering-opening and ended around the midpoint of the pot in the direction of the flow. The trace of the second pulse spreads between the end of the first pulse and the exiting bottleneck base. Maximal spreading diameter of the slug inside of the pot was around 88.9mm and is the same for both pulses.



Figure 2.27 Pulsing flow left cavity indicating two pulses.

In the second experiment (Fig.2.28), a clear trace of projectile's path through the wax content of the pot indicates a single pulse during piercing of the pot. The trace of the pulse spreads between the entering opening and exiting opening. Maximal spreading diameter of the slug was 152.4mm and it is located around the midpoint of the pot in the direction of the flow.



Figure 2.28 Pulsing flow left cavity indicating one pulse.

2.6 Laser Beam Projectile Interception Velocity Measurement

2.6.1 Velocity Measurement

Another system for measurement of projectile's forefront velocity was designed and manufactured. A schematic of the experimental set up is shown on Fig.2.29. Powder water-cannon-1 is fastened at a given distance from a target-6, which is impacted by the water projectile-2. The projectile is generated by water-cannon. During the flight the water projectile crosses two laser beams 5 and generates signals which are recorded by the velocity measuring system-4.

A general view of the experimental setup is shown on the Fig.2.30. Particularly, this picture depicts a setup for measuring jet velocity. Velocity was measured on the distance of 70mm from the nozzle exit. In each experiment 30g mass of Kruk gunpowder and 230g mass of water were used for projectile acceleration. Some of experimental results are shown in Table 2.3.

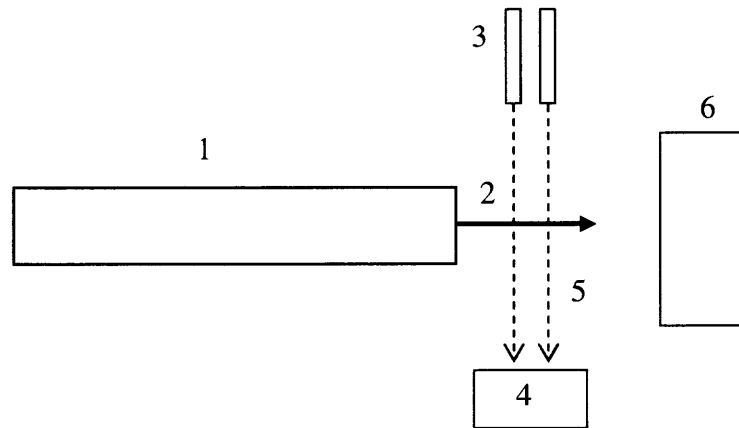


Figure 2.29 Schematic of experimental set up: 1 - HC, 2-jet, 3- laser beam sources, 4- velocity measuring system, 5- laser beams, intercepting the projectile, 6- target.

Table 2.3 Experimental Results of Standoff Distance Investigation

Exp. №	SOD, cm	h, mm plate thickness	Δt , μs time interval	V, m/s projectile velocity	Comments
1	5.5	8	35	1428	Pierced oval opening of size 15x30 mm. Velocity measured on the distance of 10 mm from the nozzle exit.
2	10.5	8	-	-	Pierced oval opening of size 12x28 mm.
3	20	8	41	1219	Pierced circular opening of size 15x15 mm.
4	40	8	38	1315	Plate not pierced, dimpled indentation created
5	40	5	31	1612	Pierced circular opening of size 30x30 mm.
6	60	6	38	1315	Pierced circular opening 10x10 mm.
7	60	6	45	1111	Pierced circular opening 25x25 mm.
8	80	6	36	1388	pierced circular opening 15x15 mm
9	100	5	36	1388	The jet impacted the edge portion of the plate. Dimpled indentation formed, plate not pierced.
10	100	5	60	830	Plate not pierced. Dimpled indentation formed at the center. Velocity measured on the distance of 120 mm from the nozzle exit.
11	100	4	53	940	Pierced opening of size 10x7 mm.
12	122	3	55	910	Pierced opening of size 15x10 mm.
13	150	3	51	980	Pierced circular opening of 10 mm diameter.
14	19	3x3	45	1110	A composite target of three identical plates separated by 42 mm thick massive plates with an opening of 90 mm diameter (Fig.3). All plates were pierced. Sizes of openings: first-60x50, second-40x30, and third-25x20 mm. Velocity measured on the distance of 70 mm from the nozzle exit.

General view of experimental set up is shown on the Fig. 2.30 and set up for velocity measurements which was described before can be depicted from it. From

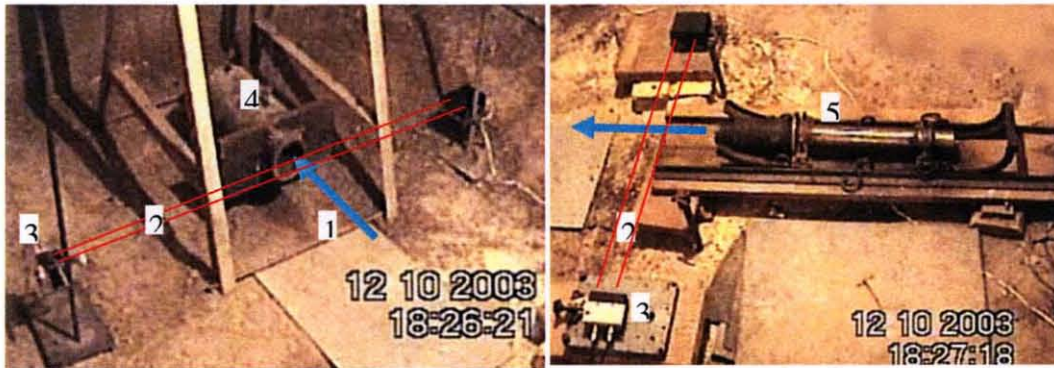


Figure 2.30 1 - Water jet, 2 - laser beams, 3 – speedometer, 4 – pendulum, 5 –water cannon.

measured values of projectile forefront velocity we can see that velocity has stable output for distances which are not far from the nozzle, up to 80cm. From these experiments we recorded that jet head velocity starts to decrease at stand of distance around 1m which complies with previously given statement that projectile efficiency decreases as the projectile moves away from the nozzle.

2.6.2 Velocity and Momentum Measurement

Experiments were carried out with water cannon under experimental conditions:

- barel diameter 32mm
- nozzle diameter 15mm
- nozzle length 70mm
- collimator length 60mm
- water projectile mass 230g

- length of acceleration path 110mm
- mass of gun powder 30g
- volume of combustion chamber 41.7cm^3
- initial pressure of combustion gasses 5MPa
- breaching pressure of combustion gasses 30MPa
- adiabatic coefficient of combustion gasses 1.257
- co-volume of combustion gasses $0.00121\text{m}^3/\text{kg}$
- mass of target holder 15.2kg

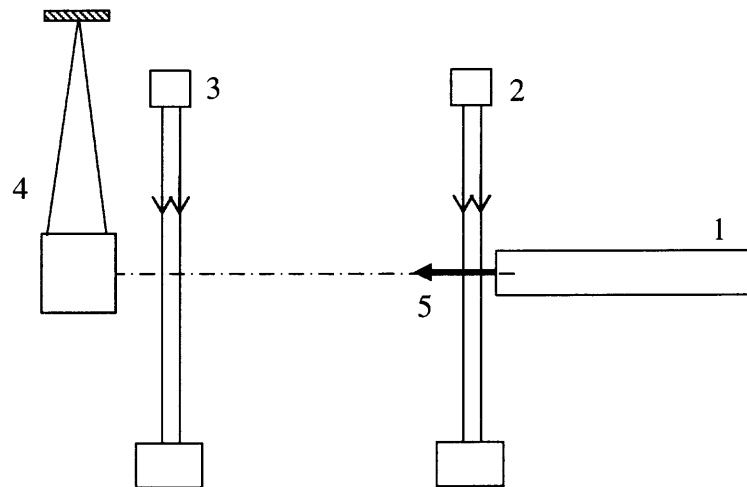


Figure 2.31 Schematic of experimental set up: 1 – water cannon, 2 – first laser beam, 3 – second laser beam, 4 – ballistic pendulum, 5 – water projectile.

During experiments two measurements of projectile's velocity were conducted, first by the exit of the nozzle of the cannon and second by the target. Impulse of reaction force on the target was measured as well. Velocity measurements were conducted by same types of laser beam projectile interception. Impulse of reaction force was measured at the standoff distance of 1.2m, and this was done by measuring displacement angle of

ballistic pendulum which has mass of 110kg, and hanging radius of 1405mm. Schematic of experimental set up is shown on Fig. 2.31.

Table 2.4 Experimental Results of Velocity Measurements

Exp. №	SOD, cm Standoff distance	$\Delta t_1, \mu s$ time	$\Delta t_2, \mu s$ time	$V_1, m/s$ projectile velocity	$V_2, m/s$ projectile velocity	α , degrees displacement angle of ballistic pendulum,
1	120	49	34	1020	912	14
2	120	41	28	1219	1107	15
3	120	47	29	1063	1068	15
4	120	45	29	1111	1068	14
5	120	51	33	980	939	14,5

Calculated projectile velocity at the nozzle exit was 1100m/s, impulse of reaction force was 147kgm/s calculated displacement angle of ballistic pendulum was 20 degrees. Analytical parameters of projectile formation and development are computed until the exit of the nozzle. Stand off distance was 120cm. It was estimated that velocity decay at that distance is around 10%, and consequently impulse decay is around 20% (around 16 degrees). By comparing analytical results to the measurements (Table 2.4) it can be concluded that they are within acceptable range.

2.7 Conclusion

Measurements of velocity, momentum and reaction force of water projectiles were accomplished. Monitoring of the development of projectiles in the air was accomplished by high speed filming and 2-dimensional velocity measurements of supersonic water projectiles were for the first time accomplished. Pulsing nature of water projectiles was discovered and documented. Nature of projectile development was investigated and interpreted.

CHAPTER 3

INVESTIGATION OF PROJECTILE ENERGY

3.1 Introduction

Main objective of this study was to investigate water projectile energy by varying the projectile size (water amount) and the amount of gun powder used to propel projectiles. The task performed during these experiments included punching 4mm thick steel plates against circular die of 21.5mm diametric opening. Computational model was used to estimate main process parameters at the experimental conditions. The obtained numerical data were compared with the experimental results in order to develop a comprehensive description of the projectiles development. The acquired data were used for development of material processing technique.

3.2 Experimental Technique

An experimental setup for the study of the impact based material forming was designed and constructed (Fig. 3.1). This setup constituted a laboratory scale prototypes of the

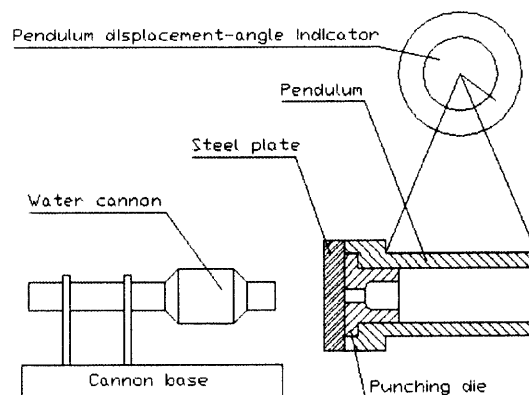


Figure 3.1 Schematic of the experimental setup. Notice that mounting of the target on a ballistic pendulum allows measuring the impact momentum.

water cannon [34]. The targets were mounted on a heavy pendulum (Fig. 3.1). Angular displacement of pendulum was measured in each experiment. This enabled us to calculate impact impulse and therefore impact momentum. For each experiment the launcher was placed at a desired standoff distance from the sample and water impact based punching of steel plate was performed. Material for samples used for this investigation included a hot rolled carbon steel with 0.22% carbon content which has tensile strength of 450MPa, yield strength of 320MPa and maximal % elongation of 26%. Samples were 4mm thick and 40mm by 40mm square shape. The acquired experimental data collected in the performed experiments was used to effectively plan investigations of liquid impact based piercing, extrusion, stamping, bending, forging; micro-forming, welding and brittle materials boring.

3.3 Experimental Investigation of Effect of Water-Projectile Mass on Energy of Projectile

Energy of a projectile depends on several process parameters such as the mass of powder and water, projectile velocity, dynamic impact pressure, impact impulse, ect. In this study a series of experiments was performed in which mass of projectiles and mass of powder varied while punching 4 mm thick steel plates. During testing each steel sample was tightly attached against the die and mounted on the pendulum. Punching was performed against the die with an opening of 21.5mm in diameter (Figure 3.2). Amount of water used in this study ranged between 30g and 240g, which were propelled by combustion of powder loads ranging between 15g and 30g (Table 3.1). The standoff distance was 16cm in each experiment. For powder load of 30g circular openings were created in plates by the impact at all selected water loads except for the water mass of 30g. Lower limit of the

water mass was determined to be 38g of water. Investigation of punched openings confirmed strong repeatability of punching process since circular opening of stable geometry was created by each particular impact. Mathematical model was used for calculation of parameters of internal and external ballistics of projectiles and they were compared with the acquired experimental data. It was shown that decrease of the water mass resulted in the increase of the projectile velocity while its effect on the impact impulse was opposite. Calculated outflow velocity of the projectile head ranged between 1051m/s and 1566m/s, while calculated maximum pressure inside the nozzle ranged between 341MPa and 843MPa. These data were used in planning of the future experiments.

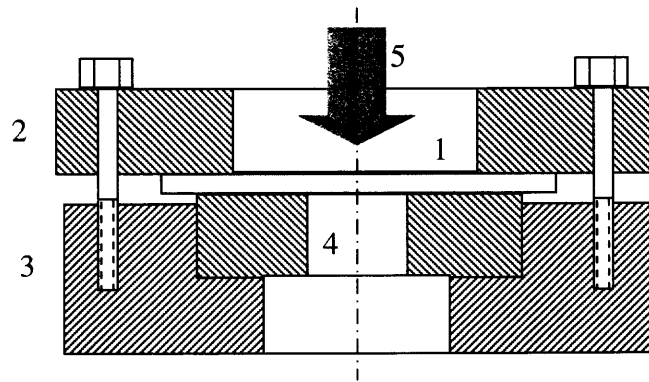


Figure 3.2 Working sample-1, clamping plate-2, die holder-3, die-4, high speed liquid projectile-5.

Table 3.1 Results of Punching of 4mm Steel Plates

M water [g]					
240	Yes	Yes	Yes	No	
200	Yes			Yes	
150	Yes	Yes		Yes	
100	Yes		Yes	No	
50	Yes	Yes	Yes		
40	Yes	No	No		
30	No				
	30	25	20	15	M powder [g]

3.4 Experimental Investigation of Effect of Gun Powder Mass on Energy of Projectile

This study was performed with the objective to estimate effect of gun powder mass on the water projectile performance. Experimental conditions were same as in water mass study. As a part of this study a mathematical model was used for estimation of parameters of internal and external projectiles ballistics. The compliance between the acquired numerical and experimental data was determined. It was shown that increase of the gun powder amount resulted in the increase of both projectile velocity and the impact impulse. Calculated velocity of the projectile head ranged between 475m/s and 1407m/s. Calculated maximal water pressure inside the nozzle ranged between 87MPa and 1122MPa. Same incremental trend was confirmed for impact momentum by measurements of angle of pendulum displacement as well. It was shown that increase in gun powder mass causes increase of all relevant parameters of projectile performance, such as maximal pressure in the nozzle, projectile velocity, and projectile momentum.

3.5 Analytical Investigation of Effect of Water-Projectile Mass on Energy of Projectile

Computational model developed by Atanov and Semko, A.N. at Donetsk National University [34] was used for analytical investigation of the effect of water projectile mass on energy of projectile. Table 3.2 summarizes projectile parameters and Figures 3.3, 3.4, and 3.5 depict graphic representation of trends of dynamic parameters.

Table 3.2 Results of Computations of Parameters of Water Projectile for Various Water Loads Masses

m_w , g	250	230	200	180	160	140	120	100	80	60	40
v_{\max} , m/s	1051	1108	1195	1247	1299	1342	1396	1446	1502	1561	1566
I , N·s	127	121.6	111	108	100	88.7	72.9	62.6	55.3	47	42.5
α , deg	18	17.2	15.7	15.2	14.1	12.5	10.3	8.8	7.8	6.6	6
p_{\max} , MPa	544	600	645	680	712	757	805	843	766	631	381
v_{in} , m/s	335	384	424	465	485	510	550	580	610	620	670

m_w –water mass,

v_{\max} – maximal outflow velocity,

I –analytical water projectile impulse,

α -analytical pendulum displacement,

p_{\max} – maximal pressure in the nozzle,

v_{in} – initial water velocity at the entrance of the nozzle (velocity at the end of barrel)

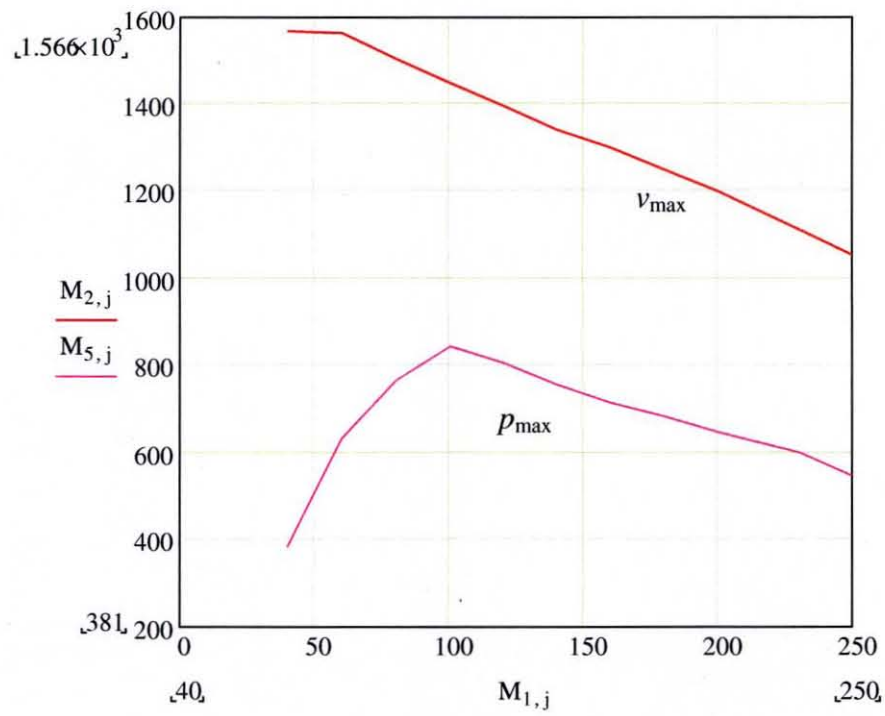


Figure 3.3 Dependence of maximal outflow velocity and maximal pressure in the nozzle on the water projectile mass (40g to 250g).

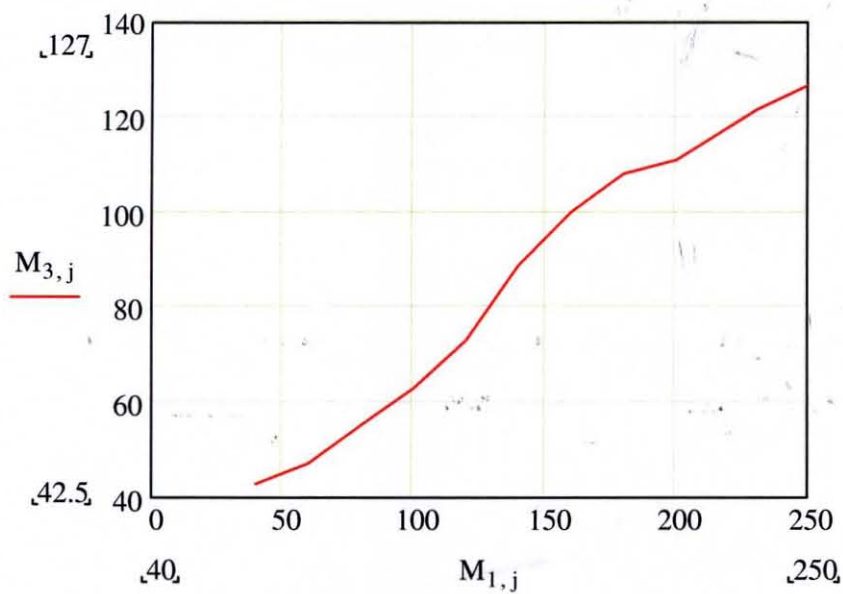


Figure 3.4 Dependence of projectile impulse on water projectile mass.

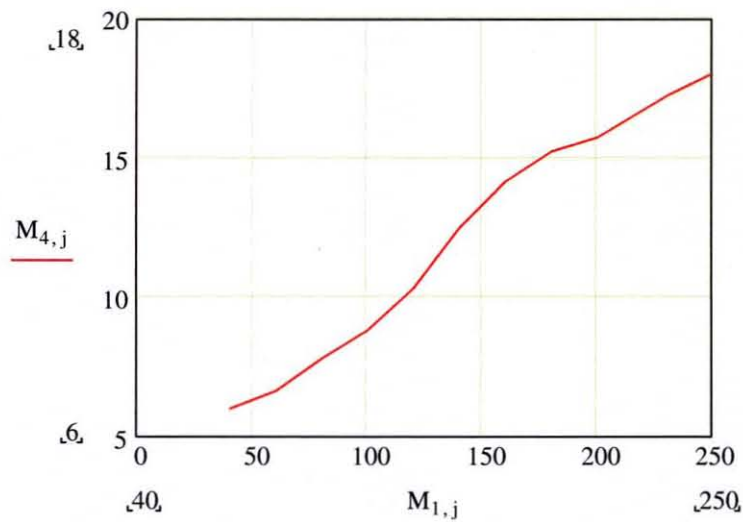


Figure 3.5. Dependence of pendulum displacement angle on water projectile mass.

3.6 Analytical Investigation of Effect of Gun Powder Mass on Energy of Projectile

Analytical investigation of effect of gun powder mass on energy of projectile was performed and calculated projectile parameters are shown in Table 3.3, and Figures 3.6, 3.7, and 3.8 depict graphic representation of dynamic parameters.

Table 3.3 Results of Computations of Parameters of Water Projectile for Various Gun Powder Masses

m_{p0} , g	10	15	20	25	30	35	40	45	50	55	60	65	70	72
v_{\max} , m/s	475	630	785	941	1108	1168	1217	1251	1283	1337	1371	1392	1410	1407
I , N s	32.9	50.9	65.2	94.6	121.6	140.5	150	159.7	169	178.6	182.8	191.5	195	201.7
α , deg.	4.6	7.2	9.2	13.3	17.2	19.8	21.2	22.6	23.9	25.3	25.9	27.2	27.7	28.6
p_{\max} , MPa	87	175	287	420	600	686	763	844	916	990	1015	1090	1114	1122
v_{in} , m/s	132	185	250	310	384	400	406	412	407	407	394	375	342	320

m_{p0} – powder mass,

v_{\max} – maximal outflow velocity,

I - analytical water projectile impulse

α - analytical pendulum displacement,

p_{\max} - initial water velocity at the entrance of the nozzle (velocity at the end of barrel)

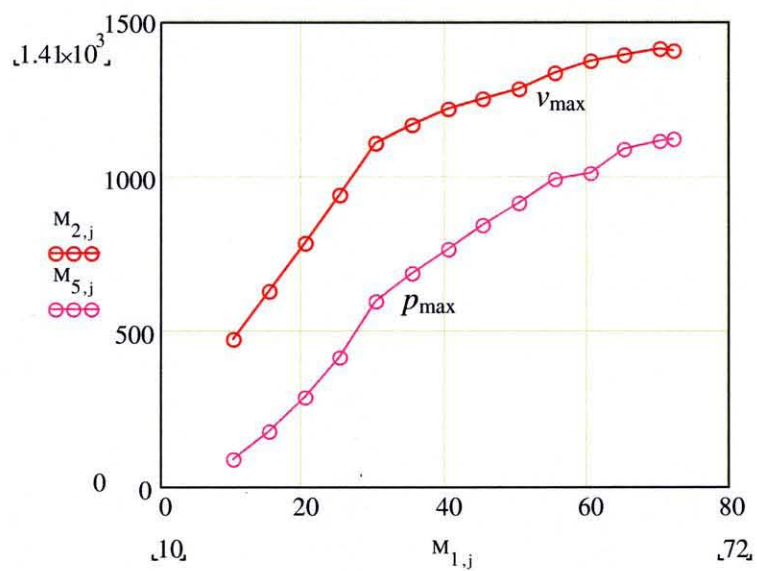


Figure 3.6 Dependence of maximal outflow velocity and maximal pressure in the nozzle on the gun powder mass (10g to 72g).

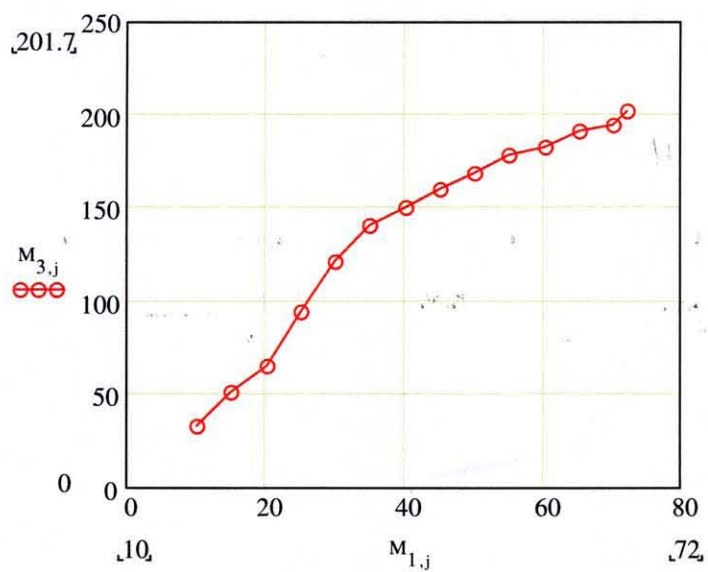


Figure 3.7 Dependence of projectile impulse on gun powder mass.

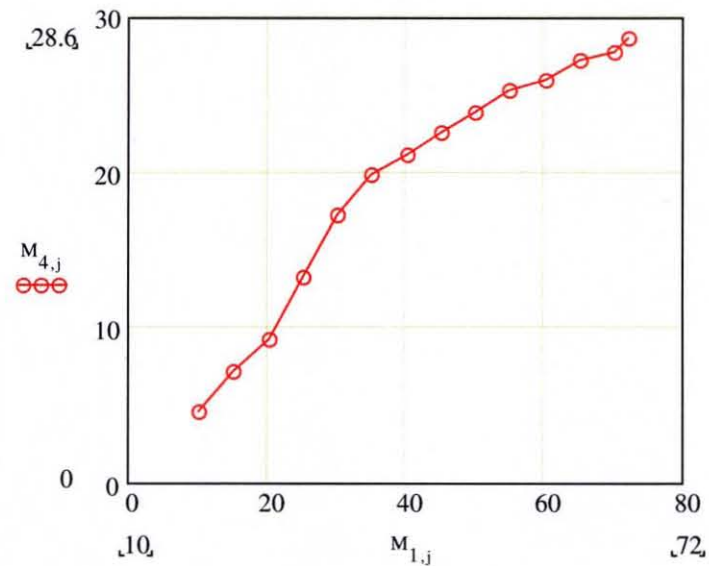


Figure 3.8 Dependence of pendulum displacement angle on water projectile mass.

3.7 Conclusion

Energy potential of water projectiles was investigated. Punching of 4mm thick steel plates against a die with circular 21.5mm diametric opening was chosen as evaluation task. Two sets of experiments were performed, first while keeping gun powder mass constant water projectile mass was varied between 30g and 240g, and second when water projectile mass was constant and gun powder mass was varied between 15g and 30g. Punching was successful with as little as 40g of water and with as little as 15g of gun powder. The obtained experimental and computational data enabled us to determine the admissible range of the conditions of the projectiles formation and the scope of projectile energy potential. This information was a base of experiments planning for material processing studies which are presented in following chapters.

CHAPTER 4

INVESTIGATION OF RESIDUAL DEFORMATION IN THE COURSE OF BALLISTIC TESTING

4.1. Introduction

Main objective of this study was to investigate metal deformation occurring during liquid projectiles impact on metal targets. The deformation induced by the solid impact is well understood and documented. [39]. By contrast the deformation caused by the high speed liquid impact is not sufficiently investigated. Nature of deforming of ductile and brittle metals by impact of high speed water projectiles is unknown to the engineering community. In this study investigation of strains and strain rates induced on the impacted materials are investigated. Deformability limits of tested materials are investigated as well. Several modifications of the water jets have been adopted by industry as manufacturing tools. Continuous water jets found wide applications in cleaning, cutting, transportation etc. The use of the pulsed streams instead of the continuous one improves the energy utilization in the course of the jet-target interaction and, thus, enhances productivity of the existing processes and makes possible development of new jets applications. Pulse jets, for example, are successfully used for rock fragmentation and mining [34, 35]. Energy utilization in the course of jet-target interaction can be improved still further if the pulsed jet is replaced by the impulsive one which is also termed as the liquid projectiles. Exploration of target deformation by the impact of the liquid projectiles is objective of this study. The performed experimental study showed that high speed liquid projectiles induce high strain rate deformation in both ductile and brittle materials including high strength hard to machine materials. The information acquired in the course

of this investigation enables better understanding of liquid impact and provides knowledge needed for development novel materials processing tools using high speed liquid projectiles.

4.2. Experimental Procedure

An experimental setup for the study of the impact based forming was designed and constructed (Figures 3.1, and 4.1). This setup constituted a laboratory scale prototypes of the water cannon [34, 35]. For each experiment the water cannon was placed at a desired standoff distance from the sample and a particular water impact based operation was performed. Metal samples in form of square plates included A36 hot rolled steel, cold rolled steel, spring steel and heat treated aluminum alloy. Piercing of metal plates was performed without a supporting die. The acquired experimental data collected in the performed experiments was used for the study of peculiarities of material deformation in the course of the liquid impact.

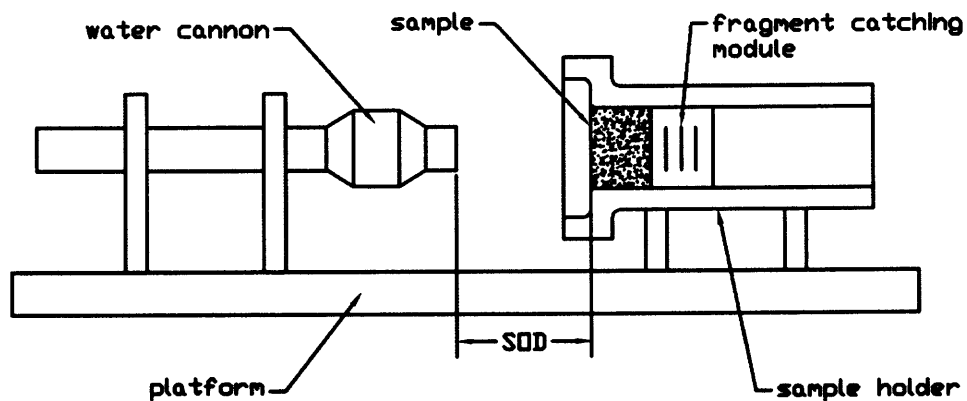


Figure 4.1 Metal plates piercing experimental set up schematic.

4.3. Piercing of Metal Plates

For investigation of metal piercing steel and aluminum samples were tested in repetitive manner in order to ensure consistency of results. Steel plates were tested as single plates, and double and triple layers sandwiches. In the first experiment a composite target combining three 4.8mm thick A36 hot rolled steel plates of 12 inch by 11.5 inch size was exposed to the impact of 230 grams ultra high speed water slug propelled by the combustion of 65 grams of the rifle powder. The standoff distance was 2.5cm (Fig 4.1). As a result a composite target (Fig 4.2) was successfully pierced. All three plates have a bottle neck type deformed section (plastic dome) with an opening. Size of each opening is as follows: front plate has a circular opening of 26.67mm diameter; middle plate has a circular opening of 32.46mm diameter and the back plate has an opening of slightly oval shape with large axes of 35.51mm and small axes of 34.29mm. The front plate has a bottle neck deformed section 27.94mm deep, which is measured from the impact base plane. This depth is uniformly distributed along the circumference of the opening and clean cut is observed along the edge of the opening. The depth of the bottle neck deformed section of the middle plate is uniformly distributed as well. Its depth measured from the front plane of the plate is 29.31mm. The opening on the middle plate has rougher edge compared to the front plate but it can still be characterized as a relatively clean cut edge. The depth of the bottle neck deformed section of the back plate is 37.36 mm, measured from the front plane of the plate. The edge of the opening on this plate consists of 13 primary cracks and number of small secondary cracks which gives ruptured appearance to the opening. All three plates failed in a ductile overload manner which was already confirmed by examination of same type of samples generated in

previously conducted experiments. During the course of impact 3 grams of steel were removed from the front plate, 9 grams were removed from the middle plate and 8 grams of steel were removed from the back plate.

Aluminum plates were tested in double layer sandwich. Projectiles were aimed to the composite target made of two combined 9.9mm thick aluminum alloy plates which were of rectangular shape, 11.5 inches by 7 inches in size. This target was exposed to the impact of 230grams ultra high speed water slug propelled by combustion of 57 grams of the rifle powder. These plates failed in a manner similar to that of the steel plates and have a plastic dome (bottle neck type) deformed area (Fig. 4.3). Pierced openings of these two plates have different appearance indicating different mode of failure. Front plate has an opening of irregular oval shape with 28 mm large axes and 23 mm small axes (Fig 4.3 c).

Back plate has a star like opening which was generated by propagation of six primary cracks leading down to the base of the plastic dome area (Fig 4.3d). This opening has the largest dimension of 33mm and the smallest dimension of 21mm. Several aluminum fragments generated by piercing action of the slug were captured by a fragment catching module (Fig. 4.1). These fragments varied in shape and size and the largest fragment recovered was weighting 3 grams and it was 21.59mm long, 13.46mm wide and it has variable thickness from 9.78mm on one end and 4.32mm on the other end (Fig.4.3 b). This fragment broke of from the front plate's plastic dome root area. Other fragments were much smaller weighting 1 gram or less. Second by size fragment weights 1 gram, it is 12 mm long, 7mm wide and has variable thickness from 4.8mm on one end and 5.1mm on the other end. Smaller fragments were between 7.87mm and 12.2mm long

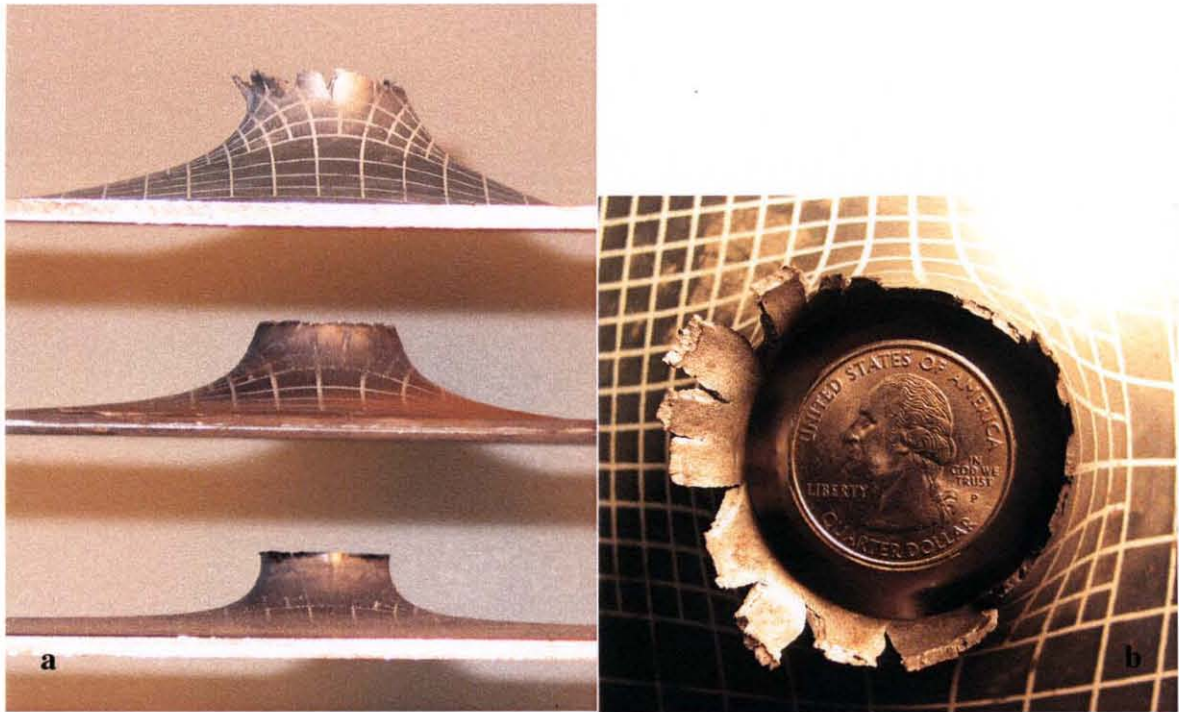


Figure 4.2 a) Side view of three 4.8 mm steel plates simultaneously pierced by 230g water-slug with 64.69g of rifle powder charge; b) Top view of back plate.

and between 3.81mm and 4.9mm wide. The highest thinning of fragments before failure was indicated among the group of the smallest particles and it was 2.175mm.

Results obtained in these experiments demonstrated high potential of the armor piercing. As expected they were consistent with results obtained in the previous experiments. High energy high speed water projectile is definitely a means for successful dealing with metal target piercing.

4.4. Characterization of Deformation of Pierced Plates

In order to explore deformation and deformability limits of tested plates under water projectile impact all samples were prepared in the same manner. High adhesion paint was used to paint a 16cm x16cm square grid with 0.5cm spacing in the central portion of the grid 8cm x8cm square, and with 1 cm dense spacing in the outside portion of the grid

(Fig. 4.4). The grid was designed to quantify the plate's deformation. The grid deformed in the course of the impact is shown on Fig's 4.2 and 4.3. Deformed plates were scanned using CNC machine and a set of data containing X, Y and Z grid coordinates was generated. Nondestructive ultrasonic technique was used for flaw detection and thickness gauging. Time of flight scanning technique was used to generate a set of thickness distribution measurements. Each thickness reading corresponds to X, Y and Z coordinates combination at the gridlines intersections. These sets of data were uploaded to Mat Lab and geometry of deformed plates was reproduced (Fig. 4.5). Precise mapping of engineering strain and thickness distribution was conducted. Engineering strain e was determined using equation shown below where L_f stands for final length of measured unit of the grid and L_i stands for initial length of the same %AR grid unit.

$$e = \frac{L_f - L_i}{L_i} = \frac{\Delta L}{L} \quad (2.1)$$

Percent elongation ($\%EL$) is determined by following equation:

$$\%EL = (e) 100\% \quad (2.2)$$

Percent thickness reduction ($\%TR$) was determined using the equation:

$$\%TR = \frac{T_f - T_i}{T_i} 100\% \quad (2.3)$$

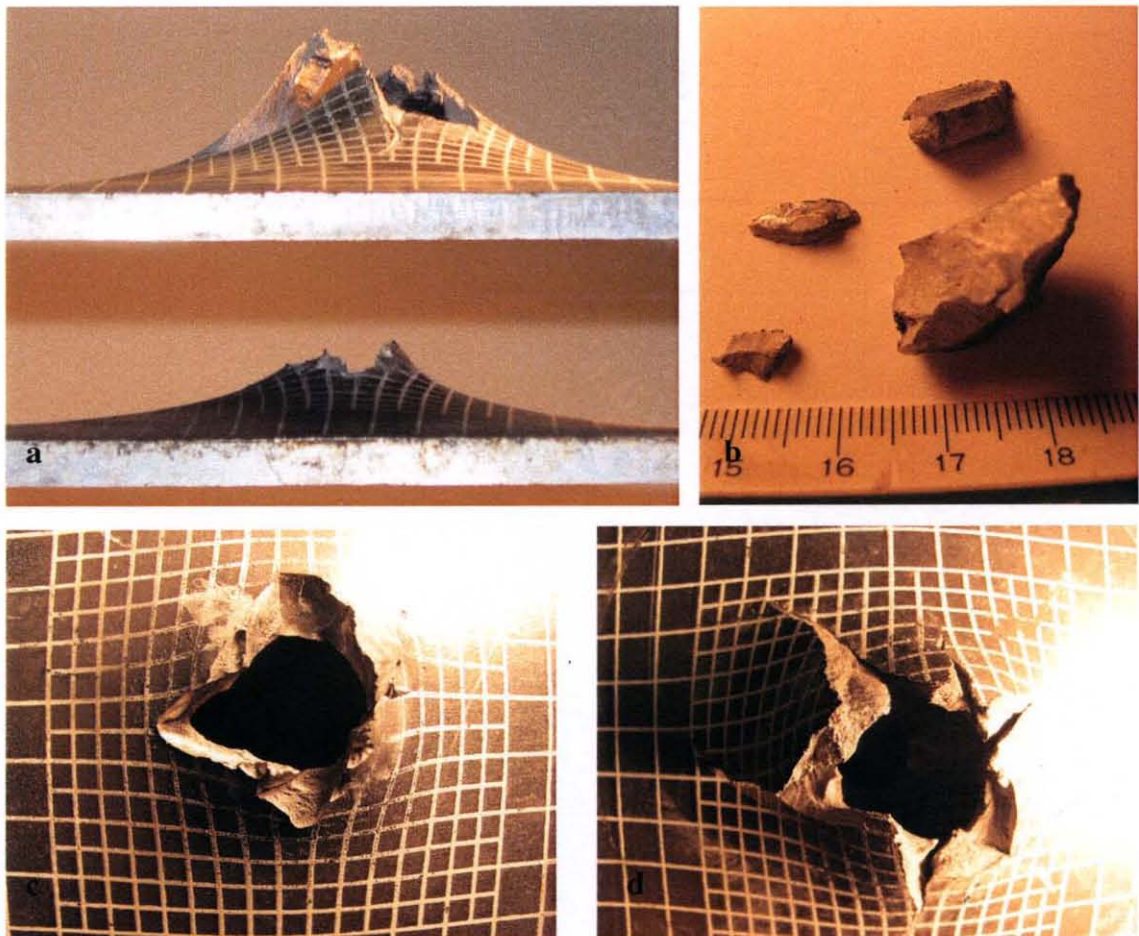


Figure 4.3 a) Two 9.9 mm thick Aluminum plates pierced by 230g water- with 57 g of powder; b) Captured fragments; c) Top view of front plate; d) Top view of back plate.

where T_f stands for final thickness and T_i stands for initial thickness of the plate.

Percent area reduction ($\%AR$) of cross section of deformed plates was estimated based on maps of strain and thickness distribution since accurate measurements of area reduction was not possible.

In all performed experiments plates were deformed in the same manner. The central portion of the impact zone of each tested plate was transformed into plastic dome. The range of the nodes displacement demonstrates high metals plasticity during the

impact. For example the percent elongation ($\%EL$) of the metal samples ranges between 10% and 120%. Maximal thickness reduction of 93.75% in the vicinity of fractured zone was observed while the cross section percent area reduction ($\%AR$) was in the range of 35%-40%. Plastic dome surfaces on entering and exiting sides gained smoother texture in comparison to undeformed surface portions of tested samples. Besides the vicinity of pierced openings no voids or laminations were detected in the tested samples.

Nozzle and collimator of the cannon have a circular shape and the projectiles develop forefront of mushroom-like or hemispherical shape which pierces targets in such way to make openings of circular or slightly elliptical shape. Compared to deformation induced by typical solid projectiles results from these experiments look very similar to them. Solid projectiles produce symmetric deformation [39] of ductile targets and the difference in appearance of impacted target depends mainly on material properties and geometry of the target.

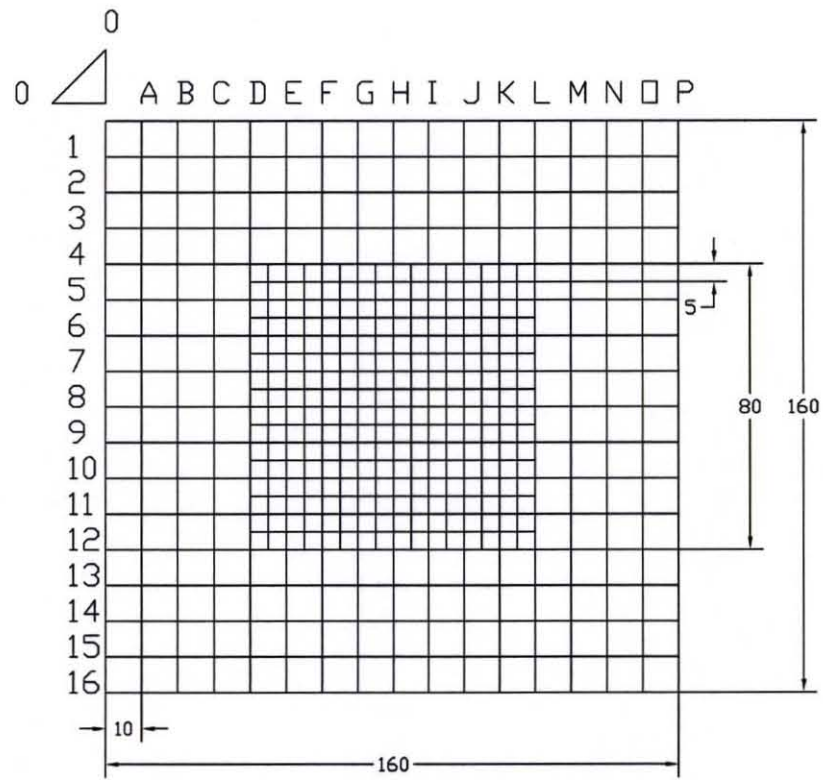


Figure 4.4 Schematic of square mesh grid painted on each sample (dimensions in mm).

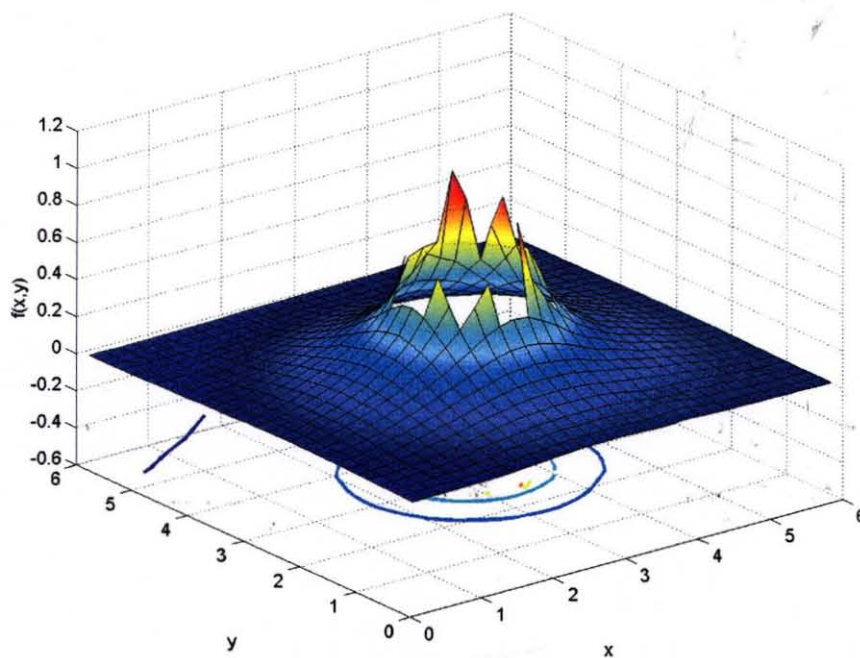


Figure 4.5 A 3-D reproduction of upper surface of deformed plate.

In these experiments detailed mapping of water projectile induced deformation of metal plates indicated deviation from typical deformation induced by solid projectile. However, mapping the grid deformation shows that the shape of pierced opening doesn't necessarily project to the base of the plastic dome. Specifically it was observed that plates with symmetric circular pierced openings do not have circular but elliptical base of plastic dome. Namely, range of plastic deformation of plates in longitudinal direction (Fig. 4.4, X-axes A-P) does not match the range of plastic deformation in the transversal direction (Fig. 4.4, Y axes 1-16), which is also demonstrated on Fig. 4.6.. Peculiarity of this difference in impact effect of liquid projectile from the effect of solid projectile is due certain flow instabilities. Liquid projectiles can have 1-D, 2-D or 3-D instabilities of the fluid flow within the projectile. These instabilities can be induced by different causes such as cavitations, shockwave interactions, surface imperfections of the cannon barrel, etc. As a result of instable flow the projectile can deform and in different ways and therefore induce particular pressure field in projectile target interface, therefore causing nonsymmetrical deformation zone.

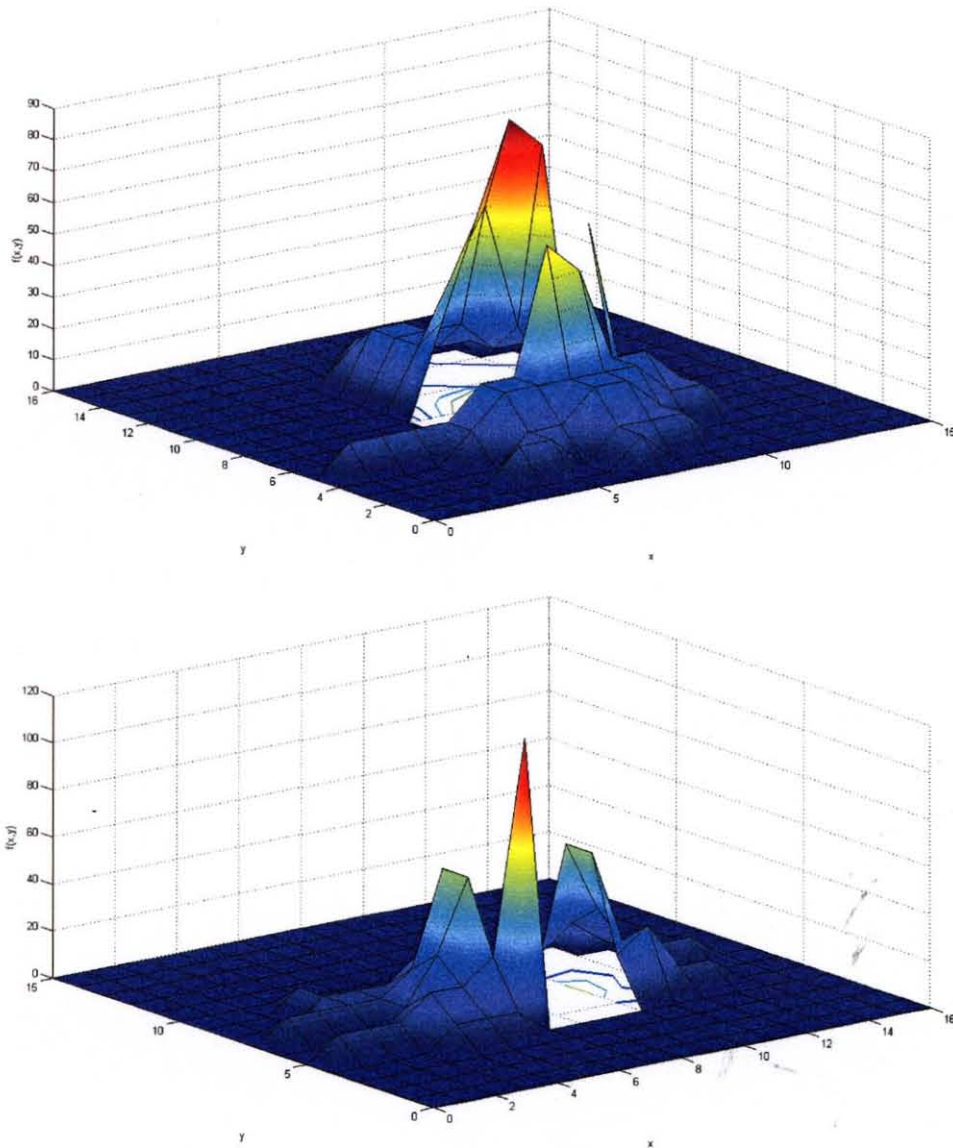


Figure 4.6 Percent elongation in longitudinal (X-axes, above) and transversal direction (Y-axes, below).

Tested A36 hot rolled steel by manufacturer's specification has % elongation range between 18% and 22%. Measurements of deformed grid lines indicate high plasticity of deformation with up to 120 % elongation of line segments between the nodes. Maximal elongation is observed in the central impact zone and degree of deformation drops as the distance from the impact center increases. The % elongation ranges between 10 and 120%. Similar mode of thickness reduction is observed by

characterization of thickness distribution of impacted plates. Extreme zone of thickness reduction is observed along the fractured edges of pierced openings of tested plates. Maximal thickness reduction of 93.75% is observed in that zone. Within the distance of 5mm from the fractured edge thickness reduction drops to around 76% and within another 5mm band thickness reduction is around 55% leading to much smaller thickness reduction as the distance from the impact center increases. The area of tested plates displaced in Z direction is bound by plastic dome as shown on Fig.4.7.

In order to explore deformability of tested samples besides mapping of strain and

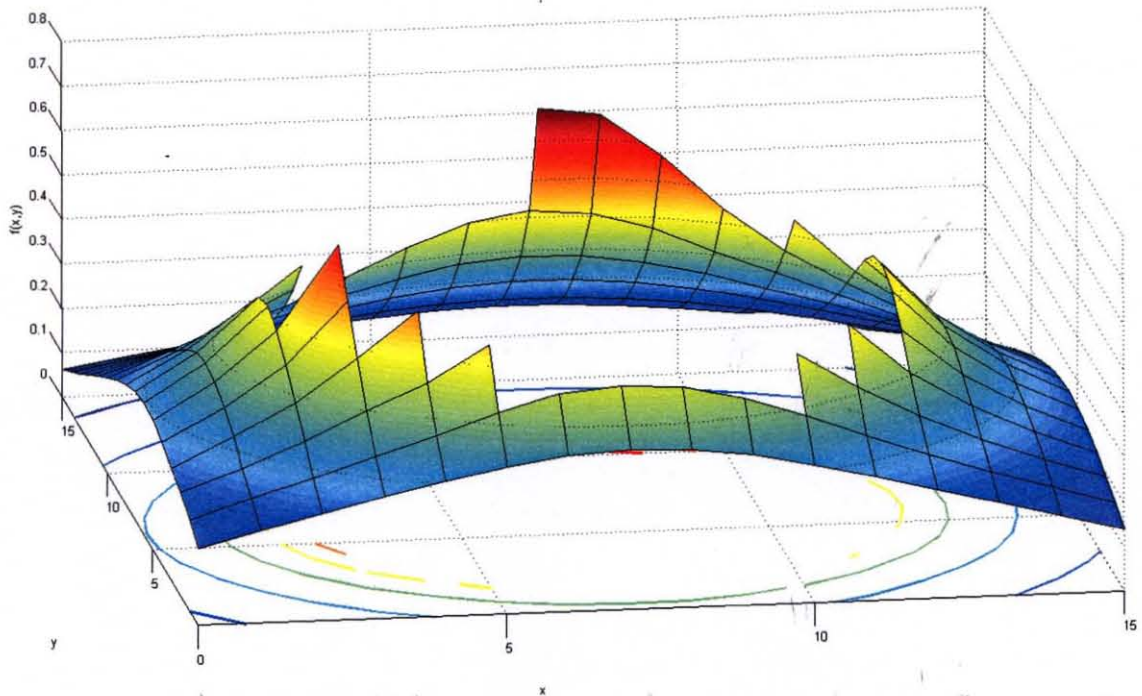


Figure 4.7 Node displacements in impact direction (Z –axes).

thickness changes micrography was employed to observe impact-induced changes of microstructure. Samples for microstructure investigation were cut from plates in longitudinal and transversal direction. Micrographs showing gradual grain deformation

from the periphery of plastic dome with increased degree of grain deformation and more pronounced inclusions towards the impact center were documented. Here we show examples of micrographs of non-deformed microstructure in transversal direction (Figure 4.8 insertion window) and highly deformed grains at the fracture zone (Figure 4.8 main window). In this investigation high strain (up to 120% elongation) and high strain rate are observed as characteristics of the process of deformation of metal plates by impact of water projectiles. Estimated strain rate of 8.5×10^{-6} 1/sec as compared to 10×10^{-5} 1/sec for solid projectile induced deformation of metal plates [39]. Study of strain rates will be further pursued and additionally verified in our near future work.

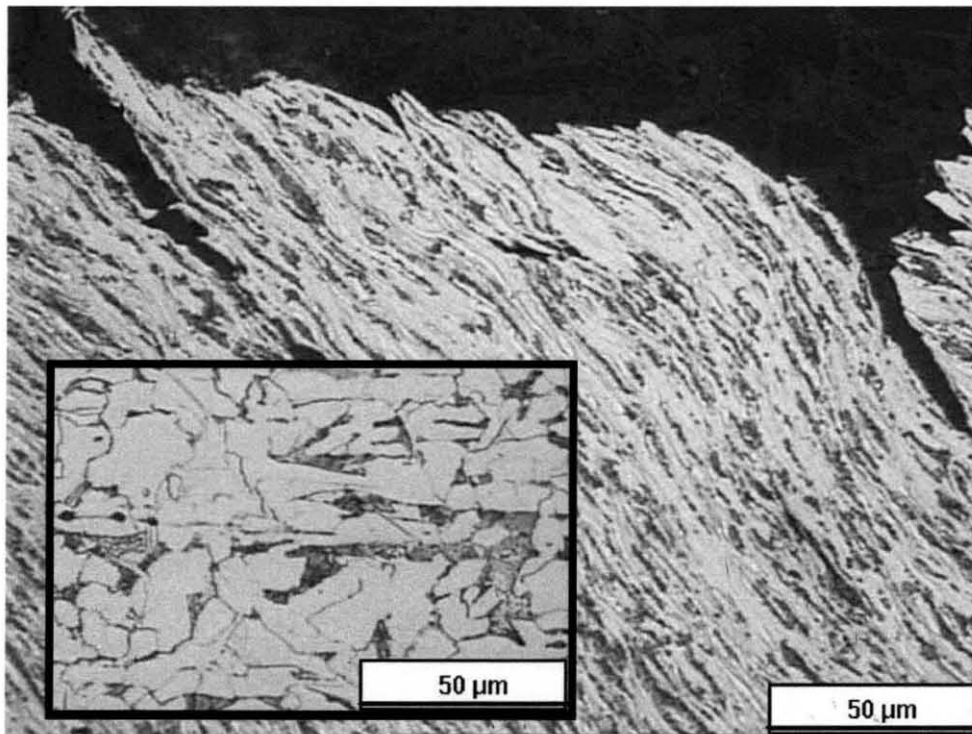


Figure 4.8 Microstructure from non-deformed and fracture zones in transversal direction.

4.5. Mechanism of Piercing of Metals

The process of piercing can be divided following phases: first-elastic part of impact duration (1), second-beginning phase of plastic deformation(2), third-during which hemispherical plastic dome (3) is being formed by mushroom-shaped projectile head, and final piercing phase (4) during which material gets ruptured due to rapid primary cracks propagation (as shown on Fig.4.9).

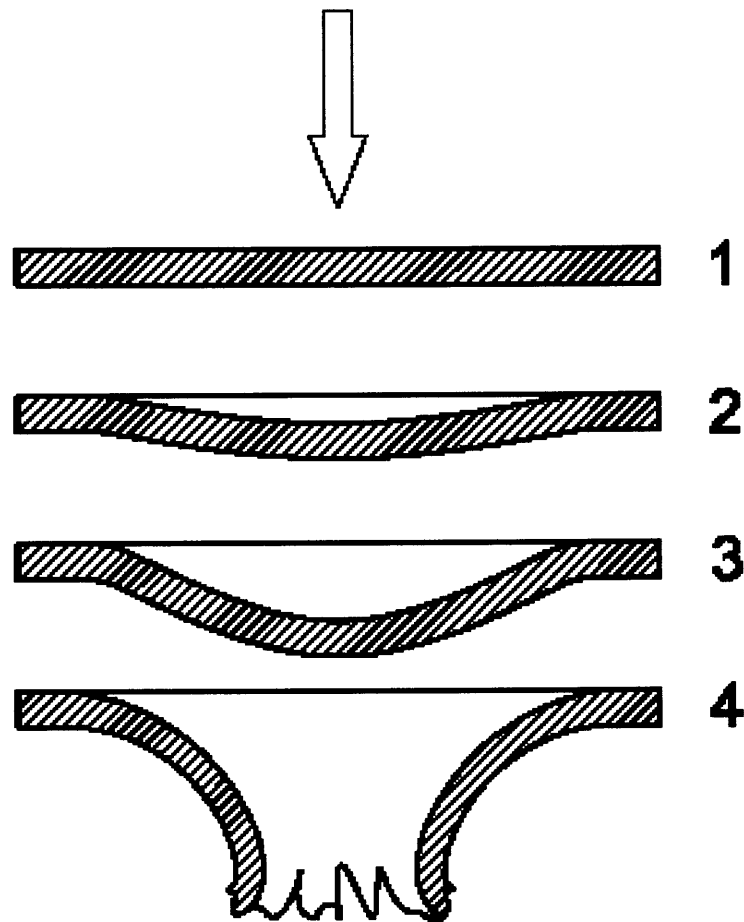


Figure 4.9 Schematic of phases of piercing: 1- initial state, 2-beginning of plastic deformation, 3-plastic dome forming, and 3-final shape forming.

4.6. Conclusions

It was shown that a high speed water projectile is able to deform heavy metal targets at an extremely high rate and generates high strains. Deformability limits under high strain rates were determined. Strains and strain ranges were determined. It was demonstrated that water projectiles provide similar but not identical effects as solid projectiles. Peculiarity of nonsymmetrical deformation of metal plates by water projectiles was documented. Characterization of deformation of impacted plates involved variety of instruments and together with data processing technique can be effective tool for deformation evaluation.

CHAPTER 5

INVESTIGATION OF FAILURE OF MATERIALS UNDER HIGH SPEED LIQUID IMPACT

5.1 Introduction

The objective of this study was to investigate failure and modes of failure of ductile and brittle materials under impact of high speed water projectiles. Fractography is a science of examining fracture surfaces. In this study fractography analysis of metal plates was conducted and failure was classified for steel and aluminum plates. Granite and concrete were used for investigation of failure brittle materials. Modes of failure of all tested materials were investigated and identified. Six modes of failure were identified and documented.

5.2 Failure of Metals Under High Speed Liquid Impact

Steel and aluminum plates were used for investigation of failure of metals under impact of high speed liquid projectiles. Piercing of steel (Figs. 4.3 and 6.1) and piercing of aluminum (Fig. 4.3) was used to generate fracture evidence for fractography study. It was observed that steel plates failed mainly in ductile overload mode. Saying mainly means that upon initiation of plastic phase of deformation process stresses generated in the impact zone continue to grow and reach ductile overload levels. During the deformation process, rapid thinning of impacted plates takes place and due to heating of impact zone mechanical response of impacted media changes continuously. For steel plates evidence gathered during experiments confirmed that the impact zone undergoes complex temperature field with heated zones ranging from around 400°C to melted metal zones.

Considering the fact, that steel when reaching temperature of about 500°C loses half of its load carrying capacity the response of the target material changes as heating of the impacted media takes place. Therefore, due to complex heat field impacted material response is complex as well. Examination of fractured surfaces revealed three distinctive zones corresponding to different failure modes along cross section of fractured surface. Predominant zone of ductile overload covers around 75% of fracture thickness. Another zone which has smeared appearance was found next to ductile overload zone and finally thin zone of brittle failure is to be assigned to the final moments prior to separation of fractured fragments of impacted steel.



Figure 5.1 General view of 4.8mm thick steel plate pierced by 230g water projectile.

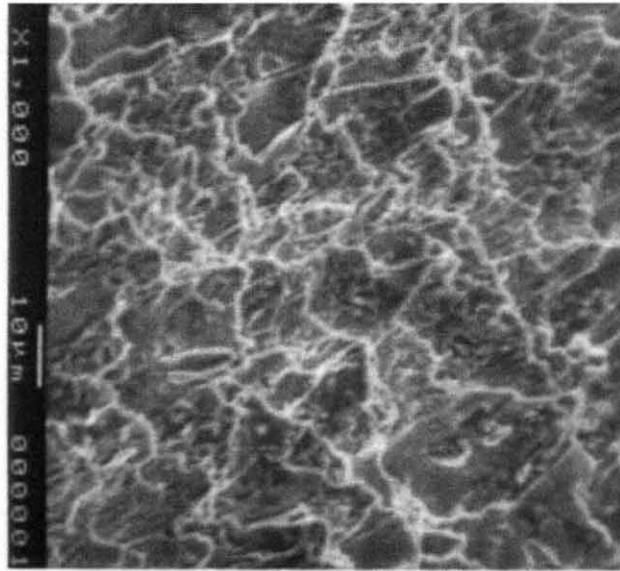


Figure 5.2 Fractograph (X1000) generated from fractured surface of steel plate shown on Fig. 5.1. Ductile overload is the failure mode corresponding to the shown field of view.

In addition existence of phase change on fractured surfaces was observed. It was documented that liquefactions of portions of metals in the fracture zone took place (Figs. 5.3, 5.4) and that entire portions of fractured surfaces were covered with glaze of liquefied phase formed in the final moments of material separation. The entire fields of view surrounding solidified droplets shown on Figs 5.3 and 5.4 are covered with glazy phase.



Figure 5.3 SEM micrograph (X1100) of solidified egg like droplet formed in the final stage of steel failure.

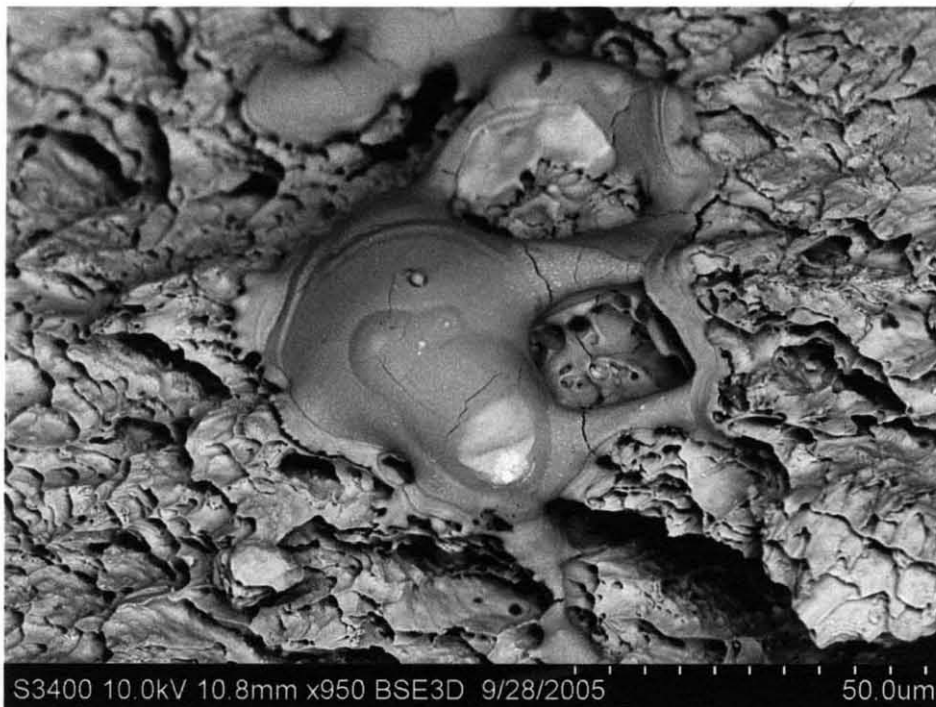


Figure 5.4 SEM micrograph (X950) of solidified spill like droplet formed in the final stage of steel failure.

Chemical analysis of liquefied-solidified zones revealed variety of chemical compositions. Locations 1, 2 and 3 from Fig. 5.5 correspond to the chemical analysis. All three locations are covered with new phase having oxides and pure elements. At the location 1, elements found were: Carbon, Oxygen, Iron, Silicon, Chloride, Sodium, Potassium, Sulfur and combinations elements listed (Fig. 5.6). At the location 2 elements found were: Carbon, Iron, Oxygen, Manganese, Aluminum, Silicon, Sulfur, Chloride, Potassium and combinations elements listed (Fig. 5.7). At the location 3 elements found were: Iron, Carbon, Sodium, Sulfur, and combinations elements listed (Fig. 5.8). It should be noted that very different phase compositions are found on such small area (field of view is 120μ by 85μ). Hypothesis is proposed that as separation along the fracture surface propagates approaching final separation moments the very last parts of metal still connected get rapidly stretched and get melted due to extremely high strain rate. As final separation takes place liquid portions of metal solidify on each part of fractured surface.



Figure 5.5 SEM micrograph (X750) of solidified combination of egg like droplet and pipe like formed in the final stage of steel failure.

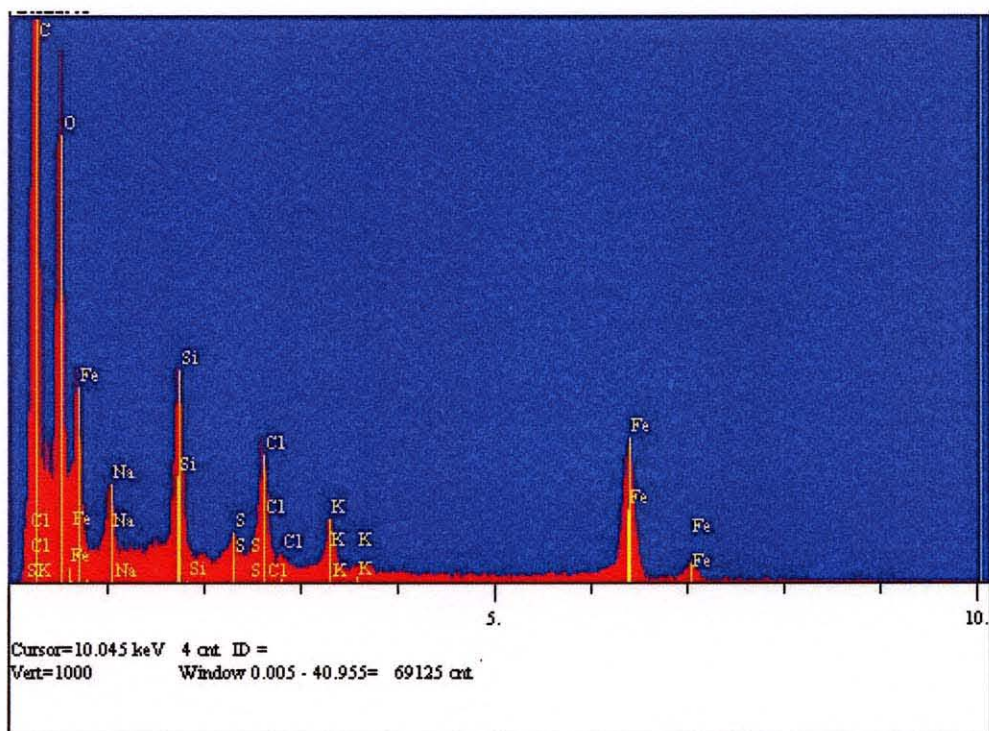


Figure 5.6 SEM chemical analysis of new phase (pipe-like structure) at the location 1 shown on Fig.5.5.

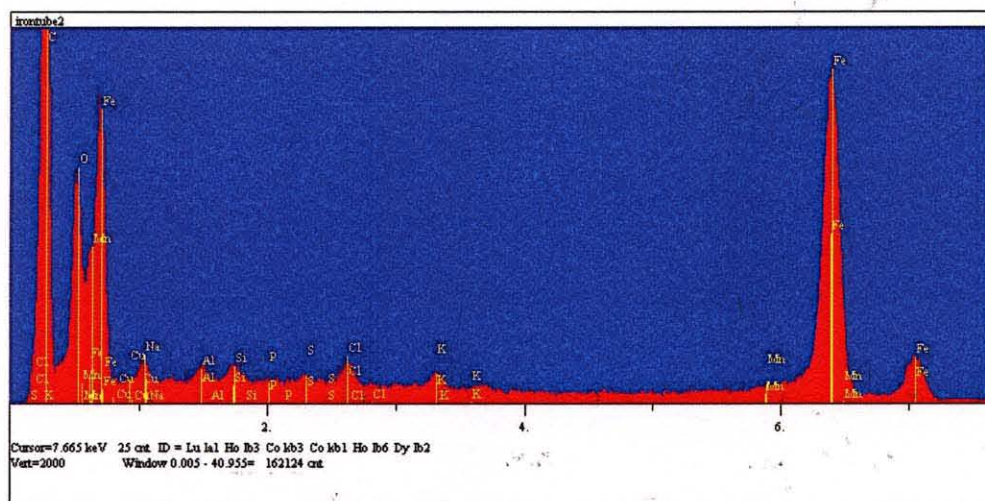


Figure 5.7 SEM chemical analysis of new phase (rectangle area) at the location 2 shown on Fig.5.5.

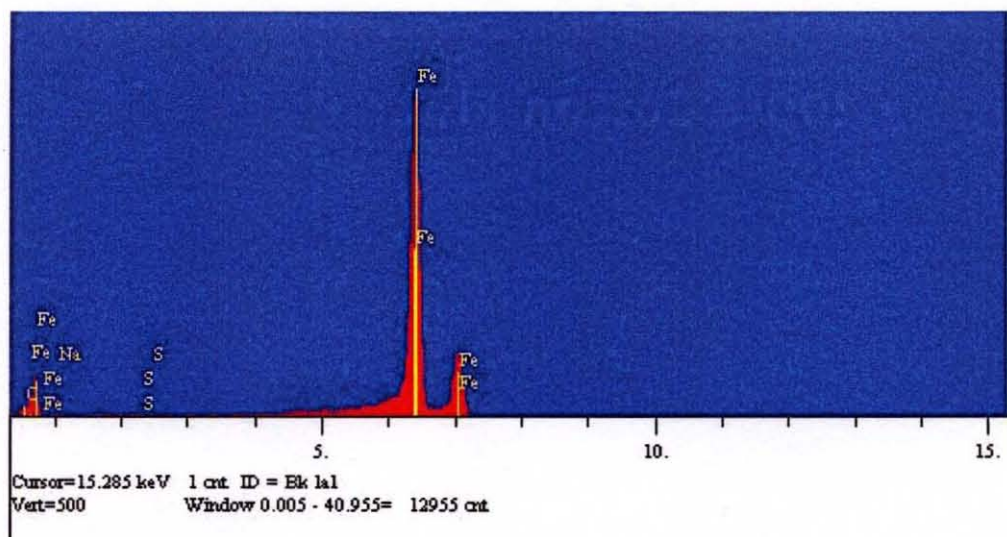


Figure 5.8 SEM chemical analysis of new phase at the location 3 shown on Fig.5.5.

Analysis of aluminum fracture revealed brittle mode of failure which was expected since aluminum plates used in the experiment were heat treated. General views of fractured plates and recovered fragments are shown on Fig. 4.4 and 3-D image of portion fracture surface is shown on Fig. 5.9.

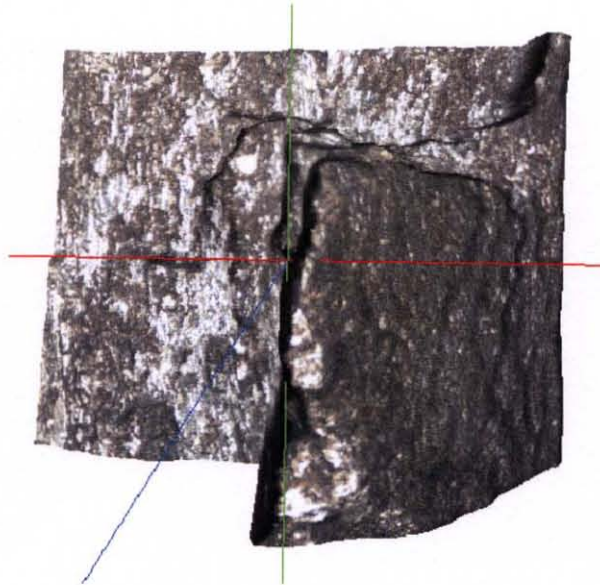


Figure 5.9 3-D image of portion fractured surface of aluminum plate. The appearance is typical for brittle fracture.

5.3 Modes of Failure of Materials Under High Speed Liquid Impact

During this study six modes of failure of materials were identified, documented, and proposed. Ductile hole growth (Fig. 5.10) takes place when projectile penetrates the target material by pushing target mass in radial direction and therefore creates a hole. Piercing of a pot filled with wax is excellent example of this mode of failure (Fig 2.27).



Figure 5.10 Graphic representation of ductile hole growth mode of failure (see Fig 2.27).

Radial fracture mode (Fig. 5.11) of failure takes place when a set of primary cracks get initiated on the back side of impacted plate (Fig. 4.3d). As these cracks propagate in radial direction they govern failure of impacted target.

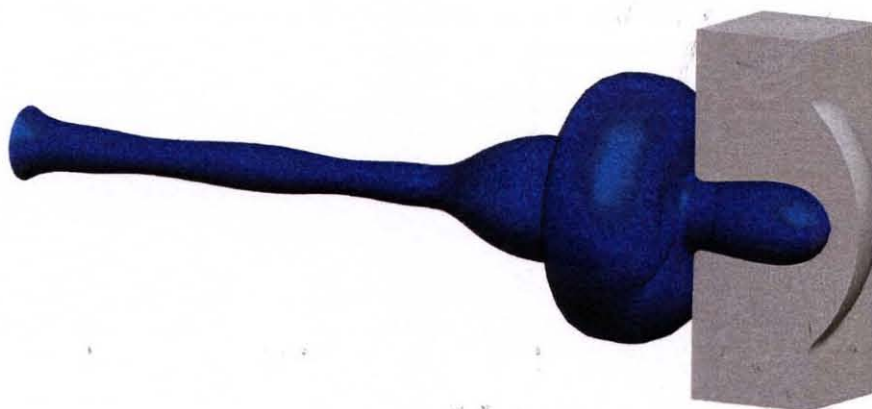


Figure 5.11 Graphic representation of radial fracture mode of failure (see Fig. 4.3d).

Plugging mode (Fig. 5.12) of failure takes place when during the penetration process due to adiabatic shearing a plug is being created and extruded as a single entity (Figs 6.6 and 6.17).



Figure 5.12 Graphic representation of plugging mode of failure (see Figs 6.6 and 6.17).

Fragmentation mode (Fig. 5.13) of failure takes place when a set of primary cracks get initiated on the back side of impacted plate. As formed cracks propagate fragments form and separate from back side of the plate.

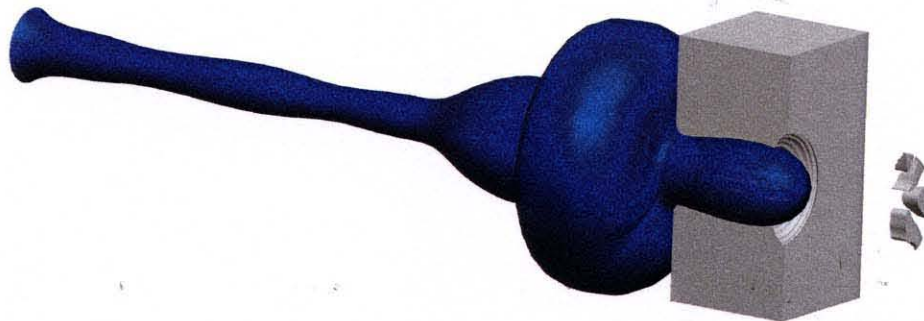


Figure 5.13 Graphic representation of fragmentation mode of failure (see Fig 4.3b and c).

Petaling mode (Fig. 5.14) of failure takes place when large numbers of intergranular cracks almost simultaneously propagate resulting in failure which resembles flower petals (Figs. 4.2 and 5.1)



Figure 5.14 Graphic representation of petaling mode of failure (see Figs. 4.2 and 5.1).

Brittle fracture mode of failure takes place when impacting brittle materials such as concrete and granite. Due to porosity (large number of stress raisers) of concrete simultaneous multiple crack initiation takes place leading to high rate chain crack propagation which results in explosion like failure (Fig.5.15).



Figure 5.15 Example of brittle fracture mode of failure (concrete demolition).

5.4 Discussion of Results and Conclusions

Fractography analysis was used to characterize failure of metals. Detailed interpretation of steel and aluminum failure was provided. As a result several distinctive failure zones were identified and presented. Ductile overload, brittle fracture and transitional zone between the two were observed. Mechanisms of failure of metals and brittle materials under liquid impact were explained. Investigation of phase change on fracture surface was conducted and presented. Six modes of failure of materials were identified: ductile hole growth, radial fracture mode, plugging mode, fragmentation mode, petaling mode and brittle fracture mode were explained and presented.

CHAPTER 6

FORMING OF METALS USING HIGH SPEED WATER PROJECTILES

6.1 Introduction

Exploration of the potential applications of the liquid projectiles is objective of this study. Namely, punching and forming of metals was investigated. The performed experimental study showed that high speed liquid projectiles are an effective material processing tool. Particularly, the objective of this study was to investigate metals processing using a high speed liquid impact. Conventional metal punching and forming are costly and water projectiles could be more economic tool for some operations [40]. The effect of the standoff distance and the target thickness on the workpiece deformation was investigated. Such processes as punching of circular and complex shape openings in steel plates and liquid impact based forging were explored. Experimental data acquired in the course of the performed experiments was incorporated into the knowledge base of the material processing by high speed water projectiles. As a result of the performed experiments feasibility of the use of high speed water projectiles for a number of material processing operations was demonstrated.

6.2 Experimental Procedure

An experimental setup for the study of the impact based forming was designed and constructed (Fig. 3.1). With minor modifications this setup was used in all performed experiments. Laboratory scale prototypes of the water cannon [34, 35] were used in this study. The targets were mounted on a heavy pendulum (Fig. 3.1). Angular displacement of pendulum was measured in each experiment. This enabled us to estimate impact impulse and therefore impact momentum. For each experiment water cannon was placed at a desired

standoff distance from the sample and particular water impact operation was performed. Experimental data collected in the performed experiments was used for the study of material deformation and processing by high speed water projectiles.

6.3 Experimental Investigation of Punching of Steel Plates

6.3.1 Punching of Circular Openings

Three objectives were pursued in this study. First, the feasibility and limits (maximal plate thickness, minimal punched opening diameter and maximal punched opening diameter) of the operation were explored. Second, punching of complex shape opening in steel plates of various thicknesses was studied. The third objective was to investigate punching of multiple

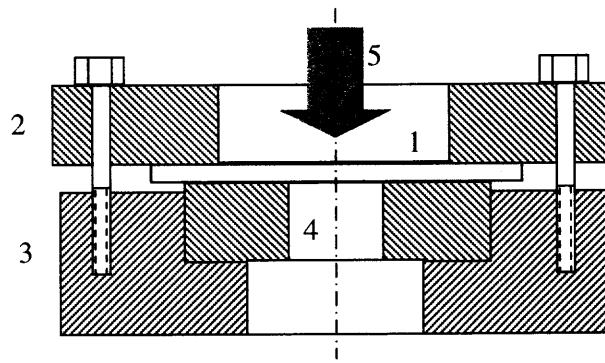


Figure 6.1 sample-1, clamping plate-2, die holder-3, die-4, high speed liquid projectile-5.

holes by a single water projectile impact. A close up schematic of the impact zone subassembly is shown on Fig. 6.1 In this investigation the exit diameter of the launcher was 15mm. For punching of steel plates dies were designed and manufactured out of die-steel. All dies were heat treated.

Hot rolled carbon steel with 0.22% of the carbon content which has the tensile strength of 450MPa, the yield strength of 320MPa and the maximal relative elongation (plasticity) of 26% was used in the first series of the experiments. Plates of 2.5, 4.2, 6, 8 and 10mm thicknesses were tested. In each experiment the steel sample was tightly attached against the die and mounted on the pendulum. A water load of 200g was propelled by combustion of 40g of powder. The standoff distance was 16cm in each experiment. Dies with round openings of 16.5 and 25mm diameter were used in this part of investigation (Fig. 6.3). Against both dies circular openings were created in plates of 2, 4, 6 and 8mm. The opening of 25 mm in diameter was created in the 10 mm thick plate while the opening of 16.5mm in diameter was not completed in the similar plate. In this case the deformation process on the impact side has been initiated and shearing cutting on the die side was started but not

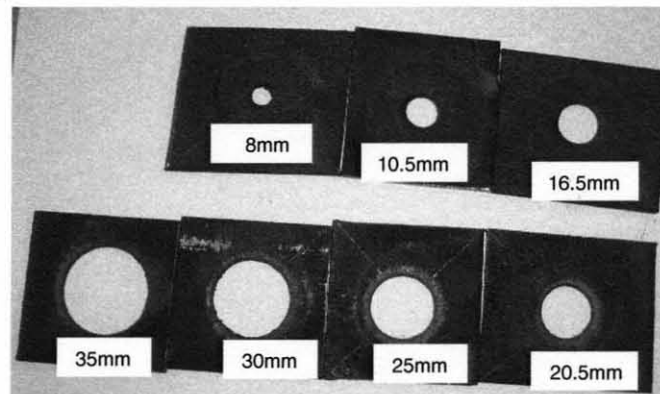


Figure 6.2 Piercing of 4mm steel plates. Notice feasibility of generating different openings using the same jet.

completed. Entering side of each opening has slightly rounded edges due to the flow of punched portion of material and exiting side of circular opening has sharp edge which was cut against the die. Calculated velocity of the projectile head prior to the impact was 1500m/s.

Another series of experiments involved evaluation of the maximal opening generated by the impacting jet. In these experiments the 4 mm thick steel plates were punched against dies with the openings of 4, 8, 10.5, 16.5, 20.5, 25, 35, 40, and 45mm. The water projectiles

of 200g were propelled by 40g of powder and at the standoff distance to the target of 16cm. An array of clean cut openings was created against dies with: 4, 8, 10.5, 16.5, 20.5, 25, 30, and 35mm diametric openings (Fig.6.2). The attempt to generate the opening of 40mm failed. The sample was not pierced and it failed in petaling mode. Diametric opening of 45mm was punched around $\frac{3}{4}$ of circumference and punched portion of the material was still holding on $\frac{1}{4}$ of circumference. In this part of investigation $D/d=2.5$ was reached and maximal thickness of $h=0.67d$ was punched. Here D is the opening diameter, mm; d is the projectile diameter, mm and h is the standoff distance.

Selected experimental results are shown in Table 6.1



Figure 6.3 Dies for punching of metals, diameters 25, 16.5 and 12mm.

Table 6.1 Punching of Steel Experimental Results (Figures 6.5, 6.6, 6.7, 6.8, 6.9, and 6.10)

Ex p. №	Plate thickness, mm	Die diameter, mm	Stand of distance, cm	Result	Impulse[kgm/s]/ Pendulum displacement* α [°]	Experimental conditions and comments
1	4	16.5	16	Punched	251.22/*18	Mass of powder 40g. Mass of water 200g. Calculated projectile velocity 1500m/s. Opening punched.
2	6	16.5	16	Punched	244.47/*17,5	Mass of powder 40g. Mass of water 200g. Calculated projectile velocity 1500m/s. Opening punched.
3	8	16.5	16	Punched	257.96/*18,5	Mass of powder 40g. Mass of water 200 g. Calculated projectile velocity 1500m/s. Opening punched.
4	10	16.5	16	Not punched	278.05/*20	Metal deformed, sheering started but opening not punched.
5	4	25	16	Punched	278.05/*20	Opening punched.
6	8	25	16	Punched	257.96/*18.5	Opening punched.
7	10	25	16	Punched	251.22/*18	High quality opening punched. Exiting side of the opening has sharp edge with diameter which is equal to die opening diameter while impact side has slightly smaller diameter with rounded edges due to rollover.

Figures 6.4 and 6.5 show general view of three experimental results involving punching of steel plates against a die with an opening of 25mm (Table 6.1, experiments 5, 6 and 7). Photographs show impact side of punched plates (Fig.6.4 which have rounded edges, and projectile-exiting side (Fig.6.5) of punched openings which have sharp cut edge. Exiting



Figure 6.4 Impact side views of punched openings in plates 4, 8 and 10mm thick. Punching was done against die opening 25mm in diameter.

side of the opening has sharp edge with diameter which is equal to die opening diameter while impact side has slightly smaller diameter with rounded edges. At the impact side it is evident that metal was drawn into the die opening. This is even more evident on punching of thicker plates. General view of both, impact and exit sides on 10mm thick plate punched against the die with 25mm opening is shown on Fig. 6.5. It is noticed that the hole-dimension difference between entering and exiting sides is higher for thicker plates. In this particular case the exiting hole matches the die opening size (25mm) while the entering side due to drawing of material ends up with smaller opening (22.5mm).

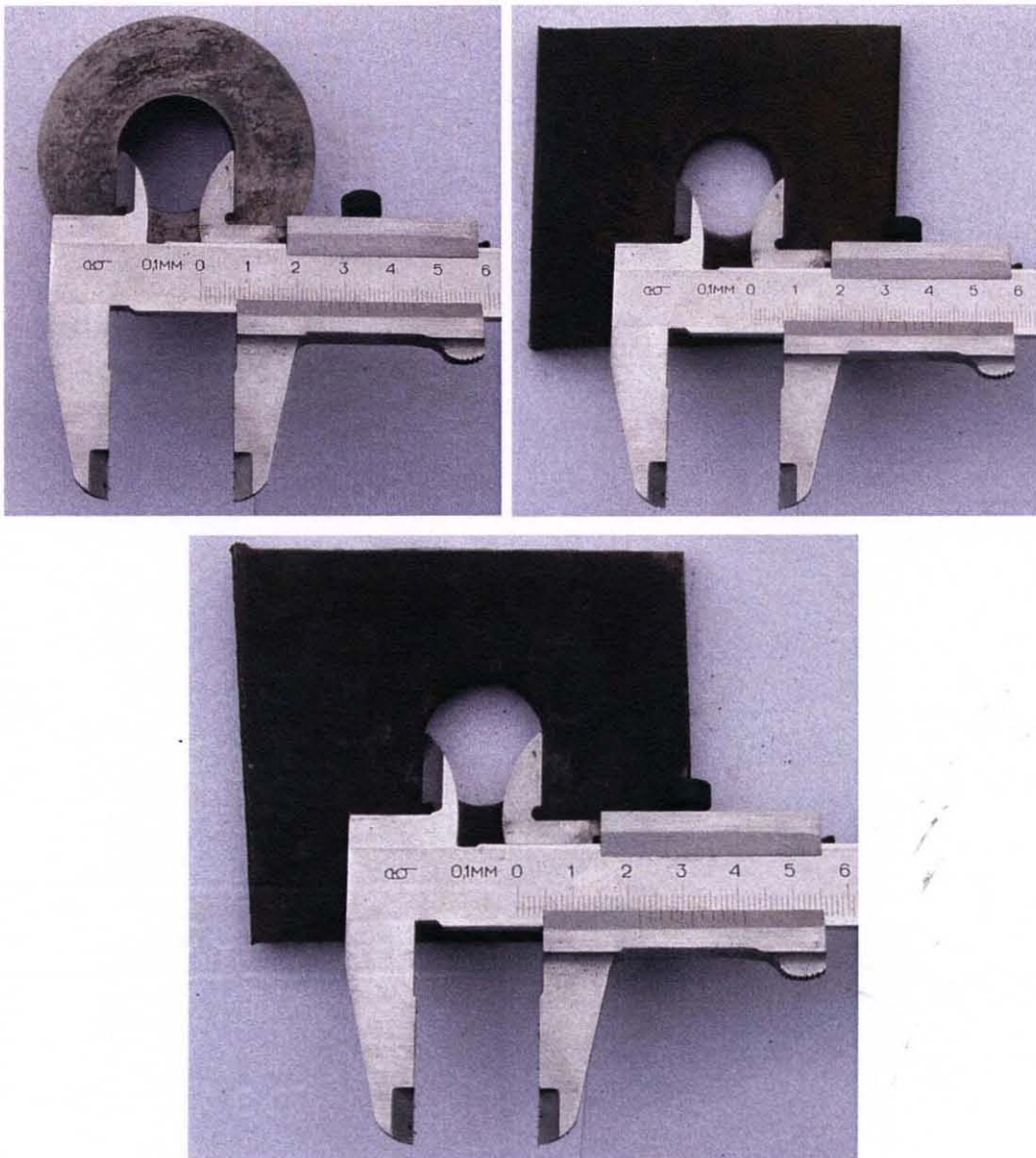


Figure 6.5 Punched opening of 10mm thick steel plate against 25mm diameter opening of die. Exit (25mm) and impact side (22.5mm) views.

Figure 6.6 shows general view of 10mm thick plate having 25mm punched opening. Punched blank of metal is placed on the plate. During punching process blank is extruded in a single piece and it is slightly deformed after the punching is completed due to collision with pendulum. It is evident that blanking takes place uniformly along the diameter of the die opening.



Figure 6.6 A 10 mm thick plate with 25mm punched opening with punched part.



Figure 6.7 Impact side views of punched openings in plates 8, 6 and 4mm thick. Punching was performed against die opening of 16.5mm in diameter.

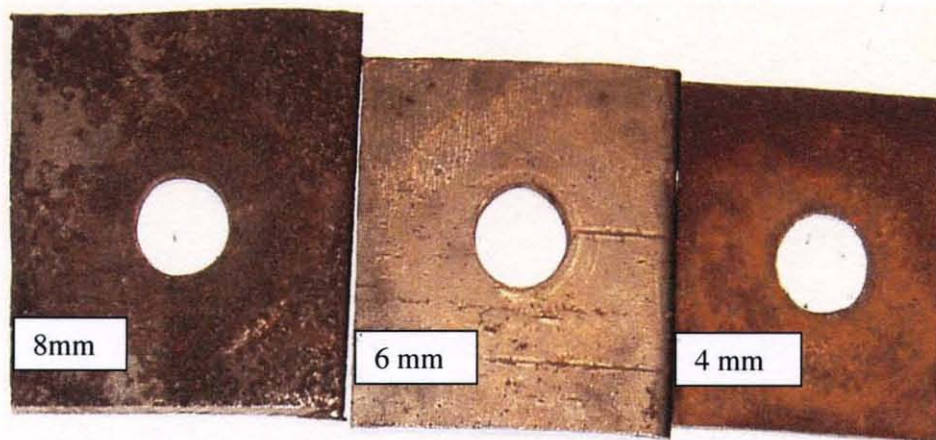


Figure 6.8 Projectile exit-side view of punched openings in plates 8, 6 and 4mm thick. Punching was done against die opening 16.5mm in diameter.

Figures 6.7 and 6.8 show results of generated openings in plates 8, 6 and 4mm thick. Punching was done against die opening 16.5mm in diameter (Table 6.1, experiments 1, 2 and 3).

On the impact side of each sample the zone of high impact pressure is marked by circular imprint which reaches 3.5 diameters ($d=15$ mm) of the nozzle. The whole series of experiments was used to determine diametric punching limit which turned out to be $3d$ ($3d=45$ mm, Fig.6.9). Two types of setups for punching were used: projectile engulfing setup and flat impact setup (where projectile flows free in radial direction). Figure 6.1 shows close up schematic of punching setup (projectile engulfing setup). It was determined that projectile engulfing setup provided significantly higher punching potential versus flat impact setup (where projectile flows free in radial direction) which is due to better conservation of projectile momentum in case of engulfing setup.

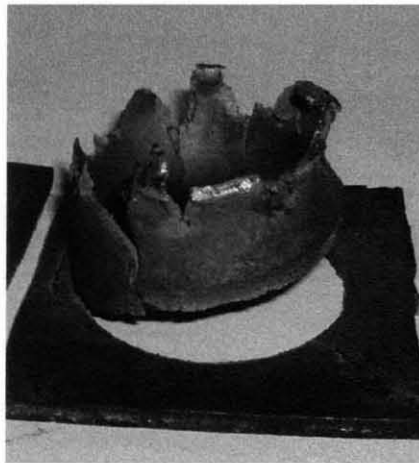


Figure 6.9 Example of punching of 4 mm thick steel plate against die of 45mm diameter. Punched piece was barely holding on the plate.

Investigation of punching of spring steel was carried out as well. Spring steel 3.175mm thick was punched against die with circular opening 10mm in diameter. Clean cut opening was generated which is shown on Fig.6.10.

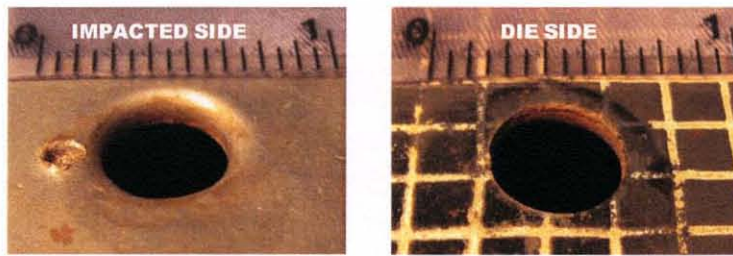


Figure 6.10 Piercing of spring steel. Notice feasibility of precision deformation of a difficult-to-shape material. $h=3.175\text{mm}$, $D=10\text{mm}$.

In the performed experiments an array of various round openings was created at a single (15mm) projectile diameter. This shows that a high speed water projectile is an effective punching tool. Thus, a novel material processing operation has been demonstrated.

6.3.2 Experimental Study of Complex Shape Openings in Steel

The next series of the experiments involved investigation of punching of complex shape opening. Steel plates of various thicknesses were punched against dies of three different shapes. In the first series of experiments a die contained three overlapping circles having

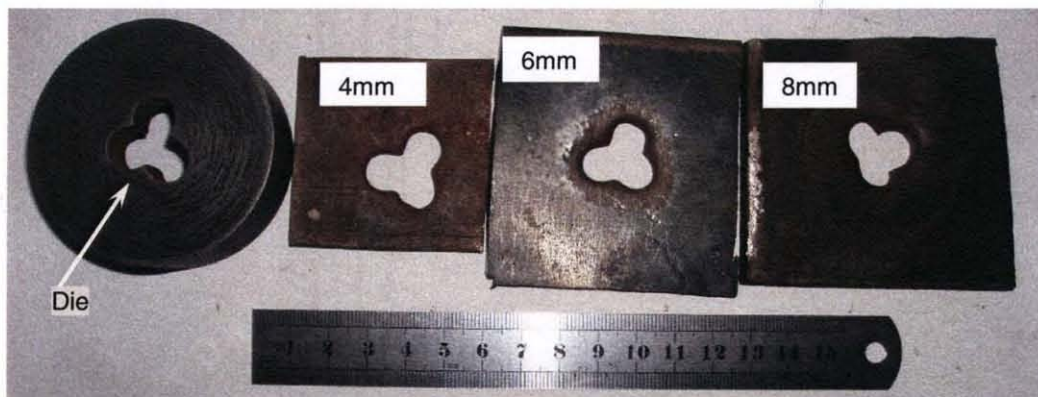


Figure 6.11 Formation of shaped openings using a round jet. Notice that the workpiece thickness does not affect the accuracy of the piercing. the same diameter of 15mm. The second die had the triangular equilateral opening with 20mm side. Third, a die with multiple 4 mm diameter holes placed at 4 mm distance from each other, was used. Experiments with composite circle and triangular openings were

performed with steel plates of thicknesses: 4, 6, 8, and 10mm (Figures 6.11 and 6.12). In each test 200g of water was used and a standoff distance was 16cm. For punching of plates of 4 and 6mm thickness 40g of powder was used which was sufficient to punch the tested plates. For 8mm thick plates it was necessary to use 45g of powder in order to create the openings. For 10mm thick plates 50g of powder was used, however this charge was not sufficient to create an opening. With both dies material was extruded to slightly more than 50% of original thickness of the plate. For punching of multiple circular openings of 4 mm diameter 3.2mm

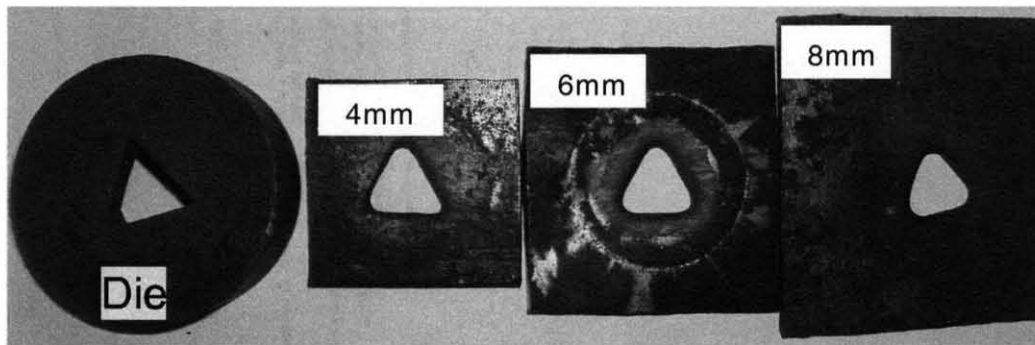


Figure 6.12 Formation of triangular openings using a round jet. Notice that the workpiece thickness does not affect the accuracy of the piercing.

thick steel plate was impacted by 200g of water. Impact was carried at the standoff distance of 16 cm and the powder charge of 40g. As a result, 6 openings were created in the central region of the impact zone and 37.5mm round depression was forged by the impact (Fig.6.13).

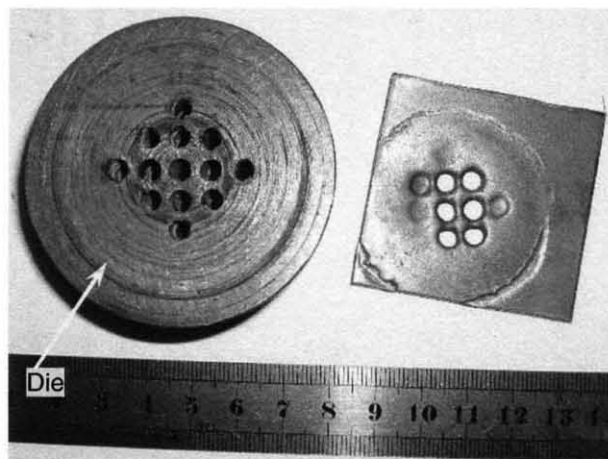


Figure 6.13 Formation of the multiple openings by a single impact of a round jet. Steel sheet thickness is 2.5mm and the opening diameter is 4mm. Notice that the liquid penetration into the workpiece can be controlled by the impact condition.

Repeatability of the results was demonstrated on the various samples

The performed experiments show that complex shape openings other than circular can be reproduced by the impact of the circular projectile. Feasibility of new technology introduced in previous part of this work was broadened by this study.

6.3.3 Mechanism of Punching of Steel Plates

Figure 6.14 shows result of failed punching of 10 mm thick steel plate against 16.5mm die diameter (Table 6.2, experiment 4). Impact side was shaped in the form of hemispherical indentation while the exiting side has smaller hemispherical bulge which is edged by sharp circular wall created by die. Shearing process has begun but not completed and an uneven extrusion of height ranging between 1 and 2mm was achieved. Uneven extrusion took place due to slight deviation from perpendicular impact angle.

The process of punching can be divided into two distinctive phases: penetration and fracture (Fig.6.15). Penetration phase of deformation begins when material starts deforming by impact forces and lasts until initiation of fracture. Penetration process has two distinctive phases which are rollover and burnish phases and they take place in sequence as presented on



Figure 6.14 Failed punching of 10mm thick steel plate against 16.5mm die diameter. Impacted and die side views.

Fig.6.15 Rollover is initial phase of penetration that takes place upon projectile impacts the workpiece and working material is being drawn into the die cavity. As a result of rollover punched hole has round edge on the impact side. Burnish process begins upon completion of

rollover and lasts until beginning of fracture. Burnished portion of the hole is the smoothest portion of the hole. Fracture, as final phase of punching begins when penetration ends and lasts until final separation of blank from generated hole. On the exiting side of the hole and impact side of the blank burr edge is created along circumference of die opening as shown on Fig.6.16. Burr height depends on properties and thickness of work metal.

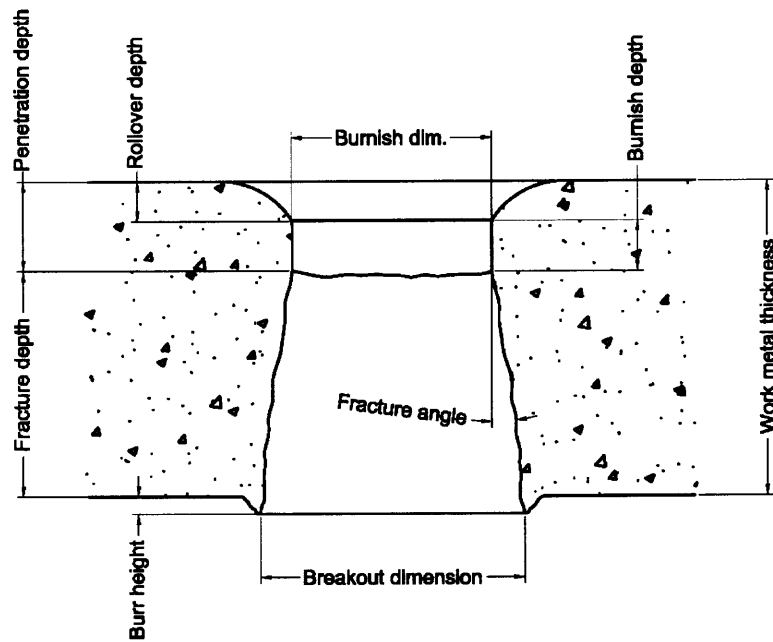


Figure 6.15 Schematic presentation of characteristics of punched hole.

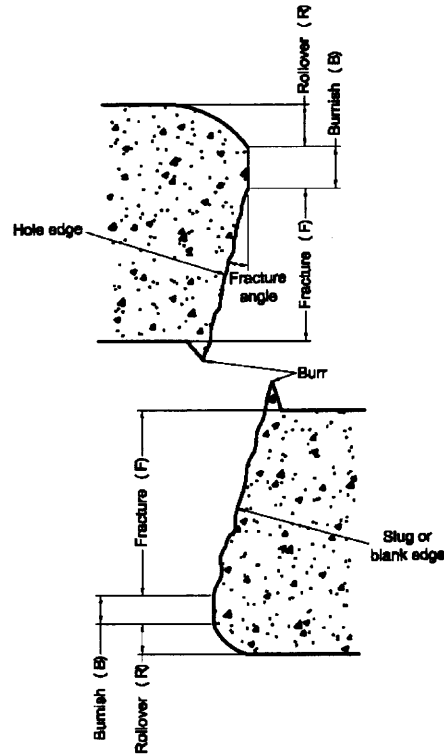


Figure 6.16 Schematic presentation of characteristics of punched hole and the blank.

Investigation of microstructure of deformed media revealed presence of adiabatic shear phenomenon during steel punching process. In metals exposed to high strain rates at room temperature about 90% of deformation work goes into heat. Adiabatic shearing (shearing without heat flux into surrounding) is process which takes place in metals exposed to a high strain rate deformation during which heat generated in localized shear bands can not dissipate [39]. This is caused by high strain rate and affected by thermal properties of the material. The truth is the higher the strain rate more heat gets retained within the shear bands. During the penetration process after rollover phase is completed nucleation of adiabatic shear bands takes place (Figures 6.17, 6.18). This micro-specimen show cross section of two initiated but not completed 4mm diameter holes from the sample shown on Fig.6.13. Adiabatic shear bands are clearly seen on Fig. 4.8 (enlarged detail from Fig 6.17).

Comparison of these results to the results obtained by solid projectile impact [39] water projectiles and solid projectiles produce the same effect such as shown on micrograph (Figures 6.17, 6.18) where adiabatic shear bands are observed. In this investigation high strain (up to 120% elongation) and high strain rate are observed as characteristics of the process of punching of steel plates. Strain rate of 8.5×10^{-6} 1/sec was determined by the author in a separate ballistic study [21]. An example of effect of water projectile impact during die free piercing of steel plate is shown on Fig.4.8 where micrographs show nondeformed microstructure in transversal direction (Figure 4.8 insertion window) and highly deformed grains at the fracture zone (Fig. 4.8 main window).

It is observed that water projectile induced punching provides similar results to those produced by conventional mechanical tool punching [40]. Namely, same deformation phases and same characteristics of holes are observed in conventional (solid punch and die) punching. It is observed that duration of each deformation phase for liquid projectiles differs from durations of deformation phases during conventional punching processes. Full comparison with conventional technologies of punching and piercing would require studies for wide range of variations in steel composition, but based on already obtained experimental evidence it appears that water projectile impact versus solid punch provides deeper penetration which results in delayed fracture initiation. This results in shorter fracture length which is desirable since deeper penetration provides smooth wall of generated hole. Actually for thin samples thickness up to 5mm water projectiles generated holes by full penetration without fracture wall. This effect is especially observed in case of spring steel punching (Fig.6.10). This can be due to transient nature of impact pressure and transient water projectile impact interface. Advantages of this process versus conventional processes are such as: the need for second die is eliminated, manufacturing of punching tool is eliminated, no mechanical contact between launcher and work piece (therefore no transfer of high forming

forces back to the system), same size projectile can form range of dimensions and shapes, no need for use of special lubricants to prevent cold welding between die and blank (which is necessary in conventional punching).

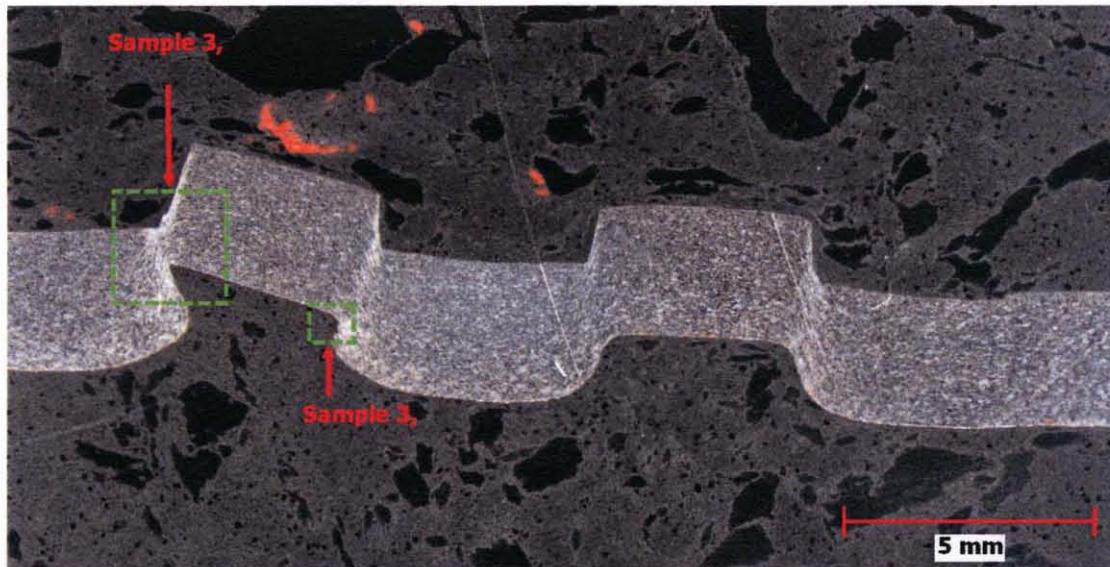


Figure 6.17 Cross-section of uncompleted punching of two 4mm diameter holes (see Fig.6.13).

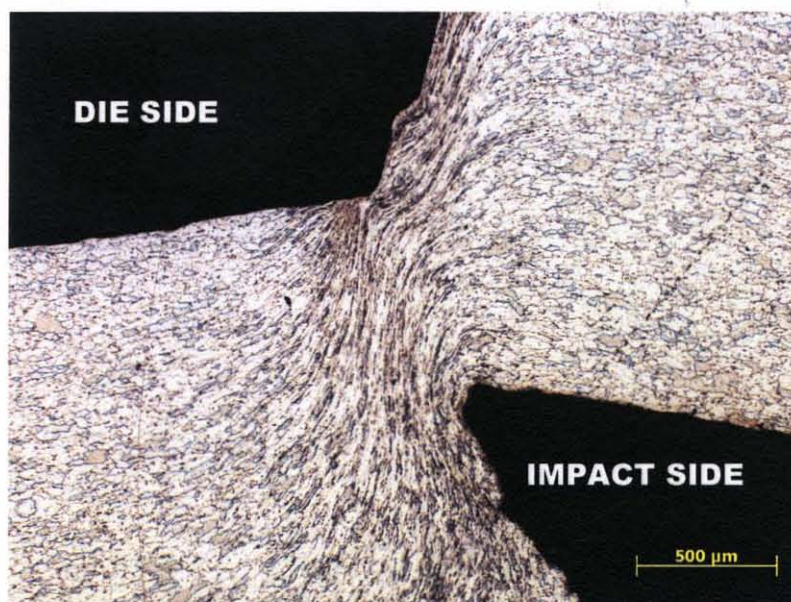


Figure 6.18 Adiabatic shear bands in intermediate phase of blanking of steel.

6.4 Experimental Study of Forging by High Speed Water Projectiles

The objective of this study was to demonstrate the potential of the application of liquid projectiles for forging of metals. The experiments involved use of three dies of various geometries which were designed and manufactured. Material of targets used for this part of the investigation included copper, an aluminum alloy and a high ductility steel. The steel sample has elongation 46%, tensile strength of 323MPa, and yield strength of 195MPa, which is a high ductility steel alloy with addition of aluminum generally used for deep drawing (this steel is used for forming of housing compressors for refrigerators). Plates used were 2.5mm thick.

Properties of steel:

- ultimate strength $\sigma_u = 250 - 350\text{MPa}$, most common value 323MPa,
- breaking strength $\sigma_c = 258\text{MPa}$,
- elasticity limit $\sigma_T = 195\text{MPa}$
- maximal relative elongation (plasticity) $\delta = 46\%$



Figure 6.19 Dies for forming.

Forming was performed against three types of dies: shallow, medium and deep, profile of each is shown under corresponding top view on Fig.6.19. The launcher (water cannon) was loaded by 230g water and 30g powder. The standoff distance was 16cm. Forming against shallow die M1 which has topography of concentric channels 1 mm deep with step of 2mm and inclination angle of 90° (Fig. 6.20). Figure 6.21 shows the views of

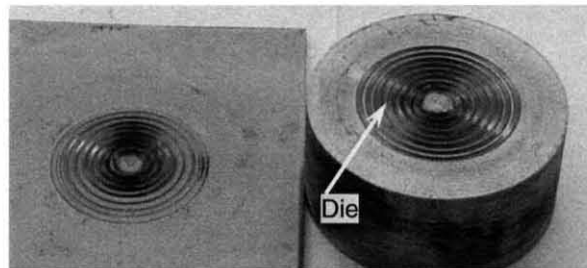


Figure 6.20 Concentric grooves (1mm deep, with 2mm pitch and 90 degrees inclination) on a 2.5mm thick steel plate formed by the impact of 200g of water against the die. Notice the compliance of the die and the part geometry.

shallow die (middle), top view of formed geometry(left) and top view of die geometry (middle), and impact side of formed plate(right). As a result of the impact a shallow die geometry having concentric grooves of 1 mm deep, 2mm pitch and 90 degrees inclination (Fig.6.21) was precisely reproduced on the central portion of the surface of the steel target. The obtained results show that the impact pressure is inverse proportional to the distance of the impact center. While at the center of the target the geometry of generated grooves accurately reproduces the geometry of the die, as the distance from the center of the impact increases the compliance between the die and the workpiece geometries reduces and reproducibility of the die image weakens. This experiment demonstrates that there is a zone in the vicinity of impact where precise reproduction of the shape of a die is possible.

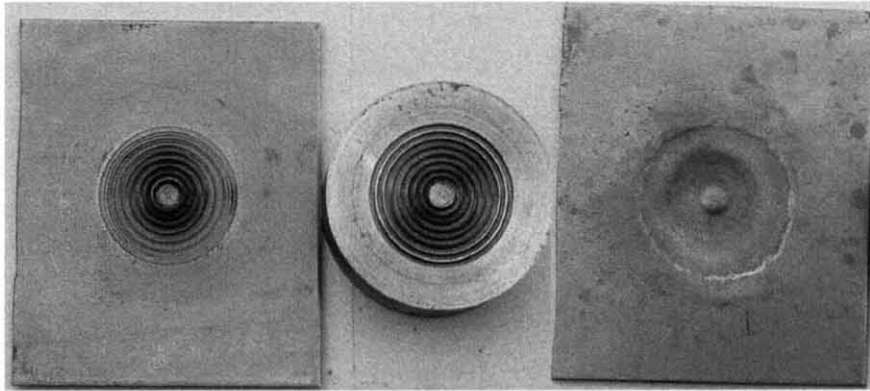


Figure 6.21 Results of forming of 2.5mm thick, ductile steel sample against shallow die M1. Die side (left), die (middle) and impact side (right) views.

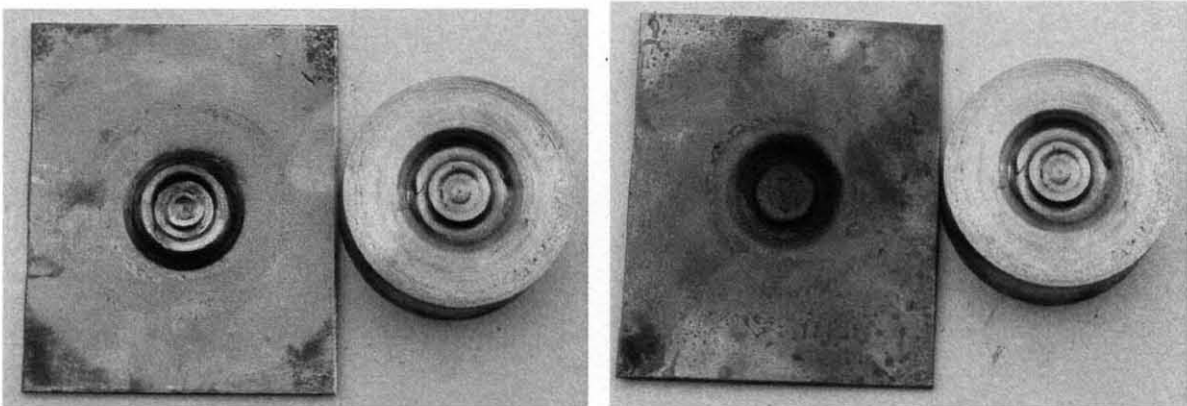


Figure 6.22 Results of forming of 2.5mm thick, ductile steel sample against medium die M2. Die side (left), and impact side (right), views.

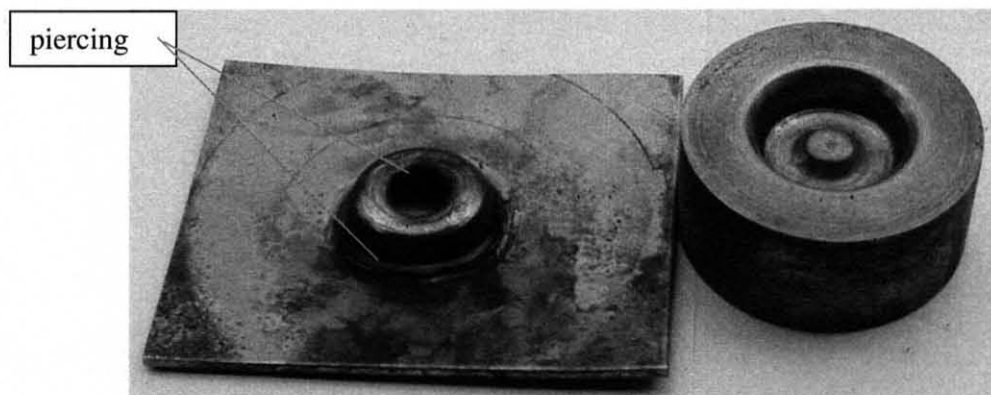


Figure 6.23 Results of forming of 2.5mm thick, ductile steel sample against deep die M3. Notice the compliance of geometries of the die and the generated part.

Forming against medium die (M2) resulted in excellent reproduction of die geometry (Fig.6.22). Results of fine forming were achieved and principal possibility of micro-forming was deduced from experiments with shallow and medium dies.

Another experiment involved the study of the deep forging. During forming against deep die, deeper forging was achieved and geometry of the die was reproduced, but punching of central portion and cracking along top circular edge took place as shown on Figures 6.23 and 6.24. This sample was impacted by 350g of water which was propelled by 30g of powder at the standoff distance of 16cm. The calculated impact velocity was 700m/s. It appears that deep forging can be performed with higher quality with thicker plates. Forging of 6mm thick carbon steel resulted with no cracks only central portion was punched. Since all of experiments were done under same experimental conditions it is clear that projectiles carried excessive energy. Projectile energy level can be controlled by modifying experimental conditions. Specifically, the impact intensity can be controlled by sizing the powder and water loads as needed for a particular task. Changing the standoff distance is another way to control the impact effect. Consistency of forming operations was confirmed by repetition of these experiments. The stable output was obtained at each test. This experiment showed that forming of deep and complex 3-D parts can be accomplished by the high speed liquid impact. Again, the proposed material processing technique was validated.

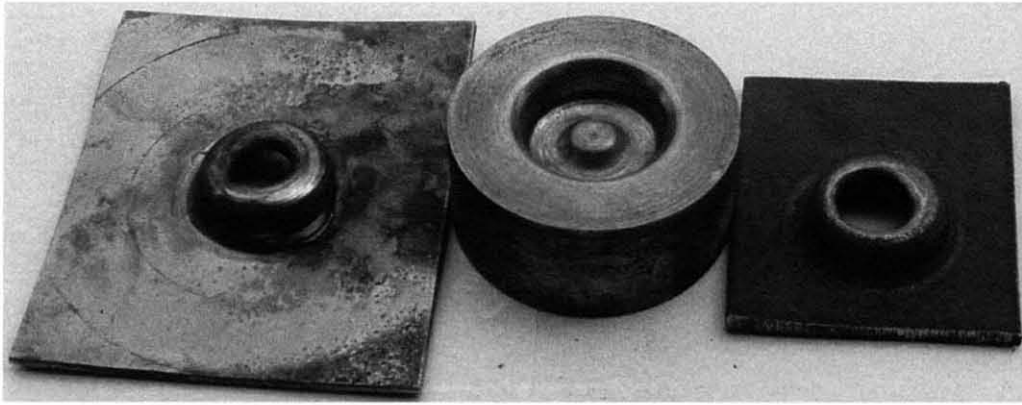


Figure 6.24 Results of forging against deep die M3. High ductility 2.5mm thick sample(left), and 6mm thick carbon steel 1020 sample (right).

Several results of forging are summarized in Table 6.2. During each experiment angle of displacement of ballistic pendulum was measured which was used to calculate impact impulse of projectile. Projectile impact angle was 90° .

Characteristics of ballistic pendulum are:

- moment of inertia $I = (214.04 \pm 0.61) \text{ kg}\cdot\text{m}$
- distance between rotation axes and pendulum center $R_c = (1.3904 \pm 0.001) \text{ m}$
- mass of ballistic pendulum 109.95 kg
- oscillation period $(2.357 \pm 0.005) \text{ s}$
- logarithmic decrement of attenuation $\lambda = 2.557 \cdot 10^{-3}$
- attenuation coefficient $\beta = 1.085 \cdot 10^{-3} \text{ s}^{-1}$
- relative energy loss during the measurement $\Delta E/E_0 = 1.3 \cdot 10^{-3}$

Table 6.2 Forming of Steel Experimental Results

Exp. №	Plate thickness, mm	Die	Stand of distance, cm	Result	Impact Impulse[kgm/s]/ Pendulum displacement* α [°]	Experimental conditions
1	2,5	M1	16	Excellent forming	230.9/*16.5	Shallow die M1(Figs 1 and 2). Cannon shooting mode. Powder mass 30g. Water mass 230g. High ductility steel. Die geometry: concentric channels 1 mm deep with step of 2 mm and inclination angle of 90°.
2	2,5	M2	16	Excellent forming	237.69/*17	Medium die M2(Fig.1). Cannon shooting mode. Powder mass 30g. Water mass 230g. High ductility steel.
3	2,5	M3	16	Sample pierced and cracked	394.14/*29	Deep die M3 (Fig.1). High ductility steel. Extruder shooting mode. (nozzle and barrel filled with water). Starting projectile velocity at the nozzle is 0 m/s. Calculated maximal velocity 700m/s. Sample pierced and cracked.
4	4	M3	16	Central portion pierced	394.14/*29	Deep forming (M3). Carbon steel 20. Cannon shooting mode.
5	6	M3	16	Central portion pierced	375.39/*27.5	Deep forming (M3). Carbon steel 1020 plate 6mm thick. Cannon shooting mode. Profile almost fully formed.
6	6	M3	16	Central portion pierced	317.65/*23	Deep forming (M3). Carbon steel 1020 plate 6 mm thick. Cannon shooting mode. Powder mass 40g. Water mass 200g. Calculated projectile velocity 1500m/s. Profile fully formed and central portion pierced.

In this study consistency of forming operations was confirmed by repetition of experiments. The stable output was obtained at each test. This experiment showed that forming of deep and complex 3-D parts can be accomplished by the high speed liquid impact. Again, the proposed material processing technique was validated.

6.5 Mechanism of Forging of Steel Plates

The process of forming can be divided into three distinctive phases: first, initial rollover and penetration (in same fashion as in punching process), second during which hemispherical plastic dome (Fig. 6.25) is being formed by mushroom-shaped projectile head, and final forming phase during which material gets shaped against female die geometry (all three forming phases are shown on Fig.6.26). Maximal depth of formed dome is limited by mechanical properties and thickness of forming material, and maximal depth of the die geometry.



Figure 6.25 Hemispherical dome is being formed during intermediate phase of forming process.

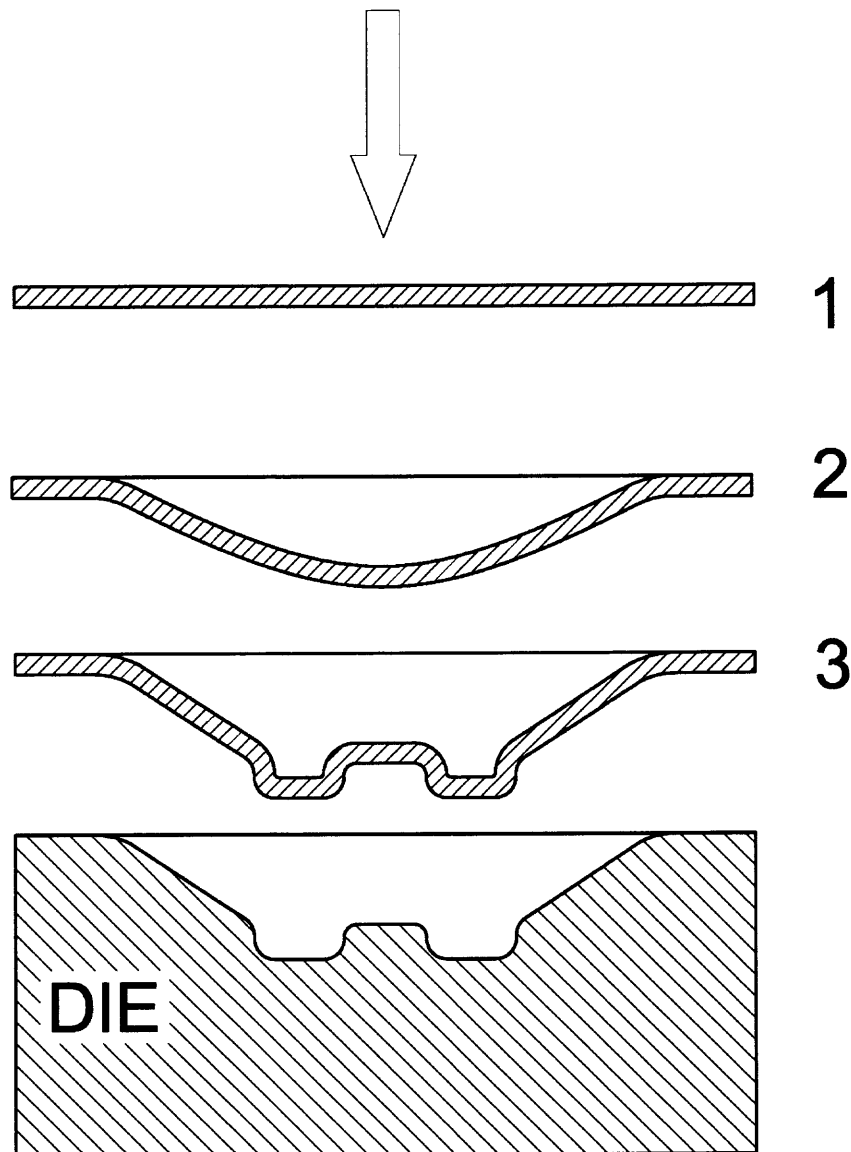


Figure 6.26 Schematic of phases of forging: 1- initial state, 2-plastic dome forming, and 3- final shape forming.

6.6 Discussion of Results

As a result of this study water projectile impact based punching and forming of steels over wide range of dimensional requirements was accomplished. Punching of circular and complex shape openings was studied and accomplished. Mechanism of punching of metals was investigated and explained. Fine forming against shallow die (M1) was excellent. Mirror geometry of die reproduction was achieved. Within the projectile diameter circular impact

zone geometry was fully reproduced, beyond the central impact zone forming rate fades in outward radial direction which is due to pressure distribution at the impact zone. Forming against medium die (M2) was excellent. Deep die (M3) forming was partially successful. Desired profile was formed in each case, but central portion gets pierced due to design of the die and due uneven deformation rate. The highest deformation rate occurs in the zones of highest stress. Mechanism of forging of metals was investigated and explained. Advantages of this process versus conventional processes are such as: the need for second die is eliminated, manufacturing of punching tool is eliminated, no mechanical contact between launcher and work piece (therefore no transfer of high forming forces back to the system), and same size projectile can be used for variety of processing operations. In the domain of each processing technique a single size of projectile can form range of dimensions and shapes.

6.7 Conclusions

The performed experiments demonstrated feasibility of the use of water projectile impact for metal punching and forging of metals. Both operations as new material processing techniques were validated and as such are a new lead for development of novel impact based technology. Dimensional stability of created products and consistency of repetitive punching and forging was achieved. Mechanisms of both operations were investigated and explained. It was shown within limits of investigation that water projectiles can deliver same or higher quality products than conventional punching and forging tools. Advantages of investigated operations over conventional processing techniques were identified and documented. Feasibility of development of novel manufacturing technologies was demonstrated.

CHAPTER 7

LIQUID IMPACT BASED MATERIAL MICRO AND MESO FORMING TECHNOLOGY

7.1 Introduction

The objective of the performed study was to investigate the application of high-speed liquid projectiles for material forming, specifically for formation of sub millimeter and micron scale parts. The proposed technology involves impacting a workpiece supported by a die by a high-speed (1000-1750m/s) water projectile (an impulsive jet) [34, 35]. The projectiles are generated by a launcher (a water cannon), which constitutes a modified gun, loaded by a round where a solid slug is replaced by a container with a liquid, e.g. water (Fig.7.1). The powder explosion accelerates water and at the end of the barrel the water speed is comparable with that of the solid projectile. The further acceleration

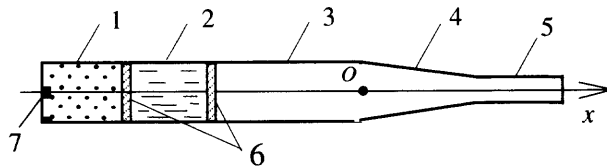


Figure 7.1 Schematic of Water Cannon. 1-powder charge, 2-water load (projectile), 3-barrel, 4-nozzle, 5-cylindrical attachment (collimator), 6-partitions, 7-primer.

occurs in a nozzle attached to the barrel. This enables us to increase significantly the water speed. In the previous experiments, a water velocity of 1750m/s was achieved. Computations show that it is possible to achieve water speed as high as 3-4km/s. At the speed of 1500m/s the pressure exerted on a target at the impact zone is in an order of 1GPa. At such a pressure a metal target impacted by the liquid projectile acquires a shape of the supporting die. Thus the liquid impact can be used for metal forming and the high speed liquid projectile can replace a punch.

A water projectile impacting a solid surface at the speed of 1000m/s and more acts as an explosive, which detonates on the target's surface. Advantages of the impact based forming [41] as well as the explosive forming [42, 43, and 44] are well understood and documented. In a number of applications, however, the use of an explosive is difficult if not impossible. In this case the high-speed liquid projectiles can be used as a forming or welding tool. Previous research showed the feasibility of the application of the liquid impact to metal forging, stamping, coining and extrusion [17, 44]. The most promising application of the liquid projectile, however, is mass production of Micro Electro Mechanical Systems parts.

Micro forming is fabrication of parts or structures with at least two dimensions in the sub-millimeter range by the use of a forming technology. The effectiveness of the application of the plastic deformation for mass production of micro parts is quite obvious. It can be the only practical way for mass production of metal and alloy micro parts. While implementation of the micro fabrication will revolutionize the MEMS fabrication technology, substantial obstacles are to be overcome in order to achieve this goal. The micro forming cannot be developed just by scaling down existing forming processes. New techniques must be found for micro scale deformation of various technological materials at desired rate and accuracy and at an acceptable cost.

Deformation of a target material in the course of a high speed liquid impact was investigated experimentally. The previous research demonstrated the feasibility of the use of high speed projectiles as a punch in conventional metal forming operations. The objective of this study is to expand the range of the application of the liquid impact to micro forming operations. The performed study involved micro- and sub millimeter

stamping and extrusion of various metals. The performed experiments showed that high-speed liquid projectiles have a potential of becoming a competitive micro forming tool. Of course a number of issues pertinent to the selection of the energy source for the water acceleration, energy transfer from a source to the projectile, reliability of the launcher and a guiding system, die design and reliability, etc. must be addressed. However, the feasibility to generate a desired micro scale deformation of a target material using the liquid impact was demonstrated by the performed experiments.

7.2 Existing Micro Forming Technologies

Research in micro and meso manufacturing area is being conducted by a team lead by Kuniaki Dohda [45], Gifu University, Japan. Micro pressing technology has been developed. This technology involved formation of the ultra fine holes in aluminum samples using $15\ \mu$ SiC fibers as a punch. Micro forging was used to die forge micro parts out of amorphous alloy. Micro extrusion of aluminum alloys was investigated as well. A single process system was designed and used for each application (micro press, micro extruder). Development of a system which could be used for more than a single micro forming application and which would have higher efficiency was addressed by a group of Hye-Jin Lee of Korean Institute of Industrial Technology, Korea [46]. Study of forming of the sub millimeter metal parts is currently being carried out in the Friedrich-Alexander University, Germany [47]. A Group Mass-micro of Dr. Jiangho Lin, (U of B), is currently working on the development of technologies of mass production of micro parts. [48]. While the teams above are involved in one or another miniaturization of

forming facilities, the objective of the proposed study is modification of the mode of the generation of the stress field in a target.

7.3 Experimental Technique

An experimental setup (Fig.3.1), for the study of the liquid impact based forming was designed and constructed. In this setup samples to be processed were mounted on a heavy pendulum which was displaced by the water impact. The angular displacement of pendulum was measured in each experiment and the projectile impulse and momentum were calculated by the use of the measured pendulum displacement. During an experiment the water cannon was placed at a desired distance from a sample which then was impacted at selected conditions. In the course of the impact the target acquired a shape of a supporting die. The principal challenge in the die fabrication was formation of the sub millimeter and micron scale cavities using conventional machining facilities (lathe, milling machine, etc.). During each experiment the values of water mass, powder mass, standoff distance and pendulum displacement were measured and the acquired data was incorporated into a global matrix of the investigation. Upon completion of an experiment generated samples were examined visually and then sample characterization, involving scanning electron microscopy, infinite focus microscopy, optical microscopy, 3-D digital microscopy, 3-D digital profiler, was carried out.

The fabricated dies enabled us to examine various micro forming technologies. Both, the sub-millimeter and micron scale deformations were investigated. The study involved filling cavities by a target material and stamping a die shape on the target surface. The filling of the semi closed cavities (groves on the workpiece surface) and

metal extrusion into open micron scale slots was examined. Stamping using simple (cylindrical wires) and complex (a coin) dies was also investigated. Targets were fabricated from copper, brass, aluminum and steel. In one of the performed experiments extrusion of an alloy used for fabrication of Ukrainian coins was studied.

An exit diameter of the nozzle utilized in the performed experiments was 15mm, the diameter of barrel was 20mm and the total length of the launcher was 80cm. Amount of water used for the projectile formation ranged between 30g and 350g. Water was propelled by the products of the combustion of 30g of gun powder. The standoff distance was 16cm in all experiments. Calculated outflow velocity of the projectile head ranged between 850m/s and 1566m/s. The calculated maximal pressure inside the nozzle ranged from 341MPa and 843MPa. At these conditions the pressure exerted on the workpiece varied from 0.35GPa to 1.2Gpa

7.4 Details of an Experimental Procedure and Results

7.4.1 Formation of Sub Millimeter Scale Grooves

The experiments involved the study of formation of sub millimeter circumferential ridges on the target surface. For this study, a die with concentric groves was designed and manufactured. The general view of the die surface is depicted on Figure 7.2. The design

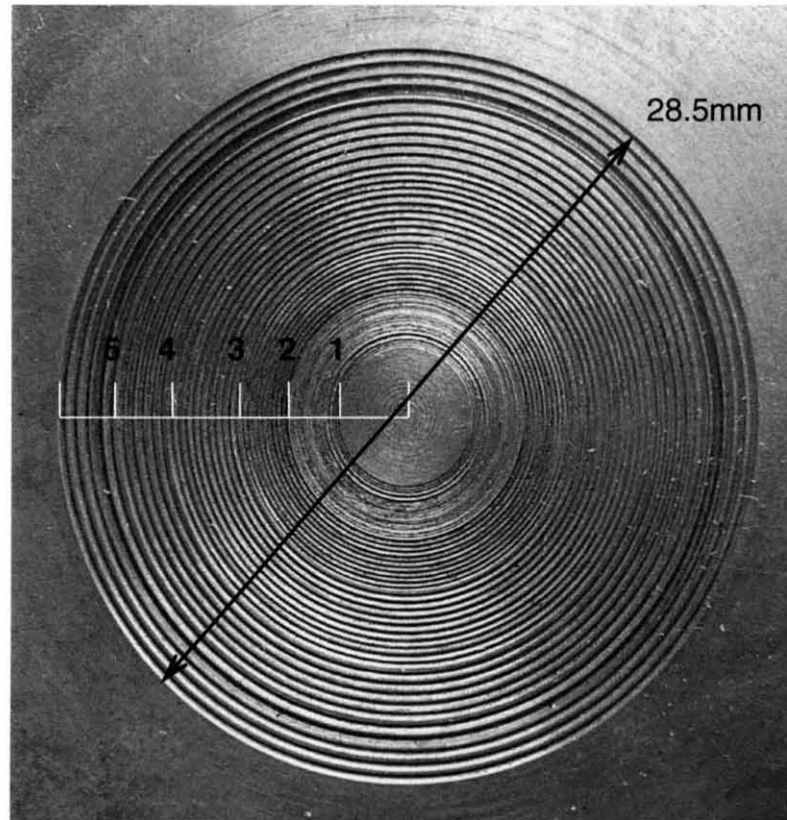


Figure 7.2 General view of the die used for fine forging of samples. Notice complexity of die geometry. Numbers 1-5 correspond to sections on the die surface. The ridges geometry of different section (Table 7.1) is different.

parameters of the die groves are given in Table 7.1 and Figure 7.3 which show desired geometry of cross section of two adjacent groves. Here b stands for the depth of the groove on the die surface and h is the pitch of the grooves. In order to investigate the effect of the groove geometry on the result of forming five distinct sets of the grooves were generated on the die surface. Correspondingly the die surface was divided in five

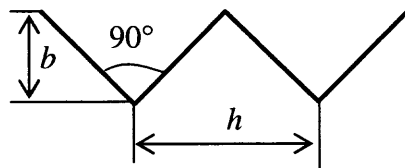


Figure 7.3 Desired geometry of the ridges.

sections. The actual shape of the die differed from the designed geometry. This difference was due to slipping of cutting tool and vibrations of tool and work piece in the course of turning. While the designed grooves had a triangular profile, due to the limitations of the machining facility used for die manufacturing the grooves and ridges generated on the die surface had a shape of a trapezium. It should be noted that the accuracy of machining of the die surface changes across the die radius. The accuracy of the sections 3, 4 and 5 was adequate while the larger deviations from desired geometry were found within the sections 1 and 2.

In the course of experiments a metal plate was placed on the die and impacted by a projectile. The impact forced the target material to fill the die grooves thus a set of ridges and grooves was formed on the target surfaces. Compliance between the geometries of the die and workpiece surfaces as well as the topography of the generated surface constituted the criterion of the quality of the performed forming operation. The performed study was carried out at the following experimental conditions: 200g of water propelled by 30g of gun powder at a stand of distance of 16cm. At these conditions a computed projectiles impact velocity was 1500m/s and a period of pendulum oscillation was 2.35s.

Table 7.1 Designed Parameters of the Grooves to Be Generated on the Die Surface. Notice Difference in Groove Geometry at Different Sections

Section	1	2	3	4	5
Step, h mm	0.1	0.2	0.3	0.4	0.5
Depth, b mm	0.05	0.1	0.15	0.2	0.25
N-of grooves	20	10	10	5	5

In order to quantify the accuracy of forming the microscopic evaluation of a work pieces was carried out using the optical microscopy, 3-D digital microscopy, and infinite focus microscopy. The optical microscopy (x200) was used for visual examination of the generated surfaces. The performed examination confirmed that at the existing tolerances of die fabrication there is sufficient compliance between the desired die geometry and the actual geometry of a work piece.

The surface geometry generated in the course of an impact of a brass sample is shown on Figs (7.4- 7.8). Close up view of segment containing three ridges reproduced by 3-D digital microscopy also confirms compliance of the shapes of the die and the work piece (Fig. 7.4). Formed shape is a mirror view of the corresponding die section. Similar result was obtained for 10 different sections of the work piece surface.

A general view of the surface of a brass target generated in the course of forming is shown on Fig. 7.5. As it follows from this figure the micro scale geometries of the die and the work piece complied sufficiently well and the geometries of the grooves and ridges on both surfaces are almost identical. This accurate reproduction of the die geometry was observed in all sections.

An infinite focus microscopy was used for quantification of the work piece surface topography. Profiles of four neighboring ridges formed on the brass surface are shown on Fig.7.6 where three ridges have height of approximately 140μ while neighboring ridge has height of approximately 200μ . The difference in size of these ridges was the same as that of the corresponding parts of the die and was caused by an unstable process of the die machining.

Investigation of other segments of the work piece surface by infinite focus microscopy produced similar results. This method was also used for analysis of the surface waviness and roughness of all generated samples. As it follows from Figs 7.7a and 7.7b the surface waviness was below 2μ and the roughness was below 0.04μ .

A general view of formed grooves and ridges on the surface of copper sample is shown on Fig. 7.8 Notice that the desired surface geometry was accurately reproduced in the course of the impact. This compliance is also demonstrated by a close up view of a segment containing three ridges and reproduced by 3-D digital microscopy (Fig. 7.9).

The infinite focus microscopy was used to examine the topography and profile of a copper sample. It was found that the waviness of the generated surface was below 2μ (Fig. 7.10) and roughness was below 0.1μ (Fig. 7.11).

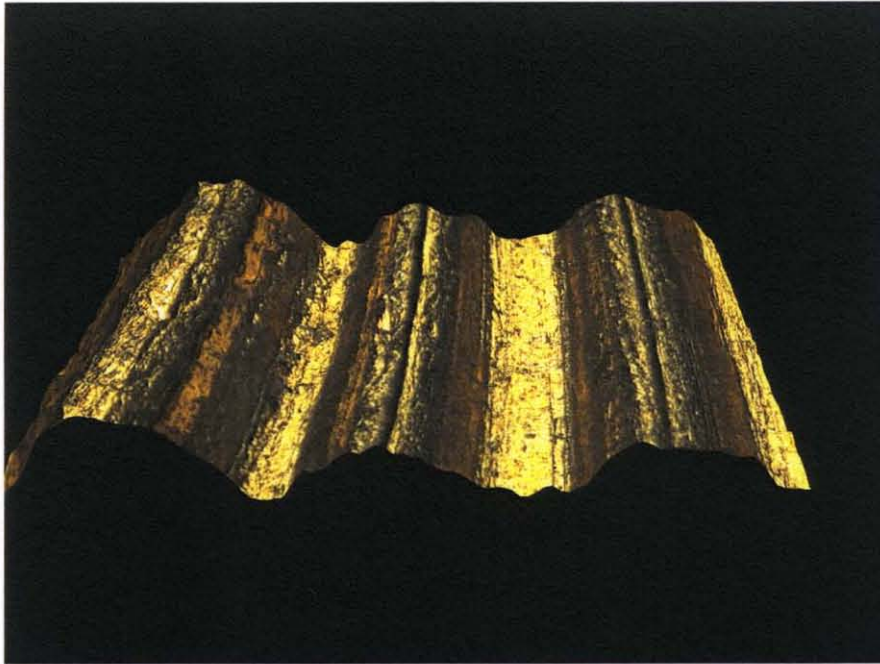


Figure 7.4 Segment of concentric grooves and ridges formed on brass. Notice that ridges and grooves of the work piece surface have the forms of a trapezium which is similar to a corresponding segment of the die.

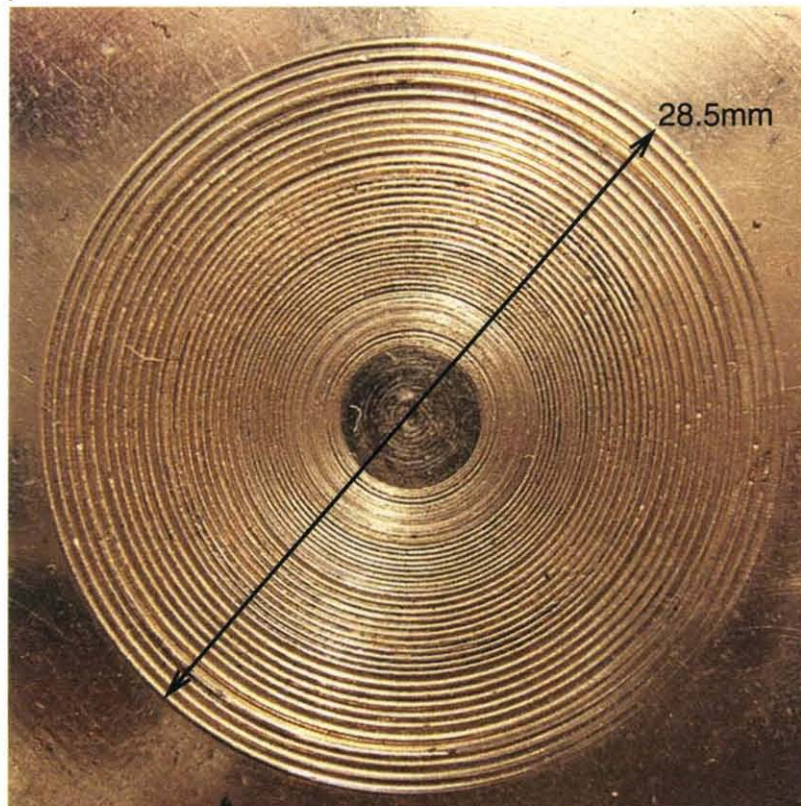


Figure 7.5 General view of concentric grooves and ridges formed on the surface of brass sample. Notice precise geometry of the generated grooves.

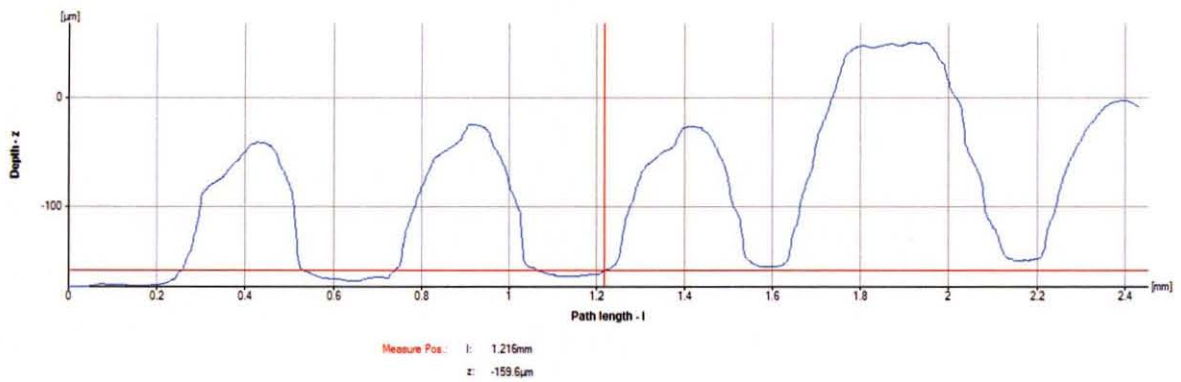


Figure 7.6 The profile of concentric grooves and ridges formed on a brass sample.

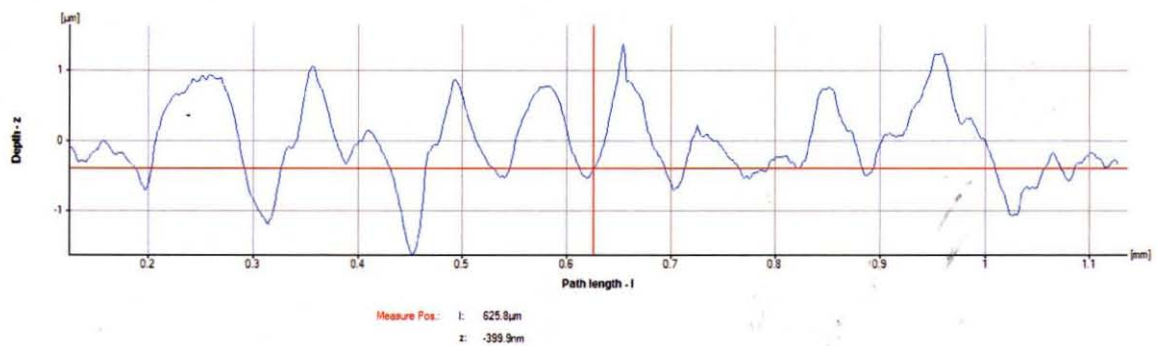


Figure 7.7a Surface waviness of grooves formed on a brass sample.

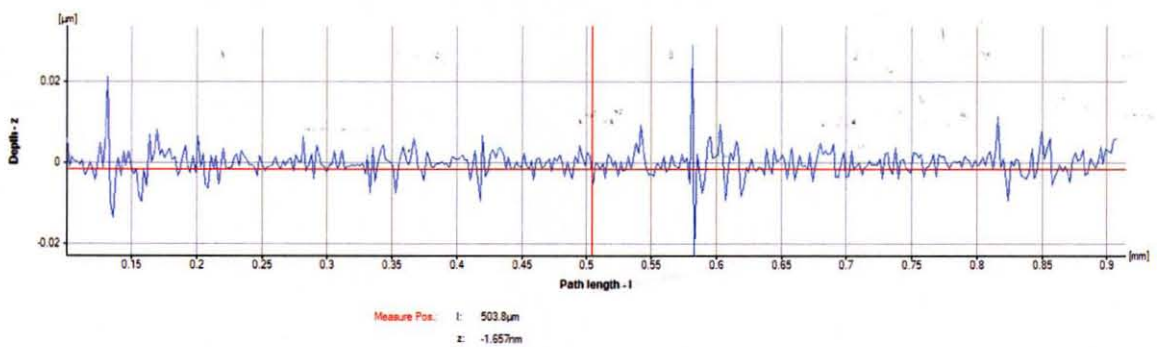


Figure 7.7b Surface roughness of grooves formed on a brass sample.

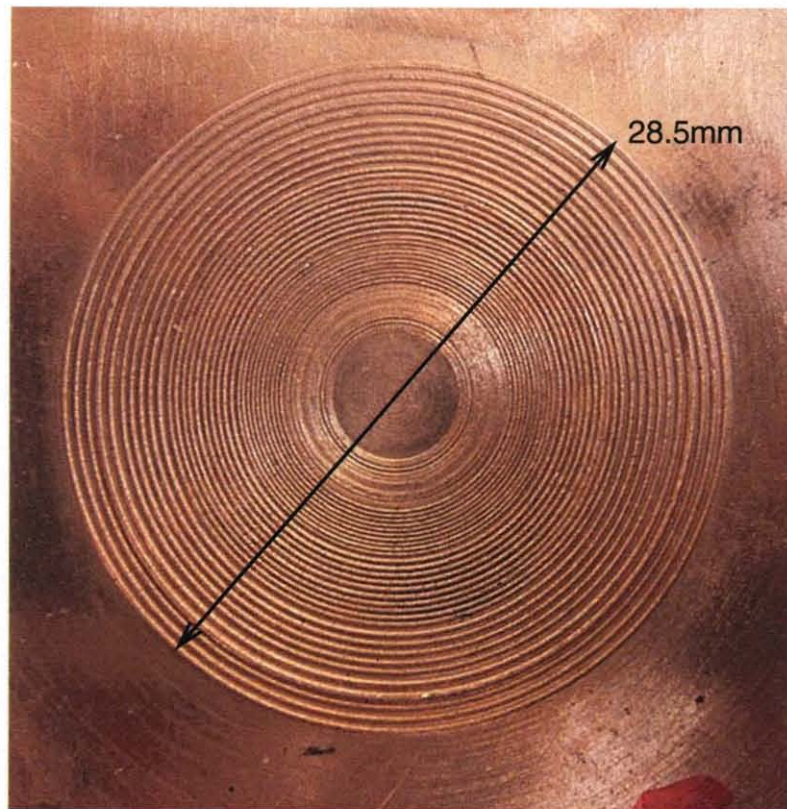


Figure 7.8 General view of concentric grooves and ridges formed on the surface of a copper sample.

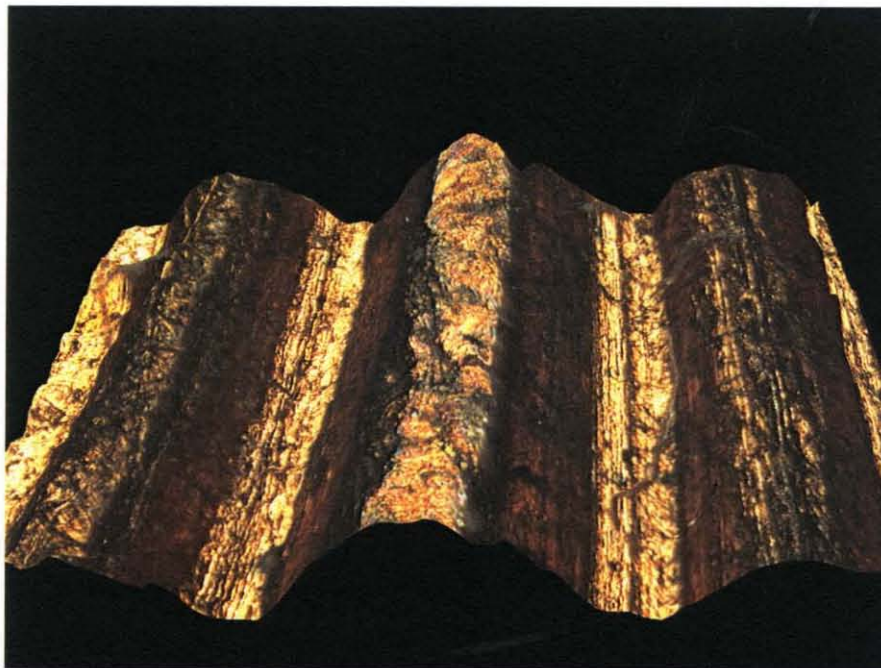


Figure 7.9 Segment of concentric grooves and ridges formed on a copper sample.

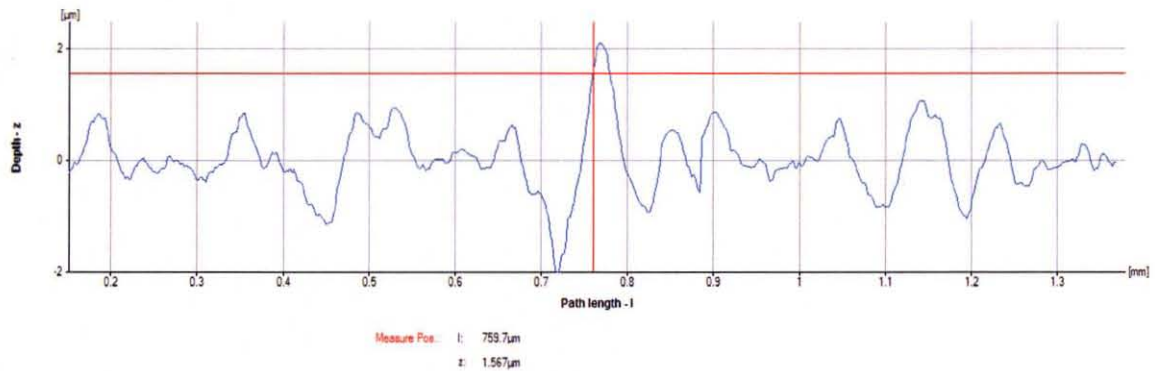


Figure 7.10 Surface waviness of grooves formed on a copper sample.

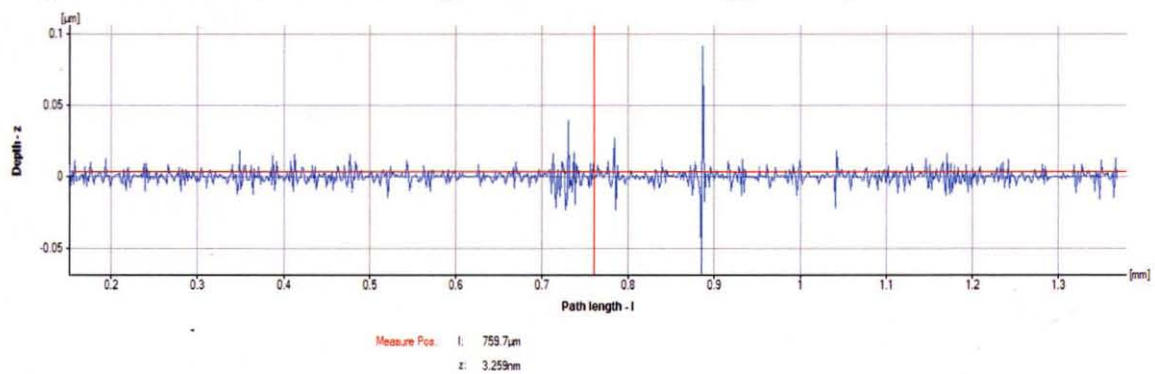


Figure 7.11 Surface roughness of a groove formed on a copper sample.

7.4.2 Fine Stamping

The objective of these experiments was the study of formation of rather complex patterns on the target surface. In this case a conventional coin was used as a supporting die. Target materials included copper, brass, aluminum and high ductility steel. The steel had 46% elongation, tensile strength of 325MPa, and yield strength of 195MPa. Thickness of the copper and brass samples was 3 mm and steel samples were 2.5mm thick.

A Ukrainian coin was used as a die for investigation of the fine stamping. As a result the coin image was stamped into copper, steel and aluminum plates. In the course of the experiments 350g of water were propelled by combustion of 35g of gun powder at a stand off distance of 16cm. A calculated impact velocity was 850m/s. Geometry of the

coin was accurately reproduced on all samples, aluminum, steel and copper. Quality of reproduced surface was characterized by two methods, infinite focus microscopy and 3-D profile analysis. Measurement of parameters of the surface geometry was performed and it was demonstrated that the coin geometry was reproduced sufficiently accurate on the surface of all targets

General view of the coin images stamped on the surface of aluminum and copper samples is shown on Fig. 7.12. An image of the coin stamped on the surface of a steel sample and generated by the 3-D profile analysis is shown on Fig. 7.13. The depth of the depression of the work piece surface was approximately $130\ \mu$. As it was demonstrated by measurements, this corresponds to the topography of the coin. In addition to the profile and depth features, top view of the work piece geometry was compared to the corresponding view of the die. The performed measurements showed almost mirror like reproduction of the die geometry on the workpiece surface. Example of a profile of the coin (Fig. 7.14) shows fine stamped features with the maximum height range of $90\ \mu$ and the roughness below $1\ \mu$ (Fig. 7.15).



Figure 7.12 General view of a coin stamped on aluminum and copper samples. Notice reproduction of fine details of the coin on the sample surface.

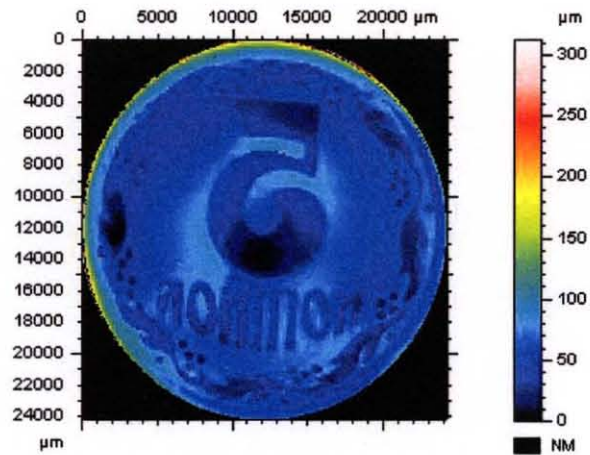


Figure 7.13 Image of coin stamped on steel created using 3-D profile analyzer.

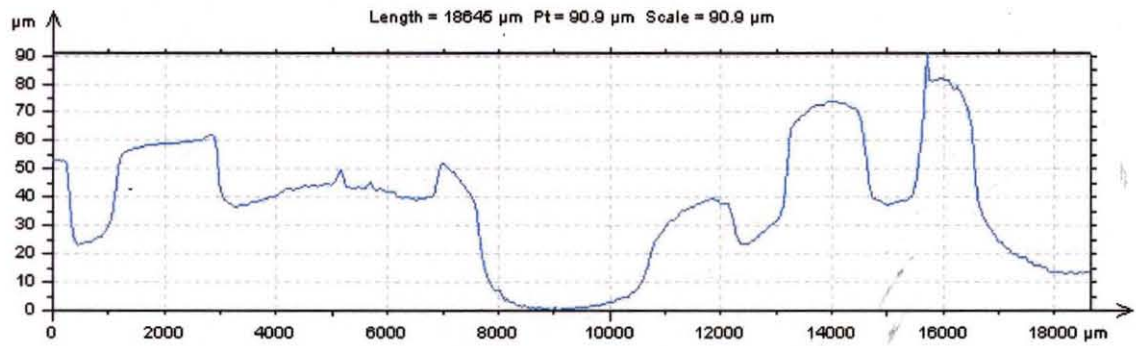


Figure 7.14 Example of profile of a coin stamped on a steel sample.

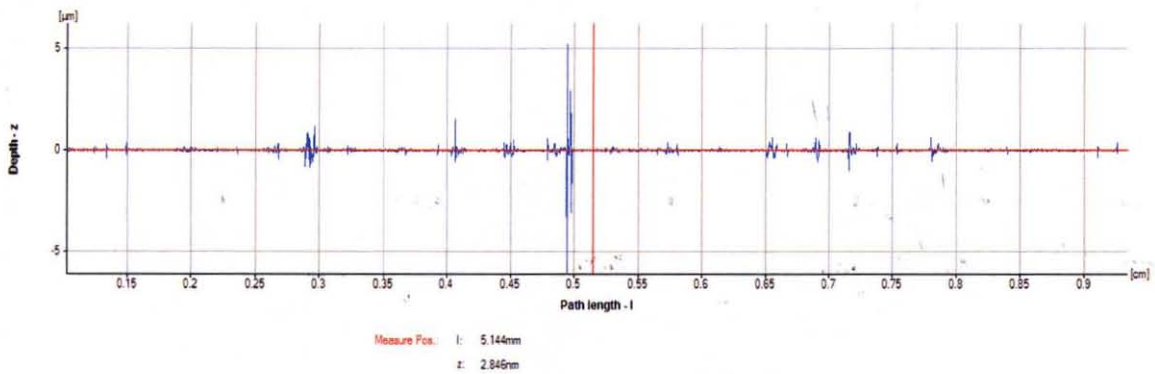


Figure 7.15 Roughness of the surface of steel sample stamped by a coin.

7.4.3 Microns Scale Forming

The objective of the performed experiments was to form micro channels on the surface of different metals. During the tests individual micro channels and networks of micro channels were formed on the surface of cooper, brass and steel samples. High ductility steel having 46% elongation, tensile strength of 325MPa, and yield strength of 195MPa was utilized in this study. A tungsten wire was used as a die. The wire diameters were 7μ and 40μ . In each experiment the wire was attached by glue to a polished surface of a metal sample in order to form a desired network. Samples were mounted on a heavy pendulum with the wire side facing the pendulum. Water projectiles impacted opposite side of the sample and as a result much harder wires were driven into softer materials of samples creating a desired network of micro channels. In the course of experiments 230g of water were propelled by 30g of a gun powder at a standoff distance of 16cm.

Geometry of the generated micro channels was examined by optical microscopy, infinite focus microscopy, scanning electron microscopy, 3-D digital microscope and surface profiler. Scanning electron microscope was used to investigate surfaces of formed micro channels. Intersection of two micro channels formed by 7μ diameter tungsten wire on brass sample is depicted on Fig. 7.16. Examination showed that formed channels are approximately 8μ wide. A view and dimensions of 7μ diameter tungsten wire imbedded into brass sample are shown on Fig. 7.17.

Infinite focus microscopy was used to perform topography, profile, waviness and roughness analyses. Intersection of two micro channels formed on brass by 40μ diameter tungsten wire is shown on Fig. 7.18.

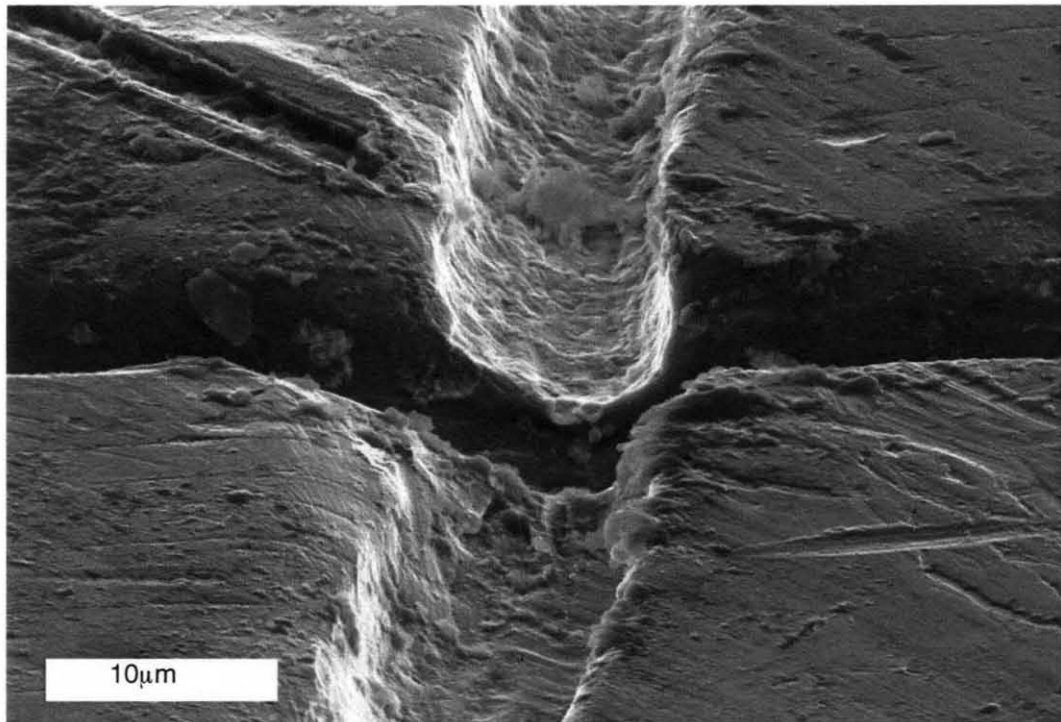


Figure 7.16 Intersection of two micro channels formed on the brass surface by $7\ \mu$ diameter tungsten wire.

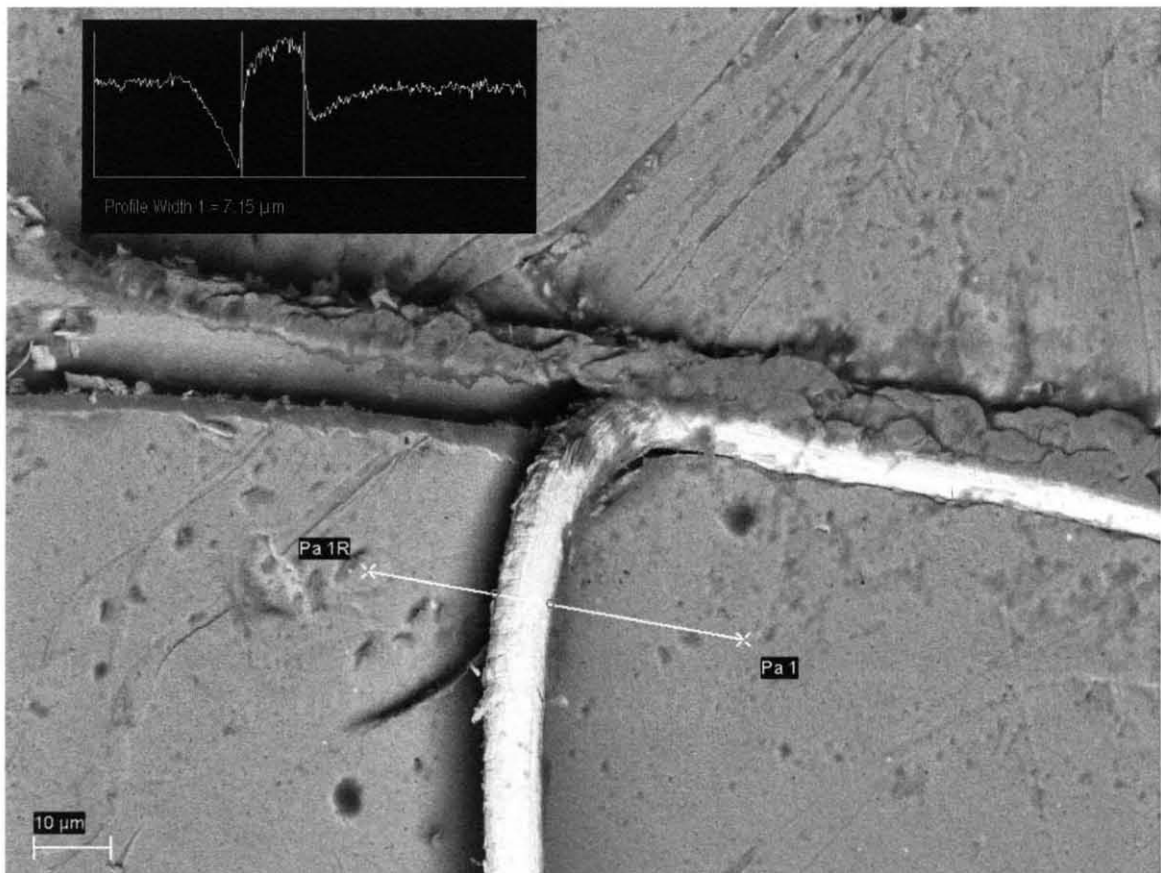


Figure 7.17 A view of the $7\ \mu$ tungsten wire embedded into brass surface generated by SEM.



Figure 7.18 Intersection of two micro channels formed on a brass sample by $40\ \mu$ diameter tungsten wires.

Three dimensional microscope was also used for examination of the formed micro channels (Figs. 7.19 and 7.20). Generated 3-D images of channels were further used for profile analysis and the results complied with previously conducted infinite focus microscopy analysis. A 3-D image of a section of the micro channel formed on the brass sample by $40\ \mu$ diameter tungsten wire is shown on Fig. 7.19 and a 3-D image of an intersection of micro channels formed on the brass sample by $40\ \mu$ diameter tungsten wire is shown on Fig. 7.20. Extensive examination of formed micro channels confirmed geometrical reproducibility and the exceptional surface quality.

Profile analysis performed by the infinite focus microscopy revealed steady geometry of the formed channels. An example of the channel profile (Fig. 7.21) indicates that both the depth and the width of formed channels are approximately $40\ \mu$. Curvature

of the $7\ \mu$ wire has better imprint on all of tested materials. This is demonstrated by two profiles which have depth and width in the range of wire diameter. At the same time the curvature of the generated channel is completely determined by the geometry of the wire (Fig. 7.22). Profile of same section of the channel is also shown on Fig. 7.23.

Additional analysis of the profile and roughness of channels was conducted by a table version of the white-light, non-contact three dimensional optical profiler. This instrument was used to scan surfaces with embedded micro-channels. This analysis yielded results compatible to those obtained by the infinite focus microscopy. This confirmed consistency of the forming

An example of profile of two adjacent channels ($40\ \mu$ and $7\ \mu$ wide) is shown on Fig. 7.24 while an example of the surface roughness measured on the bottom of the $40\ \mu$ wide channel is depicted on Fig. 7.25. As it is shown by this figure the surface roughness did not exceed $0.002\ \mu$.

In the course of the surface, study by the 3-D profiler three dimensional images of sections of the micro channels were reproduced and compliance between the die and the work piece geometries was demonstrated for all three tested materials. The roughness, waviness and profile analyses yielded satisfactory results.

As it is shown on Fig. 7.26 the brass surface contains a rectangular network of channels which is bordered by two intersecting $40\ \mu$ wide channels (Fig. 7.26-a). The thin lined rectangle represents $7\ \mu$ wide channels network. Figure 7.26 a) is accompanied by a color bar which depicts a range of the depth of the formed channels. Figure 7.26-a) also demonstrates that a channel section shown on this figure has a depth of approximately $40\ \mu$ along the all length of the wider channels. The 3-D view of the same

part the network (Fig. 7.26-b) provides more details about the channels geometry. Particularly comparative depth of two channels is illustrated.

The zoomed views of the $40\ \mu$ channels intersection (Fig. 7.27) depict fine details of channel's features. Particularly it is shown that the edges of the channels have round segments. The straight walls and the bottom of the channels are clearly shown on the 3-D image.

Roughness of the channel's surfaces was analyzed by the profiler, the infinite focus microscopy and the 3-D digital microscope. All three techniques yielded almost similar results. For example the average roughness of 1.2 mm long segment of $40\ \mu$ wide channel was $1.6\ \mu$ (Fig. 7.28 a), and the average roughness of $530\ \mu$ long segment of $6\ \mu$ wide channel (Fig. 7.28 b) was $2.53\ \mu$.

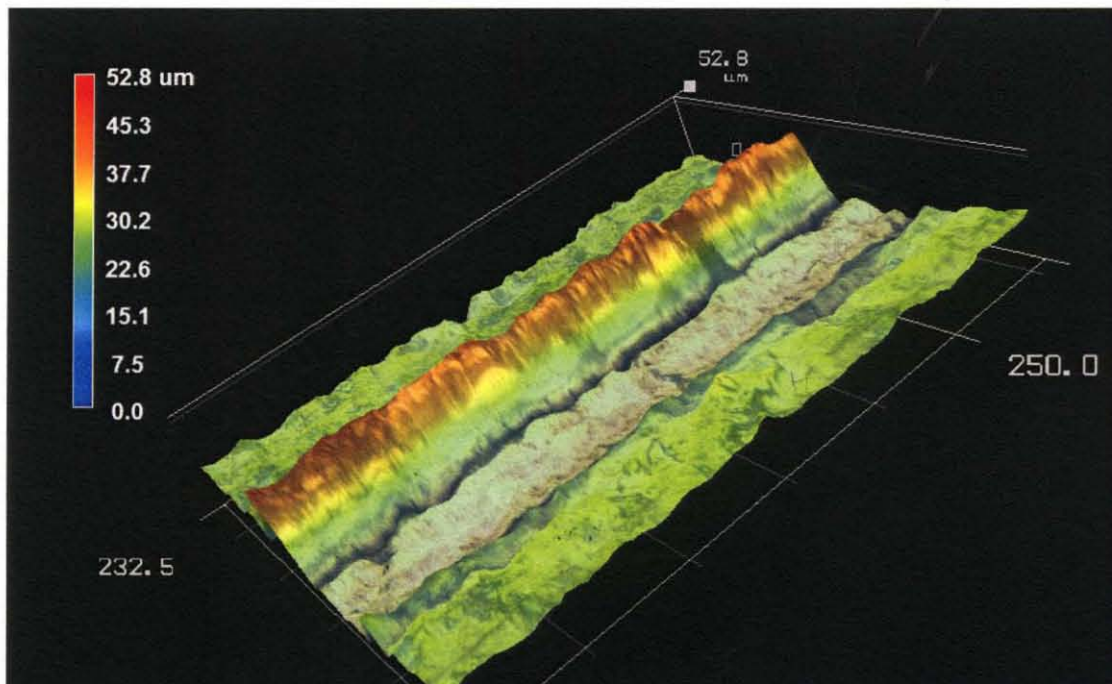


Figure 7.19 A 3D image of a section of the micro channel formed on a brass surface by $40\ \mu$ diameter tungsten wire; the image is generated by the 3-D digital microscope.

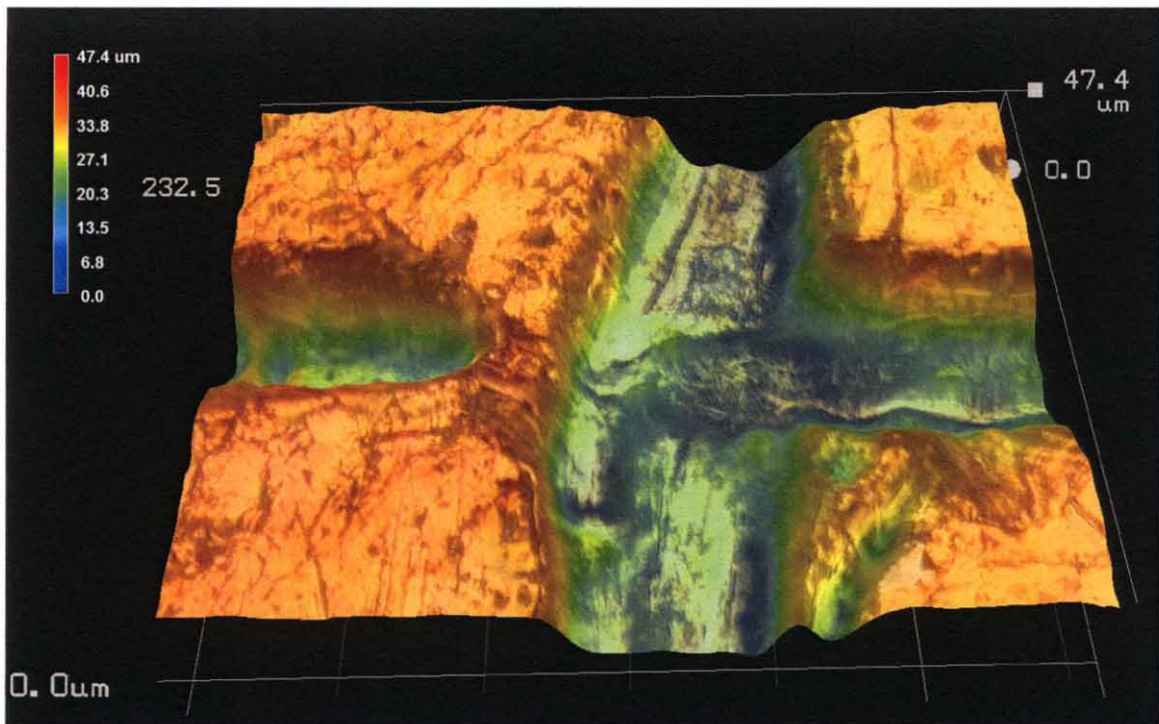


Figure 7.20 A 3D image of an intersection of the micro channels formed on a brass surface by $40\ \mu$ diameter tungsten wire; the image is generated by the 3-D digital microscope.

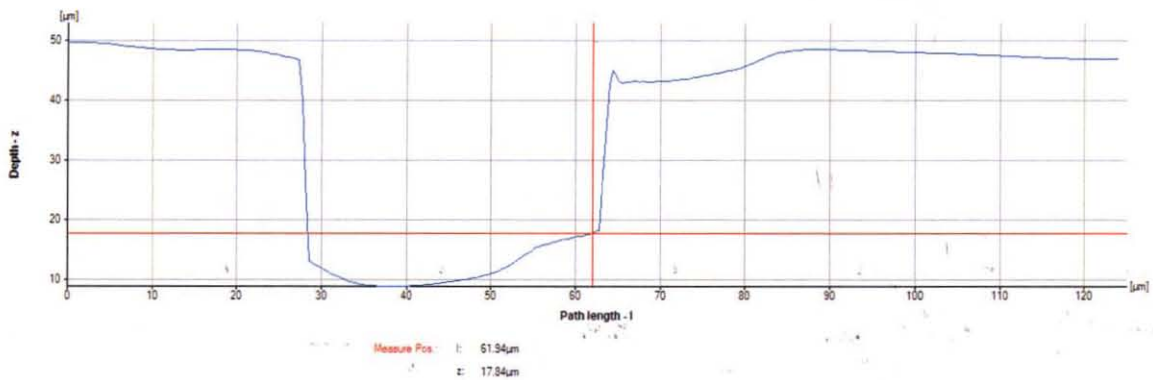


Figure 7.21 A profile of the channel formed on a brass sample by the $40\ \mu$ wire. Notice that the depth and width of the channel are approximately equal to the wire diameter.

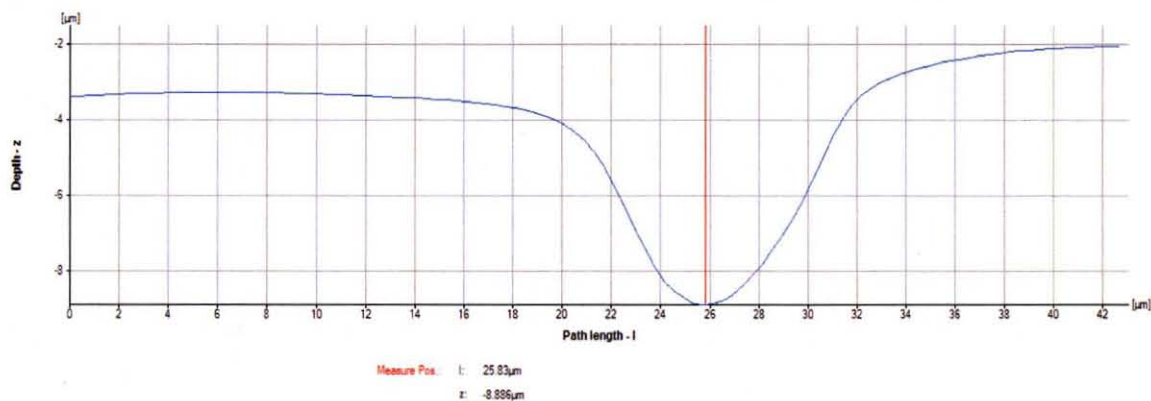


Figure 7.22 Profile of the channel formed by a 7μ diameter wire. Notice the compliance between profile of the channel and the die.

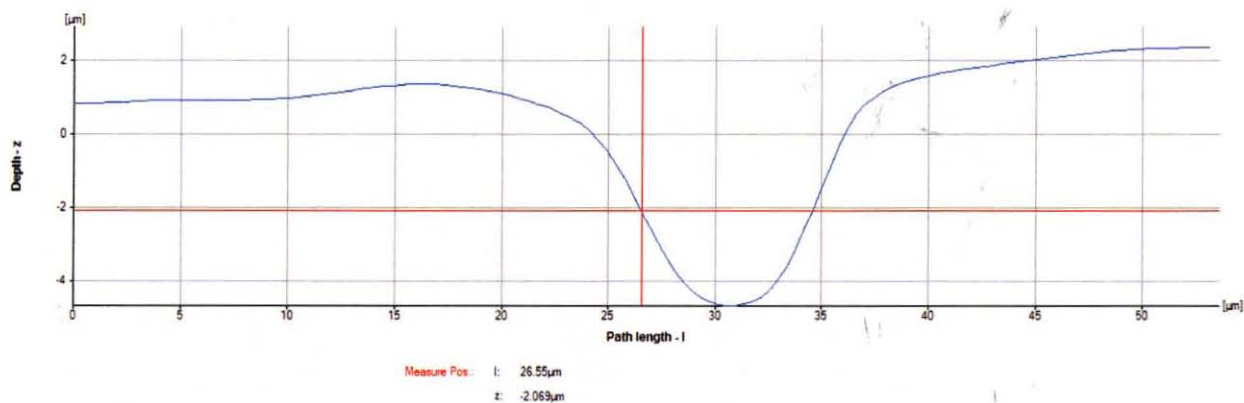


Figure 7.23 Profile of the channel formed by 7μ diameter wire. Notice the compliance between profile of the channel and the die and almost identity of profiles Figs. 7.22 & 7.23.

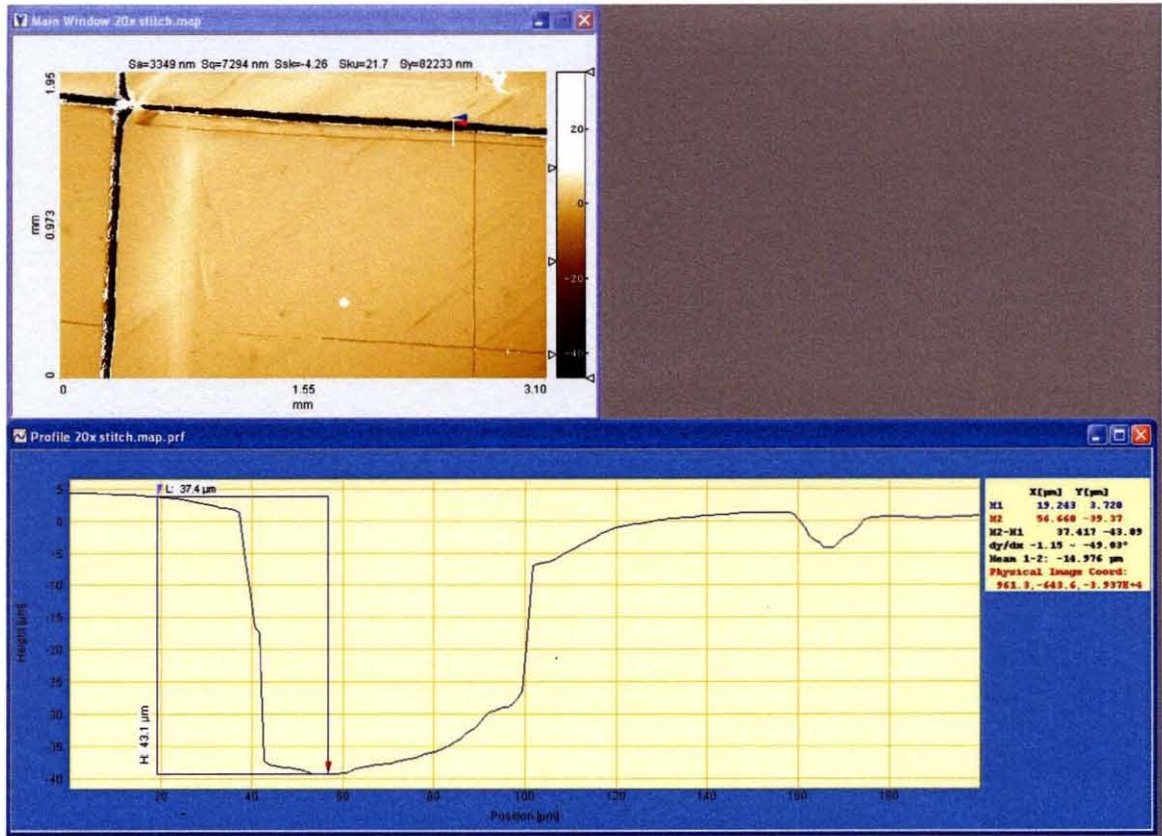


Figure 7.24 Profiles of two adjacent channels 40 μ and 7 μ wide.

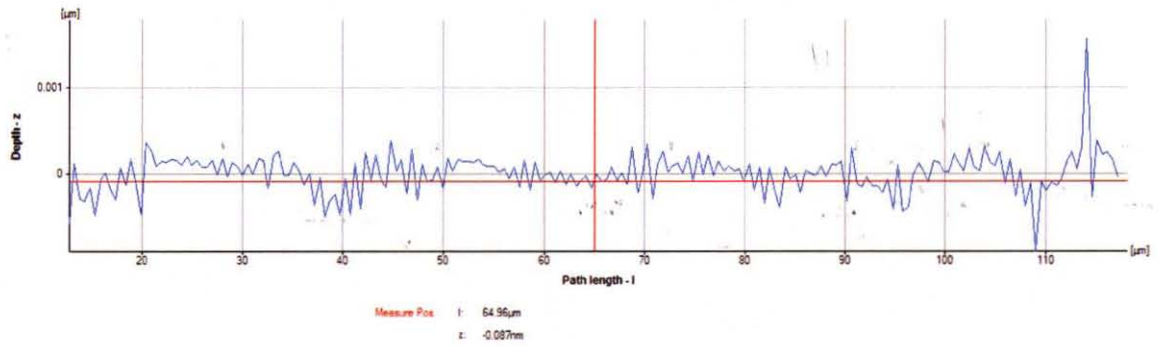


Figure 7.25 Surface roughness of a channel formed by the 40 μ wide wire.

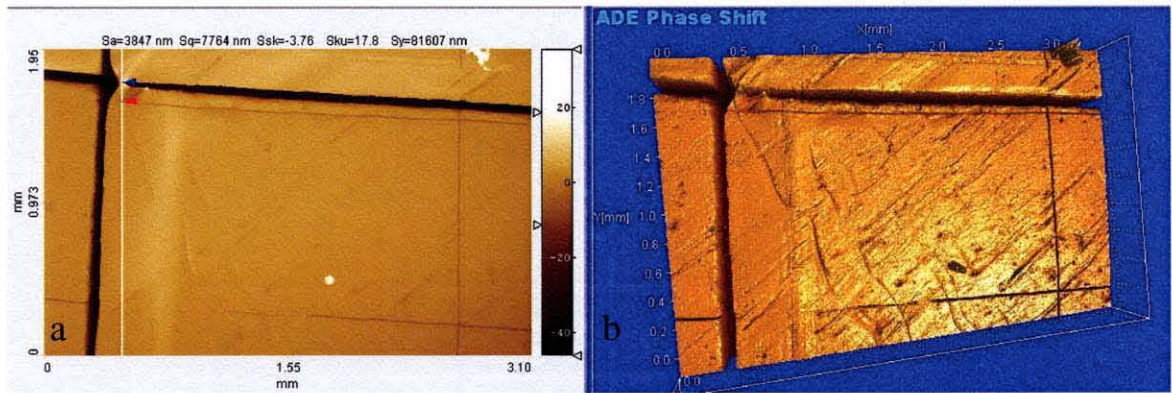


Figure 7.26 A channel network on the surface of the brass sample, a) 2-D image, b) 3-D image, 20x.

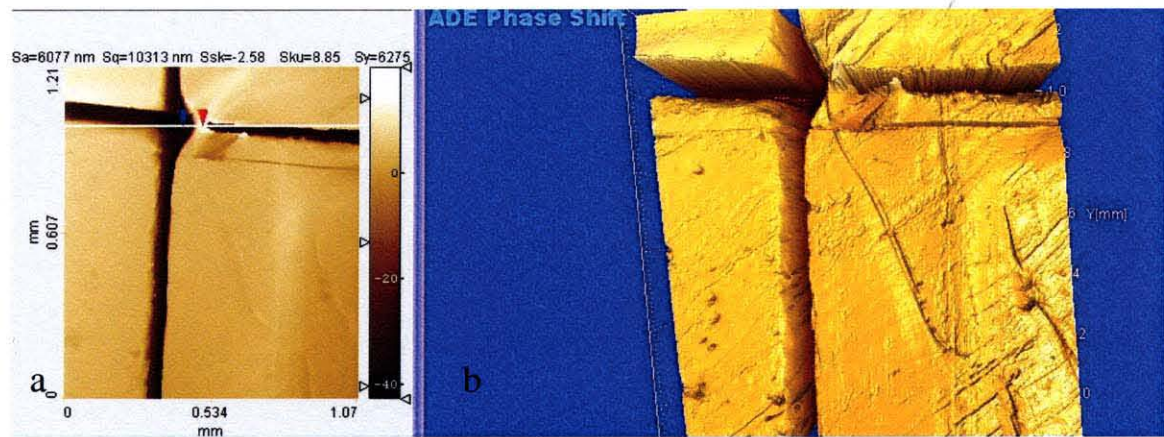


Figure 7.27 Zoomed in view of the portion of channel network shown on Fig. 27, a) 2-D image, b) 3-D image, 20x. Notice rectangular shape of the channel:

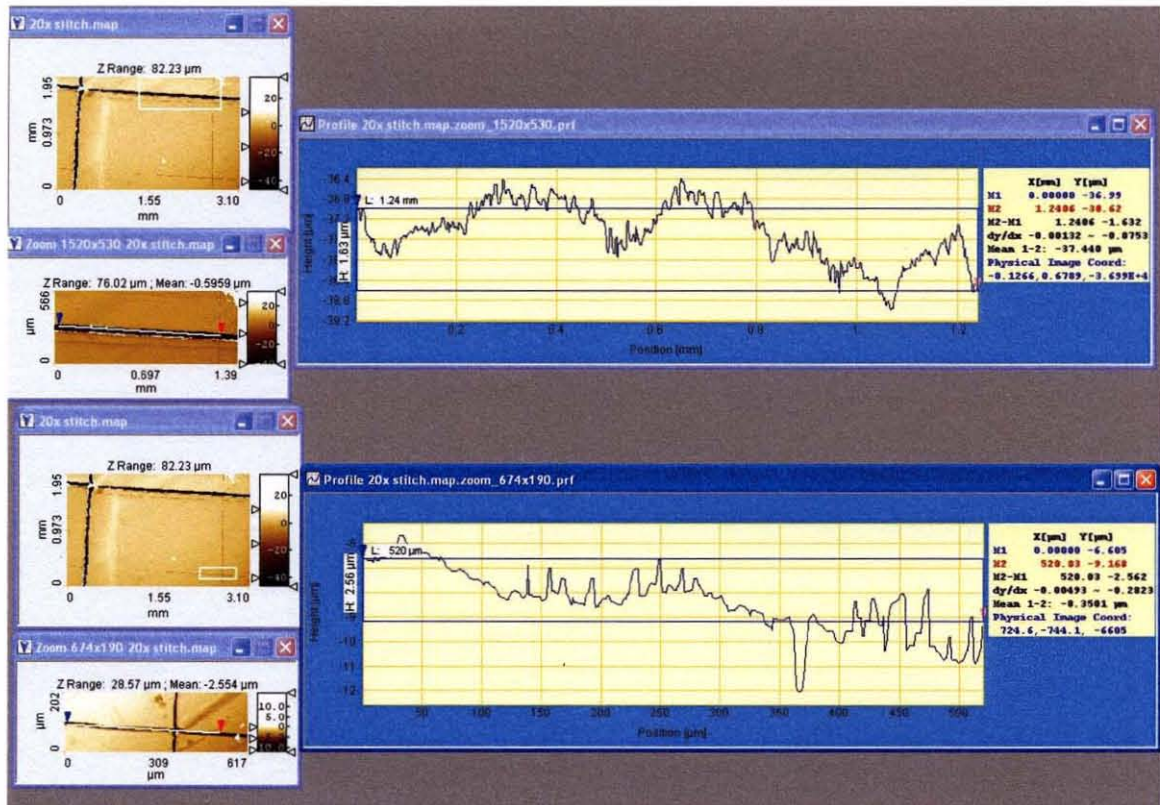


Figure 7.28 Average roughness of selected segments of channels,
 a) average roughness of 1.2 mm long segment of 40 μ wide channel was 1.6 μ ,
 b) average roughness of 530 μ long segment of 6 μ wide channel was 2.53 μ .

7.4.4 Micron Scale Extrusion

The objective of this study was to investigate extrusion of metals by filling a space between cylindrical and plane walls. The distance between the walls was ranged from 10 to 50 microns, while the wall width was in order of several centimeters and the height was in order of several millimeters. Thus, process involves filling a semi-infinite micron scale gap by an impacted metal. Copper, brass and high ductility steel samples were used. Also, some of the samples were made from an alloy used for fabrication of Ukrainian coins. Two types of dies were designed and manufactured. The first kind of dies entails 2 concentric rings and a solid cylinder. The heights of the rings and the cylinder were almost precisely equal. In the course of the die assembly the cylinder was tightly fitted into a cylindrical ring of the precisely same height. Then the obtained assembly was

tightly fitted into another ring also having the same height (Fig. 7.29). The rings and the cylinder were fabricated so that in the course of the assembly micron scale gaps were formed between the cylindrical surfaces on the forefront base of the cylindrical assembly. The base of the constructed die was placed against a target. By exposing a target to the water projectile impact, a target material was being extruded into the gap between the cylindrical surfaces creating rings (Fig.7.29). While the thickness of the rings was in order of microns, the height and the diameter were in order of millimeters. Thus micro extrusion with comparatively high extrusion ratio was accomplished.

Maximal extrusion ratio of 130 was achieved in a section of a cooper ring, and maximal extrusion ratio of 100 was obtained in a small section of the brass ring (Fig.7.30). A segment of the extruded ring reproduced by the infinite focus microscopy is shown on the Fig.7.31. A selected profile of the same segment has 1500 microns height and approximately 150 microns thickness (Fig.7.32). The extrusion ratio 10 observed in this case was substantially lower than the average one. Infinite focus microscopy was used to evaluate waviness and roughness of selected samples (Figs 7.33, and 7.34).

As it is shown on Figs. 7.30-7.32 brass extruded at comparatively high extrusion ratio forms rings having almost straight wall and almost plane surface. The surface topography was also adequate. According to Fig. 7.33 the roughness of a sample was less than $1\ \mu$ while the waviness was approximately $10\ \mu$ (Fig.7.34). The performed profile and roughness analyses demonstrated that the extruded rings had stable micro geometry. A segment of the extruded copper ring reproduced by the infinite focus microscopy is shown on Fig.7.35. A selected transversal cross section of the segment (a foil profile) is $250\ \mu$ high and $50\ \mu$ thick (Fig.7.36). A segment of the extruded steel ring is shown on

the Fig.7.37 and a selected profile form the segment $400\ \mu$ high and $90\ \mu$ thick (Fig.7.38).

The second die was used for the study of the formation of plain foils having the micron scale thickness. In order to fabricate a die the calibration strips (15 and $25\ \mu$ thick) were placed between $1\ \text{cm}$ thick tool-steel slabs. This die assembly had $6\ \text{mm}$ deep gaps which were 15 , and $25\ \mu$ wide. The die was fastened by a plane support. A high strength alloy used for fabrication of the Ukrainian coins was used as a target. The target materials were extruded into the gaps (Fig. 7.39) and the extrusion ratio between 100 and 200 was attained in the course of these experiments.

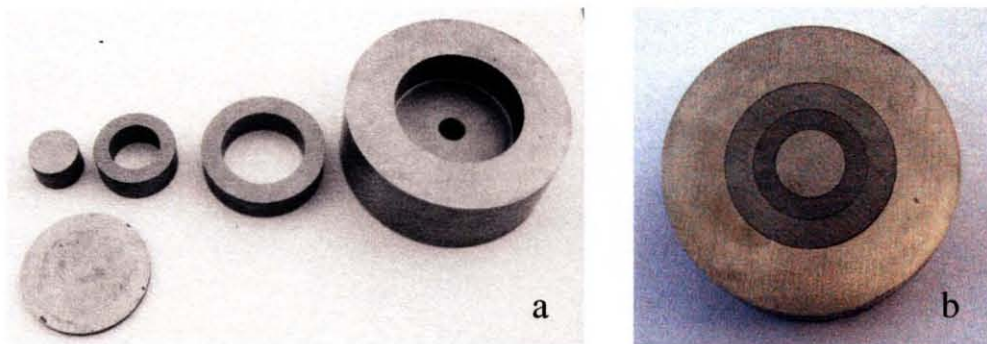


Figure 7.29 A die for ring formation: a) disassembled, b) assembled.



Figure 7.30 Extruded circular brass rings.

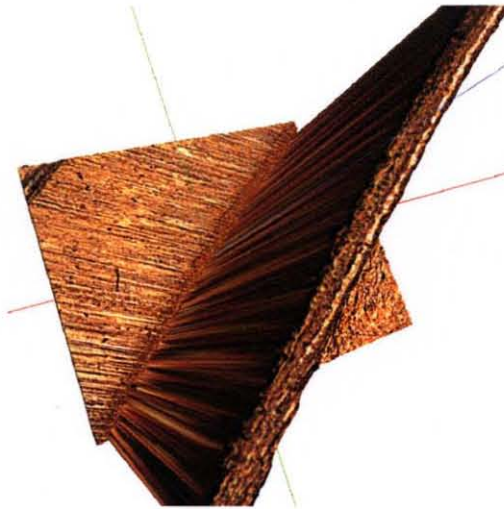


Figure 7.31 3-D image of a section of the extruded brass ring, the section is $1500\ \mu$ high, $150\ \mu$ thick.

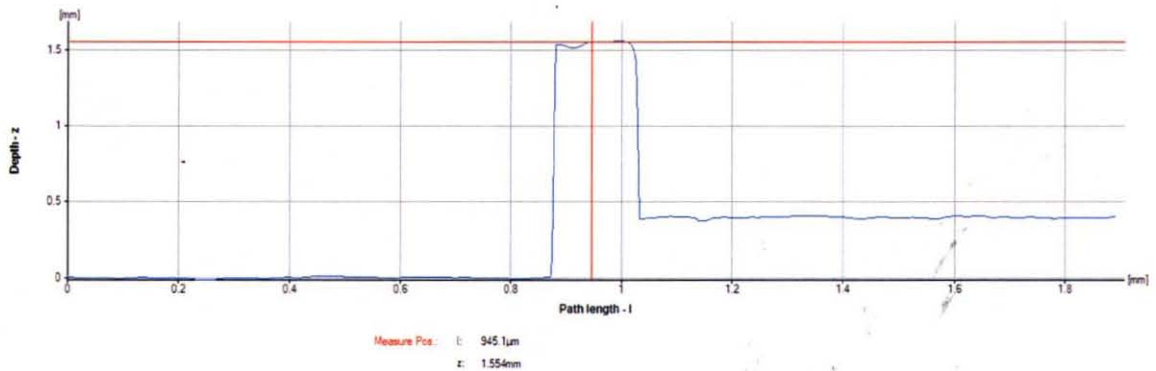


Figure 7.32 Profile of a section of the extruded brass ring, the section is $1500\ \mu$ high, $150\ \mu$ thick.

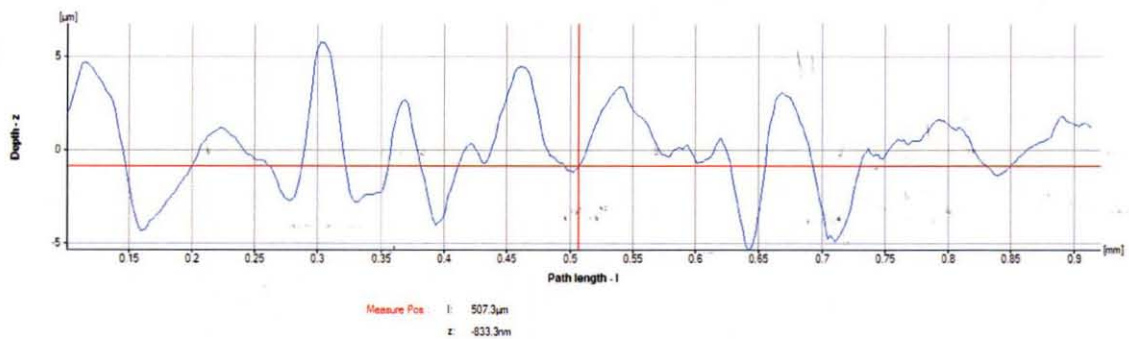


Figure 8.33 Surface waviness of brass wall section.

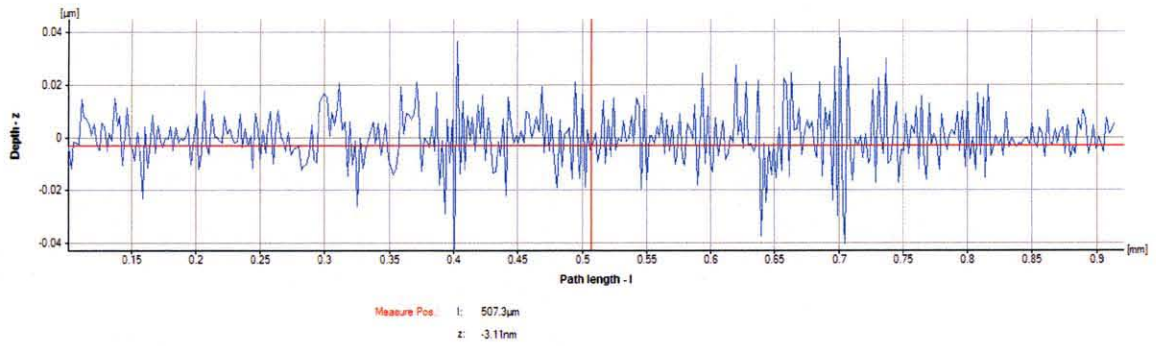


Figure 7.34 Roughness of a section of the extruded brass ring.

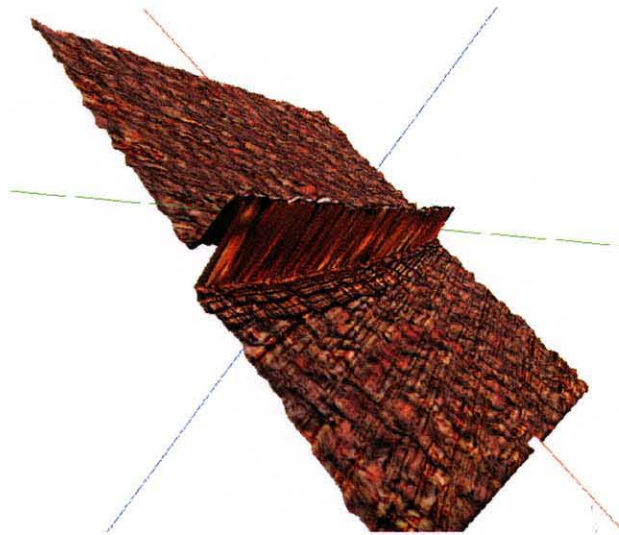


Figure 7.35 A 3-D image of a section of the extruded copper ring. The section is 250μ high, and 50μ thick.

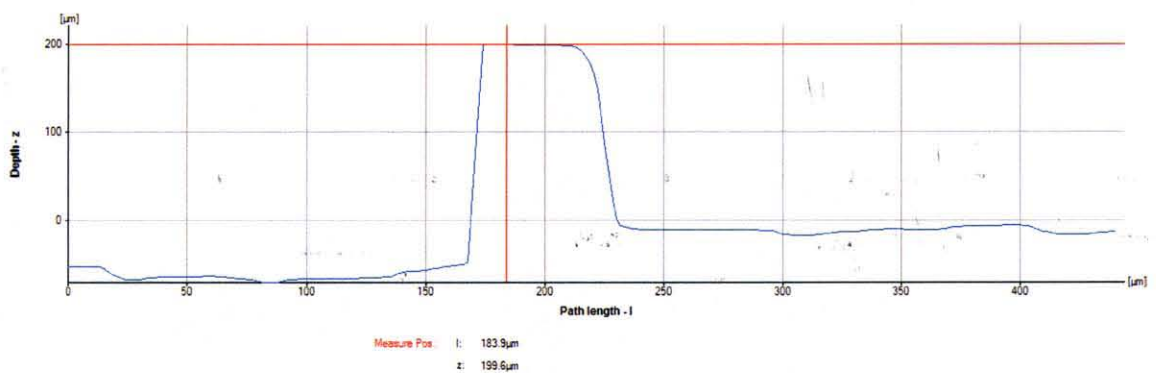


Figure 7.36 A profile of a section of the extruded copper ring. The section is 250μ high, and 50μ thick.

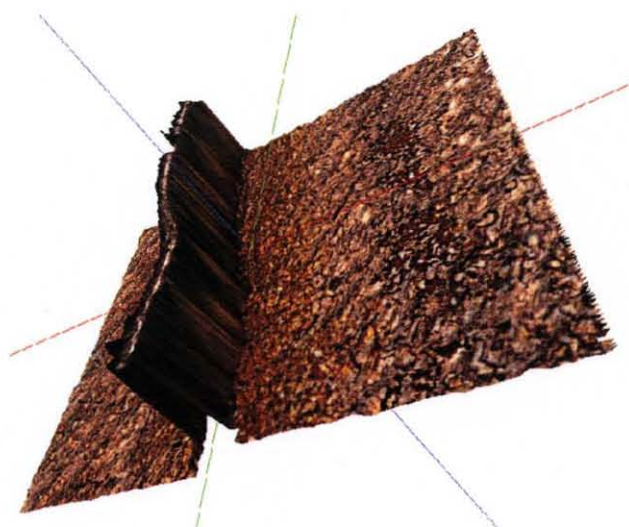


Figure 7.37 A 3-D image of a section of the extruded steel ring. The section is $400\ \mu$ high, $150\ \mu$ thick.

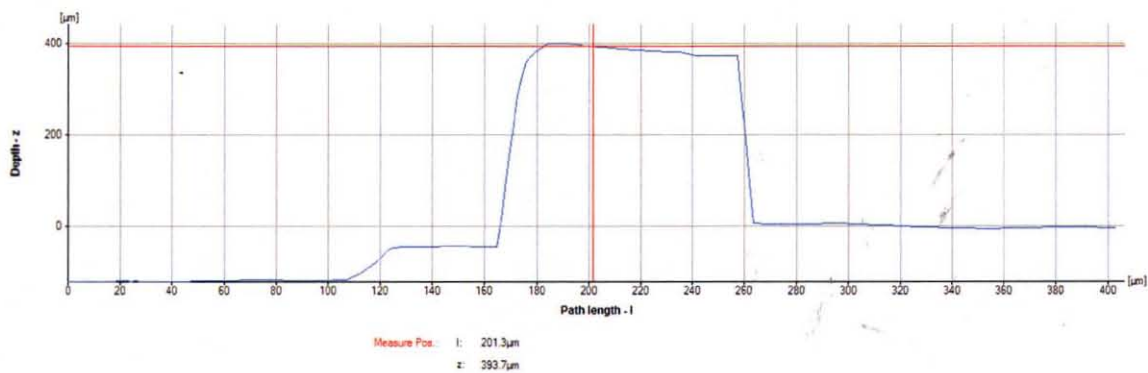


Figure 7.38 Profile of a section of the extruded steel ring. The section is $400\ \mu$ high, and $90\ \mu$ thick.

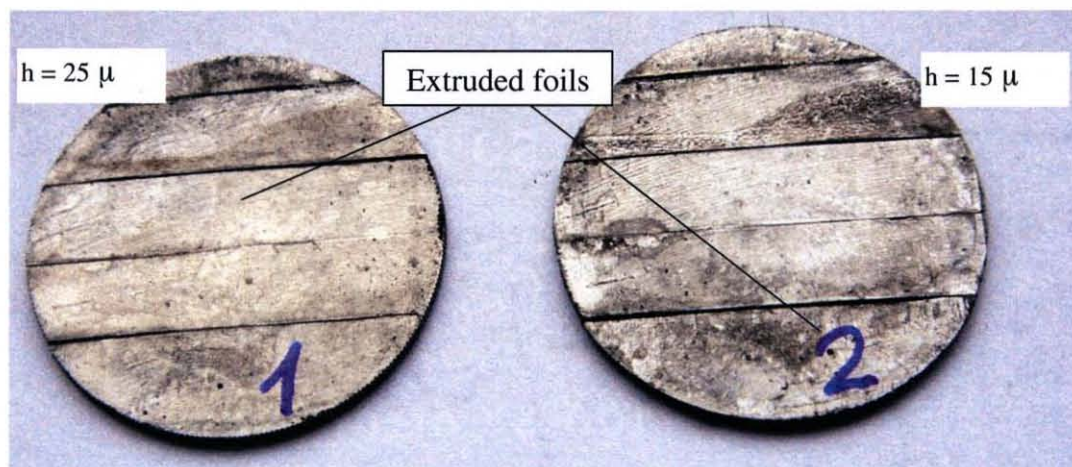


Figure 7.39 Extruded plain foils of nickel based alloy.

7.5 Discussion of Results

The liquid impact based forming has unique technological advantages. For example, similarly to the explosive forming, it requires a single die. The second die is replaced by a liquid punch. This simplifies the forming facilities and reduces its cost. A water projectile (liquid punch) could be applied to several processing operations and rapid execution of tasks would enable mass production of various parts. Contactless mode of the launcher-work piece interaction, ability of a liquid projectile to adjust to any geometry of a die, simplicity of process control assures the flexibility of the impact based micro forming. While the previous research [44] showed effectiveness of the application of high speed liquid impact to conventional forming operation, this study demonstrated feasibility to extend this application to micro forming.

In the course of the performed study totally 12 testing of extrusion into closed cavities, 12 testing of extrusion into open slots, 8 testing of micron scale stamping and 11 tests of micron scale forming were carried out. All of these tests involved deformation of various metals including steel and a special alloy at an extremely high rate determined by the speed of the water projectiles. The tests included formation of rather complex patterns such as networks of the micro scale channels or an image of a coin. The facilities used in this study (launcher, dies, targets, fixture) were fabricated using conventional machine shop capabilities and conventional materials. No special provisions for fastening a die, target or launcher or preventing die deformation were available. Even at these conditions only 2 tests did not result in completion of the selected forming operation. In the rest of experiments the results of forming were satisfactory. The desired shapes were generated, surface topography of the targets was quite adequate, no defects or damage generated in

the course of deformation was observed. Formation of shapes having a size of 6 microns was achieved.

It is expected the development of manufacturing technology will involve mass production of the precision low cost micron scale parts out of various engineering materials or formation of the micron scale pattern of the surfaces of regular parts. The performed experiments demonstrate feasibility of the use of high speed projectiles for fabrication of micro scale parts. It was shown that liquid impact driven micro forming has a potential of becoming technology of choice for micro parts fabrication. Indeed, the feasibility to generate micro scale (down to 6 microns) parts with an adequate surface topography was demonstrated. The facilities are comparatively simple and process productivity is determined by the firing rate of the launcher. For simplicity sake in the performed experiments a powder was used as an energy source. It is expected that in a manufacturing environment the chemical energy of a powder will be replaced by electrical or magnetic energy. In this case the firing rate can be as high as 1kHz. Then it can be expected the speed of the projectiles to be increased up to 2-3km/s and the accuracy and the strength of the dies will be significantly enhanced. This will enable us to generate more complicated and more accurate parts.

The performed experiments also indicate that there is a possibility to apply a proposed technology to micro forming of difficult to process materials, perhaps such as glass or ceramics. Unique advantages of the liquid impact based micro forming define the effectiveness of its application, while the performed experiments show its feasibility.

7.6 Conclusion

It was shown that forming of metals on sub millimeter and micro scale can be accomplished by high speed water projectiles. Original concept of micro machining process is validated. It was shown that micro forming can be accomplished by a single water projectile impact. It was shown that it is possible to generate a single micro object as well as an assembly of such objects, e.g. a network of micro channels. The obtained extrusion ratio shows feasibility to fabricate micron scale foils. Since commercial low cost metals were used in this study it can be suggested that the use of super-plastic materials would yield parts having grain scale dimensions. The performed experiments show that liquid projectiles have a potential of becoming a competitive micro forming tool.

CHAPTER 8

INVESTIGATION OF GEOMETRY OF GENERATED MICRO PARTS

8.1 Introduction

The objective of this study was to investigate geometries created by micro-forming operations. Infinite focus microscopy was used to characterize key features of generated geometries. Measurements of initial and generated surfaces were conducted and measurements of volumes of formed geometries were performed. Analysis of roughness and waviness of formed surfaces were measured. Thorough image analysis was performed in order to fully characterize 2-D features of formed geometries.

8.2 Measurement of Generated Surface Areas

During of process of micro-extrusion extruded foils and rings increase surface of workpiece. High extrusion ratio reaching up to 130 was achieved in experiments presented in Chapter 7 which in terms resulted in extreme increase of surface area. This is of essential significance if products created would be used in heat transfer applications. Multiple extrusions of foils would result in generation of finned surfaces which would multiply heat transfer rates. Infinite focus microscopy was used to measure generated surface of created topographies. High resolution and custom selection of field of view are features which enabled high accuracy measurements (Fig. 8.1). Measurements were performed by measuring of generated area and compare it to initial base area at the root of extruded entity. Detailed measurements of foils extruded from copper, brass and steel

were conducted. An example of one such measurement performed on copper sample is shown on Fig. 8.1 where the grid placed above extruded foil section represents projected base area of generated foil and grid points are measurement points. Same procedure was performed along the whole length of each foil in order to measure formed surface area. The technique enables very accurate measurements of generated and projected area. The highest generated surface was accomplished by extrusion of brass foils which was 11.32 times higher than original surface from which rings were extruded. For surface generated on copper foils the ratio was around 8.6 and for steel the ratio was around 8.61. Table 8.1 shows examples of such measurements for brass, steel and copper foils. Height, width and grid density are custom picked and measurements follow automatically.

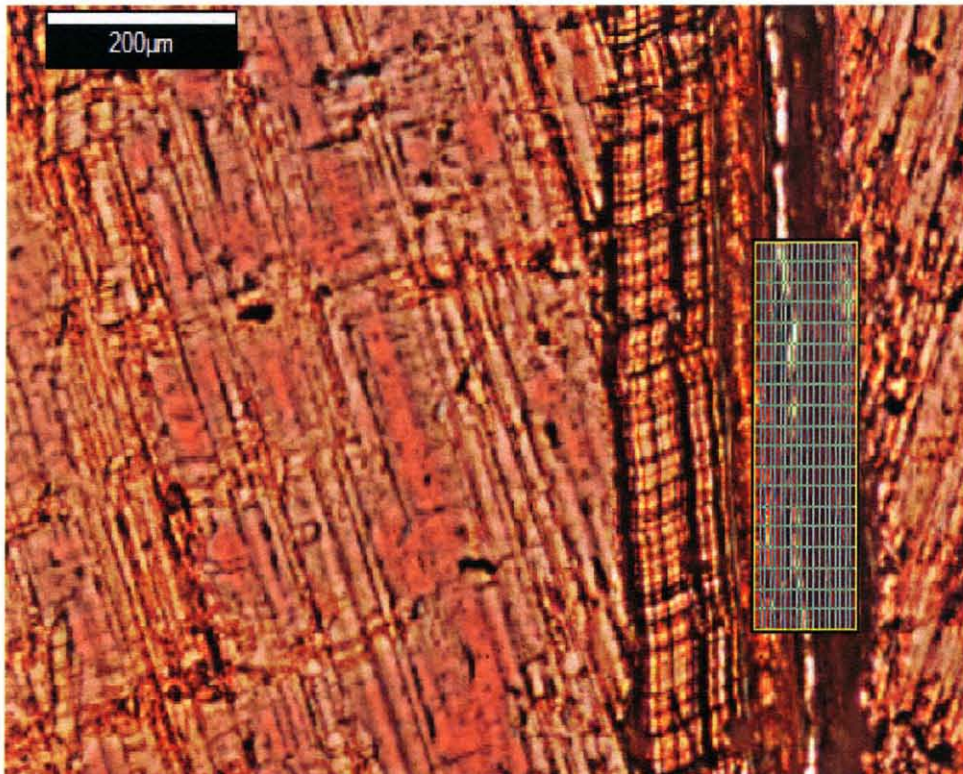


Figure 8.1 Example of measurement of generated area by extrusion of foil from copper sample.

Table 8.1 Examples of Measurements of Increase in Formed Surface Area

Material	Width[μm]	Height[μm]	Number of points	Projected Area [μm^2]	True area[μm^2]
Brass	186.9	164.6	12,051	29,654	317,617
Copper	91.08	84.68	3,021	7,161	47,023
Steel	115	107.1	4,824	11,616	100,038

Since some sections of extruded rings had extremely high extrusion ratio (100-130) we can conclude that there is high potential for creation of thin foil and films with large surface generation which can be beneficial in heat transfer applications.

8.3 Measurement of Extruded Volume

Infinite focus microscopy was used to measure extruded volume. Continuous in depth optical scanning coupled with Alicona software enables precise measurement of extruded volume. Top view of extruded geometry is used to select projected field of measurement (inscribed polygons on Figures 8.3b and 8.4b), measurement of volume follows automatically. Examples of views of analyzed samples and meshes created for calculation of measured volumes of all three tested materials are shown on Figures 8.2 and 8.3 and 8.4. Table 8.2 shows examples of measurements of volumes of all three tested materials.

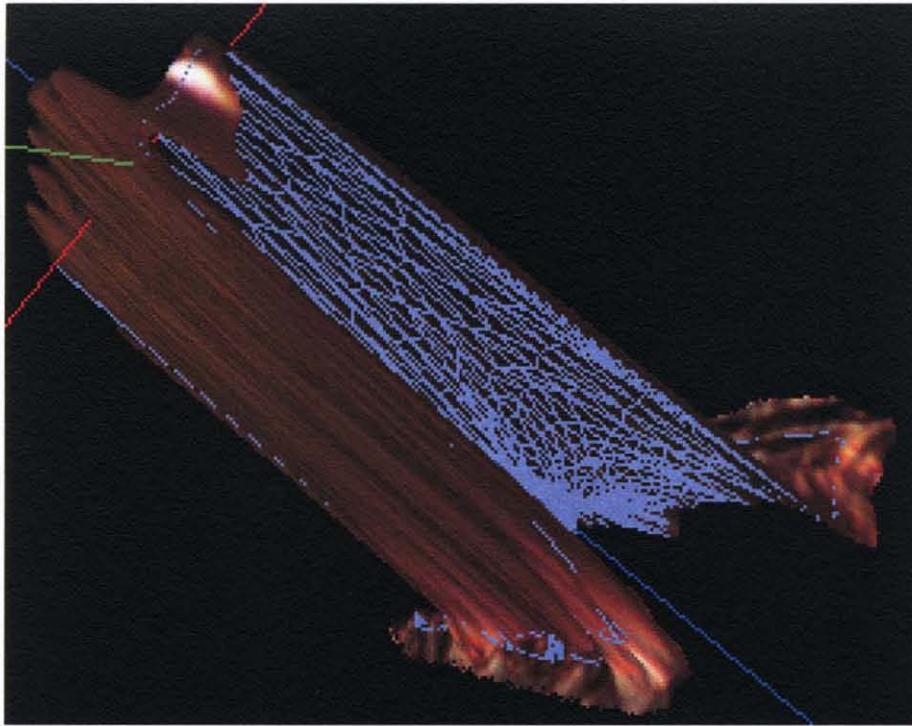


Figure 8.2. Example of measurement of generated volume of extruded copper foil.

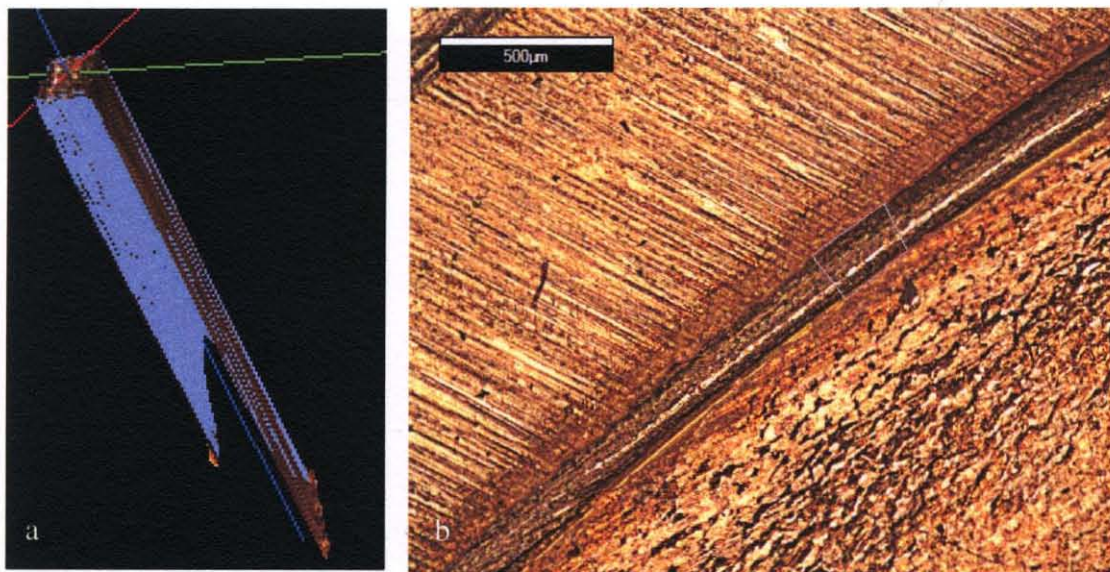


Figure 8.3 a) Example of measurement of generated volume of extruded brass foil; b) 2-D view of extruded foil; inscribed polygon indicates projected area of measurement.



Figure 8.4 a) Example of measurement of generated volume of extruded steel foil; b) 2-D view of extruded foil; inscribed polygon indicates projected area of measurement.

Table 8.2 Examples of Measurements of Extruded Volume

Material	Volume above surface [μm^3]	Volume below surface [μm^3]	Projected area [μm^2]
Brass	25,351,976	15,277	93,833
Copper	14,900,509	45,018	93,833
Steel	4,700,201	127,253	29,785

8.4 Investigation of Geometry Complacence between Die and Product

Variety of surface geometry and surface quality parameters were investigated in order to evaluate material micro-forming techniques. Profile, roughness and waviness analysis were presented in the Chapter 8. Additional analysis of both dies and formed geometries were conducted in order to evaluate accuracy of reproduction of dies geometries. Infinite focus microscopy and scanning electron microscopy were used for this task. Detailed examinations of dies and formed geometries revealed excellent complacency between dies of formed geometries. It was confirmed that forming on both micro and meso levels resulted in mirror reproductions of dies geometries. An example of section of a die section is shown on Fig.8.5 and 3-D image of corresponding extruded wall section is shown on Fig. 8.6 and one profile of extruded section is shown on Fig. 8.7. Straightness of foil walls varies along the foil and angles of steepness ranged between 2 and 8 degrees for brass, 4 and 27 degrees for copper and 5 and 27 degrees for steel. These variations came from variable geometry of dies.

Scanning electron microscopy was used to compare dies and formed geometries. General view of a coin used as a die is shown on Fig.8.8(left) and a 3-D image of geometry formed on steel surface is shown on Fig.8.8 (right). Scanning electron micrograph of the letter O from the coin is shown on Fig.8.9 and letter O formed on steel is shown on Fig.8.10. Detailed comparison of micrographs revealed excellent match between the die and stamped geometry. This procedure was used for detailed investigation of corresponding features of dies and stamped geometry. Thus the developed conditions in course of the impact are sufficient for precision shaping of hard

to process materials such as steel. As it is illustrated by the presented figures any noticeable change of the generated surface are replica of the die surface.

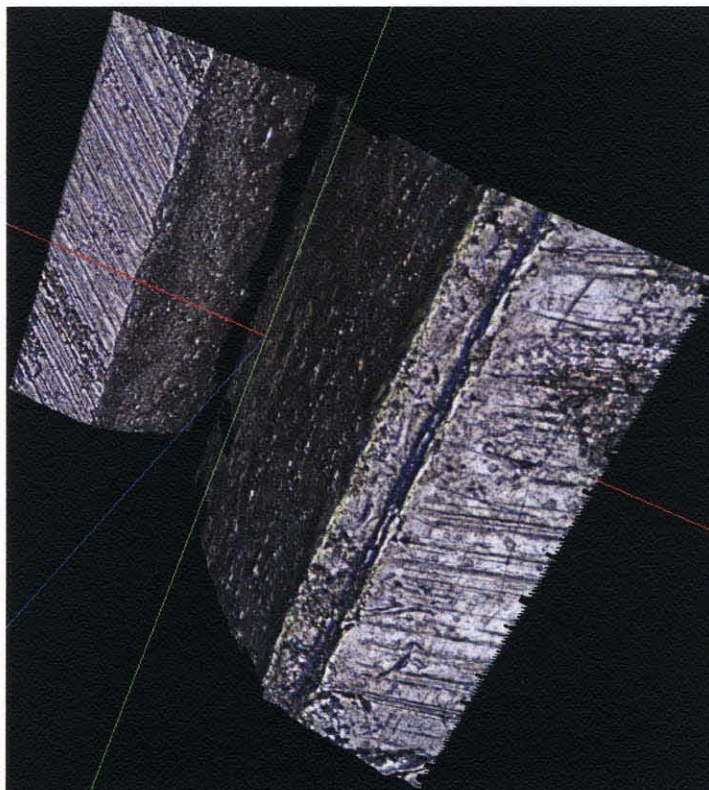


Figure 8.5 A 3-D image of die segment showing the gap.

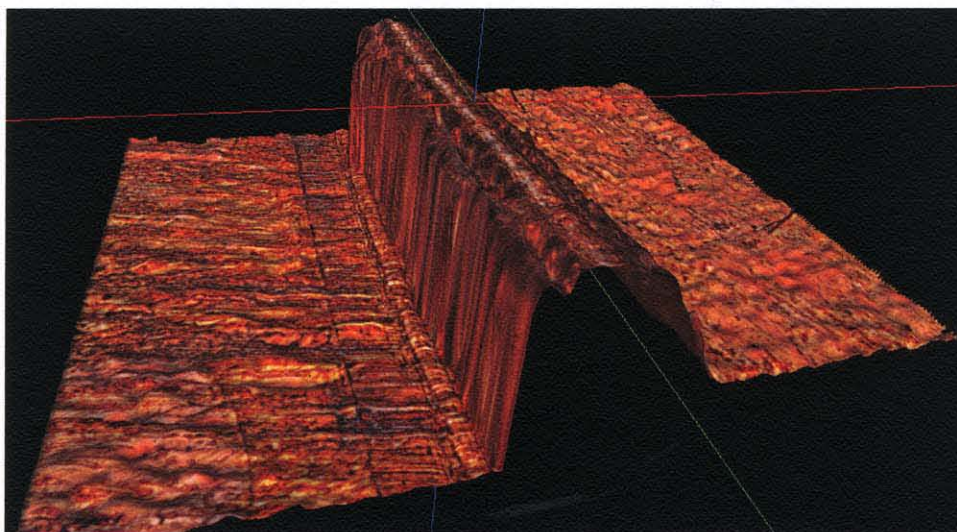


Figure 8.6 3-D image of a section of the extruded copper foil. The section is 450μ high, and 200μ thick.

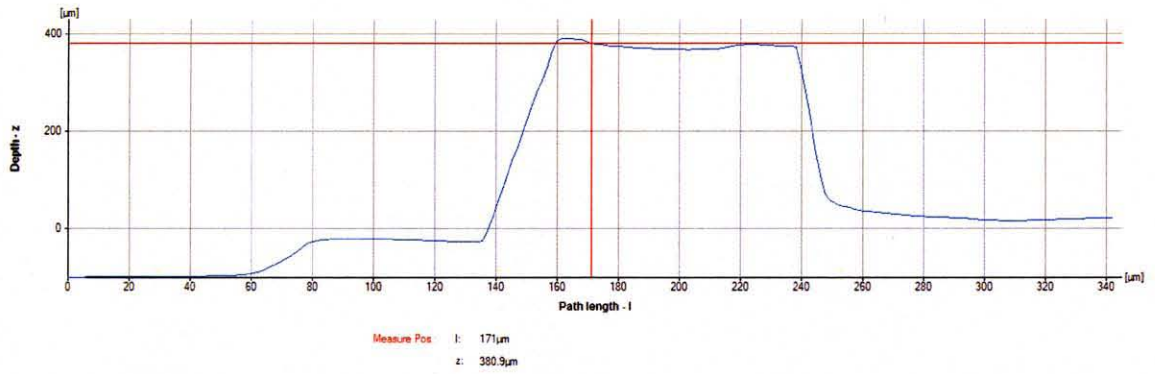


Figure 8.7 Profile of a section of the extruded copper foil. Measurement of steepness of foil sides showed 19 degrees for left inclination angle and 10 degrees for right inclination angle.

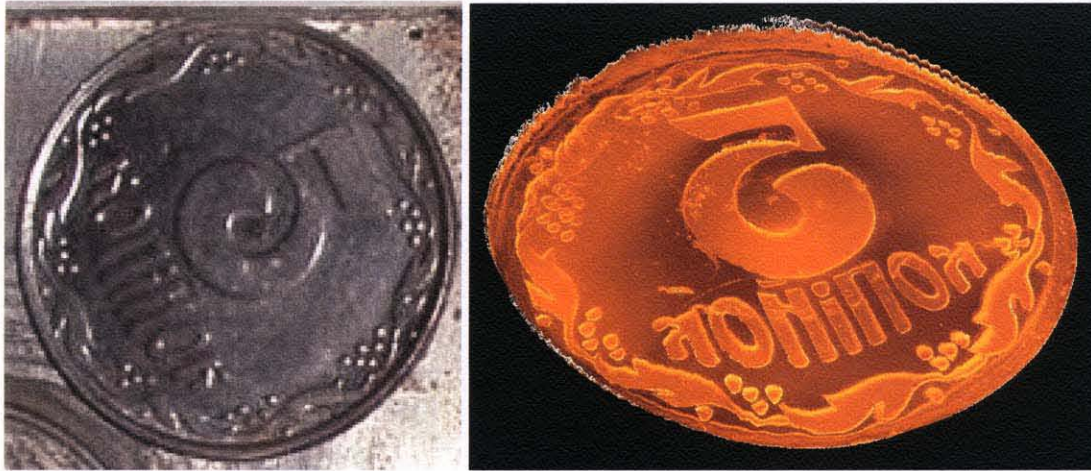


Figure 8.8 General view of a coin used as a die for stamping on steel and 3-D reproduction of formed image.



TM-1000_0077

2007/02/06

14:31

L

x40

2 mm

Figure 8.9 SEM image of letter O from the die (coin).

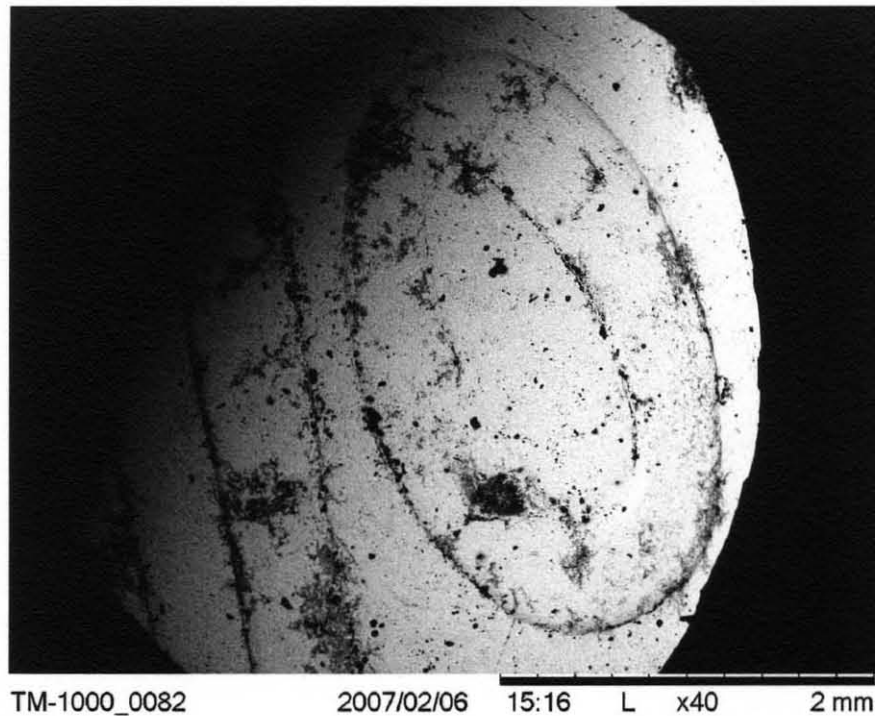


Figure 8.10 SEM image of letter O forged on steel.

8.5 Discussion of Results and Conclusions

It was confirmed that accurate reproduction of micro and meso-scale geometry features can be reproduced by liquid impact. Lower limit of formed dimension was 7μ but it was confirmed that forming of smaller dimensions is feasible. During microextrusion experiment cracks in die were initiated and they were instantaneously filled as they propagated. As a result cracks were completely filled proving that formability limit would most likely be in the nano-scale. It was confirmed that these forming processes are predominantly pressure driven and not momentum and or inertia driven processes. Therefore it appears that any gap can be filled. Mechanical properties and grain size of forming material may be limiting factors of minimal characteristic dimension of forming geometry which was not the case in this investigation.

CHAPTER 9

MECHANICAL PROPERTIES OF FORMED METAL SURFACE

9.1 Introduction

Investigation of mechanical properties of networks of micro-channels such as shown on Fig. 7.26 was performed by nano-indentation. The tested materials included brass, steel and copper. Tribo Indenter was used to accurately determine differences in the mechanical properties of three materials. In all performed experiments the tested area was imaged with the optical microscope (Figs. 9.3, 9.5, and 9.7) prior to testing in order to determine indent location. Scanning Probe Microscopy imaging was performed with the same tip after testing (Figs. 9.4, 9.6, and 9.8). Three areas on each sample were tested, inside the micro-channel (inside track), next to the micro-channel (next to track) and away from the micro-channel(away form the track) to act as a control (Fig.9.1). Nano-indentation testing was performed on each sample to determine hardness and reduced modulus.

9.2 Experimental Procedure and Results

Examination of all samples was performed on a Tribo Indenter, which is a high resolution nano-mechanical test instrument that performs nano-scale indents by applying a force to an indenter tip, while measuring tip displacement into the sample. During indentation, the applied load force and tip displacement are continually measured, creating a load-displacement curve for each indent. Nano-indentation tests were performed on three

materials: brass, steel and copper. All indents had a max peak load of $2000\mu\text{N}$, and were performed from an in-contact mode with a Berkovich tip. Every quantitative indent consisted of a three second linear hold at peak load to stabilize any creep in the sample. Steady load cycle was applied throughout complete testing. Example of load-unload curves for steel sample testing is shown on Fig. 9.2. Three tested areas are shown in Fig. 9.1 each area had at least 3 indentations. Results are summarized in Table 9.1 for brass sample, Table 9.2 for steel sample and Table 9.3 for copper sample.

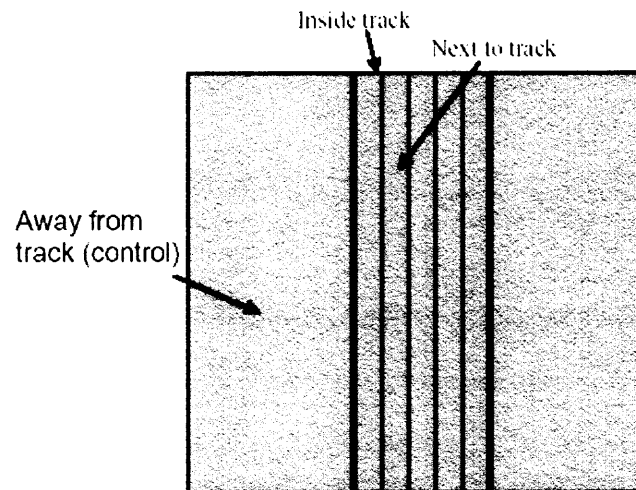


Figure 9.1 Cartoon image of areas where testing occurred on samples.

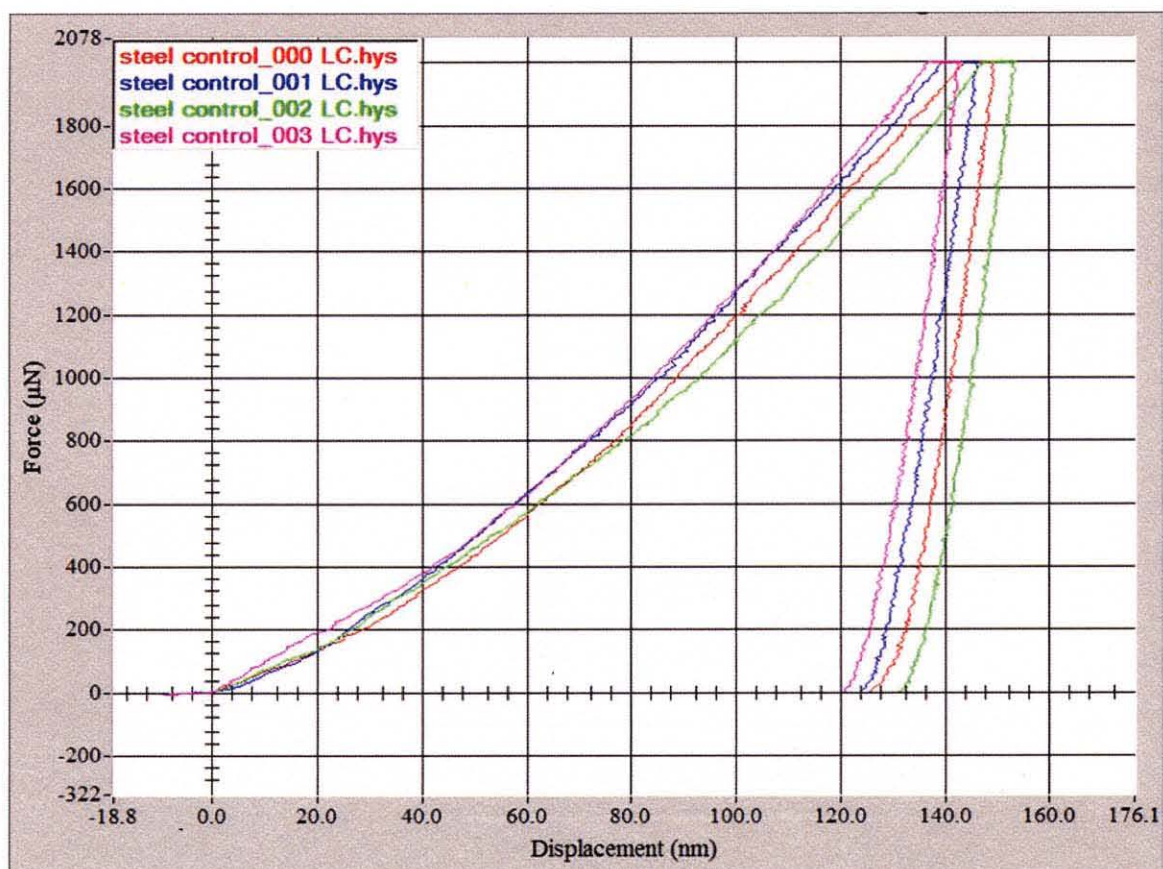


Figure 9.2 Set of load-unload curves for steel sample testing.

Table 9.1 Results from Nano-Indentation Testing of Brass Sample, Showing Increased Hardness Inside Track When Compared to Top Surface of Sample

Brass			
	In track	Next to track	Control
Hardness (GPa)	3.39 ± 0.05	2.80 ± 0.28	2.94 ± 0.14
Modulus (GPa)	116.44 ± 4.96	115.45 ± 2.72	117.69 ± 4.48



Figure 9.3 Optical microscope images of areas tested on brass sample. a) inside track, b) next to track, c) control.



Figure 9.4 SPM images after testing on brass showing residual indent impressions left on sample surface. a) inside track, b) next to track, c) control.

Table 9.2 Results from Nano-Indentation Testing of Steel Sample, Showing Increased Hardness Inside Track When Compared to the Top Surface of Sample

Steel			
	In track	Next to track	Control
Hardness (GPa)	4.32 ± 0.14	3.16 ± 0.24	3.40 ± 0.21
Modulus (GPa)	168.4 ± 5.29	165.00 ± 6.52	149.31 ± 5.53



Figure 9.5 Optical microscope images of areas tested on steel sample. a) inside track, b) next to track, c) control.

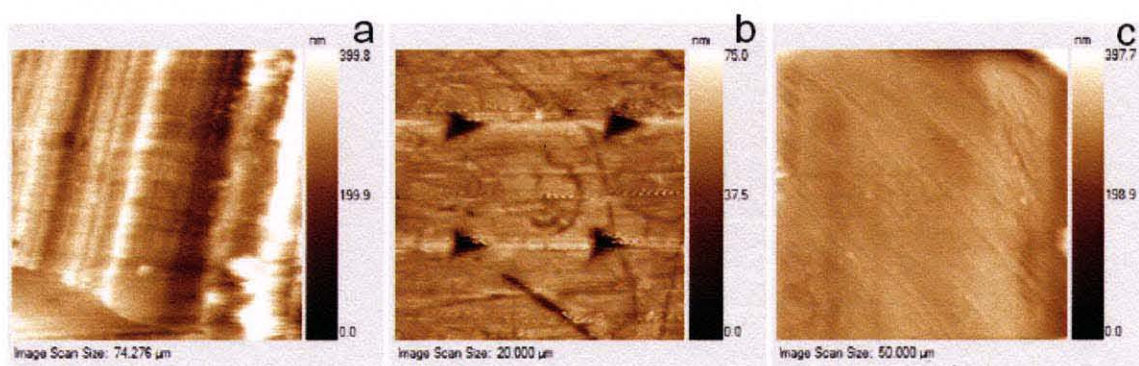


Figure 9.6 SPM images after testing on steel showing residual indent impressions left on sample surface. a) inside track, b) next to track, c) control (taken before test).

Table 9.3 Results from Nano-Indentation Testing of Copper Sample, Showing Increased Hardness and Modulus Inside Track When Compared to Top Surface of Sample

Copper			
	In track	Next to track	Control
Hardness (GPa)	2.58 ± 0.26	2.11 ± 0.17	2.22 ± 0.45
Modulus (GPa)	156.53 ± 14.50	134.53 ± 7.90	120.95 ± 15.14

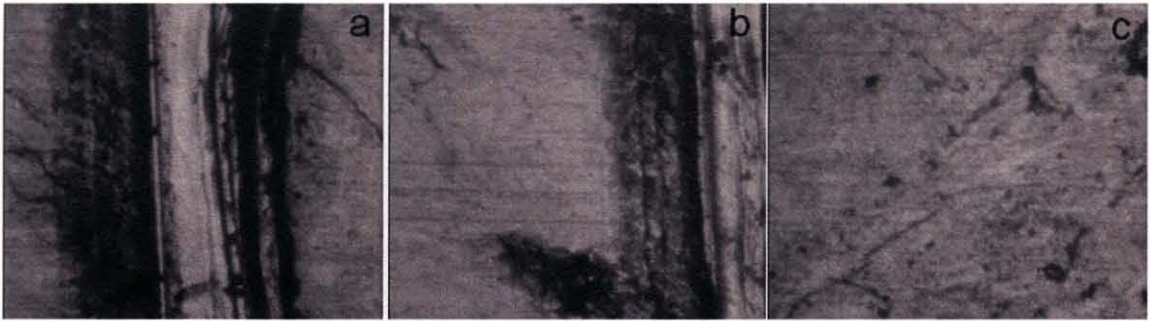


Figure 9.7 Optical microscope images of areas tested on copper sample. a) inside track, b) next to track, c) control.

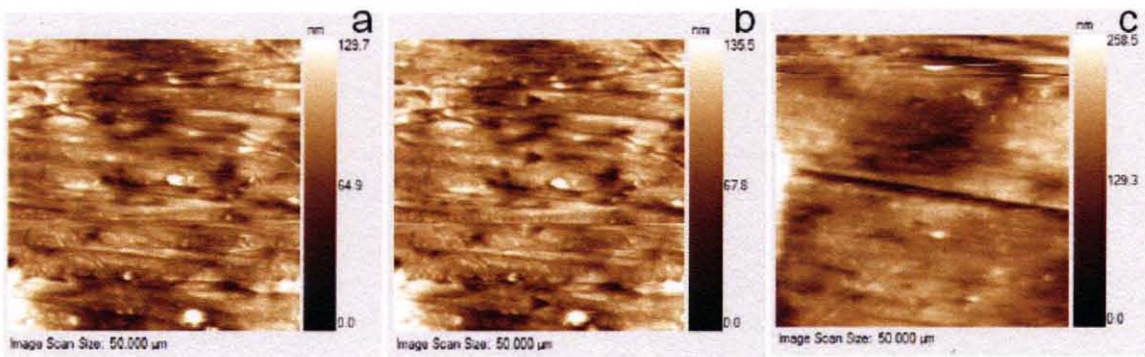


Figure 9.8 SPM images after testing on copper showing residual indent impressions left on sample surface. a) inside track, b) next to track, c) control.

9.3 Discussion and Conclusions

Hardness and modulus of all three tested materials showed same trend which is an increase of both, hardness and modulus within the micro-channel when compared to the virgin surface of the sample. This was found from the SPM images not to be topography dependent. Regarding the topography of the micro-channels, it was similar to the surface, and the standard deviations were low in the data which is representative of a good surface.

CHAPTER 10

EXPERIMENTAL STUDY OF SIMILAR AND DISSIMILAR METAL WELDING BY IMPACT OF HIGH SPEED WATER PROJECTILES

10.1 Introduction

Main objective of this study was to investigate the welding of similar and dissimilar metals using high speed water projectiles. Liquid projectile based solid state welding and cladding were explored experimentally. Similar technology of explosive welding requires special conditions [42, 43]. Metals plates used in this study included high ductility steel, brass, copper and nickel based alloy. As a result, ten similar and dissimilar combinations of metals were successfully welded by impact of water projectiles. The performed experimental study showed that high speed liquid projectiles can be used to assemble heterogeneous metal structures. Experimental data acquired in the course of the performed experiments was incorporated into the knowledge base of the metal welding by high speed water projectiles. As a result of the performed experiments feasibility of the use of high speed water projectiles for water projectile impact based welding was demonstrated.

10.2 Experimental Procedure

Water projectiles moving at super high velocities carry tremendous amount of energy and when impacting the target do so at extremely high impact factor (1500 and up). These projectiles act similarly to an explosive charge activated at the impact surface. Investigation of metal welding by water slug impact was performed with the objective to

explore experimentally joining of two or more similar (same) and dissimilar (different) metals by water projectile impact.

An experimental setup for the study of the water projectile impact based forming was designed and constructed (Fig. 3.1). This setup constituted an industrial scale prototype of the water cannon [34, 35]. The targets were mounted on a heavy pendulum (Fig. 3.1). Angular displacement of pendulum was measured in each experiment. This enabled us to estimate impact impulse and therefore impact momentum. For each experiment the water cannon was placed at a desired standoff distance from the samples and water projectile impact operation was conducted. Metal samples in form of circular and square plates including high ductility steel, brass, copper and nickel based alloy were used. Sample shapes were square plates 40×40mm and circular plates of 31.7mm

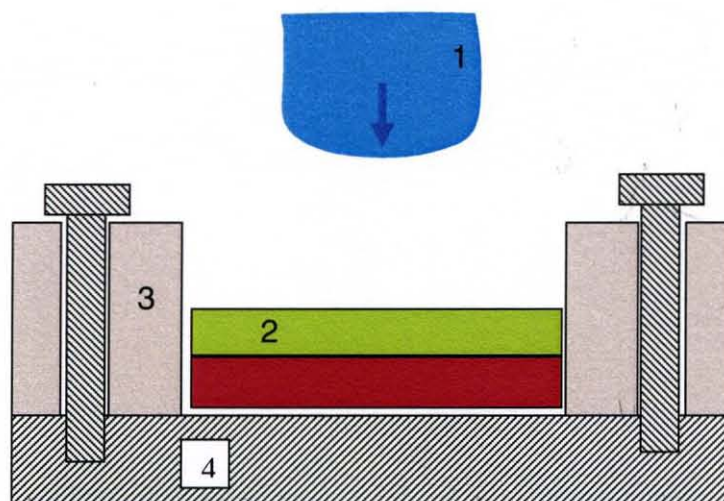


Figure 10.1 Schematic of impact zone for nested experimental set up: 1 –water projectile, 2 –nested metal samples to be welded, 3 – fasteners, 4 –back support.

diameter. Variety of placements of samples was investigated. Included setups were such as: setup without the distance between plates (Fig. 10.1), and with separation distance between plates, setup with no radial boundaries to dissipation of the jet and nested setup

(with fasteners engulfing the projectile and not allowing radial dissipation of the jet (Fig. 10.1, Fig. 10.2). The acquired experimental data collected in the performed experiments was used for the study of peculiarities of material welding in the course of the liquid projectile impact. Particularly, the feasibility of such technologies as the liquid impact based welding was investigated.

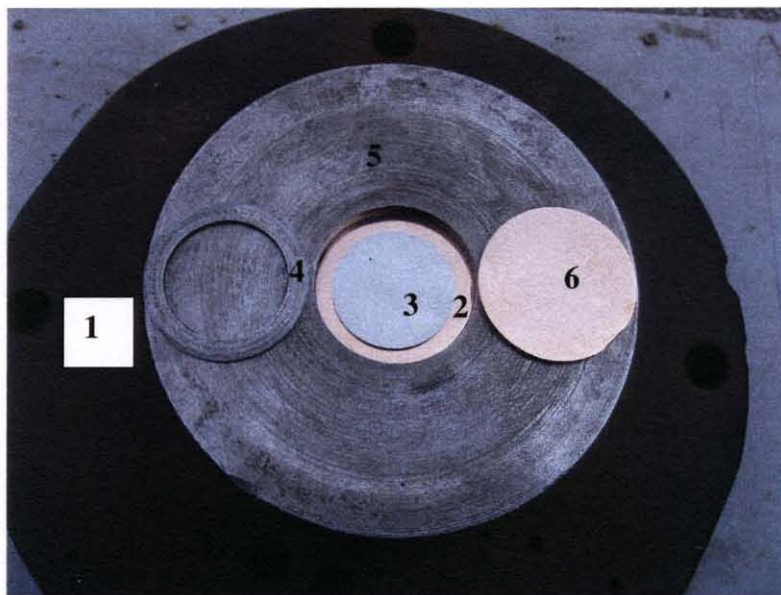


Figure 10.2 Front view of nested experimental set up prior to assembly for welding. 1 – back support, 2 – rear copper plate to be welded, 3 – middle layer to be welded(nickel alloy coin), 4 – separation ring, 5 – fastener, 6 – impact side copper plate to be welded.

10.3 Experimental Results

Supersonic and hypersonic water projectiles by impacting introduce wave disturbances to impacted media which results in changes which cause welding of similar and dissimilar metals. Propagation of the waves through the target consisting of composite metal layers cause melting of very thin layers at the interface of plates to be joined, which results in metallurgical bond along joining interface.

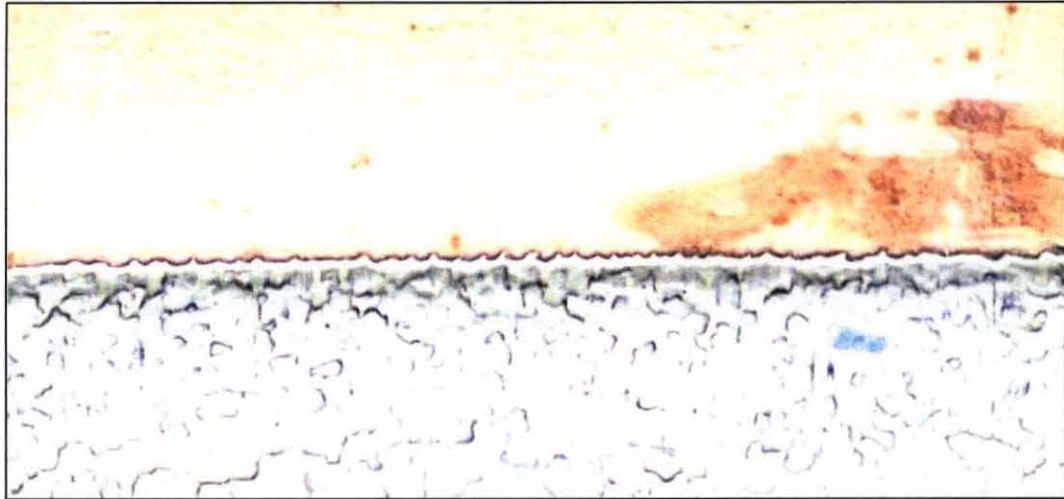


Figure 10.3 Copper and nickel-alloy plates welded by the water projectile impact at the water velocity 1500 m/sec. Micrograph of wavy interface of joined copper-nickel plates.

Investigation of metal welding by water slug impact was performed with the objective to explore experimentally joining of two or more similar (same) and dissimilar (different) metals by water projectile impact. Disturbances introduced to impacted media by supersonic and hypersonic water projectiles result in changes which cause welding of similar and dissimilar metals when exposed to the impact. Materials used for testing during this study were: copper, brass, and high ductility steel which has % elongation 46%, tensile strength of 325MPa, and yield strength of 195MPa. Thicknesses of metal samples used in this study were: 1mm for copper, 1.5 and 1mm for brass, and 2.75mm for steel. Two set ups were used in this study: first, with no acceleration of one of the metal samples to be welded (single impact), and second, with acceleration of one of metal samples to be welded (double impact). For the tests with no acceleration mode a nickel based alloyed coin was placed between two metal samples of identical composition (copper-copper, brass- brass and steel-steel) and such assembly was mounted on a heavy pendulum. Initially experiments were done using super high speed shooting mode (1500m/s) where 240g water was driven by combustion of 30g of gun powder (Table

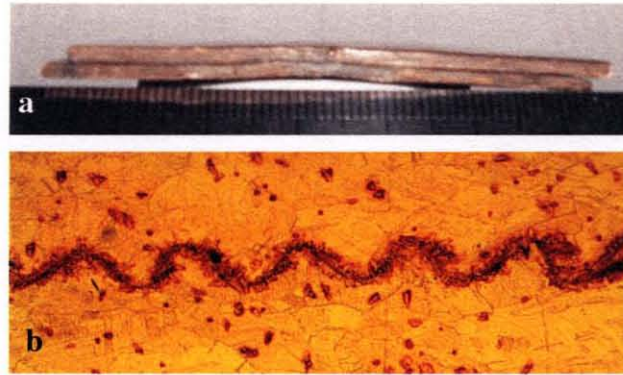


Figure 10.4 a) Copper plates welded by the water-projectile impact at the water velocity 1500m/sec and $h=3\text{mm}$. b) Zoomed-in section of micrograph of wavy interface of joined copper plates.

10.1.). Figure 10.3 shows micrograph of welded interface between copper and nickel based alloy plates (Table 10.1, Experiment 3), where welded seam exhibits wavy appearance such as commonly observed in explosive welding joined structures.

Figure 10.4 shows micrograph of welded interface between two copper plates (Table 10.1, Experiment 2), where side view of joined plates is shown on a) and micrograph of section of wavy welded seam is shown on part b). Figure 10.5 shows long segment of same section of wavy welded seam where stable wavy pattern of welded seam along entire welded section is observed.

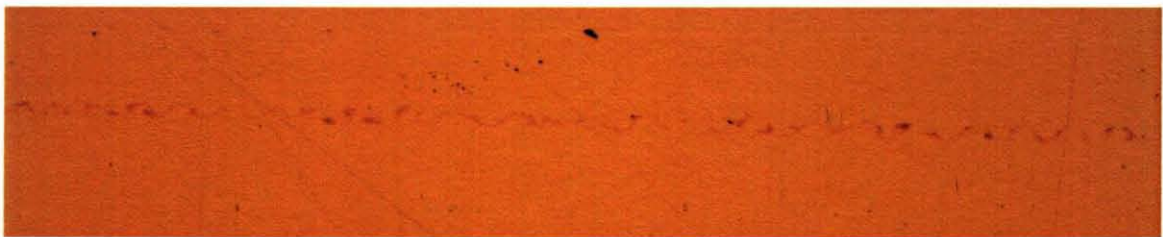


Figure 10.5 Two copper plates welded by the water-projectile impact at the water velocity 1500m/sec and $h=3\text{mm}$. Notice uniformity of wavy seam along entire bond length(x100).

After initial examination of successfully joined structure it was decided to switch to lower speed shooting mode (750-850m/s), which proved to deliver weld of higher strength. After the exposure to the water projectile impact (single impact), each

combination of metals was welded together. Experimental conditions were: 350g of water propelled by 25g of gun powder at a stand of distance of 16cm for the copper-nickel coin-copper combination, and 350g of water propelled by 35g of gun powder at a stand of distance of 16cm for the brass-nickel coin-brass and steel-nickel coin-steel combination, As a result all three items were welded to each other in each test. Testing with acceleration mode was carried out by separating metal samples to be welded by steel separation rings (1mm and 2mm thick). In this case two impacts were contributing to the welding process, first water projectile impact to the front sample (to accelerate the front sample) and second impact of accelerated sample to the fixed one. In this part of investigation experiments with samples of similar metals (copper-copper, brass- brass and steel-steel) and combinations of dissimilar metals (copper-steel, copper-brass and brass-steel) were tested. Experimental conditions were: 350g of water propelled by 25 - 35g of gun powder at a stand of distance of 16cm for all tests (Table 10.1). Consistency of operation was confirmed by sufficient repetition of experiments. Each of these tests resulted in welded assembly of investigated combinations. Automatic ultrasonic scanning (A, B and C-scans) was used for examine integrity of welded seam and metallurgical bonding was confirmed for all of tested combinations. By repetition of experiments consistency of operation was confirmed. After initial investigation of samples and forceful mechanical separation of several welded samples it is estimated that acceleration mode provides better conditions for welding than mode without acceleration of sample. Additional characterization of samples is needed, namely mechanical strength of weld should be tested. Since standard mechanical tests are not adequate for testing of samples generated in this study I am working on the original design for evaluation of mechanical

strength of welded seam. Initial characterization confirmed a high potential of this technique for industrial application of stitched seam spot welding.

Shooting in extruder mode gave better results. Samples were less deformed and they were well joined. Micrographs of welded interface revealed wavy interface of joined plates. Wave length of wavy interface has magnitude of grain size of used materials.

Table 10.1. Experimental Results of Welding by Water Projectile Impact

Exp.#	M	m	H	Mo	V	J	R	S	C
1	30	240	16	251	1500	G	N	F	Cu-Ni -Cu
2	30	240	16	264	1500	G	N	F	Cu- Cu,
3	25	350	16	394	750	G	N	F	Cu-Ni -Cu
4	25	350	14	356	750	G	N	F	Cu-Ni -Cu
12	25	350	16	314	750	E	1	E	Cu-Ni-Cu
13	35	350	16	369	850	V	1	E	Br-Ni-Br
14	35	350	16	327	850	P	1	E	St-Ni-St;
15	25	350	16	237	750	No	3*1	E	Cu-Cu
16	35	350	16	369	850	P	1/	E	Br-Br
28	30	350	16	169	850	G	1	E	Cu-Cu
29	30	350		378	850	P	1	E	Br-Br
40	30	350	16	466	850	E	1	E	Br-Br
41	30	350	16	217	850	E	2	E	Br-Br
42	30	350	16	442	850	E	1	E	St-St
43	30	350	16	430	850	E	1	E	Cu-St
44	30	16	16	N/A	850	E	1.5	E	Cu-Br
45	30	16	16	N/A	850	E	2	E	Br-St

##-Number of the experiment

M-mass of the powder, g (kind of the powder see below)

m- mass of the water, g

H-standoff distance, mm

Mo-projectile momentum, kg.m/s

V-projectile velocity, m/s

J-result (joint E-excellent, VG-very good, G-good, F-failure)

R-separation ring, mm (N-no separation)

S-support (F-flat or E-engulfing)

C-combination of metals to be jointed, (Cu-copper, Al-aluminum, St-steel, N-nickel alloy, Br-Brass)

Details:

Shape-S (square a**x**b= 40**x**40mm) or R (round d= 31.7mm)

10.4 Nondestructive Testing

Ultrasonic technique was employed for nondestructive testing, examination and characterization of welded interface region. Scanning of all generated samples was conducted in order to examine integrity of joined structures and to test metallurgical bonding. Automatic ultrasonic scanning (A, B and C-scans) of all generated samples was conducted to examine integrity of welded seam and metallurgical bonding was confirmed for all of tested combinations. Welded samples were submerged into water filled tanks

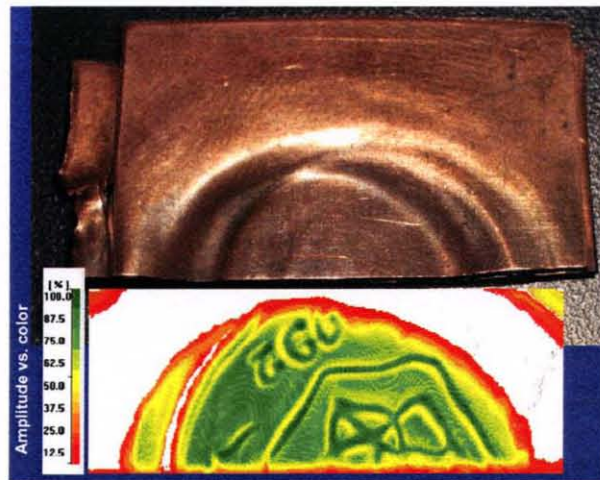


Figure 10.6 Copper –nickel alloy-copper plates welded by the water projectile impact at the water velocity 1500m/sec, and ultrasonic scan of welded plates.

and they were submitted to automatic ultrasonic scanning. Example of copper-nickel based alloy-copper welded sandwich (Table 10.1, Experiment 3) is shown on Fig. 10.6 where amplitude vs. color ultrasonic scan of joined structure is shown as well.

General view of welded copper-nickel alloy-copper plates obtained during experiment #12(Table 10.1) is shown on Fig.10.7, these plates were welded by the water projectile impact at the water projectile velocity of 750m/sec. Sample of ultrasonic

verification of integrity of formed structure and metallurgical bonding of plates is shown of Fig. 10.8. The time differential of ultrasonic reflection peaks is the time needed for ultrasound to travel through entire thickness of the structure which confirms integrity and metallurgical bonding of plates.

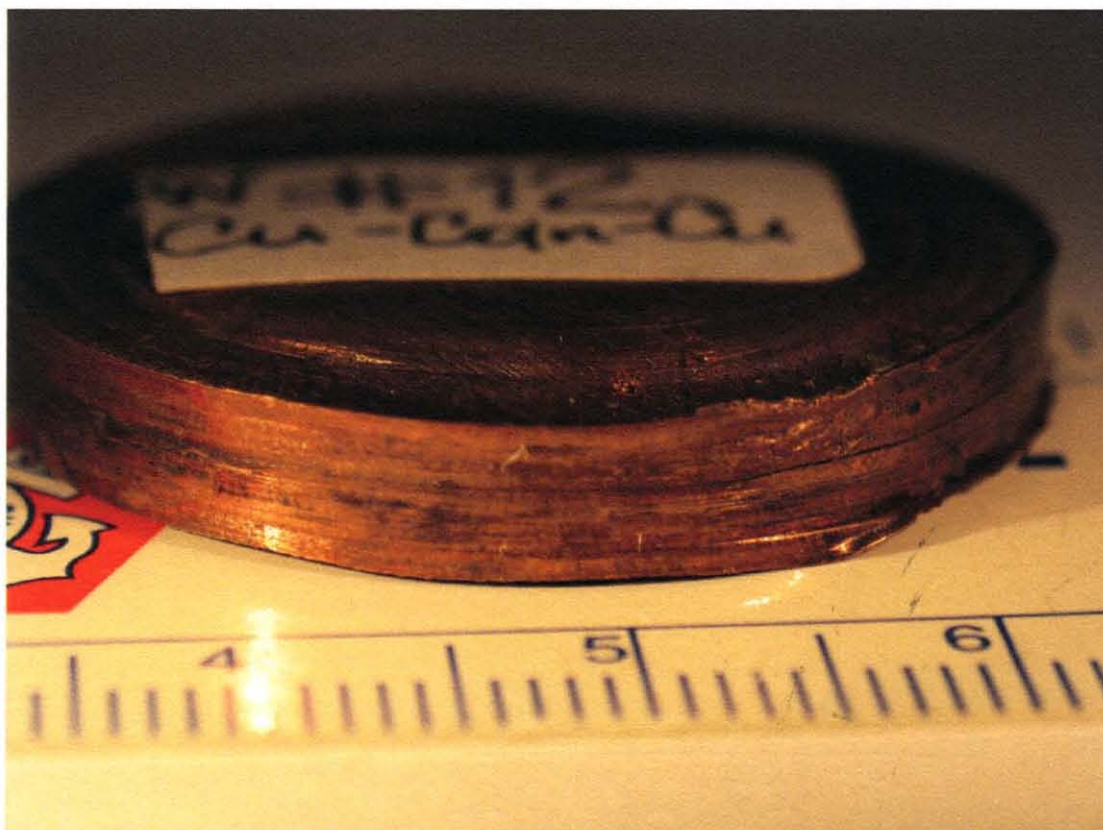


Figure 10.7 General view of copper-nickel-alloy coin-copper plates welded by the water projectile impact in Exp. #12 at the water velocity 750m/sec.

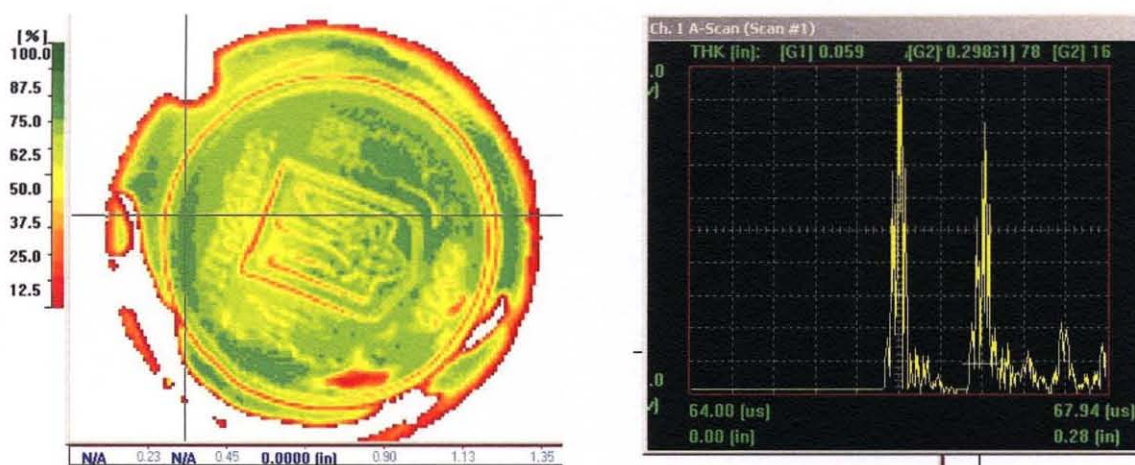


Figure 10.8 Ultrasonic verification of integrity of formed structure and metallurgical bonding of plates welded in experiment 12.



Figure 10.9 General view of brass-nickel-alloy coin-brass plates welded by the water projectile impact in Exp. #13 at the water velocity 750m/sec.

General view of welded brass-nickel alloy coin -brass plates obtained during experiment #13(Table 2) is shown on Fig.10.9, all three plates were welded and integrated into a single structure by the water projectile of velocity around 750m/sec. Figure 10.10 shows ultrasonic scan of brass-coin-brass welded structure.

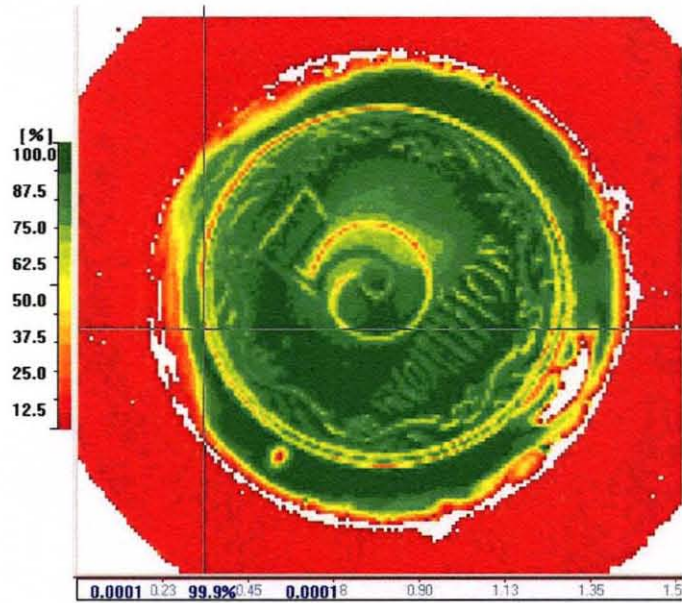


Figure 10.10 Ultrasonic scan of welded structure obtained in experiment 13. Brass-coin-brass combination.

General view of copper and brass plates welded by the water projectile impact at the water projectile velocity around 750m/sec (Exp. 44. Table 10.1) is shown on Fig.10.11. Integrated structure was obtained including 1mm separation steel ring which is welded and locked between welded plates. Scanned sample of ultrasonic verification of integrity of formed structure and metallurgical bonding of plates is shown of Fig. 10.12.

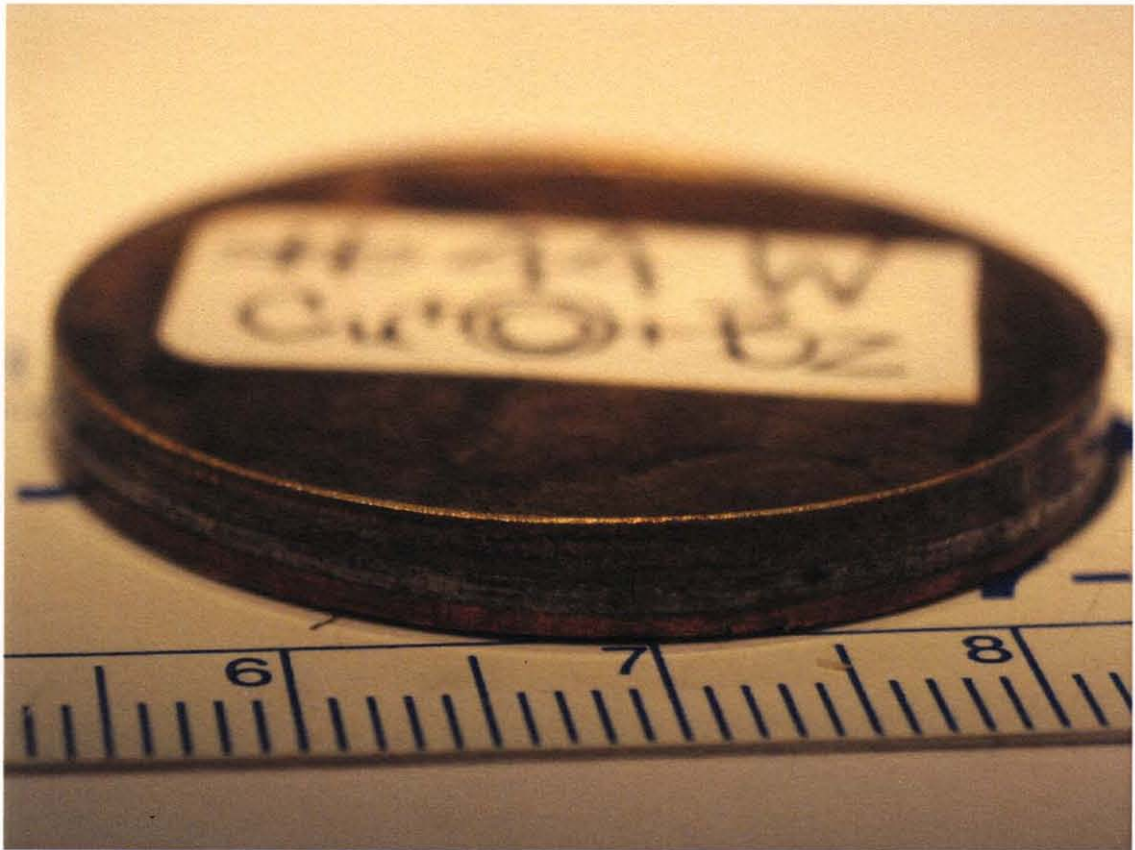


Figure 10.11 General view of copper and brass plates, welded by the water projectile impact at the water velocity 750 m/sec (Exp. 44, Table 10.1).

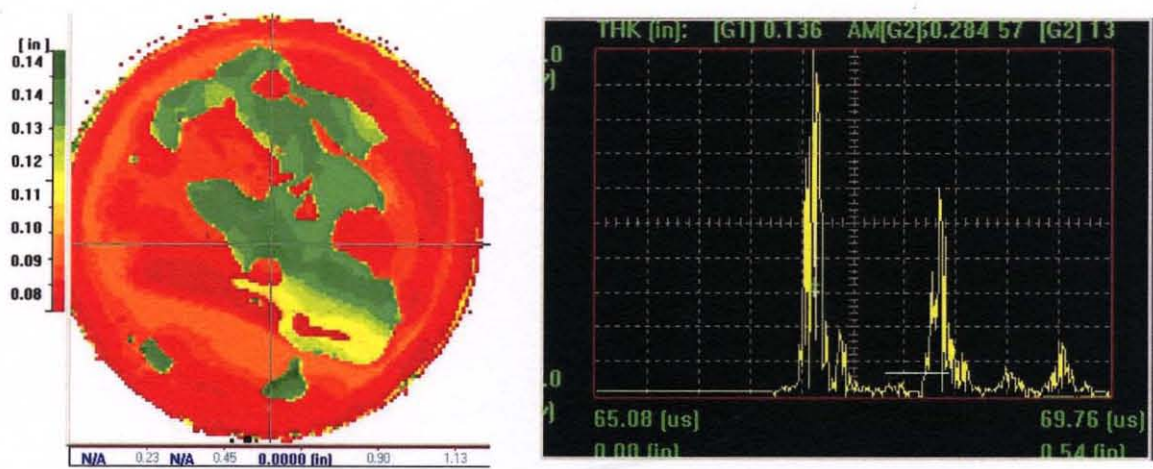


Figure 10.12 Ultrasonic verification of integrity of formed structure and metallurgical bonding of plates (Exp. 44, Table 10.1).

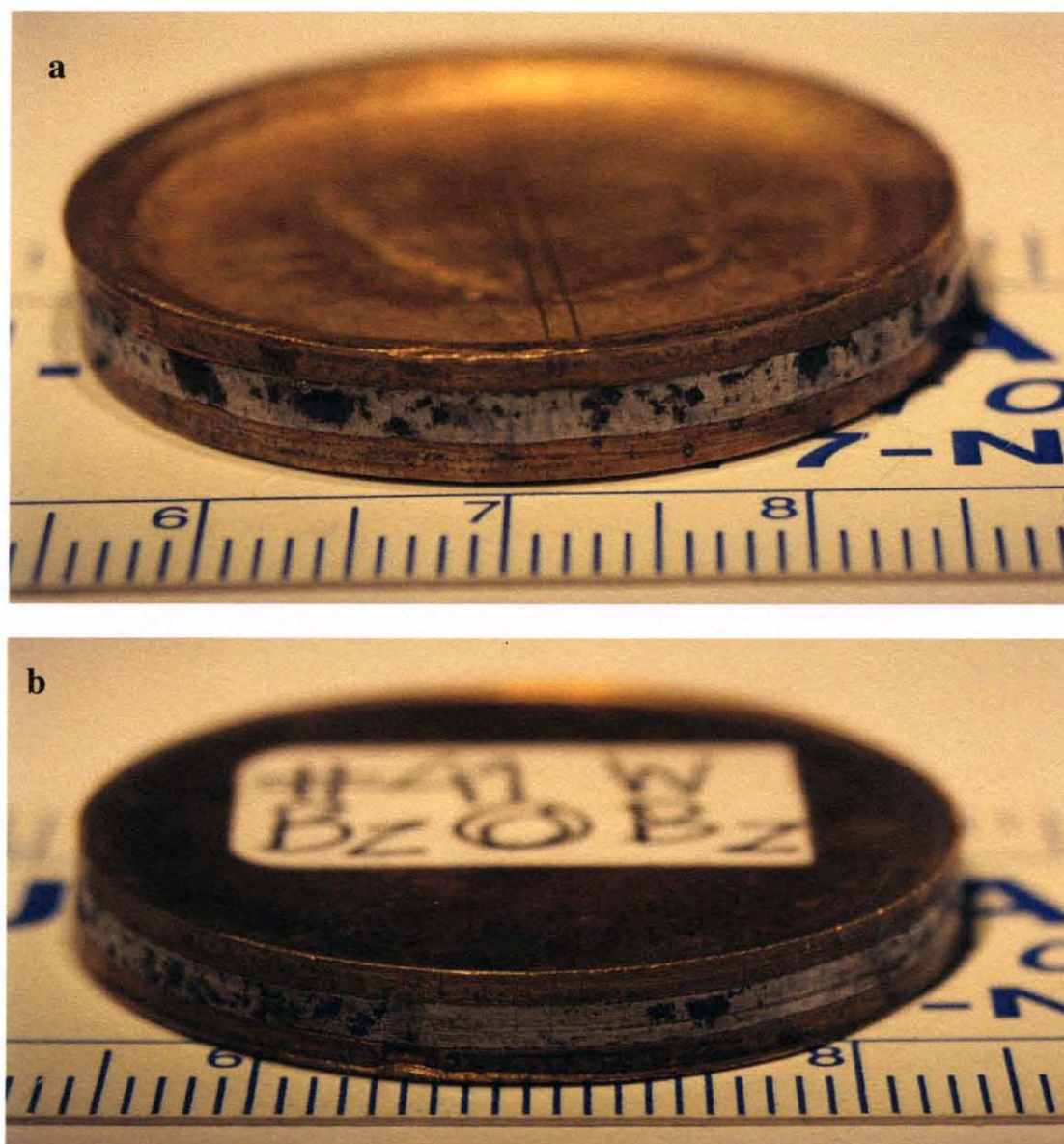


Figure 10.13 a) general view of impact side of two brass plates welded by the water projectile impact at the water velocity 750m/sec; b) back side view of same structure (Exp. 41, Table 10.1).

General view of two brass plates welded by the water projectile impact at the water velocity 750m/sec (Exp. 41, Table 10.1) is shown on Fig.10.13. Integrated structure was obtained including 2mm thick separation steel ring which is welded and locked between welded plates. Scanned sample of ultrasonic verification of integrity of formed structure and metallurgical bonding of plates is shown of Figure 10.14.

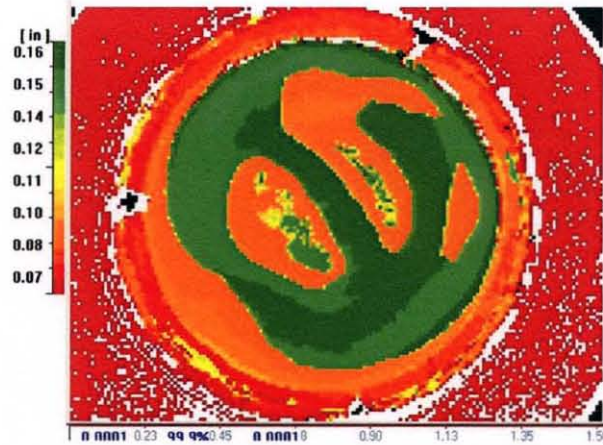


Figure 10.14 Ultrasonic verification of integrity of formed structure and metallurgical bonding of two brass plates (Exp. 41, Table 10.1).

General view of copper and steel plates welded by the water projectile impact at the water velocity 750m/sec (Exp. 41, Table 10.1) is shown on Fig.10.15. Integrated structure was obtained including 1mm thick separation steel ring which is welded and locked between welded plates. Scanned sample of ultrasonic verification of integrity of formed structure and metallurgical bonding of plates is shown of Figure 10.16.

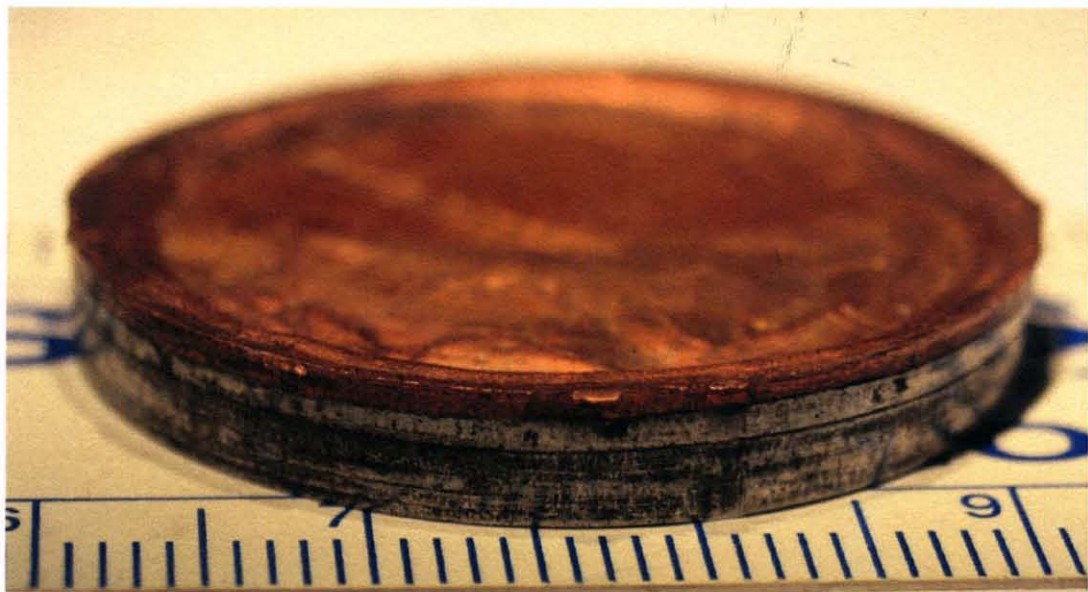


Figure 10.15 General view of copper and steel plates welded by the water projectile impact at the water velocity 750m/sec (Exp. 43, Table 10.1).

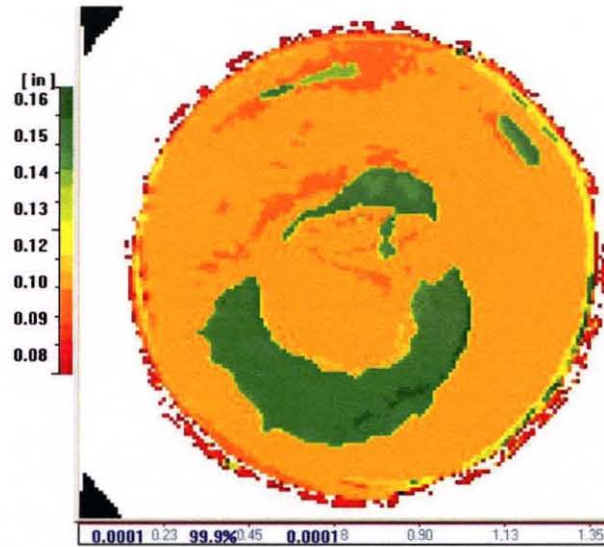


Figure 10.16 Ultrasonic verification of integrity of formed structure and metallurgical bonding of copper and steel plates (Exp. 43, Table 10.1).

General view of two steel plates welded by the water projectile impact at the water velocity 750m/sec (Exp. 42, Table 10.1) is shown on Fig.10.17. Integrated structure was obtained including 1mm thick separation steel ring which is welded and locked between welded plates. Figure 10.18 shows ultrasonic scan of welded steel plates.



Figure 10.17 General view of two steel plates welded by the water projectile impact at the water velocity 750m/sec (Exp. 42, Table 10.1).

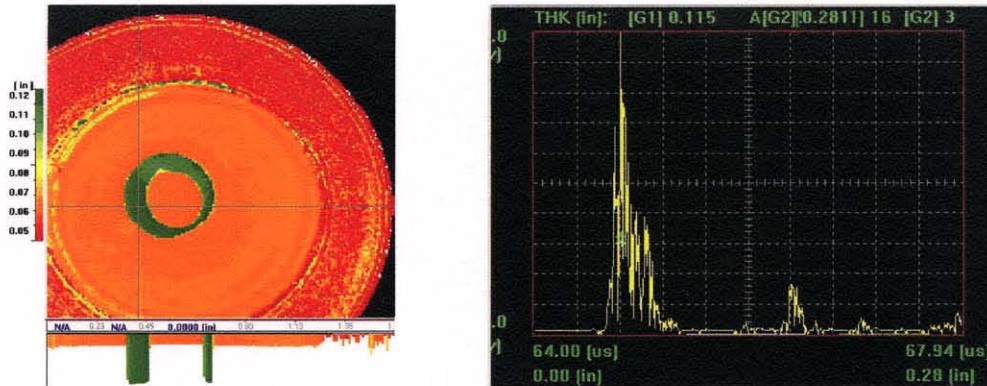


Figure 10.18 Ultrasonic verification of integrity of formed structure and metallurgical bonding of two steel plates (Exp. 42, Table 10.1).

General view of brass and steel plates welded by the water projectile impact at the water velocity 750m/sec (Exp. 45, Table 10.1) is shown on Fig.10.19. Setup with acceleration mode (2mm thick separation steel ring) was used to obtain integrated structure. Separation steel ring is welded to the steel plate as well. Scanned sample of ultrasonic verification of integrity of formed structure and metallurgical bonding of plates is shown of Fig. 10.20.

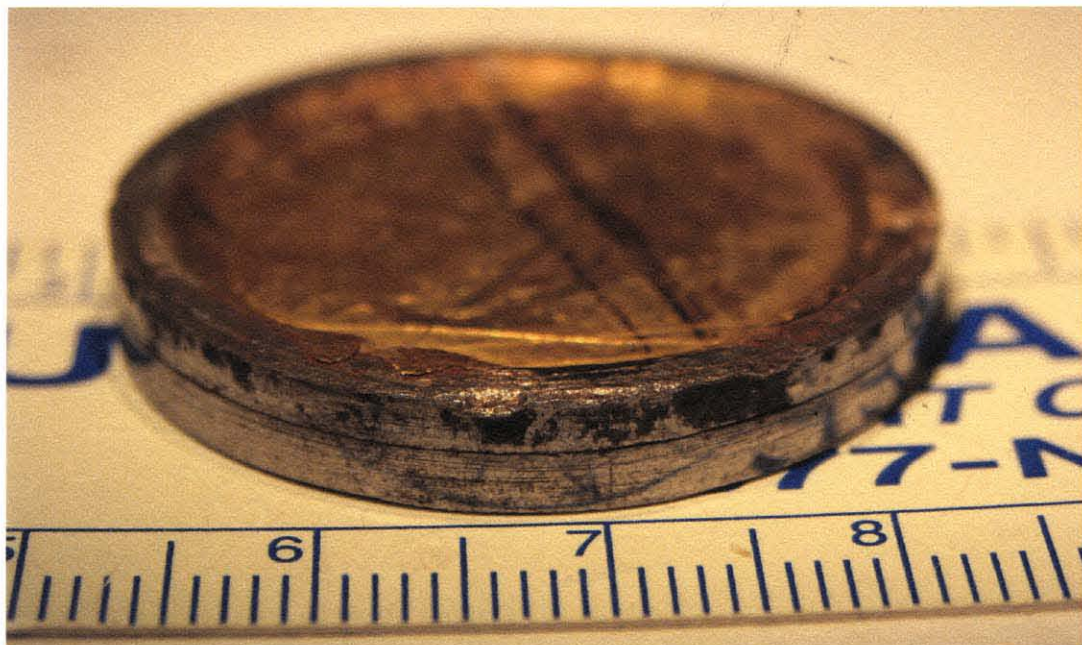


Figure 10.19 General view of brass and steel plates welded by the water projectile impact at the water velocity 750m/sec (Exp. 45, Table 10.1).

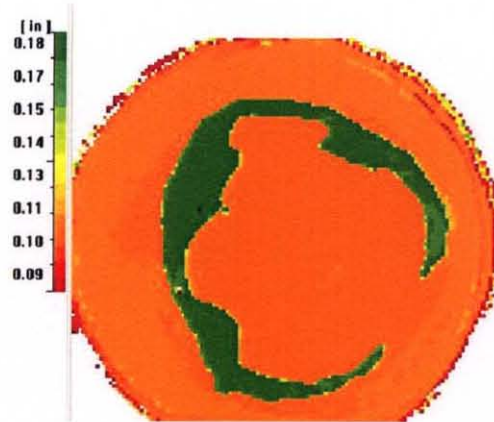


Figure 10.20 Ultrasonic verification of integrity of formed structure and metallurgical bonding of two brass and steel plates (Exp. 45, Table 10.1).

General view of two copper plates welded by the water projectile impact at the water velocity 750m/sec (Exp. 45, Table 10.1) is shown on Fig. 10.21. Excellent weld was obtained.

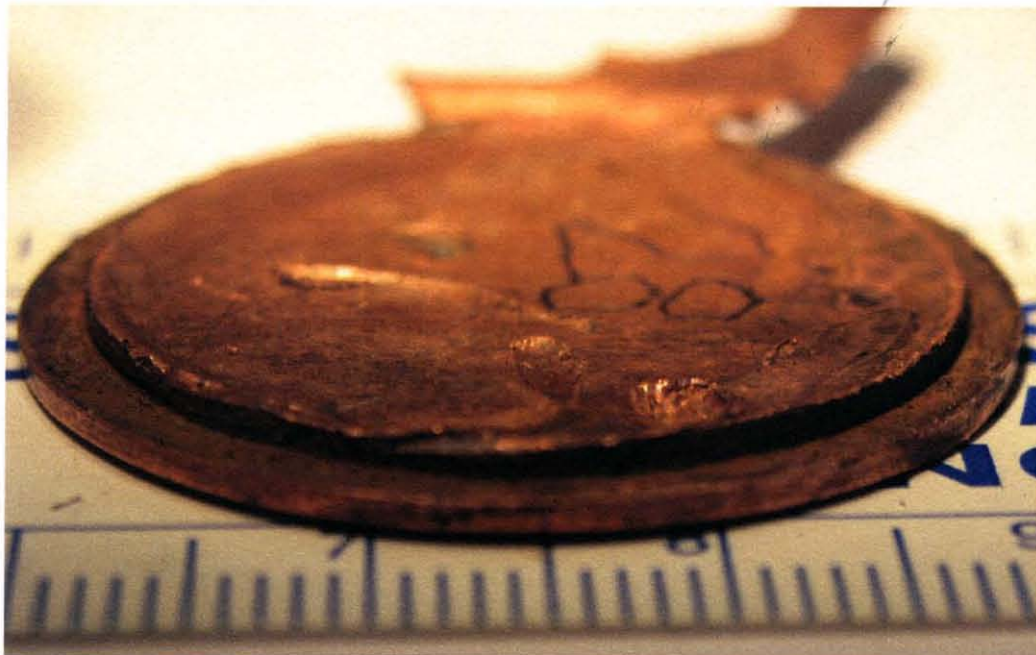


Figure 10.21 General view of two copper plates welded by the water projectile impact at the water velocity 750m/sec (Exp.28, Table 10.1).

All experiments were conducted using incidence impact angle of 90 degrees except experiments 12-16, which were performed without aiming device since the aiming device was destroyed during experiment 13. It is observed that incidence impact angle of 90 degrees gives best results but welding takes place at angles smaller than 90 degrees as well. For example Fig. 10.22 shows warped but well welded nickel-alloy coin and a steel plate joined in experiment 14. In this experiment shot was performed without aiming device which resulted with projectile incidence angle much different from 90 degree.



Figure 10.22 General view of nickel alloy coin and steel plate welded by the water projectile impact at the water velocity 750m/sec (Exp.14, Table 10.1).

10.5 Discussion of Results

In this study I explored original and novel idea to weld similar and dissimilar metals by high speed water projectiles. As high energy carriers water projectiles can introduce high energy flow into the impacted media and when this energy is sized properly changes

induced within impacted materials results in variety of materials processing techniques. Like materials processing techniques, already described in previous chapters welding carries high potential to contribute qualitatively and competitively versus conventional means of materials welding. Unlike similar conventional welding such as explosive welding which needs separation distance between items to be welded, water projectiles can conduct welding without and with the separation distance. Besides that, samples welded during this study were not subjected to special preparation (cleaning, polishing) which is necessary for explosive welding. Industrial needs for consecutive stitch welding when large plates does not need to be joined in a continuous weld seam fashion can be met by water projectile stitch weld processing.

This investigation demonstrated excellent degree of success, namely out of 20 experiments only one was not successful. It is observed that distance between joining items can play a role but being that several of investigated process variables can be controlled, welding can be conducted within a range of setup parameters. Namely besides of mass of water projectile, energy input (mass of gun powder) and standoff distance affect the result with equal importance. Reaction impulse of impact force was calculated based on the displacement of ballistic pendulum. Reaction impulse ranged between 169 and 466.3kgm/s. It is observed that acceleration of one of joining plates enhances conditions favoring welding process. For example two copper plates were not welded using no acceleration setup at reaction impulse of 237.69kgm/s while same combination was well welded with 1mm separation ring between at significantly lower reaction impulse of 169kgm/s. In the case of unsuccessful weld slight melting of meant to join surfaces is observed which shows that degree of melted interface plays vital role in the

welding process. Also, mechanical separation of several welds revealed evidence of melted layers on each of welded samples. It is confirmed that melting of extremely thin layers at the joining interface takes place which results in metallurgical weld of joined metals. Duration of the process is of order of microseconds during which micro-diffusion may take place as well and therefore may be contributing as a welding mechanism as well.

During this investigation it is observed that mechanical properties and thicknesses of joining materials require optimal selection of process variables in order to achieve successful welding. Duration of metal exposure to water projectile impact influences the end result therefore control of projectile velocity and optimal sizing of projectile mass resulted in range of well welded materials combinations. The best results had been achieved at 90 degrees incidence impact angle but it is observed that projectiles carry sufficient energy to conduct welding of metals at angles smaller than 90 degrees. Previously gained experience during investigation of other material processing techniques played important role in high success degree of welding study, which resulted in appropriate setup selection for variety of similar and dissimilar metals welding tasks.

Feasibility of novel technology was validated which is that similar and dissimilar metals can be welded by high speed water projectiles impact. Metallurgical bonding was confirmed for all of tested combinations of metals.

10.6 Conclusions

The performed experimental study demonstrated feasibility of the use of water projectile impact for similar and dissimilar metal welding. Welding of ten metal combinations was demonstrated. Metallurgical bonding was confirmed for each of these combinations. Projectile impact reaction impulse was determined in each experiment. Two welding modes were examined: without acceleration and with acceleration of one of joining plates. Welding was successful in both modes but it was determined that welding can be conceived at substantially lower impulse (impact force) when performed with acceleration of one of joining plates. Welding of large metal plates can be effectively performed by generation of weld-stitch seams by use of consecutive water projectile impacts. Feasibility of development of novel manufacturing technologies was demonstrated.

CHAPTER 11

INVESTIGATION OF GRANITE BORING USING HIGH SPEED LIQUID PROJECTILES

11.1 Introduction

Application of high energy water streams for fracturing brittle materials in mining and construction was studied in a number of works. The previous studies [34, 35] indicated that the high speed projectiles have a potential of becoming a tool for boring brittle materials, e.g. a rock layer. The development of a launcher for generation of these projectiles constitutes a mission of the proposed study. The immediate objective of this study was to estimate the energy required for granite crushing and to evaluate the effectiveness of the use of the launchers as a part of a rock boring system.

Bench scale launcher prototypes and setups for fastening the launchers and granite targets were designed and constructed. While the design of the launcher used for the performed experiments was determined by the available resources rather than by the optimization conditions, the boring of granite was successfully attained. A sequence of the projectiles impacting a granite target crashed it and converted into rubble which then can be removed by the water stream from the impact zone. This will assure the advance of a boring head and its penetration through a layer of a brittle material.

The projectiles were generated by powder combustion which expels a water load through a nozzle. The pressure of the combustion products and the geometry of the launcher assured desired acceleration of the projectile. The material fracturing by the projectile depends on the stress waves generated in the target as well as on the change of the properties of the target material due to high hydrostatic pressure developed in the

impact zone. Both, the stress waves and hydrostatic pressure are determined by the momentum density that is projectile velocity and cross section area. This study, however, was carried out at a nozzle exit diameter of 2mm. Thus the variation of the area of impact was limited and the impact conditions were practically determined by the projectile momentum. At this study water was used as a working fluid and commercially available gunpowder provided the necessary energy.

While the exit nozzle diameter in all performed experiments was constant, the process variables included the mass of water (working fluid) and powder (energetic fluid), standoff distance, target material and, finally, the distribution of a multiple impacts on the target surface. The amount of the energy used was estimated by the heating value of the powder charge. High speed filming was employed to estimate the variation of the projectiles velocity between the nozzle exit and the target surface. Because no comprehensive parametric study of the process was carried out, the determined energy and media consumptions constitute a lower estimate of the process requirements.

Previously a number of experiments involving concrete demolition, metal piercing and forging were carried out [6, 11 and 13]. It was demonstrated that at the speed of 1500-1750m/s a single water projectile having the mass of 350-400g readily demolishes a concrete plate 16" thick and a reinforced concrete plate 30cm thick. When a concrete plate was protected by a steel sheet the projectile pierced the steel and broke through the concrete. The water projectiles also successfully forged and pierced steel and other metals. At a lower speed the impact did not result in the concrete demolition. However, the damage accumulation in the course of several impacts brought about concrete fracturing.

While effective granite demolition was achieved at the water speed of 1000m/s, the process could be significantly improved if the projectile speed is increased up to 4-5 km/s. The performed computations showed that this speed could be attained as the result of process optimization.

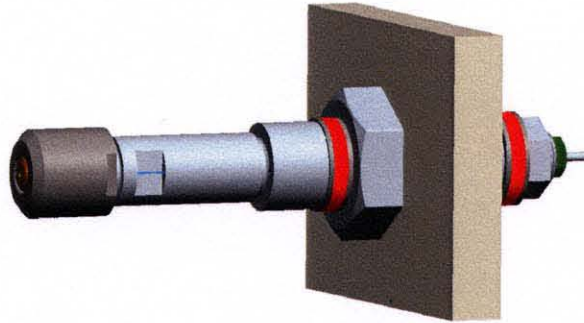


Figure 11.1 Launcher of high-speed water projectile.

11.2 Experimental Procedure

The experimental technique involved impacting of a granite half-space by a sequence of water projectiles and subsequent examination of the generated cavities and debris. It also included the use of high-speed imaging technique for estimation of the projectile velocity. The nozzle diameter was 2mm and the estimated projectile speed changed in the range of 1000-1050m/s. The amount of a powder charge was fixed within tolerances of commercial factory-loaded blanks. Accuracy of water load mass was assured by loading with a syringe. Prior to firing the standoff distance and the position of the impact zone were determined. The shots resulted in formation of holes in a granite plate. In the most cases, when it was possible, the volume and the geometry of the generated cavities were measured. The volume, which determined the amount of the granite removed, was

measured by filling the cavity by water and subsequent water extraction by the syringes. Because of water absorption by and penetration through the cavity wall the measured water volume, that is amount of the granite removed, were below the actual value. An error of such estimation will be determined later. The geometry of the cavity was estimated by the cavity depth and the dimensions of the surface area. This area was approximated by a circle or an ellipsis.

The initial phase of the work involved design and construction of a medium launcher followed by launcher integration in a setup for granite demolition. The launchers (Fig. 11.1) having the exit nozzle diameter of 2mm were used. The maximal water load of this launcher was 8g. The attempt to load 8.5g water resulted in powder wetting. Of course, any reduction of the water load below 8g was trivial. The 0.38caliber Winchester rounds were used in the performed experiments. The powder load of a round, equal to 1.2g was the energy source of the process.



Figure 11.2 Modified Remington Power Tool.

Because the powder mass that is the energy consumption per a shot, in the launcher above was constant, another launcher (Fig. 11.2) was used to investigate the effect of the energy change. This launcher constituted a modified Remington power tool

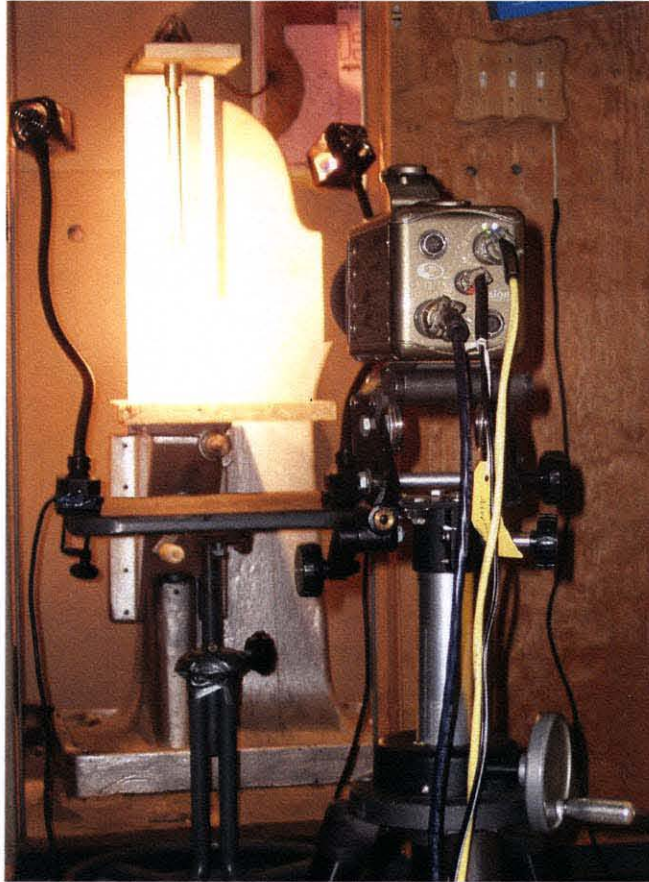


Figure 11.3 Experimental setup for investigation of high-speed liquid projectiles.

and was used in the previous study of the projectile formation, performed by NJIT Waterjet laboratory. It is important to notice, that while the launcher Fig. 11.1 used the combustion products as a driving media, in the launcher Fig. 11.2 the water load was driven by a moving piston. The difference of the water acceleration mechanisms had limited effect on the projectile properties which were completely determined by the boundary conditions and the channel geometry.

During the experiments the launcher was held by a special vice while the granite plate was supported by a moveable base. The position of the base determining the standoff distance was precisely controlled (Fig. 11.3). The experiments were carried out in an isolated cabin equipped by a continuously operating exhaust.

11.3 Experimental Results

11.3.1 Investigation of the Effect of the Standoff Distance on the Granite Excavation

(Figs 11.4-11.6)

The objective of the experiment was to determine an available range as well as an efficient value of the standoff distance. In the course of this experiment a granite plate was impacted by a water projectile at different SODs. The resulted volume of material removed and the size of the generated pit were measured. The experiments were carried out at the identical conditions (1.2g of powder, 8g of water, and the same kind of granite).

In the course of this experiment it was found that at SOD less than 150mm the excavation rate of 1cm^3 was exceeded almost in all cases (Fig. 11.4). A noticeable material removal occurred up to the SOD of 266mm. This was the maximal SOD attainable in the given experimental setup (Fig. 11.3). Because the most stable material removal was achieved at SOD=6mm, this SOD was used in the most of the following experiments.

The enhanced granite removal ($v > 10\text{cm}^3$) occurred in 3 cases (Fig. 11.5), while the weak ($v < 1\text{cm}^3$) material excavation took place in 8 cases (Fig. 11.6). The observed process performance in both cases was similar thus it can be expected that the difference in material removal was due to the peculiarities of the granite structure. The conditions

which assure enhanced and prevent weak projectile performance will be determined in the following study.

11.3.2 Investigation of the Effect of a Water Load on the Material Removal

The objective of this experiment was to estimate a near optimal value of the water load. The performed experiments showed the steady increase of the absolute and specific rates of the material removal, as the water load increased (Figs 11.7 and 11.8). Because at the selected launcher design the water load was limited to 8g, this amount of water was used in the following experiments. It is expected that increase of the water load will increase the boring rate.

11.3.3 Investigation of the Granite Boring: Same Site Impact (Figs 11.9-11.11)

The objective of this experiment was to estimate the superposition of the sequential impacts. Experiment 3 involved investigation of the dynamics of the granite removal at impacting a same site of the target. In the course of the experiment the mass of powder was 1.2g per a round and the water mass was 8g per shot. The results of the experiments are shown on Figs 11.9 and 11.10. As it is demonstrated by these figures both the depth of the penetration and the rate of the excavation rapidly decrease as the depth of the cavity increases. The acquired information is not sufficient for the explanation of the cause of this decrease, which will be explained in the course of the further study.

11.3.4 Investigation of the Granite Boring (Figs. 11.12, 11.13)

The objective of this experiment was to demonstrate feasibility of generation of a channel of a desired length and 2.5" in diameter. A sequence of projectiles impacted the surface of a granite plate. These impacts enabled us to remove the first layer of the granite. The following second, third, etc. layers were removed similarly. It was possible to measure

amount of granite removal only for first 26 shots. The rate of removal was around 1 cm^3 per shot. While the objective of boring was to create a cylindrical channel and the granite removal had to be limited to the area within the channel boundary, a significant amount of granite was removed from the regions outside of this channel. This unwanted excavation could be prevented by the proper nozzle positioning in a boring head. In the final analysis this experiment demonstrated feasibility of the boring a 2.5" channel by the projectiles generated by a 2mm nozzle.

11.3.5. Investigation of the Granite Boring Using Distributed Impacts

(Figs. 11.14-11.17)

The objective of this experiment was to investigate enhancement of the granite removal due to superposition of the effects of two or more neighboring impacts. In the course of this experiment a target was impacted by several projectiles at different locations and at a different sequence. The impact sites were distributed as a Cross, Line and Triangle. Each site was impacted once or twice.

It was found that two consecutive neighboring impacts were more efficient than consecutive shooting at the same site. No choking effect (decrease of the rate of removal as the depth of a cavity increases), noticed for the impacts of a same spot was observed in this experiment. Further enhancement of the material removal was recorded when three spots arranged in the equilateral formation were consecutively impacted. In this case only two first shots at one corner of the triangle resulted in the penetration at the depth of 38.71mm. The enhancement was evident in the volume increase as well. Consecutive impacts of neighboring spots increased efficiency of excavation. It was noticed that first four shots removed about 8 cm^3 of granite. However, as the depth of excavation increases

the average granite removal becomes 1 cm^3 per shot. The overall result can be enhanced further by optimization of standoff distance and by optimal positioning of the nozzle.

11.3.6 Investigation of the Effect of the Stresses Induced on a Granite Target

(Fig. 11.18)

In the course of this experiment granite plate was exposed to compressive stresses induced by four vices (Fig. 11.18). As a result the rate of material removal of 2.6 cm^3 per shot was attained. Thus effectiveness of the granite boring under stresses was demonstrated.

11.3.7 Investigation of the Granite Removal Using a Low Power Projectile

Because the safety consideration precluded change of powder load in the course of these experiments, another launcher (a modified Remington power tool) was used for granite removal. The powder charge in this case was 0.3g and the water load was 4.2g. The specific rate of granite removal in one of experiments was 2 cm^3 per 1g of powder. This result exceeded in two times the specific rate of removal (1 cm^3 per 1g of powder) at a larger charge. While in former the water-to-powder ratio was $4.2/0.3=14 \text{ g/g}$ in the later this ratio was $8.0/1.2=6.67 \text{ g/g}$. While the increase of the impact effectiveness can be at least partially determined by the powder properties, the effectiveness of the optimization of the energy-to-working fluid mass ratio (the specific energy of the process) was demonstrated.

11.3.8 Investigation of marble removal by a water projectile (Fig. 11.19)

In order to examine the boring other than granite materials a marble plate was impacted by high speed liquid projectiles generated by the Remington power tool. The performed

experiments showed that due to marble ductility the rate of the marble removal was almost two times less than that of the granite.

11.3.9 Investigation of Size Distribution of the Granite Particles Generated in the Course of a Single Shot

The debris generated in the course of an impact was collected. The observed distribution of the particles size shows the feasibility of the debris excavation from the impact site.

11.3.10 High speed Filming of the Projectile Motion (Fig. 11.20)

A high speed camera Phantom V-7 of Vision Research Incorporated (30,000 frame/s and 150,000 frame/s) was used to acquire digital images of projectiles (Fig. 11.20). The observed speed of the projectile head was 539m/s immediately after leaving the nozzle. Then the speed of the projectile head increased to 865m/s at 14cm away from the nozzle and reached 1065m/s at the impact zone. The variation of the velocity of the head of projectile was similar for both launchers. However, high removal rate for the launcher Fig 12.20 shows that the average velocity (momentum) of its projectiles is higher.

11.4 Evaluation of the Feasibility of the Use of a Launcher as a Boring Tool

Let us assume that it is required to bore a granite layer and to generate a tunnel having the diameter of 2.5" and length of 1m. Total volume of the granite to be removed is:

$$100 \times 3.14 \times 7^2 / 4 \sim 4000 \text{ cm}^3.$$

In the course of the performed experiments it was found that in order to remove 1 cm³ of granite it is necessary to spend 1.2g of a powder and 8g of water. Thus removal of 1cm³ of the granite required 10g of fluids. If the media consumption during the operation will be the same as during the experiments then the total required amount of the media is: 4000*10=40,000g =40kg of the media.

Let us now estimate the required process duration. Because 1 shot brings about removal of 1cm^3 of granite, removal of 4000cm^3 will be accomplished by 4000 shots. Thus the launcher should fire 4000shots. A numerical modeling of the launcher operation shows that the duration of the explosion/expulsion process required 1-2 milliseconds (Fig. 11.21). Thus the process can be carried out at the firing rate of $1/0.002=500\text{shot/sec}=30,000\text{shot/min}$.

It is necessary now to estimate feasibility of the launcher operation at such firing rate. An internal combustion engine can operate at a rate of 10,000 combustion cycles per minute. Because the only moving part of a launcher is a check valve it can be assumed that such frequency is also attainable by a launcher. Thus it is assumed that the operational firing rate will be 10,000shots/min rather than 30,000shots/min. At the selected frequency the duration of the firing 4000shots that is the process duration is $4000\text{shots}/10,000\text{shots/min}=0.40\text{min}$.

Thus, the estimated duration of the excavation will be below 1 min. However, the actual weight of the required working and energetic fluids as well as the process duration could be below these estimations. Even in the course of the performed experiments it was found that the rate of the removal can be as high as 10cm^3 per 1g of media (Fig. 11.22). It is 10 times more than mass removed used for the above estimation. Then, the high frequency movie shows that the speed of a projectile at the impact zone was 1000m/s. The projectile speed of 1750m/ was already attained in the course of the previous experiments. A numerical analysis (Fig.11.21) shows that the speed of the projectile can be as high as 5-6km/s. It is expected that the optimization of the launcher operation will enable us to accelerate the projectiles to the speed of 3000m/s. Thus the kinetic energy of

the impact and, correspondingly, the rate of granite removal, will be at least 10 times more than that observed in the performed experiments. Consequently, optimization of the conditions of the projectile formation as well as the projectile-workpiece interaction at least theoretically enables us to increase the specific material excavation. Thus the estimated weight of the media (40kg) and the process duration (1min) are realistic.

11.5 Conclusions

1. The feasibility of the granite crushing by high speed (1000m/s) water projectiles was demonstrated.
2. The feasibility of formation of a channel 100m*2.5” during 40min or less using about 5000kg of the working media was shown.
3. The generated debris is suitable for excavation
4. The effective crashing occurs up to the standoff of 75 nozzle diameters (150mm at the nozzle diameter of 2mm).
5. The induced stresses and previous damage significantly enhance granite excavation.
6. The following issues should be additionally addressed:
 - 6 a. The existing launcher design which resembles the design of a rifle is not suitable for the desired boring operation. The launcher should generate pulse stream, where the amplitude of each pulse (the maximal speed of a projectile) should be in order 2-4km/s.
 - 6 b. Currently, a launcher operates as a rifle using a round as a source of working and energetic fluids. Such mode of operation is not suitable for high rate deep boring. The launcher should use only liquid media.

6 c. While the use of different working and energetic fluids is feasible it dramatically increases complexity and thus dramatically reduces reliability of the boring head. A single mixture of fluids or slurries must be supplied to the launcher.

6d. While a room temperature projectiles are suitable for crashing and pulverization of brittle materials they could not fracture ductile materials, e.g. steel bars. It is necessary to generate high temperature impact zone to enable us to excavate ductile materials.

11.6 Nomenclature

- m_c -mass of powder, g

-SOD-standoff distance, mm

- t -depth, mm

- v -removed volume, cm^3

- w -mass of a boring media (water), g

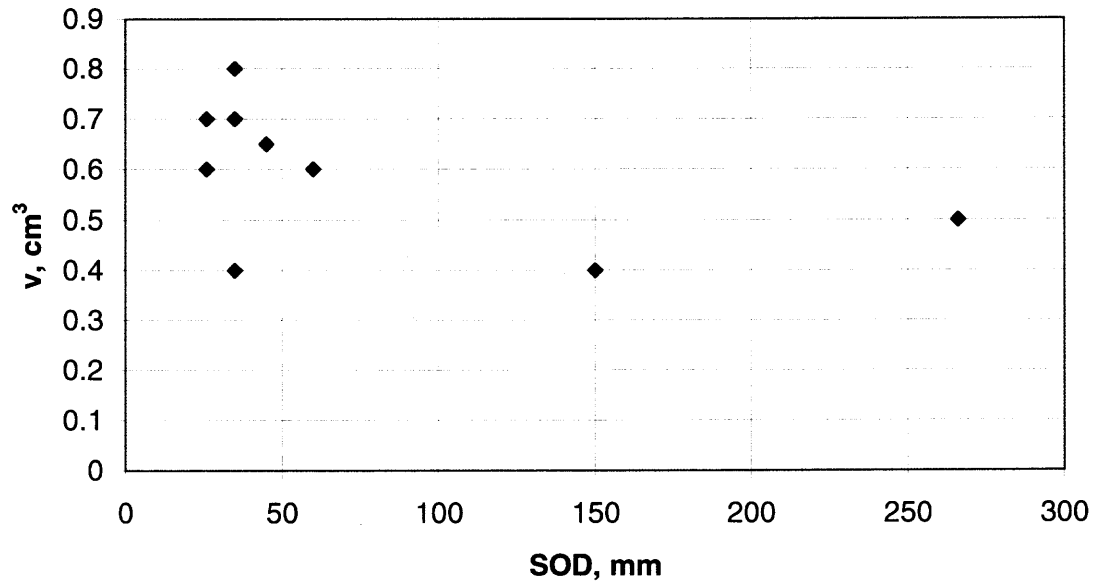


Figure 11.6 Effect of the standoff distance on the weak granite removal (Low removal rate).

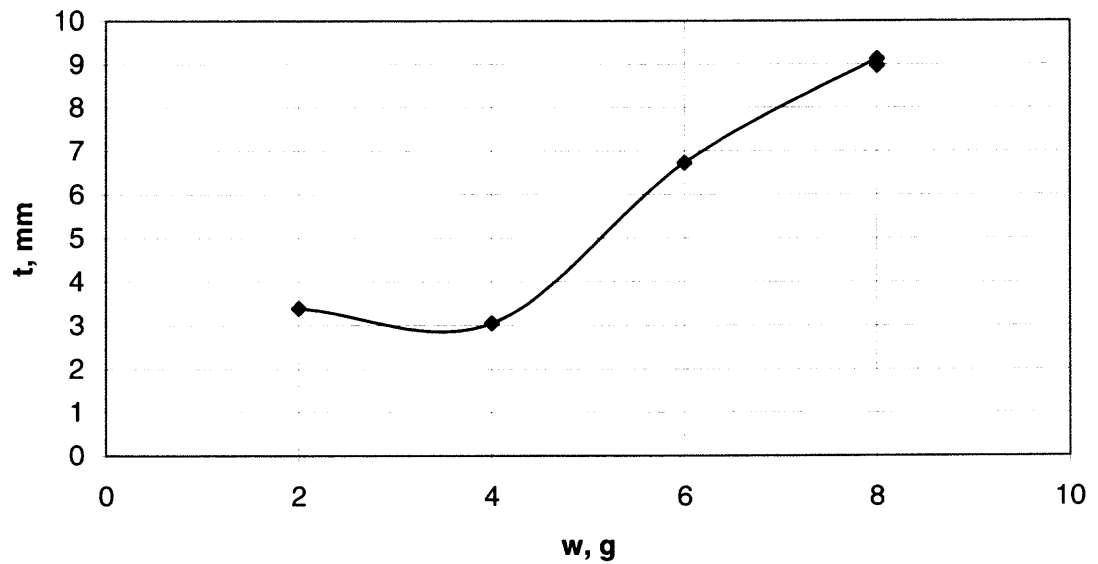


Figure 11.7 Effect of the water load on the depth of penetration.

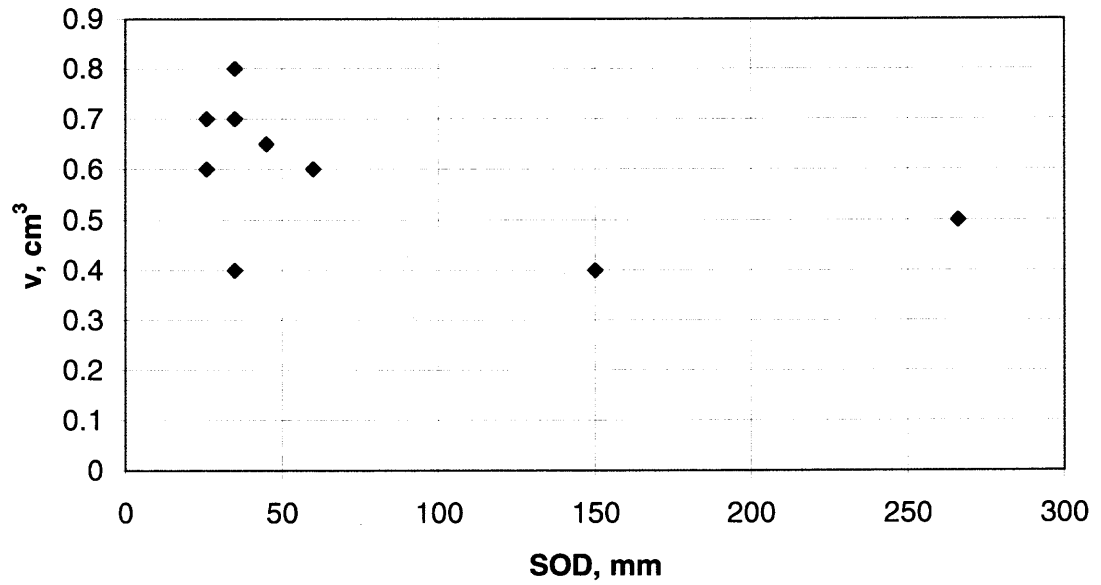


Figure 11.6 Effect of the standoff distance on the weak granite removal (Low removal rate).

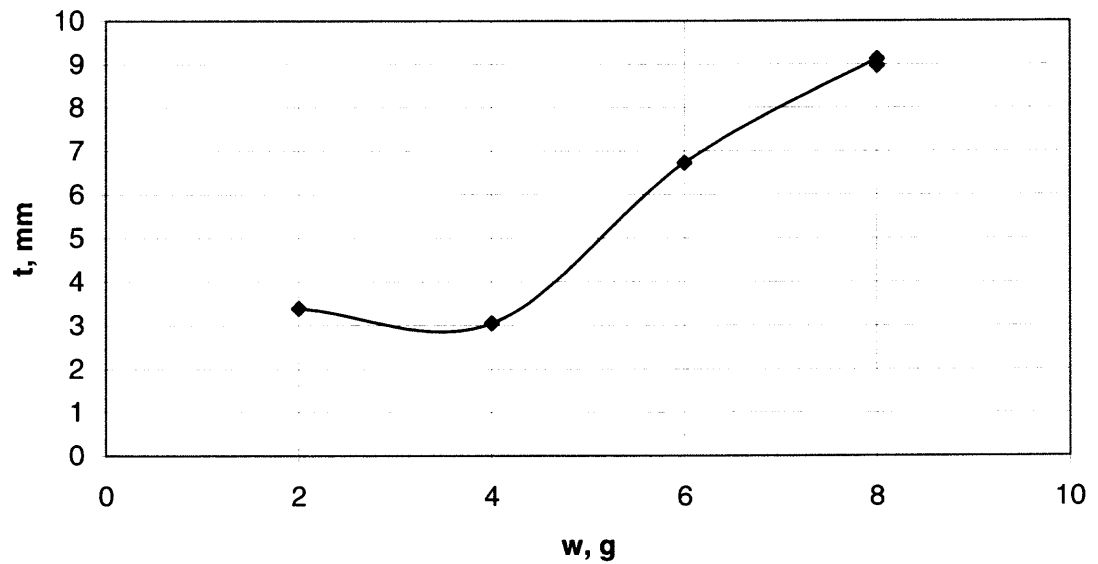


Figure 11.7 Effect of the water load on the depth of penetration.

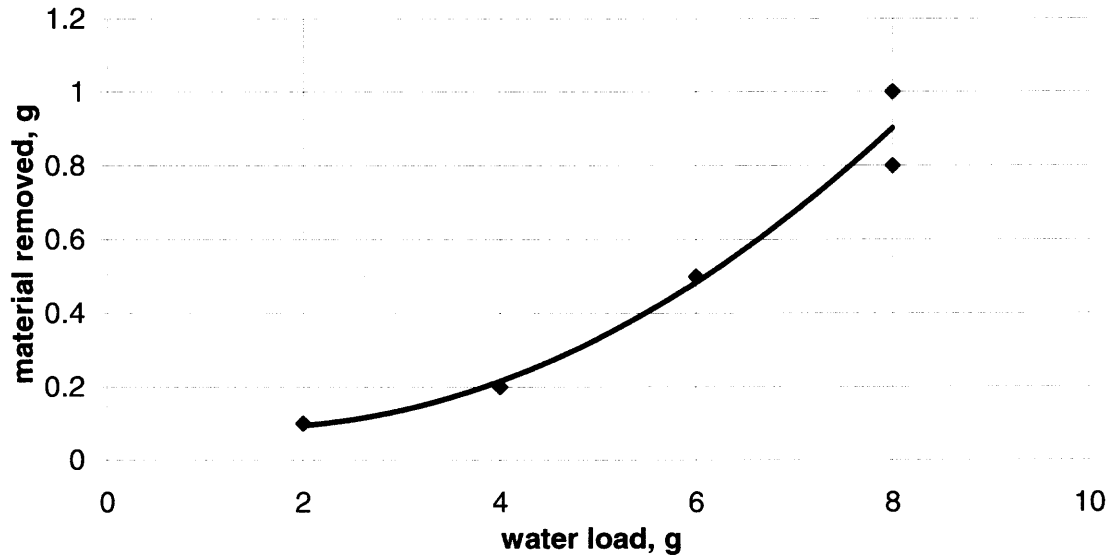


Figure 11.8 Effect of the water load on the granite removal.

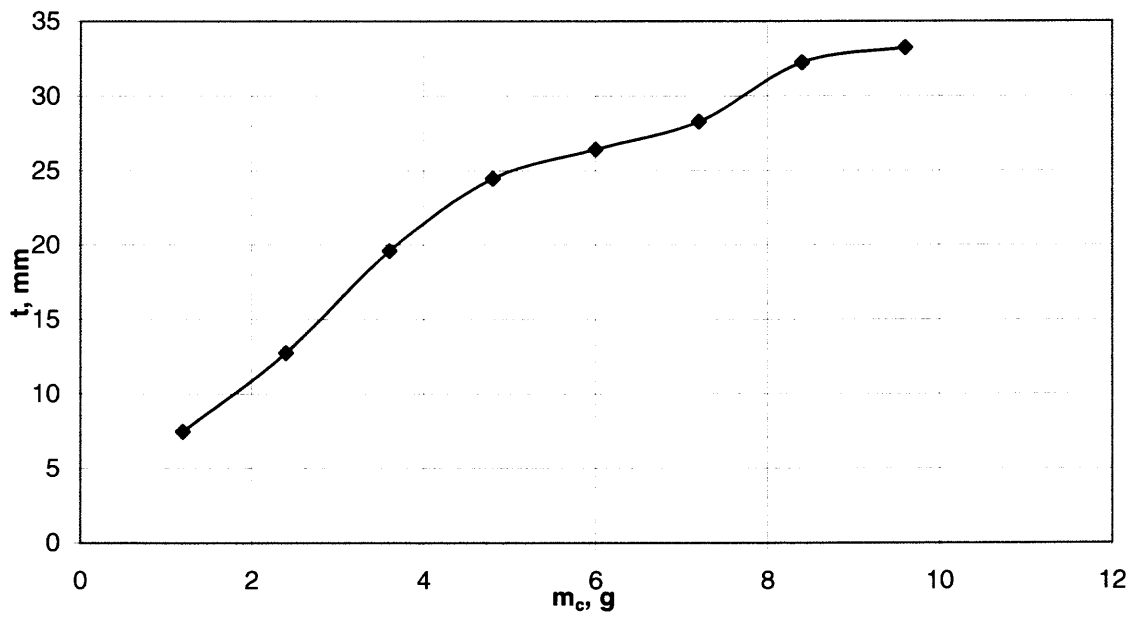


Figure 11.9 Effect of cumulative (total) powder consumption on the depth of penetration.

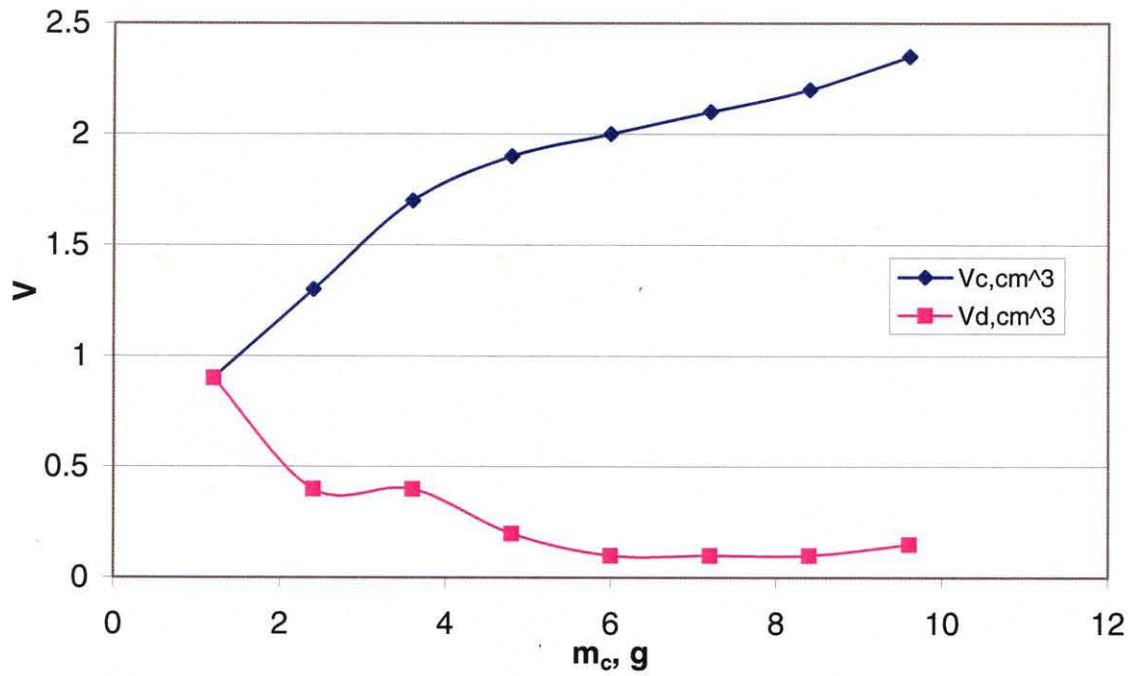


Figure 11.10 Effect of total (cumulative) powder consumption on the granite removal. Here V_c -total removal, V_d -granite removal per a shot.



Figure 11.11 Boring of a granite plate by sequential impacts of projectiles at the same site.



Figure 11.12 Boring of granite by 52 sequential impacts. Notice dimensions of the generated cavity.



Figure 11.13 Boring of granite by 52 sequential impacts.

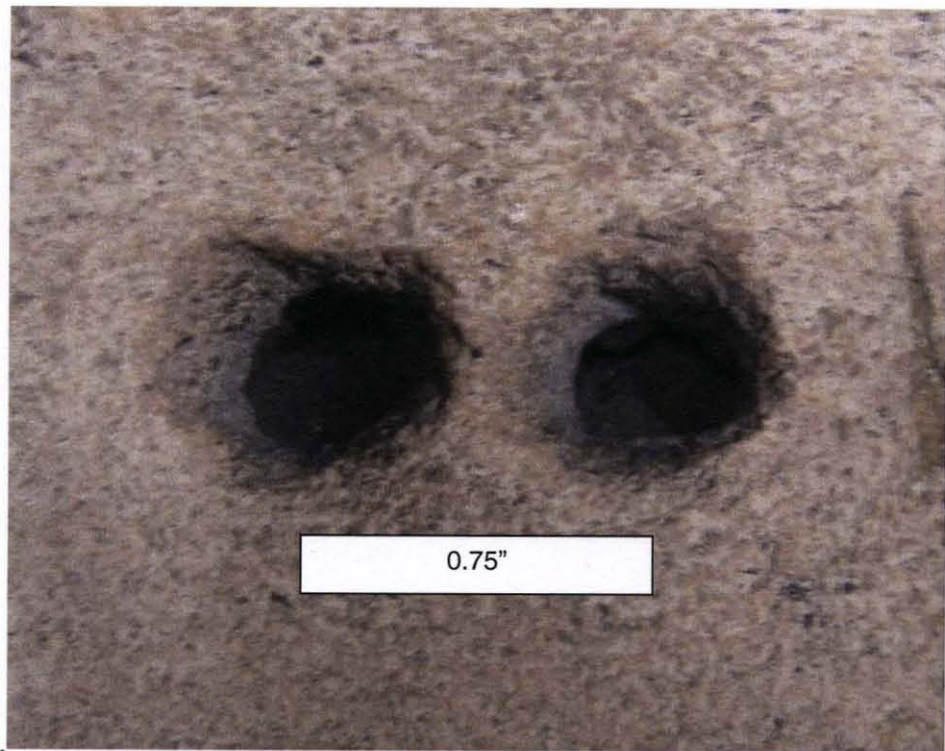


Figure 11.14 Two impacts with the distance of $\frac{3}{4}$ " between axes of the impact zone. Notice absence of interference.



Figure 11.15 Three impacts at the distance of $\frac{3}{4}$ " between axes of impact zones. Notice minimal interference.



Figure 11.16 Three impacts at the distance of $\frac{1}{2}$ " between axes of impact zones. Notice significant interference between two shots.



Figure 11.17 Boring of a granite plate by sequential impact with a cross-like pattern of impact distribution.



Figure 11.18 Setup for granite boring at induced compressive stresses.



Figure 11.19 Granite removal by impact of a projectile generated by low-power launcher.

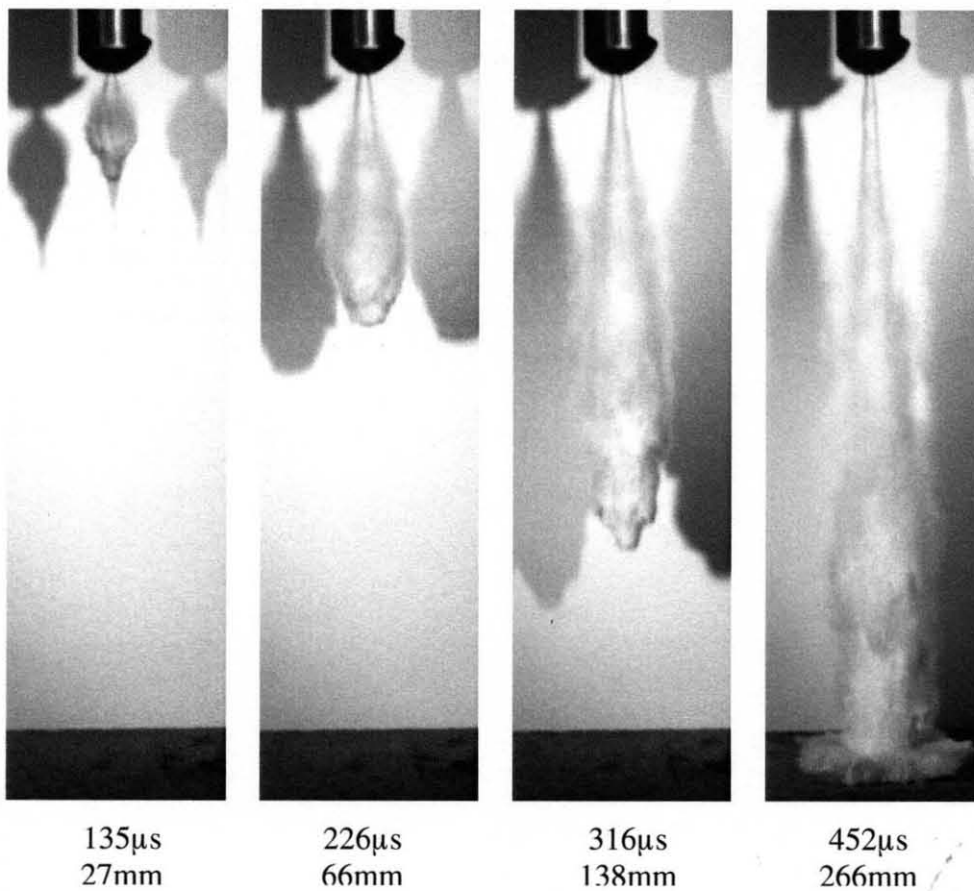


Figure 11.20 Development of a water projectile in air. The distance above is the distance from the exit of the nozzle.

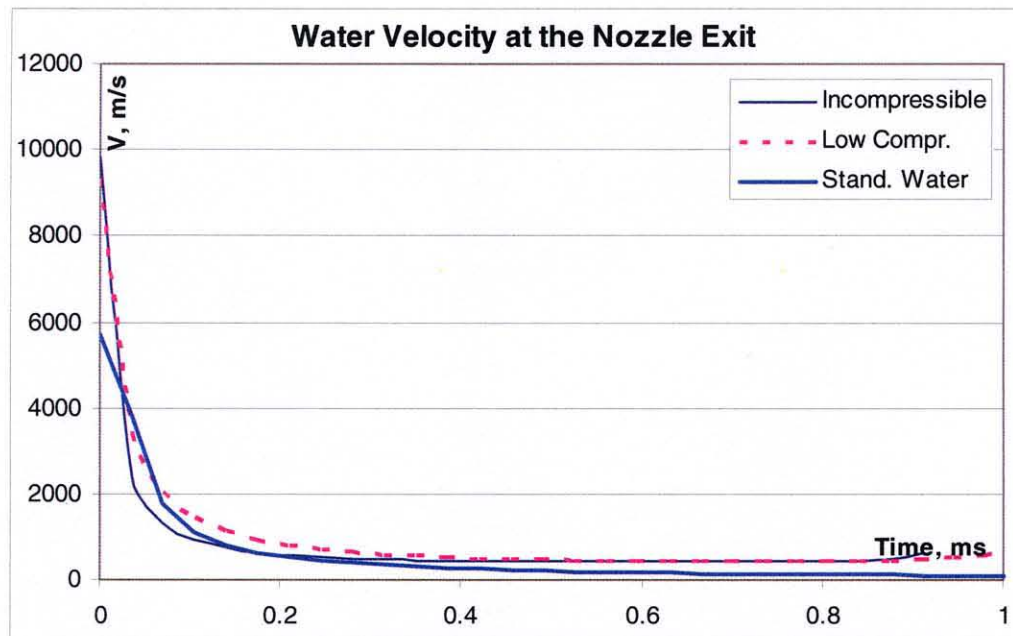


Figure 11.21 Numerical modeling of the variation of the water velocity at the launcher exit, Notice that the speed of the water at the head of the projectile was as high as 5,500m/s.

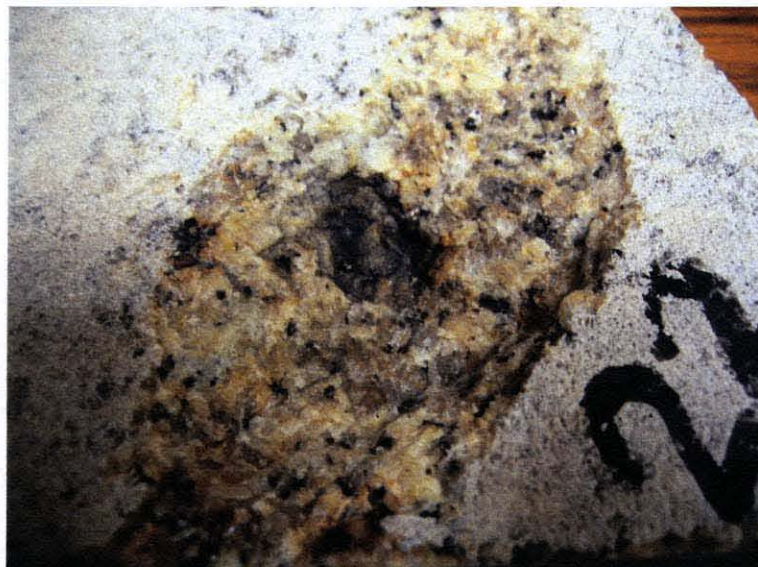


Figure 11.22 Impact of a granite plate at SOD=80mm. Notice intensive granite removal in the course of this impact.

CHAPTER 12

CONCLUSIONS

The experimental study of water projectiles generated by three types of water launchers resulted in development of new technology of materials processing by high speed water projectiles. Two patent applications for new technologies had been filed.

Namely, investigation of deformation, forming, micro-forming, and welding of ductile materials was carried out. Demolition and boring of brittle materials performed. Investigation of explosive set up neutralization and piercing of composite targets was performed as well. Modes and mechanisms of deformation of ductile and brittle materials were studied and explained. High plasticity, high rate of deformation, temperature at the impact zone, hardness and micro-hardness distribution and degree of deformation work for ductile materials were determined and materials behavior knowledge base needed for materials processing was acquired. Modes and mechanisms of failure of ductile, brittle and composite materials were studied. Fractography study revealed three mechanisms: ductile overload fracture, brittle fracture and combination of the two. Six failure modes: brittle fracture, radial fracture, ductile hole growth, plugging, fragmentation and petaling were identified.

Mechanisms of punching and forming of metals were identified and proposed. Welding of similar and dissimilar metals was conducted and high potential for novel stitch and spot welding formations was confirmed. Micro scale materials processing investigation involved range of studies. Submillimeter geometry scale forming of metals, fine stamping, micron scale forming and micron scale extrusion investigation were conducted and validation of novel technologies was achieved. Full scale characterization

on all levels of conducted materials processing was conducted and effect of high speed water projectile impact on mechanical properties of impacted materials was quantified and presented. Investigation of peculiarities of impact based micro-forming was conducted. The info acquired as result of investigation of geometry and topography of micro-forming processing. Accuracy of micro scale deformation was estimated, particularly it was shown that deviation of actual part from the die was at the acceptable level. Also was shown that size of generated parts was rather stable and roughness and waviness of the generated surfaces was in the acceptable range.

The foundation of knowledge base for liquid based forming, welding and demolition processes was developed and the process technology will be developed on the base of the acquired knowledge. Theory of impact based high rate material deformation was enhanced. The emerging industrial scale demolition, forming and welding technologies will utilize the acquired knowledge. Patent application based on work of this dissertation for novel material processing technology is being prepared.

REFERENCES

1. O. Petrenko, E. Geskin, B. Goldenberg, V. Samardzic, G. Atanov, A. Semko, A. Kovaliov, (2004), "Numerical Modeling of Formation of High-Speed Water Slugs". Transactions of ASME, Journal of Fluids Engineering, March 2004, pp.206-210.
2. G. Atanov, E. Geskin, A. Kovaliov, A. Semko, (2004), "A Powder Hydro-Cannon at a Wide Range of the Parameters Change". *Prikladnaya Hidromekhanika*, Vol. 6 (78). № 3. - pp. 3 –9 (in Russian).
3. E.S. Geskin, O. Petrenko, O. Rusanova, A. Semko, (2006), "Strength Analysis and Optimization of the Barrel of a Powder Water Cannon" *Strength of Materials*, Vol. 38, No 2. pp. 206 – 213.
4. V. Samardzic, E. S. Geskin, G. A. Atanov, A. N. Semco, A. V. Kovaliov, (2007), "Liquid Impact Based Material Micro Forming Technology", *Journal of Materials Engineering and Performance*, Vol. 3, June, pp.375-389.
5. V. Samardzic, E.S. Geskin; G.A. Atanov, A.N. Semko, V.N. Kovaliov, (2008), "Investigation of the Material Welding Using The High Speed Liquid Impact", *Journal of Materials Engineering and Performance*, June 2008.
6. V. Samardzic, E, S. Geskin, ; G.A. Atanov, A.N. Semko, V.N. Kovaliov, (2008), "Investigation of the Liquid Impact Based Macro, Meso and Micro Forming Processes", *Journal of Materials Engineering and Performance*, June 2008.
7. E.S. Geskin, B. Goldenberg, G.A, Atanov, (2001), "Investigation of Metal Piercing Using High-Speed Water Slugs", Proceedings of 2001 WJTA American Waterjet Conference, Minneapolis, MN, Edited by M. Hashish, pp. 395-412.
8. O. Petrenko, E.S. Geskin, G.A. Atanov, A.N. Semko, B. Goldenberg, A. Semko, B. Goldenberg, (2002), "Numerical and Experimental Investigation of Formation of High-Speed Water Slugs", NSF Report to DMII, San Juan.
9. O. P. Petrenko, E.S. Geskin, G.A. Atanov, A.N. Semko, B. Goldenberg, (2002), "Numerical and Experimental Investigation of Formation of High Speed Water Slugs", *Proceedings of 16th International Conference on Water Jetting*, Ed. P. Lake, BHR Ltd, Cranfield Aix-en-Provence, France, Oct 2002, pp 533-547.
10. O. P. Petrenko, E.S. Geskin, G.A. Atanov, B. Goldenberg, A. Semko, (2002), "Investigation of Material Deformation by High Speed Water Slugs", *Proceedings of International Mechanical Engineering Congress and Exhibition (IMECE2002)*, Nov 2002, New Orleans, LA, Submitted for publication to Journal of Fluids Engineering.
11. Petrenko, E.S. Geskin, GA. Atanov, A.N. Semko and B. Goldenberg, (2003), "Investigation of Material Fracturing by the High Speed Water Slug",

- Proceedings of 2003 DMII NSF Grantees Conference*, Birmingham AL, Jan. 2003.
12. G.A. Atanov, A.N. Semko, O.P. Petrenko, E.S. Geskin, (2003) "The Peculiarities of the Powder Hydro Cannon Operation", *Proceedings of the 2003 International Mechanical Engineering Congress and Exhibition (IMECE2003)*, USA, Washington, D.C., November, (2003).
 13. O.P. Petrenko, V. Samardzic, E.S. Geskin, B. Goldenberg, G.A. Atanov, A.N. Semko, (2003) "Investigation of the High Speed Water Slugs", *Proceedings of the 2003 Water Jet Technology Conference*, Edited by M. Hashish, USA, Houston, TX, November, 2003.
 14. E. S. Geskin and D. Watts, (2003), "High Pressure Water Jets for Anti-Personnel Capability", Presentation at the Symposium *Nuclear Weapon Security Enhancement Summit*, Albuquerque, NM, April, 2003.
 15. Petrenko, E.S. Geskin, GA. "Atanov, A.N. Semko and B. Goldenberg, (2004), "Investigation of Material Fracturing by the High Speed Water Slugs," *Proceedings of 2004 DMII NSF grantees conference*, Dallas, TX, Jan.2004
 16. E.S. Geskin, V. Samardzic, O. Petrenko (2005), "Demonstration to the Division of Precision Munitions", Mines and Demolition Division of USARDEC.
 17. E.S. Geskin, V. Samardzic, O. Petrenko, T. Bitardse, G. Atanov, A. Semko, A. Kovaliov, O. Rusanova, (2005), "Feasibility Study of the Solid Freeform Fabrication of Heterogeneous Parts Using the Liquid Impact", *Proc. NSF DMII Grantees Conference. Scottsdale, Arizona*.
 18. O. Petrenko, E.S. Geskin, O. Rusanova, A. Semko, T. Bitardse "(2005), "Application of Numerical Techniques for Optimization of the Water Cannon Design" in *Proceedings of Waterjet Technology Association Conference*, Editor M. Hashish, August, Houston , TX; paper 3A-1.
 19. V. Samardzic, O.P. Petrenko, E. S. Geskin G.A. Atanov, A.N. Semko, A. Kovaliov, (2005), "Innovative Jet Based Material Processing Technology", *Ibid*, Paper2A-2.
 20. O.P. Perenko, E.S. Geskin, A.N. Semko , (2005), "Mechanics of the Powder Hydro Cannon for Incompressible Fluids", *Ibid*, 3B-3.
 21. V. Samardzic, O. Petrenko, E.S. Geskin, R. Petrova (2005), "Investigation of the Residual Material Deformation in the Course of Ballistic Testing" *Proceedings of ASM International Conference*, Pittsburg, PA.
 22. E.S. Geskin, O. Petrenko,(2006), "Potential Applications of Supersonic Liquid Streams in Direct Steelmaking", *Proceedings of Sohn International Symposium in Advanced Processing of Metals and Materials*, TMS, San Diego, V5, Aug 2006.
 23. Ernest S. Geskin, V. Samardzic, K. Kluz, O. Petrenko, W. A. Berger; J. Carter; M. Mazurkiewicz; R. Pell; R. Spalletta, (2006), "Experimental Study of Granite

Removal using High Speed Liquid Projectiles” , Final Report to Air Force/Scranton University, December, 2006.

24. V. Samardzic, E. S. Geskin, G. A. Atanov, A. N. Semco, A. V. Kovaliov, (2006), “Liquid Impact Based Material Micro Forming Technology”, Materials Science & Technology 2006 Conference and Exhibition, (MS&T '06), Cincinnati, Ohio, October 15-19, 2006.
25. V. Samardzic, E. S. Geskin; G.A. Atanov, A. N. Semko, A.V. Kovaliov, (2007), “Investigation of Metal Processing Using A High Speed Liquid Impact”, *Proceedings 2007 Conference of the Waterjet Technology Association*, Houston, Texas, August, 2007.
26. V. Samardzic, E.S. Geskin, G.A. Atanov, A.N. Semko, A.V. Kovaliov (2007), “Investigation of Metal Microforming Using High Speed Liquid Impact”, Ibid.
27. V. Samardzic, K. Kluz, O. Petrenko, E.S. Geskin, M. Mazurkievitz, , A. Berger, (2007), “Investigation of Granite Boring Using High Speed Liquid Impact”, Ibid.
28. K. Kluz, E.S. Geskin, O.P. Petrenko, (2007), “Numerical Approximation of Propellant Driven Water Projectiles Launchers”, Ibid.
29. E. S. Geskin, O. Petrenko, V. Samardzic, K. Kluz, (2008) “Supersonic Liquid Projectiles: a Novel Materials Processing Tool”, FLUIDS'08, International Conference of WSEAS, Acapulco, Mexico, January, 2008.
30. E. S. Geskin. (2008), “High Speed Liquid Projectile: an Efficient Energy Conversion Tool”, Entropy Challenge, MIT Press.
31. O. Petrenko, (2006), “Investigation of Formation and Application of High Speed Liquid Projectiles”, Ph.D. Dissertation, NJIT.
32. J. J. Kollé, (1968), “Compressed Water Cannons for Civil Engineering”, Tempres Technologies Inc., Kent, WA, USA.
33. M. C. Rochester. J.H. Brunton, (1972) “High Speed Liquid Jets on Solids”, *First International Symposium on Jet Cutting Technology*, Coventry, UK, 2007.
34. G. A. Atanov, (1991), “The Impulsive Water Jet Device: A New Machine for Breaking Rocks”, *International Journal of Water Jet Technology*, 1991.
35. G. A. Atanov, (1998), “Impulsive Hydrodynamic Method of Breaking Rocks and Concrete”, *International Journal of Water Jet Technology*, 1998.
36. B. Lemcke, W. Locher, (1975), “Water Jet Driven Shock Waves in Gases”, *Proceedings of 10th International Shock Tube Symposium*, Ecublens, Switzerland, 1975.
37. N. Torasaki, H. Wada, S. Fujikawa, N. Takasugi, (1997), “Cavitation and Erosion in Submerged Waterjet”, *Proceedings of International Conference- AIRAPT-16 and HPCJ-38- ON HIGH Pressure Science and Technology*, Toyama, Japan, 1997.

38. M. Noumi, K. Yamamoto, (1992), "Flow Characteristics and Impact Phenomena of Pulsed Water Jets", Proceedings of Water Jet Technology Conference, Taiwan, 1992.
39. T. Z. Blazynsky, (1982), Materials at High Strain Rates, Elsevier Applied Science, London and New York, 1982.
40. ASM HANDBOOK, (2006), Metalworking: Sheet Forming, Volume 14B, ASM International, OH, 2006.
41. M. D. Verson, (1969), Impact Machining, Verson-Allsteel Company, 1969.
42. J.S. Reinhart. (1963), *Explosive Working of Metals*, Macmillan, 1963.
43. A.V. Krutin et.al. (1975). *Explosion Deformation of Metals*, Metallurgia, Moscow (in Russian), 1963.
44. V. Samardzic, O. Petrenko, E. S. Geskin, G.A. Atanov, A. N. Semco "Innovative Jet-based Material Processing Technology", 2005 WJTA American Waterjet Conference and Exhibition, ST Louis, MO.
45. D. Khuniaki, (2000), "An Overview of Micro-Forming Research and Development in Japan", Micro / Meso Mechanical Manufacturing Workshop, Gifu University, Yanagido, Gifu, Japan, 2000.
46. Lee Hye-Jin, Lee Nok-Kyu, Lee Sang-Mok, Lee Geun-An, Kim Seung-Soo, "Development of Micro Metal Forming Manufacturing System", Materials Science Forum, Vols. 505-507, 2006, pp19-24, Trans Tech Publications, Switzerland.
47. Friedrich-Alexander University, Micro Forming Technology, http://www.lft.uni-erlangen.de/SEITEN/GRUPPEN/MUT/index_e.html
48. www.masmicro.net, "New Tool Technology by Direct Heating with Laser Radiation" Mass Micro News Letter, Issue 4, September 2006, <http://www.masmicro.net/Article/A243.pdf>